The effect of obstetric forceps placement on the fetal scalp using finite element analysis

Omar Sharif Valladolid García

School of Computing Sciences

A thesis submitted for the degree of Doctor of Philosophy

July 2025

Abstract

A biomechanical model of a fetal head under the forces of compression and traction exerted by the application of obstetric forceps is presented in this dissertation. This model allows the quantitative evaluation of fetal head moulding as a result of the use of this medical instrument.

The use of obstetric forceps in an operative vaginal delivery procedure plays an important role to help extracting the baby from its mother when the efforts of the latter are insufficient or when labour is not progressing as expected. When the instrument is used by qualified obstetricians the rate of success is very high, but when the operator has insufficient training or the delivery is complicated it can lead to maternal or fetal trauma or even neonatal fatalities.

Although moderate fetal moulding is expected when the baby is passing through the birth canal, the incorrect placement of the obstetric forceps can create excessive moulding affecting the fetus health severely.

This research presents a dynamic, non-linear model of the deformation of a complete fetal head being subjected to the forces exerted by obstetric forceps when placed symmetrically and asymmetrically.

The current research considers the geometry of the different parts of the fetal head like the cranial vault, face bones, base bones, fontanelles and sutures. As well as the different material properties each of these parts have. The geometry of a model of the obstetric forceps was created to perform compression and traction on the fetal head.

A Dynamic Finite Element analysis was used to simulate the effect of obstetric forceps on the fetal head, expanding the current research in this field.

The research performed experiments on the compression force and traction at different levels. The first experiment using basic geometric shapes such as curved plates and a sphere as a representation of the forceps blades and fetal head respectively. The second replacing the curved plates for the real obstetric forceps blades model and the sphere for the model of the fetal head. A third experiment considers the rotation of the baby head. These experiments helped to evaluate qualitatively the deformation of the fetal head caused by the obstetric forceps placement.

Experiment results show a realistic contact interaction between the baby head and the obstetric forceps, realistic deformation of anterior and posterior fontanelles caused by the compression exerted by the forceps blades and the difference in deformations between symmetric and asymmetric forceps placements.

Acknowledgements

I wan to thank my family who gave me their immense love and support to overcome any obstacle, and who have been always there when I have needed them, especially to my parents and my brother that look after me from heaven.

I dedicate this research to my beloved wife and daughter, who have been by my side every stage of this journey and have helped me and cheered me until the end.

Special thanks to my supervisor Dr. Rudy J. Lapeer, for all his guidance, teachings, support and help to complete this thesis. I hope I have contributed my grain of sand in this beautiful field of research.

Finally I would like to thank all my old and new friends for all their good wishes and for being aware of my work.

Contents

List of Figures

List of Tables

List of Algorithms

List of Listings

List of Acronyms

ACOG The American College of Obstetricians and Gynaecologists. 25, 26

AoP Angle of Progression. 6

AP Anteroposterior. vi, 15, 16, 26

AR Augmented Reallity. 41

AVB Assisted Vaginal Birth. 1, 24

BC Boundary Condition. iii, iv, viii, ix, xii, xiii, 74, 75, 88, 109, 110, 116, 128, 135, 149

BH Baby Head. 58, 60, 67, 68, 102

BMC BioMed Central. 26

CAE Computer-Aided Engineering. 54

CS Caesarean Section. 1, 36

DFEA Dynamic Finite Element Analysis. 49, 149

DoF Degree Of Freedom. 36

EAS External Anal Sphincter. xxi

ECS Emergency Caesarean Section. 25

FB Forceps Blades. 68

FE Finite Element. 47

FEA Finite Element Analysis. ii, viii, ix, 2, 40, 44, 47, 49, 54, 75, 100, 109, 198

FeH Fetal Head. xii, 58, 60–63

FeHS Fetal Head Station. 5

FEM Finite Element Method. 47, 69, 70

FEMo Finite Element Model. 45

FHM Fetal Head Moulding. 10, 44, 49

FLB Forceps Left Blade. ix, x, 67, 68, 73, 76–85, 88–98, 107, 108, 110–114, 116–126, 128–133, 135–143, 146

FRB Forceps Right Blade. ix, x, 67, 68, 73, 76–85, 88–98, 107, 108, 110–114, 116–126, 128–133, 135–143, 146

HFE Hydrostatic Fluid Elements. 45

IAS Internal Anal Sphincter. xxi

ICP Intra-cranial Pressure. 45

IFeH Improved Fetal Head. viii–x, xii, xiii, 63–65, 102–108, 110–115, 117–147

IFeHC Improved Fetal Head Constraint. ix, 109, 110, 116, 135

IVD Instrumental Vaginal Delivery. 3, 24, 25, 33, 42

LB Left Blade. ix, 73, 74, 108

LB_C Left Blade Constraint. viii, ix, xii, xiii, 74–76, 83, 88, 89, 96, 109, 110, 116, 117, 122, 129, 135, 136, 141

LOA Left Occiput Anterior. 19, 26, 27

LOP Left Occiput Posterior. 20, 26, 27

LOT Left Occiput Transverse. 20

MRI Magnetic Resonance Images. 37

MV Mentovertical. 15

NHS National Health Service. 1, 24

OA Occiput Anterior. 19, 27

OF Occipitofrontal. 15

OFD Obstetrics Forceps Delivery. 41

OOP Object Oriented Programming. 178, 183

OP Occiput Posterior. 19, 27

OVD Operative Vaginal Delivery. i, vii, xii, 1–3, 24, 25, 33, 34, 40, 42, 54, 150

PDE Partial Differential Equation. 47

PDF Portable Document Format. 175

PPH Postpartum hemorrhage. xx

RB Right Blade. ix, 74, 108

RB_C Right Blade Constraint. viii, ix, xii, xiii, 74–76, 83, 88, 89, 96, 109, 110, 116, 117, 122, 129, 135, 136, 141

RCOG The Royal College of Obstetricians and Gynaecologists. 1

ROA Right Occiput Anterior. 19, 26, 27

ROP Right Occiput Posterior. 20, 26, 27

ROT Right Occiput Transverse. 20

SFEA Static Finite Element Analysis. viii, 46, 48, 149

SMB Submentobregmatic. 15

SMV Submentovertical. 15

SOB Suboccipitobrematic. 15

SOF Suboccipitofrontal. 15

SOM Supraoccipitomental. 15

SPH Sphere. viii, 58–60, 70, 72–74, 76–86, 89–100

SPH_C Sphere Constraint. viii, 74, 75, 88

STL Stereolithography. 175

SVG Scalable Vector Graphics. 175

USD Universal Scene Description. 175

VE Vacuum Extractor. vii, 1, 24, 25, 40, 41, 45

WHO World Heatlh Organization. 1

Glossary of medical terms

Sources of this glossary are [1, 2, 3, 4, 5, 6, 7, 8]

Postpartum hemorrhage (PPH) Severe vaginal bleeding after childbirth. 36

Abrasion A minor wound in which the surface of the skin or a mucous membrane is worn away by rubbing or scraping. 33

Anal Incontinence Inability to control bowel movements, causing involuntary loss of faeces or flatus that is adversely affecting the patient's quality of life. 33

Bruise An area of skin discoloration caused by the escape of blood from ruptured underlying vessels following injury. 33

Calvarium Portion of a skull including the braincase and excluding the lower jaw or lower jaw and facial portion. 44

Cephalhaematoma A swelling on the head caused by a collection of bloody fluid between one or more of the skull bones (usually the parietal bone) and its covering membrane (periosteum). 33

Cephalic presentation Characterized by the head being the presenting part in childbirth. 5

Cephalopelvic Disproportion A condition where the infant's head is larger than the mother's pelvis. 7

Cervical Dilatation The widening of the cervix, the entrance to the uterus during childbirth. vi, 4, 5, 7, 36

Cervical effacement The thinning or taken up of the cervix prior dilation. 4, 5, 36

Cervical ostium or cervical os Part of the cervix, which connects the main part of the uterus to the vagina. vi, 5, 7

Contraction Shortening of a muscle in response to a motor nerve impulse. This generates tension in the muscle, usually causing movement. 7

Flatus Intestinal gas, passed through the rectum, composed partly of swallowed air and partly of gas produced by bacterial fermentation of intestinal contents. xx

Haematoma An accumulation of blood within the tissues that clots to form a solid swelling. Injury, disease of the blood vessels, or a clotting disorder of the blood are the usual causative factors. 33

Haemorrhage Escape of blood from a ruptured blood vessel, externally or internally. 33

Intracranial Within the skull. 33

Introitus In anatomy, an entrance into a hollow organ or cavity. 26

Ischial Tuberosity A lump of bone forming the ring of the ischium. 42

Labia Plural (*see* labium). 26

Labium A lip-shaped structure, especially either of the two pairs of skin folds that enclose the vulva. The larger outer pair are known as the labia majora and the smaller inner pair the labia minora. xxi

Laceration A tear in the flesh caused by a blunt object producing a wound with irregular edges. 33

Macrosomia Abnormally large size. In fetal macrosomia the baby is large for its gestational age. 30

Morbidity The state of being ill or having a disease. 24, 33

Moulding The change of shape of an infant's head during labour, due to movement of the bones of the skull, brought about by the pressures to which it is subjected when passing through the birth canal. 7, 44

Multigravida A woman who has been pregnant at least twice. 4

Multipara A woman who has given birth to a live child after each of at least two pregnancies. xxi, 4, 7

Multiparous Adjective (*see* multipara). 4, 30

Nullipara A woman who has never given birth. xxi

Nulliparous Adjective (*see* nullipara). 30

Palsy Paralysis of a part of the body causing weakness of the muscles. 33

Pelvic floor Forms a part of the birth canal. 8, 26, 27

Perineal Adjective (*see* perineum). vii, 8, 34

Perineal tear An injury to the perineum (perineal trauma), which may be sustained during childbirth. Perineal tears can be classified by degree. Second-degree tears involve the perineal muscles but not the anal sphincter. Third-degree tears involve the anal sphincter complex: the external anal sphincter (External Anal Sphincter (EAS)) and internal anal sphincter (Internal Anal Sphincter (IAS)). These are subclassified as 3a (less than 50% of EAS thickness torn), 3b (more than 50% of EAS thickness torn), and 3c (IAS torn). Fourth-degree tears involve the anal sphincter complex (EAS and IAS) and the rectal mucosa. xxii, 33

Perineal trauma A physical wound or injury in the perineum (*see* perineal tear). xxi

Perineum Region of the body between the anus and the urethral opening, including both skin and underlying muscle. In females it is perforated by the vaginal opening. xxi, xxii, 8, 26

Primigravida A woman pregnant for the first time [1]. vi, 4, 5

Primipara(e) A woman who has borne only one offspring. xxii, 7

Primiparous Adjective (*see* primipara). 4

Trauma A physical wound or injury, such as a fracture or blow. 24, 33

Urinary Incontinence The inappropriate involuntary passage of urine, resulting in wetting. 33

Chapter 1

Introduction

According to the National Health Service (NHS) maternity statistics data in England, over the last decade the use of medical instrumentation has played an important role in childbirths, where on average around 12% of them were by Assisted Vaginal Birth (AVB) [9], also known as Operative Vaginal Delivery (OVD). Considering the data from the World Heatlh Organization (WHO), in the same period of time, an average of almost 800,000 births were registered in England [10] and this percentage of OVD represented approximately 96,000 of cases in the past ten years.

AVB is used when labour is not progressing as expected. There are two potential AVB methods depending on the circumstances, i.e. Obstetrics Forceps and Vacuum Extractor (VE) or ventouse [11].

Although in the last ten years we have seen a fall in the use of the VE and an increase in the use of the Obstetric Forceps in England, obstetricians should develop competency in the use of both to have a greater scope of clinical scenarios [12].

Since AVB remains an important option for obstetricians to prevent and/or reduce Caesarean Sections (CSs) - and when performed correctly by qualified doctors - both methods are safe for the mother and the baby. But it is still important to know the consequences of the misuse of medical instruments during AVB, as a number of neonatal fatalities associated with traumatic birth-related injuries have been reported to The Royal College of Obstetricians and Gynaecologists (RCOG)[13]. The correct use of obstetric forceps in AVB is imperative to avoid adversely affecting the fetal head and the maternal pelvic floor muscles.

1.1 Research objectives

The main aim of the research presented in this thesis is to create a computer-based simulation of the compression and traction effects of obstetric forceps placement on the fetal scalp when used during a prolonged second stage of labour.

More specifically, this will include the following objectives:

- As a clinical objective, the compression and traction effect of obstetric forceps when symmetrically placed around the fetal scalp.

- As a clinical objective, the compression and traction effect of obstetric forceps when asymmetrically placed around the fetal scalp, which usually occurs because of asynclitism or incomplete internal rotation.
- As a scientific objective, using dynamic Finite Element Analysis (FEA) with contact mechanics constraints between the deformable fetal head and the rigid forceps to meet the clinical objectives.

The data obtained from this study will provide obstetricians with information about the forceps contact pressure, the shear forces on the fetal scalp and the potential damage they may cause following forceps application.

1.2 Thesis structure

- **Chapter 2**: This chapter describes the fundamental knowledge about childbirth and its different stages. This includes the anatomy of the fetal head, the anatomy of the maternal pelvis, OVD and the obstetric forceps. It also includes a literature review of relevant work related to childbirth, fetal head moulding and forceps placement on the fetal head.
- **Chapter 3**: Gives details about the methods and tools utilized to create and modify the 3D models, the proposed improvements in the 3D models compared with the ones used in previous researches, and the development of a series of experiments with different outcomes.
- **Chapter 4**: Describes the experiments performed, the results obtained from them and the discussion of the results.
- **Chapter 5**: Provides the conclusions obtained from this research and the potential improvements as part of future work.

Chapter 2

Background

2.1 Childbirth fundamentals

From a medical-obstetric perspective, childbirth is described as the process where the mother delivers the fetus through a series of physiologic changes in her body. This process involves three well defined but different stages:

1. The first stage: Starts with increasing frequency of uterine contractions and ends with the full dilation of the uterine cervix.

2. The second stage: Starts at full dilation of the uterine cervix and ends with the expulsion of the fetus from the womb.

3. The third stage: Following the expulsion of the fetus, the placenta is delivered. Since the aim of this research is to analyse the effects of the forceps on the fetal head, this stage will not be discussed further.

From an engineering and mechanics perspective, childbirth is a complex process that involves body parts from the mother and the baby that are moving and having contact at the same time. This include muscles, tendons, bones, fluids, other soft tissues and their respective material properties that make a physics-based childbirth simulation challenging.

For this research, it is important to know the characteristics of the fetal head and the maternal pelvis, the different parts they have and their properties; as well as the close relation between them, and the role they play in labour to successfully and safely deliver the fetus without complications in the process.

In the next sections, I will cover the fundamental knowledge around childbirth. This includes the description of the first and second stages of labour, fetal head and skull anatomy, the maternal pelvis anatomy, the definition of OVD, the different modes of Instrumental Vaginal Delivery (IVD), the Obstetric Forceps, its different types, its constituent parts, its mode of operation and its potential risks. A review of the literature related to this work is also described.

2.2 Labour stages

Labour refers to the long process that the mother's body goes through to prepare for childbirth. It involves physiological, physical, and psychological changes that can take days or even weeks to get the body ready to give birth [14].

Labour is identified by the presence of regular (and usually painful) uterine contractions that increase in frequency and intensity with progressive stimulation of cervical effacement and dilation, and with descent of the fetus through the pelvis, finalizing in the vaginal birth of the baby, and followed by the expulsion of the placenta and membranes [15, 16].

As mentioned in section 2.1, labour is divided mainly in three stages [14, 4, 17, 16].

2.2.1 First stage

This stage last from the onset of established labour until complete dilation of the cervix [4]. It has a duration between 6 and 18 hours for primiparous patients and between 2 and 10 hours for multiparous patients [14]. According to Walsh [16], it can be between 12 and 14 hours for a primigravida and between 6 to 10 hours for a multigravida.

The first stage of labour is divided in two phases [14] (see Figure 2.1):

- **Latent phase:** In this phase the cervical effacement or thinning of the cervix and early dilatation take place.
- **Active phase:** This stage starts when the cervix is dilated between 2-4 cm when regular uterine contractions are taking place [14, 16]. The cervical dilatation is occurring rapidly, and the minimal dilation for primiparous and multipara women is nearly the same, about 1 and 1.2 cm/hr respectively.

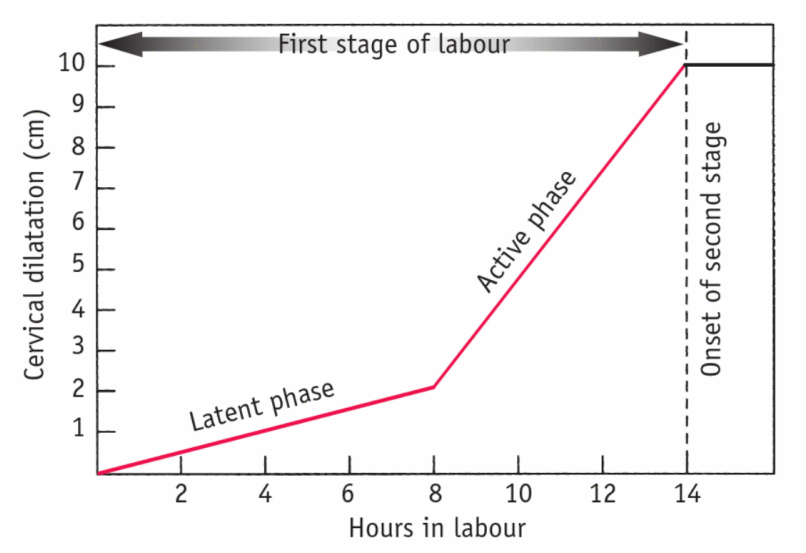

Figure 2.1: Relationship of cervical dilatation (cm) and phases of labour (hours) in the first stage of labour (taken from [16]). Cervical dilatation occurs at a slower rate per hour in the latent phase vs a faster dilatation rate per hour in active phase.

During this stage, the progress of labour is measured considering cervical effacement, cervical dilatation and descent of fetal head in cephalic presentation (Figure 2.2).

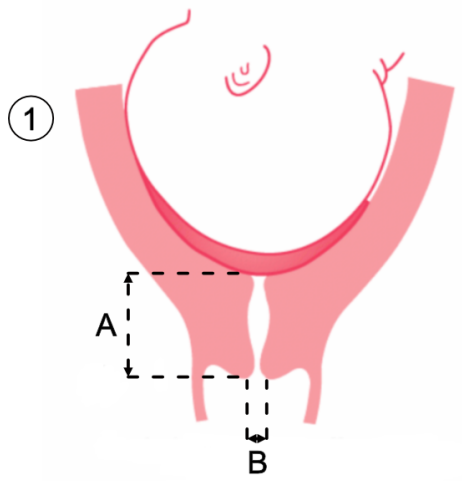

(a) Cervical canal before effacement and dilatation.

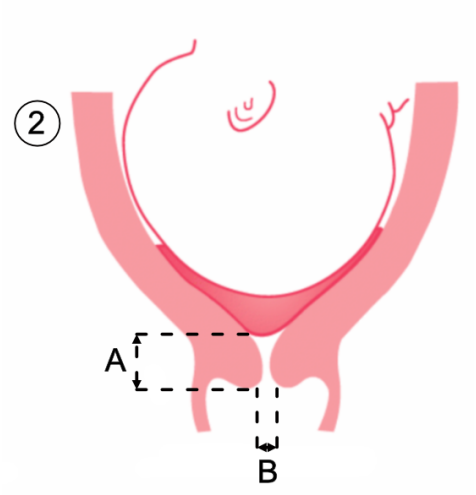

(b) Partial effacement.

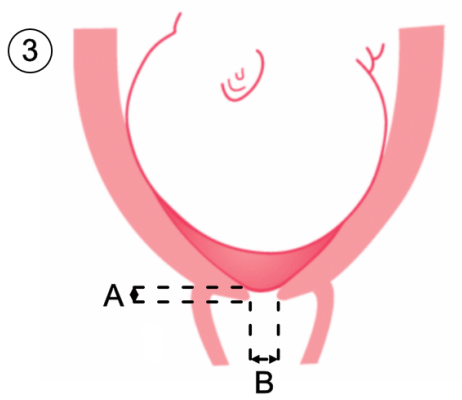

(c) Cervix effaced and dilating.

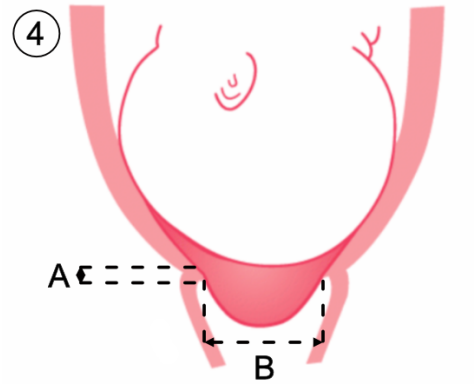

(d) Cervix almost fully dilated.

Figure 2.2: Different stages of cervical effacement (A) and cervical dilatation (B) in a primigravida (modified from [16]). Distance A and B show the thinning and widening of the cervix respectively during the first stage of labour. Figure 2.2a, shows the cervical canal before labour where there is no effacement neither dilation. Figure 2.2b shows the cervical ostium partially effaced or partially thinned (distance A is shorter compare to previous state) but not dilated or widened (distance B stays the same). Figure 2.2c shows the cervix effaced and starting to dilate (distance A is even shorter and distance B starts to increase). In Figure 2.2d, the cervix is effaced and nearly fully dilated (distance A is very small and distance B has increased almost at maximum).

The descent of the fetus in a cephalic presentation is measured by the level of the presenting part in relation to the maternal ischial spines as quantified by the Fetal Head

Station (FeHS)[1], they are palpable slight protuberances on either side of the bony pelvis called ischial tuberosities. Descent should be progressive and it is measured in centimetres as indicated in Figure 2.3 [16].

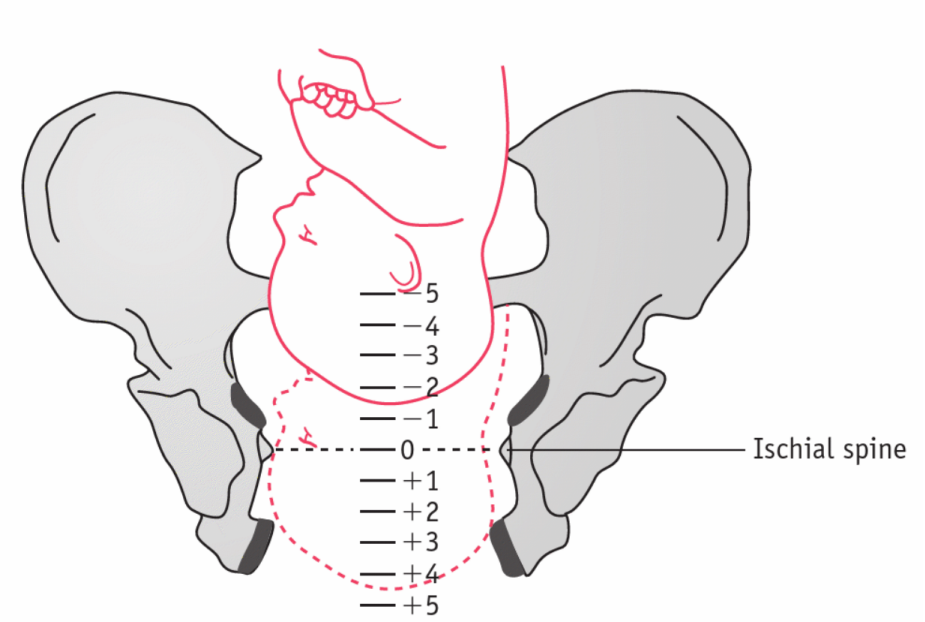

Figure 2.3: Fetal head station is measured from −5cm to +5cm in relation to maternal ischial spines (taken from [16]). Negative and positive values indicate that the presenting part is above or below the ischial spines respectively, while zero indicates that the presenting part is at the level of the ischial spines.

This stage ends when the cervix is fully dilated at approximately 10 cm in diameter. Figure 2.4 shows the cervix at the beginning of the stage where it can be seen that the cervix is not dilated, and its counterpart at the end of the stage where the cervix is fully dilated.

[1]Although this method is widely used, recent studies demonstrated that other measurements like the Angle of Progression (AoP) should also be considered [18], which is not considered in this work and its discussion is out of the scope of this research.

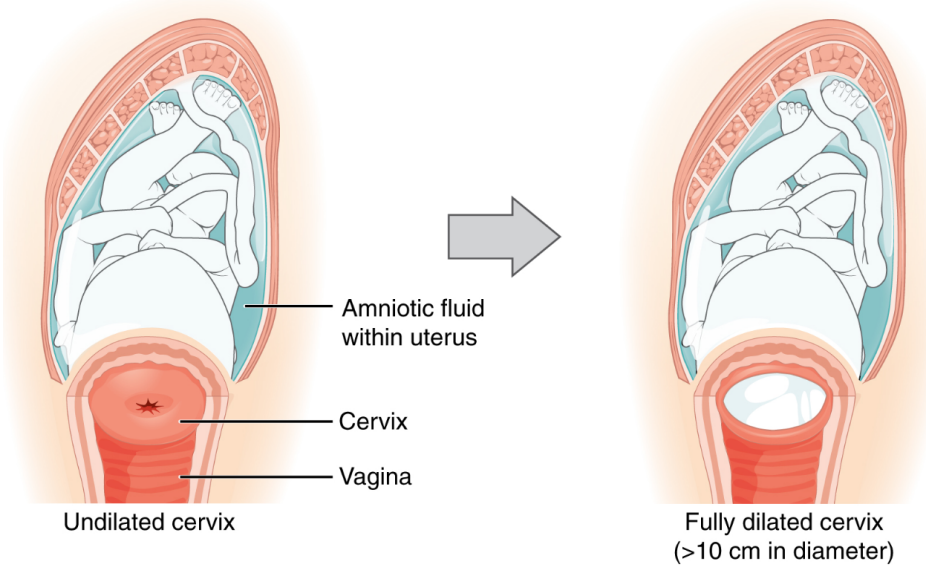

Figure 2.4: Cervix comparison at the start (left) and at the end (right) of the first stage of labour (taken from [19]). Left image shows the birth canal with a non-dilated cervix, and right image shows cervix fully dilated.

2.2.2 Second stage

The second stage commences after completion of the Cervical dilatation, it has a duration between 30 minutes to 3 hours for primiparas and between 5 to 30 minutes for multiparas [14].

Distinctive physiological changes that occur between the late first stage and early second stage of labour around the time of full dilation of the cervix are called transition, where during or following this phase, the woman has a desire to bear down with each contraction, typically cervical ostium will be between 7 and 9 cm dilated [14, 20].

The mother experiences uterine contractions and abdominal pressure, these two forces combine to expel the fetus making the presenting part to descent through the birth canal. The compression force applied over the fetal head by the bony pelvis, creates an alteration of the shape of the fetal skull structure called **Moulding**. This skull shape alteration is normal due to the forces applied, but in a Cephalopelvic disproportion presentation, where the relation between the size of the fetal head and the maternal pelvis is not the same, the amount of moulding can be more prominent.

As labour progresses and the fetus is pushed through the birth canal, a series of motions are induced to accommodate its way along the contours of the maternal pelvis, these set of movements are known as **Mechanisms of Labour**, also known as the **Cardinal Movements of Labour**. In a vertex presentation, either occipitoanterior or occipitoposterior position at engagement, the mechanism is described as follows [14, 20]:

- Descent: The fetal head moves into the pelvis due to the uterine contractions, maternal bearing-down efforts, and gravity if the patient is upright. When the widest diameter of the presenting part enters the pelvis, engagement occurs (see Figure 2.5a).

- Flexion: Cervical spine flexion (fetus chin is approaching the chest) is increased by the resistance of the cervix, walls of the pelvis and the pelvic floor.
- Internal rotation: The occiput encounters resistance from the pelvic floor and rotates forward around 45° towards the hollow of the sacrum. Here the fetal head station is zero (see Figure 2.5b).
- Crowning: The internal rotation allows the head to emerge in the longest diameter of the pelvic floor, the occiput moves under the pubic arch and the head is crowned. At this point the fetal head station is +5.
- Extension: It takes place to allow the bregma, forehead, face and chin to pass over the perineum.
- Restitution or external rotation: Once the head is delivered it returns to its original position to align itself with the shoulders and back.
- Internal rotation of shoulders: The shoulders undergo an internal rotation similar to that of the head, this rotation follows the direction of the restitution allowing the shoulder to align themselves anterioposteriorly within the pelvis.
- Expulsion: Following the rotation of the external rotation of the head, the anterior shoulder delivers under the symphysis pubis followed by the posterior shoulder over the perineal and then the body of the baby.

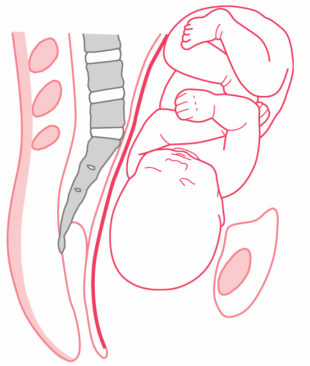

(a) Descent of fetus.

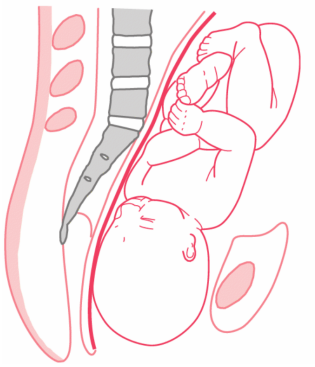

(b) Internal rotation of head.

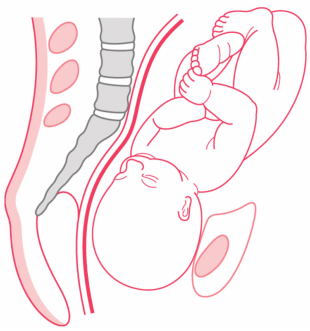

(c) Internal rotation.

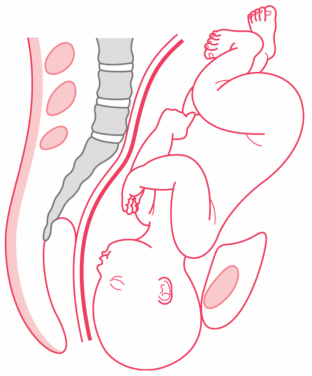

(d) Head crowned.

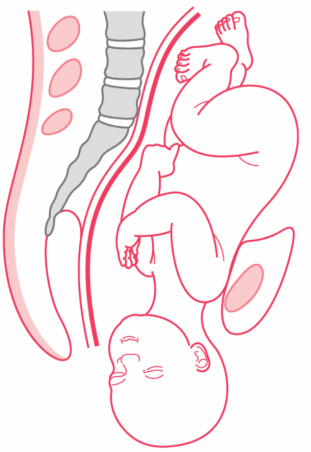

(e) Restitution.

(f) Internal rotation of shoulders.

Figure 2.5: Mechanism of labour or cardinal movements of labour with mother in upright position (taken from [16]).

2.2.3 Anatomy of fetal head

The head of a newborn baby is a complex structure and the largest part of the fetus; it is formed by multiple separated flat bones connected by fibrous tissues with soft gaps between

them [21], and mainly designed to protect the brain from injuries, but also to facilitate the baby to pass through the birth canal. At about 40 weeks of gestation, when the baby is about to be born, the fetal head presents a distinctive structure that allows the head to be compressed to some degree which is called Fetal Head Moulding (FHM). A normal degree of FHM will not cause damage to the external and internal structures of the fetal head [22] though excessive FHM may have adverse effects on the fetal scalp and brain.

The fetal skull has three main parts (see Figure 2.6):

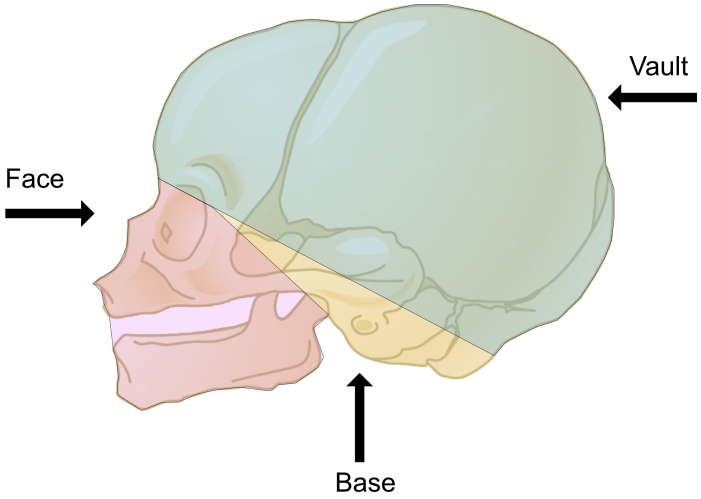

Figure 2.6: Lateral view of the main parts of the fetal skull; face (red region), vault (green region) and base (yellow region) (modified from [14]).

Base: It is the hardest and incompressible part of the fetal head, its parts are large, ossified, and firmly united bones. This strong bottom structure, helps to protect the brain steam and its connections with the spinal cord. Also is the part that connect the head with the rest of the body through the neck.

Vault: Also known as *cranium*, this part of the fetal head is responsible to protect the brain and it is formed with five different bones (see Figure 2.7). The vault area extends from the orbital ridges to the nape of the neck.

- **Two frontal bones:** These bones form the sinciput (see Section 2.2.3.3) or forehead. The ossified central area of each frontal bone is called *frontal eminence*.
- **Two parietal bones bilaterally:** They are located in each side of the vault, the ossification centre of each bone is called *parietal eminence*.
- **One occipital bone posteriorly:** It is located at the back of the vault and part of it contributes to the base of the skull. Its ossification centre is called *occipital protuberance*.
- **Two temporal bones:** They are located at each side of the vault, below the parietal bone.

Cranial bones are thin, i.e. less than 1 mm in thickness [23], compressible and weakly ossified. They are interconnected by elastic and resistant membranes called *sutures* and *fontanelles*. These membranes allow the cranial vault to modify its shape under pressure to conform to the maternal pelvis. The fontanelles can be felt on vaginal examination and help to asses the fetal station, which is defined in terms of the position of the fetal presenting part relative to the pelvic sacrum [4].

Face: Consists of fourteen small bones which are incompressible and are firmly united. These bones are located between the skull base and the cranial vault bones. The face area extends from the orbital ridges to the junction of the chin and the neck.

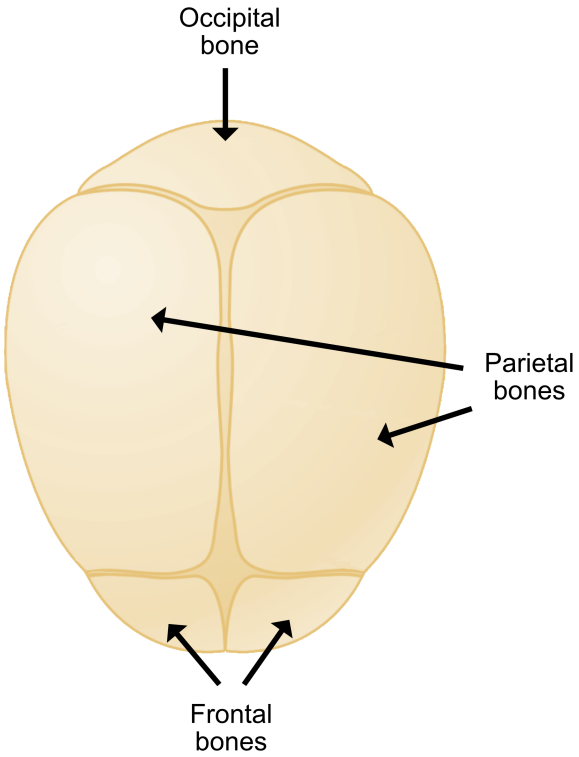

Figure 2.7: Superior view of the fetal skull showing the different cranial bones (modified from [14]).

2.2.3.1 Sutures

The membranes that fill the space between the bones are called **sutures**. They are soft fibrous tissues and due to the way the bones are located across the cranium, they can be categorized as (see Figure 2.8):

- **Frontal suture:** Unite the frontal bones and is central to the brow.
- **Coronal suture:** Links the frontal bones with the parietal bones.
- **Sagittal suture:** Connects the two parietal bones at the top of the cranium.
- **Lambdoid suture:** Unite the parietal bones with the occipital bone.

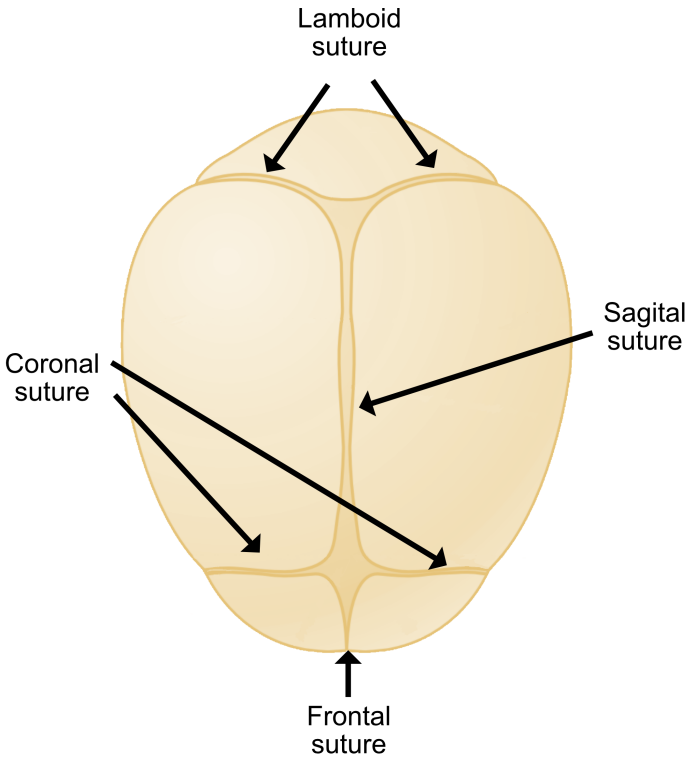

Figure 2.8: Superior view of the fetal skull showing the different sutures (modified from [14]).

2.2.3.2 Fontanelles

They are membranes filling the spaces where three or more sutures intersect with each other, and there are four types of them (see Figure 2.9):

- **Anterior or bregma:** It is a diamond-shaped membrane that connects the sagittal suture, coronal sutures and fontal suture, usually measures approximately between 2 and 2.5 cm across and between 2.5 to 3 cm long.
- **Posterior or lambda:** It has more a triangular shape, like a Y, or T shape that connects the lambdoid sutures with the sagittal suture.
- **Anterolateral or temporal:** It is located between the temporal, frontal and parietal bones. One of each side of the head.
- **Posterolateral or mastoid:** It is found between the temporal, parietal and occipital bones. One of each side of the head.

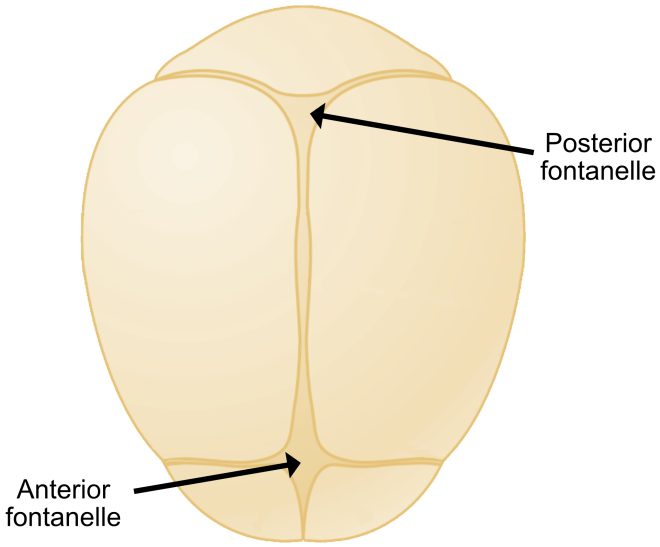

(a) Superior view (modified from [14]).

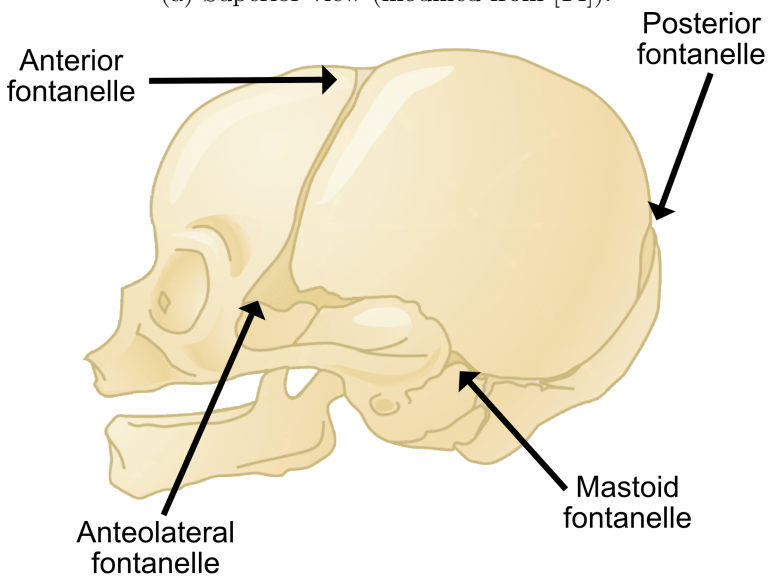

(b) Lateral view (modified from [14]).

Figure 2.9: Fetal skull showing the different fontanelles from superior and lateral views.

2.2.3.3 Landmarks

The fetal skull has a number of distinctive landmarks which help to describe the diameters start and end from front to back (see Figure 2.10).

- **Nasion:** Located in the front part of the head, belonging to the face region, it is the point where the root of the nose starts from top to bottom.
- **Glabella:** Is is located in the front part of the head, belonging to the vault region, it is the elevated protuberance between the orbital ridges.

- **Sinciput or brow:** Belongs to the vault region, it is the area between the glabella and the anterior fontanelle or bregma.
- **Anterior fontanelle landmarks:** Located in the top part of the head, it belongs to the vault region, and it is the area that fills the gap between the two frontal bones and the two parietal bones (see Section 2.2.3.2).
- **Vertex:** Belongs to the vault region, it is the area bounded by the anterior and the posterior fontanelle, and the parietal eminences.
- **Posterior fontanelle landmarks:** Located in the back of the head, it belongs to the vault region, and it is the area that fills the gap between the two parietal bones and the occiput bone (see Section 2.2.3.2).
- **Occiput:** It is located at the back of the head, it belongs to the vault region, and it is the area over the occipital bone extending from the posterior fontanelle to the nape of the neck (inferior to the lambdoid sutures).

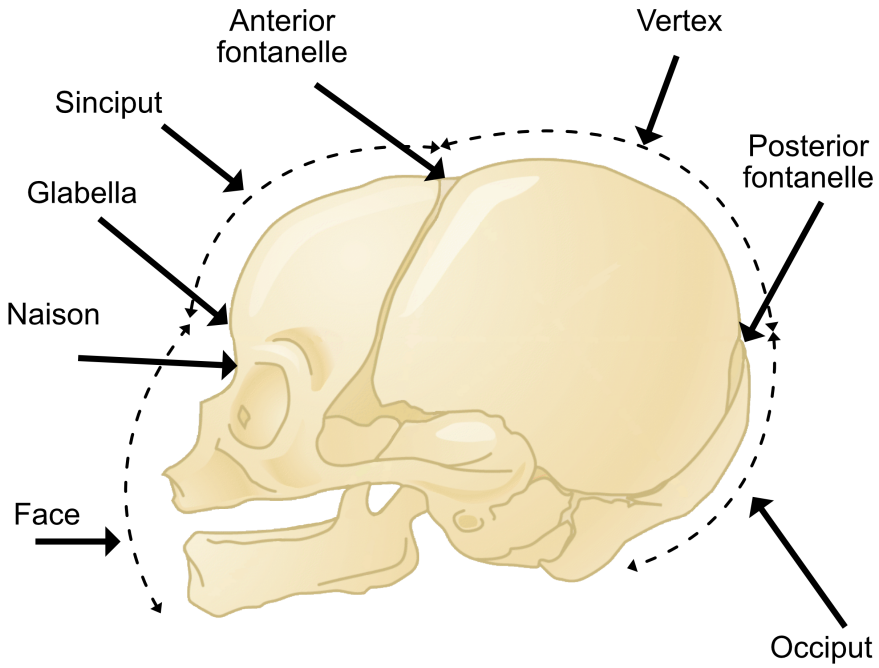

Figure 2.10: Lateral view of fetal skull showing the different landmarks (modified from [14]).

2.2.3.4 Measurements

The presentation and position of the fetal skull play an important role during the birth process, because the obstetrician and/or midwife use this information to determine the ease with which the fetus passes through the birth canal, and if any decision needs to be taken on position in labour [14, 24, 4]. To asses the size of the the fetal skull in relation to diameters of the maternal pelvis, a number of diameters of the fetal skull have been

measured corresponding to most common postures adopted by the fetal head as it enters the pelvic brim. It is important to highlight that these measurements are approximations and can vary depending on the size and weight of the baby.

2.2.3.4.1 Anteroposterior diameters The Anteroposterior (AP) diameters presenting to the maternal pelvis depends on the degree of flexion or extension of the fetal head, which is influenced by the presentation and position of the fetal head in relation to the pelvic brim.

- **Suboccipitobrematic (SOB):** AP diameter of approximately 9.5 cm, when the head is well flexed. It extends from the undersurface of the occipital bone at the junction with the neck to the center of the anterior fontanelle.
- **Occipitofrontal (OF):** AP diameter of approximately 11 cm, when the head is deflexed. It extends from the external occipital protuberance to the glabella.
- **Suboccipitofrontal (SOF):** AP diameter of approximately 10 cm, when the head is almost completely flexed. It extends from the junction of the head with the neck below the occipital protuberance to the centre of the frontal suture.
- **Supraoccipitomental (SOM) or Mentovertical (MV):** AP diameter of approximately 13.5 cm, presents in a brow presentation. This diameter is the longest AP diameter of the head. It extends from the central point of the top of the head at the vertex to the point of the chin.
- **Submentovertical (SMV):** AP diameter of approximately 11 cm, when the head is not fully extended in a face presentation. It extends from the junction of the chin with the neck to the highest point on the vertex.
- **Submentobregmatic (SMB):** Anterolateral diameter of approximately 9.5 cm, in face presentation. It extends from the junction of the neck and lower jaw to the centre of the anterior fontanelle.

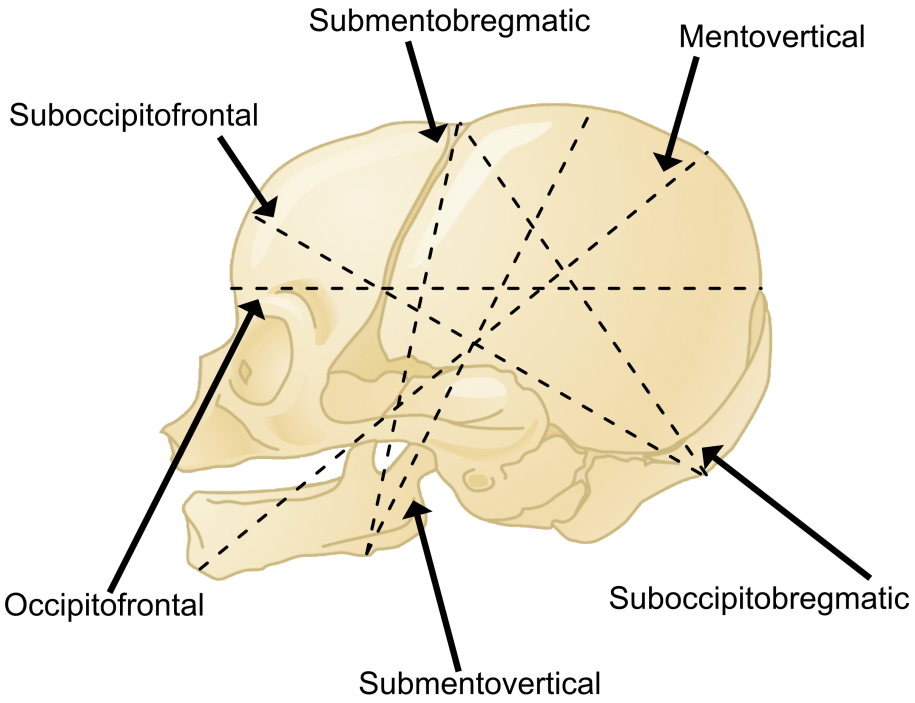

Figure 2.11: Lateral view of fetal skull showing the different AP diameters (modified from [14]).

2.2.3.4.2 Transverse diameters The transverse diameters of the fetal skull are:

- **Biparietal:** It is the largest transverse diameter of approximately 9.5 cm. It extends between the two parietal eminences of the parietal bones.
- **Bitemporal:** It is the shortest transverse diameter of approximately 8 cm. It extends along the coronal suture from its widest part and between the temporal bones.

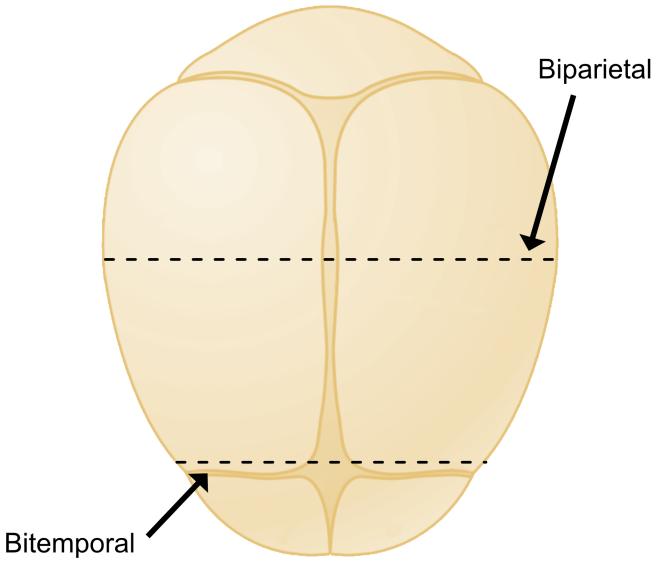

Figure 2.12: Superior view of fetal skull showing the transverse diameters (modified from [14]).

2.2.4 Anatomy of Maternal Pelvis

Since the pelvis will not be included in the obstetric forceps simulation presented in chapter 4 and 5, details of the maternal pelvic anatomy can be found in Appendix A.

2.2.5 Fetus position

Examination after 36 weeks of pregnancy facilitate assessing the position of the fetus in utero [25] by identifying the presenting part, denominator, position, attitude, engagement and lie. Knowing the exact position of the fetus helps midwives and obstetricians prepare for any adversity or complications that can occur in labour.

2.2.5.1 Presentation

The presentation is determined by the part of the fetus that is situated over the pelvis in the bottom part of the uterus, also called lower pole. There are three different types of presentations. It can be cephalic (or vertex), breech or shoulder (see Figures 2.13, 2.14 and 2.15 respectively).

Any other presentation that is not a vertex presentation is called **malpresentation**.

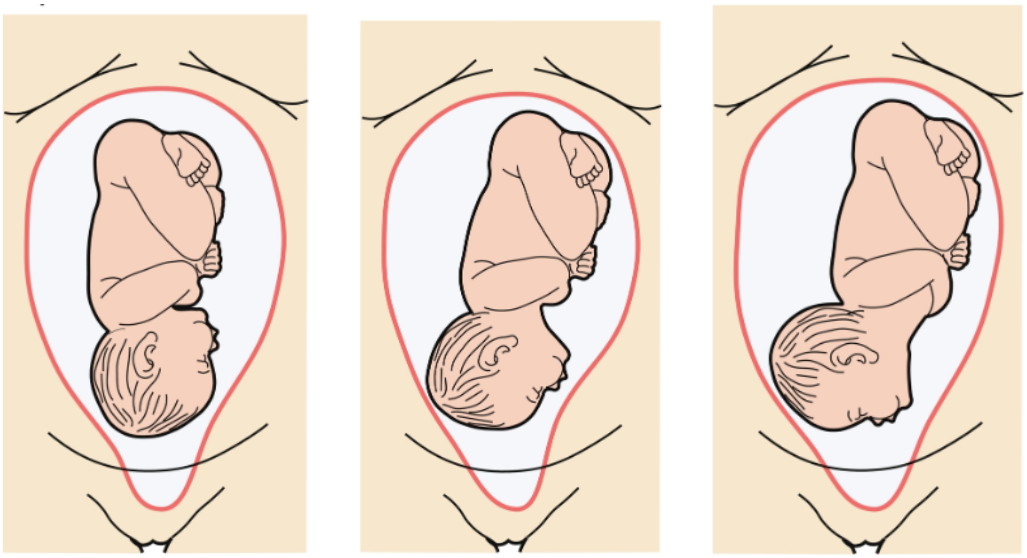

(a) Vertex (b) Brow (c) Face

Figure 2.13: Different types of Cephalic presentation (taken from [4]).

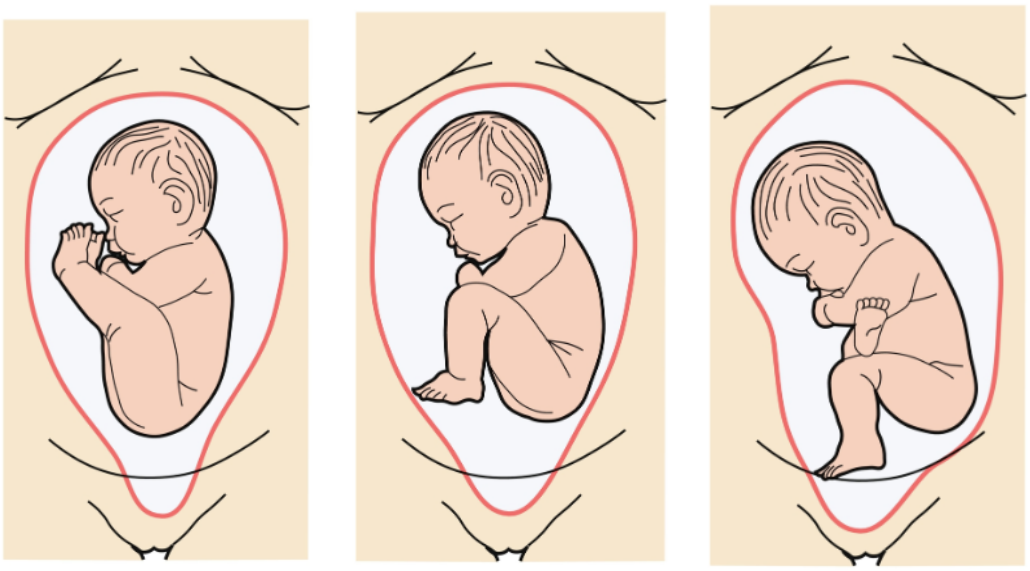

(a) Extended (b) Flexed (c) Footling

Figure 2.14: Different types of Breech presentation (taken from [4]).

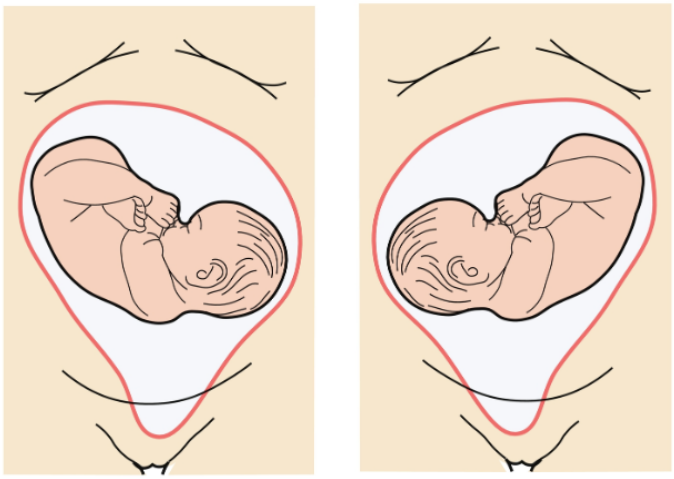

(a) Shoulder (b) Shoulder

Figure 2.15: Different types of Shoulder presentation (taken from [4]).

2.2.5.2 Denominator

Depending on the presenting part, the denominator is a fixed point used to indicate the position of the fetus [25].

Table 2.1 shows the denominator for the cephalic, breech and face presentations.

Presentation	Denominator
Cephalic	Occiput
Breech	Sacrum
Face	Chin

Table 2.1: Relationship of presenting part and its denominator.

2.2.5.3 Position

The relationship of the denominator (see previous Section 2.2.5.2) to the maternal pelvis (see Appendix A) describe the position of the fetus in the uterus [25].

In a cephalic presentation the denominator is the occiput as it was stated previously (see Section 2.2.5.2), hence the fetus position is described as follows (see Figure 2.16):

- Occiput Anterior (OA).
- Left Occiput Anterior (LOA).
- Right Occiput Anterior (ROA).
- Occiput Posterior (OP).

- Left Occiput Posterior (LOP).
- Right Occiput Posterior (ROP).
- Left Occiput Transverse (LOT).
- Right Occiput Transverse (ROT).

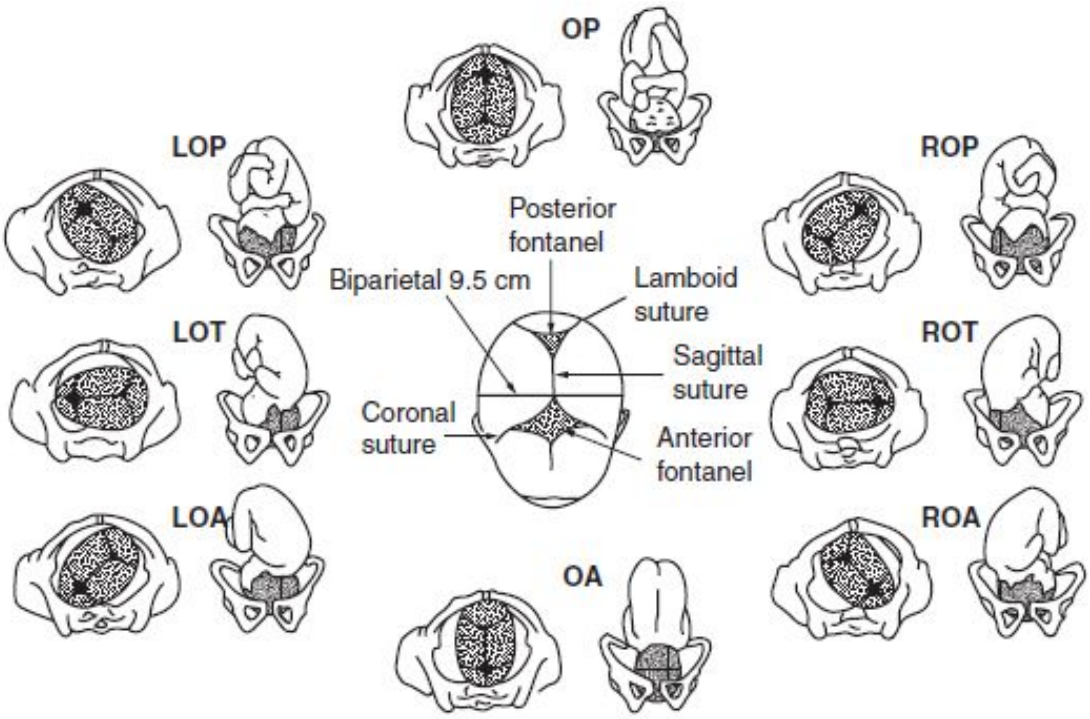

Figure 2.16: Positions of the fetus based on the relationship of the occiput to the maternal pelvis in a cephalic presentation (taken from [26]).

It is possible to determine the fetal position on abdominal palpation although it requires practice and more experience by the obstetrician. A more accurate assessment of the presenting part can be done by vaginal examination [4].

2.2.5.4 Attitude

The relationship between the fetal head and limbs to its body is known as attitude [25]. It can be fully flexed, deflexed, partially extended or completely extended (see Figure 2.17).

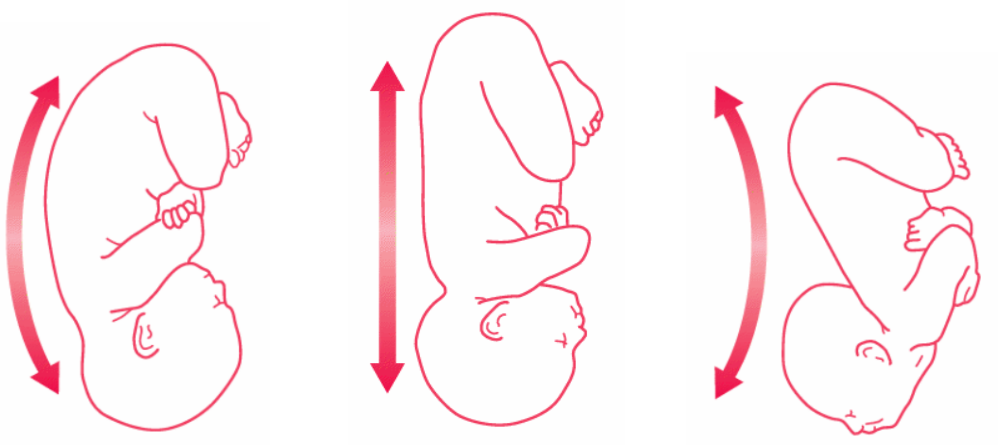

(a) Fully flexed (b) Poorly flexed (c) Extended

Figure 2.17: Types of attitude of the fetus (taken from [25]).

2.2.5.5 Engagement

It happens when the biparietal diameter of the fetal head (see Section 2.2.3.4.2) has passed through the pelvic brim of the maternal pelvis (see Appendix A.1.1) [4]. Engagement is assessed by abdominal palpation of the head in fifths as follows:

- Five-fifths (5/5): The whole head is palpated above the pelvic brim (see Figure 2.18a).
- Four-fifths (4/5): One-fifth of the fetal head cannot be palpated in an abdomen examination since it is below the pelvic brim (see Figure 2.18b).
- Three-fifths (3/5): Two-fifths of the fetal head are below the pelvic brim and are not palpable per abdomen examination. Three-fifths are palpable above the pelvic brim (see Figure 2.18c).
- Two-fifths (2/5): Three-fifths of the fetal head are below the pelvic brim and are not palpable by abdomen examination. Two-fifths are palpable above the pelvic brim (see Figure 2.18d).
- One-fifth (1/5): Four-fifths of the fetal head are below the pelvic brim and are not palpable by abdomen examination. One-fifth is palpable above the pelvic brim (see Figure 2.18e).

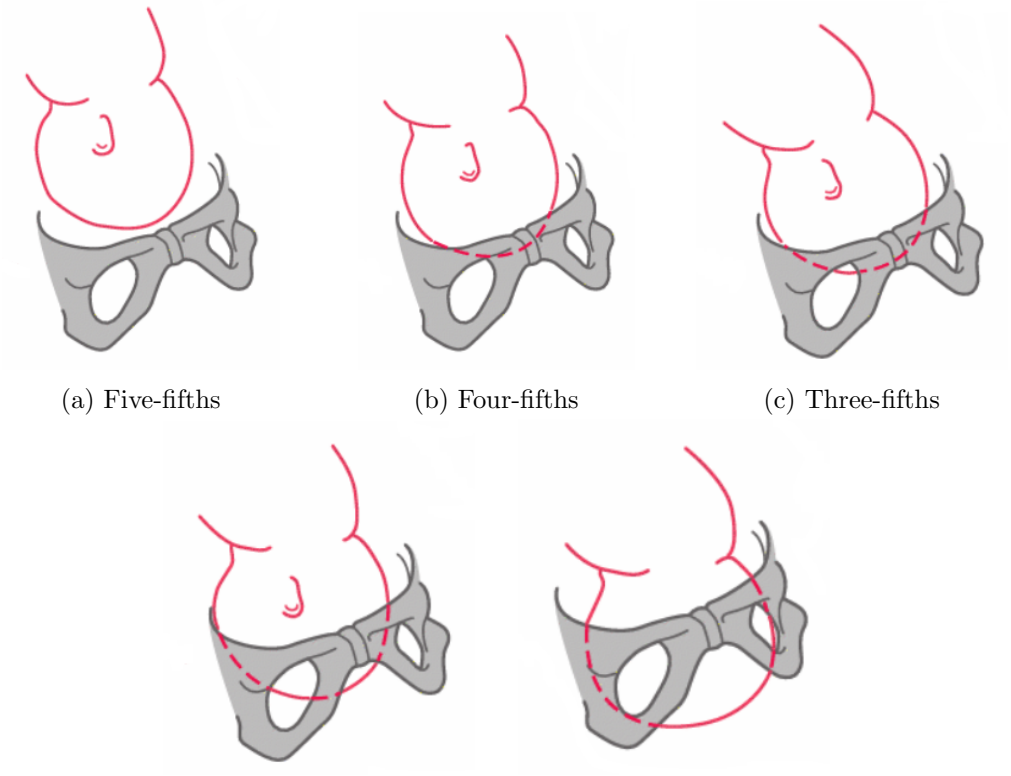

(a) Five-fifths (b) Four-fifths (c) Three-fifths

(d) Two-fifths (e) One-fifth

Figure 2.18: Different levels of engagement of the presenting part in a vertex presentation measured in fifths above the pelvic brim (modified from [25]).

2.2.5.6 Lie

It is the relationship between the long axis of the fetus and the long axis of the uterus [4, 25]. It can be longitudinal, transverse of oblique.

As it can be seen in Figure 2.19, the lie of the fetus can be longitudinal in a cephalic or breech presentation, transversal or oblique in a cephalic or breech presentation.

A longitudinal lie in a cephalic presentation is the most desired since it represents less complications in labour, but obstetricians must be prepared to manage transverse and oblique lies detected in advance after following the pregnancy progress.

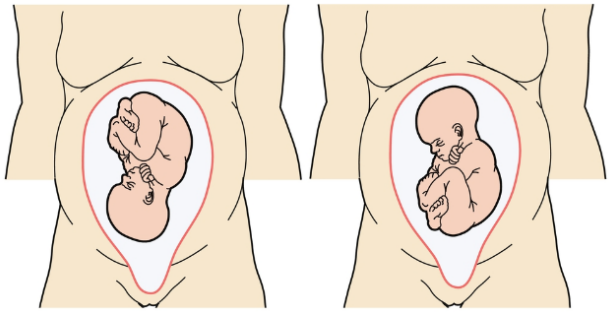

(a) Longitudinal

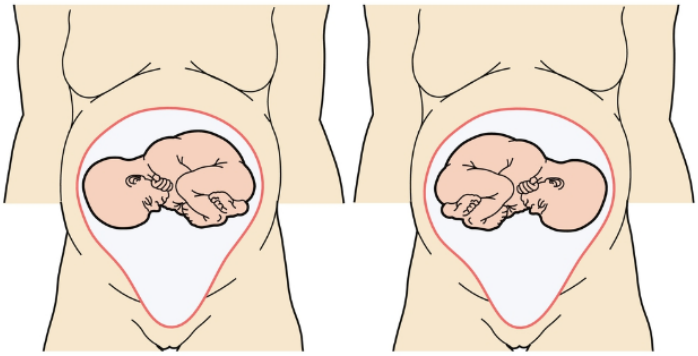

(b) Transverse

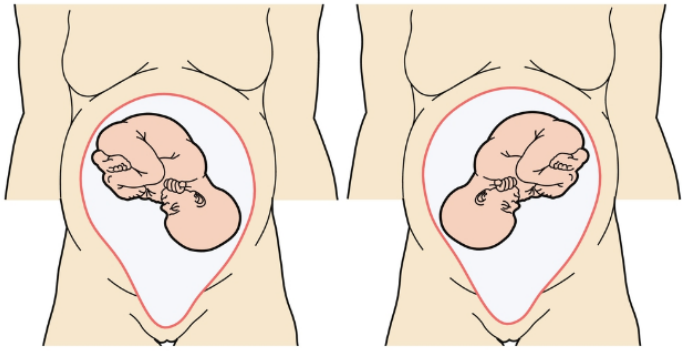

(c) Oblique

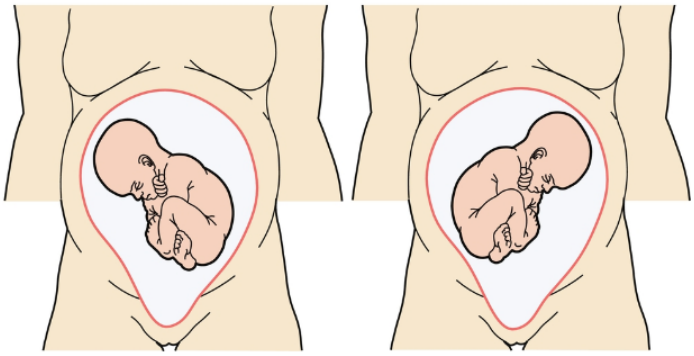

(d) Oblique

Figure 2.19: Different types of lie of the fetus (taken from [4]).

2.2.6 Operative Vaginal Delivery

Operative Vaginal Delivery (OVD) or Assisted Vaginal Birth (AVB), is described as the process to assist birth for maternal and fetal indications, with help of medical instrumentation such as Obstetric Forceps or Vacuum Extractor (VE) [13, 27], also called Instrumental Vaginal Delivery (IVD).

According to the National Health Service (NHS) statistical data in England, from 2011 to 2021, the cases of OVD represent between 12.3% and 13.0% of the total methods of delivery in this last decade [9].

The percentage of cases of OVD using Obstetric Forceps and VE between 2011-2012, represent 6.6% and 6.3% respectively of the total number of deliveries, and by the end of the period between 2020-2021 the figures changed to 7.6% and 5.1% respectively. This disproportion between the two methods, show that the use of forceps has increased at the same time that the use of the VE has decreased in the same period.

Table 2.2, shows the total number of delivery cases per year in England, and the correspondence percentage of deliveries using Obstetric Forceps and VE.

Year	**Total**	**Method of delivery (%)**	
	deliveries	**Forceps**	**Vacuum**
2011 - 2012	668,936	6.6	6.3
2012 - 2013	671,255	6.8	6.0
2013 - 2014	646,904	7.0	5.8
2014 - 2015	636,643	7.2	5.9
2015 - 2016	648,107	7.2	5.6
2016 - 2017	636,401	7.2	5.5
2017 - 2018	626,203	7.3	5.2
2018 - 2019	603,766	7.3	5.1
2019 - 2020	591,759	7.3	5.0
2020 - 2021	559,728	7.6	5.1

Table 2.2: Use of Operative Vaginal Delivery methods between 2011-2021 in England [13].

Figure 2.20, shows a clear trend in the use of both methods in OVD cases from 2011 to 2021 in England. Initially in the period between 2011-2012, the percentage of cases for both methods were similar, with a difference of 0.3%; however the tendency to use VE started to decrease over time, and by the end of the period of 2020-2021, the difference between the use of both methods increased to 2.5%.

The number of cases where OVD was performed, show that it is still playing an important role in childbirths delivery with the potential to save lives, hence the importance to keep obstetricians developing competency in the use of both methods.

Although the correct use of IVD do not represent a risk for the mother and the baby, it still has the potential to impact the health of both, where fetal head trauma with short-term and long-term morbidity and cervical, vaginal, and perineal trauma can be observed [27, 28, 29]. It is advisable to use other methods at an early stage of labour to prevent the

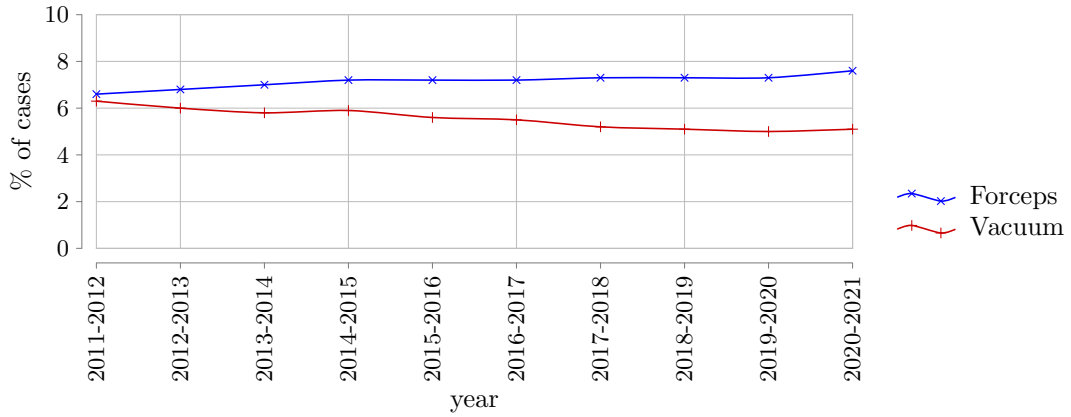

Figure 2.20: Operative Vaginal Delivery trend from 2011-2021 in England [9].

use of any IVD as it is recommended by the The American College of Obstetricians and Gynaecologists (ACOG) [30], and only use it if it is strictly necessary, as it is the case for Emergency Caesarean Section (ECS) that should be used only in cases where the option to use IVD is not advised.

Since the aim of this research is to analyse the effect of the obstetric forceps on the fetal skull, the use of the VE or any other IVD will not be discussed further.

2.2.7 Obstetric Forceps

Obstetric Forceps are used when the delivery of the fetus is in danger and the expulsive efforts from the mother are insufficient to do it safely. It is an instrument that provides traction and/or rotation of the fetal head, by placing a pair of blades on each side of it [31].

Although Obstetric Forceps were invented in the 17th century by members of the Chamberlen family [32, 33, 34] (see Figure 2.21a), it has had improvements through the years since its creation by a number of different surgeons and obstetricians such as Robert Barnes, James Simpson, and William Neville, just to mention some of them [35, 29].

In modern days, there was an attempt to create a new disposable plastic obstetric forceps with the ability to measure the traction force called Pro-Nata®, although it was removed from the website of the British company Surgical Dynamics® [36] (see Figure 2.21b).

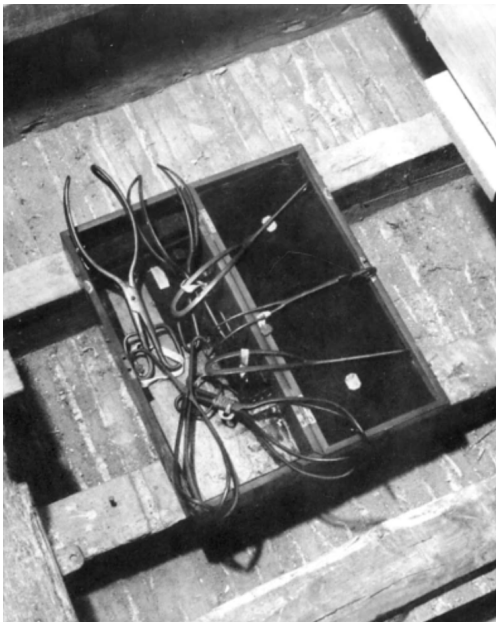

(a) Original Chamberlen Obstetric Forceps found in 1813 (taken from [33]).

(b) Modern Pro-Nata® Obstetric Forceps (obtained from [36], but no longer available).

Figure 2.21: Comparison of original obstetric forceps (left) vs modern Obstetric forceps (right).

Information about the use of the Pro-Nata® obstetric forceps in laboratory trials using the PROMPT birth simulator, can be found in the NHS web page under the title "Force Limiting Obstetric Forceps for Instrumental vagina Delivery" [37]. More details about the study proposal can be found in the BioMed Central (BMC) web site [38] with the title "Pulling forces involved with forceps delivery and its association with maternal injury during birth"[39].

2.2.7.1 Forceps Delivery Classification

Forceps application is indicated according to the station and position of the presenting part. According to the ACOG, they can be classified as follows [31, 40, 13]:

- Outlet forceps:
  - Use recommended when:
    - The scalp is visible at the introitus without separating the labia.
    - Fetal head at perineum.
    - Fetal skull at pelvic floor.
    - Sagittal suture in AP or Left Occiput Anterior (LOA)/Right Occiput Anterior (ROA) or Left Occiput Posterior (LOP)/Right Occiput Posterior (ROP) positions.
    - Rotation of the fetal head does not exceed 45 degrees.

- Low forceps:
  - Use recommended when:
    * Leading part of the fetal skull is at station +2 cm or greater (see Section 2.2.1).
    * Fetal skull is not on the pelvic floor.
    * Rotation of 45 degrees or less to LOA/ROA to OA or LOP/ROP to OP, or rotation is 45 degrees or more.
- Mid forceps:
  - Use recommended when:
    * Fetal head is engaged.
    * Leading point of the skull is above station +2 cm.

2.2.7.2 Forceps Anatomy

Forceps have five main parts [31, 27, 12] (see Figure 2.22):

- **Blade**: Its main purpose is to create a cavity where the fetal head can fit and then used to pull it out from the birth canal. This is divided in the next sections:
  - **Pelvic curvature**: From a sagittal point of view of the forceps, this curvature will fit the mother's birth canal allowing the blades be inserted in this path without complications.
  - **Cephalic curvature**: From a top point of view of the forceps, this curvature will fit fetal head shape without hurting it, allowing the obstetrician to pull it out from the birth canal.
  - **Toe**: Also known as the tip of the blade, this is the first section of the forceps to be inserted in the birth canal and the one responsible to prevent the blades to be slipped out.
  - **Heel**: Indicates the end and start of the shank and blade sections.
- **Shanks**: This section also known as the neck of the forceps, helps to separate the blades from the handles, giving the obstetrician a space to move between fetus head and his hands while gripping the forceps handles. Also is designed to separate the blades from each other and keeps them parallel. Some types of forceps have them crossed.
- **Lock**: Its purpose is to secure both sections of the instrument and keep them together while the obstetrician is gripping the handles and applying traction. This feature is not present in all forceps.
- **Finger guide/guard**: This section helps to create traction along with the handles, usually putting the index and middle fingers on each finger guide. This feature is not present in all forceps.

- **Handle**: This section provides the main source of surface used for the practitioner to create traction to pull the fetal head out from the birth canal.

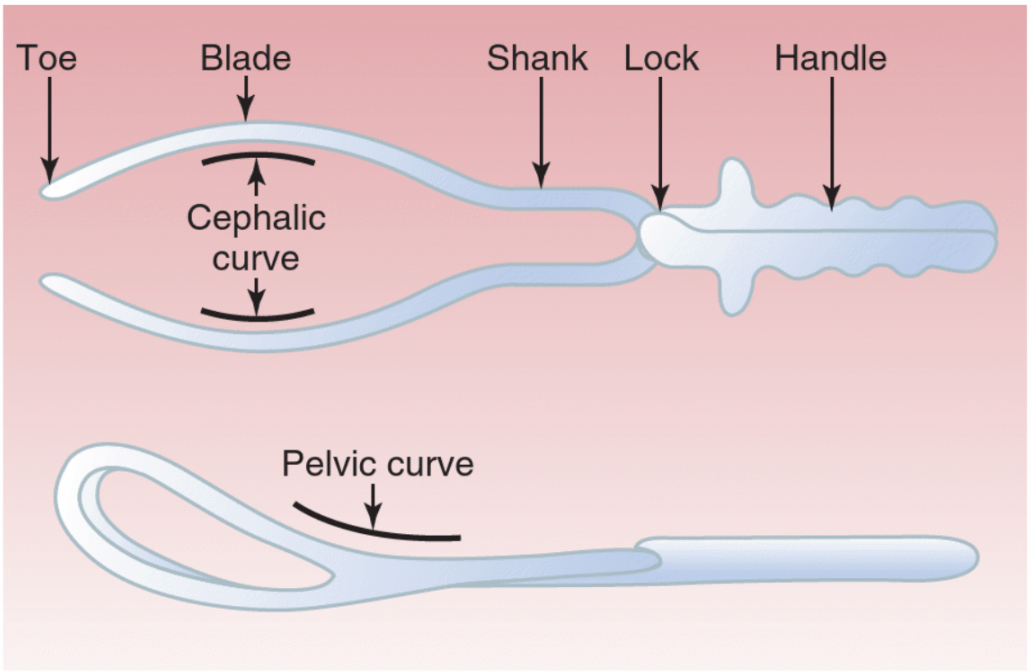

Figure 2.22: Different parts of the obstetric forceps (taken from [31]).

Depending on the station and position of the presenting part as stated on Section 2.2.7.1, there are different types of forceps and all of them contain the same parts mentioned earlier (see Figure 2.23). The two most commonly types of forceps used in a cephalic presentation are Simpsons and Elliot or Tucker-McLane forceps [40].

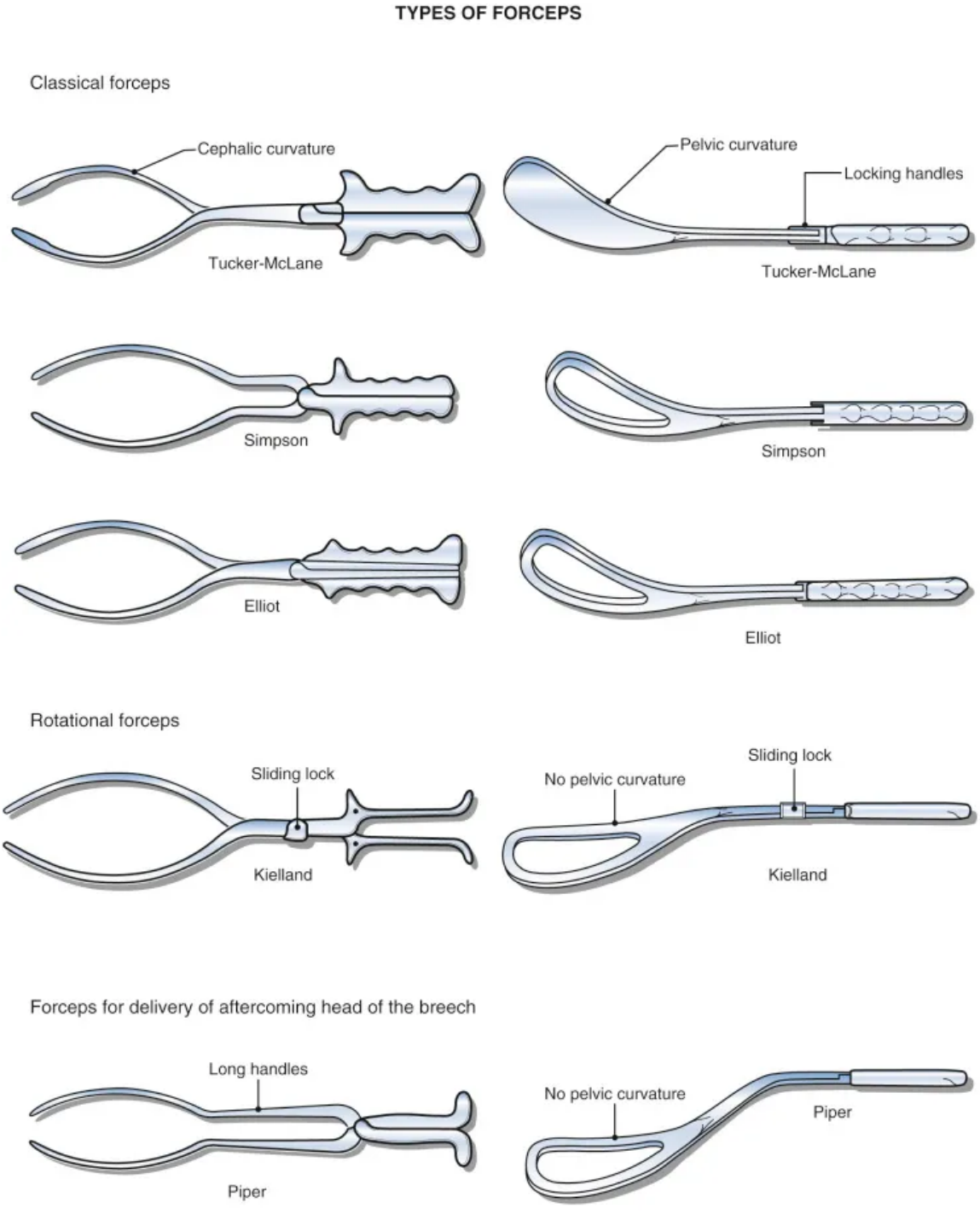

Figure 2.23: Example of different types of Obstetric Forceps (taken from [31]).

2.2.7.3 Indications

Indications should be considered individually according to the specific factors affecting each case, if several of them coexist the possibility of an intervention is lower [13, 31, 27, 40, 41].

The most common indications for the use of Obstetric Forceps are:

- Prolonged second stage of labour (see Section 2.2.2). Is defined as the lack of continuing progress for 2 hours without regional anesthesia or 3 hours with regional anesthesia for nulliparous, and for 1 hour without regional anesthesia or 2 hours with regional anesthesia for multiparous.
- Suspected fetal compromise.
- Maternal exhaustion or distress.
- To spare the mother muscular effort.
- Rupture of membranes.
- Fetal vertex is engaged.
- Fully dilation of cervix.
- Position is precisely known.
- Necessary support personnel and equipment are present.
- Assessment of maternal pelvis reveals adequacy for the estimated fetal weight.
- Adequate analgesia/anaesthesia.
- Informed consent has been obtained.
- The bladder is emptied by means of a catheter.
- Operator is knowledgeable

The use of Obstetric Forceps is contraindicated in the next cases [13, 31, 27, 40, 41]:

- Unengaged head.
- Before fully dilation of the cervix.
- Before rupture of membranes.
- Malpresentation (face/brow).
- Inability to define position.
- Fetal macrosomia greater than 4-4.5 kg.
- Inexperienced operator.

2.2.7.4 Technique

Before to start the forceps intervention, the precise position of the fetal head must be known by the operator (see Section 2.2.7.3). The steps for the application of Obstetric Forceps in a Low Forceps delivery (see Section 2.2.7.1) is explained.

- Forceps are used to exert traction without rotation when the sagittal suture is straight aligned in the midline, and rotation prior traction when the sagittal suture is not aligned, the latter is rarely performed but described here.
- Once the position of the fetal head is known, the left blade is gently but firmly introduced from left to right between the maternal pelvis and the fetal scalp, performing a slight rotation to put the blade in the correct position (see Figure 2.24a).
- The right blade is introduced in a similar fashion in the opposite direction from right to left (see Figure 2.24b).
- Carefully the blades are locked and ready to perform the traction. If the fetal head needs to be rotated then the toes of the blades must always point towards the occiput (see Figure 2.24c).
- Once the blades are secured over the fetal head, the traction motion is performed (see Figure 2.24d).
- Once the procedure has been completed, the blades are removed in the reverse order in which they were applied (see Figure 2.24e).

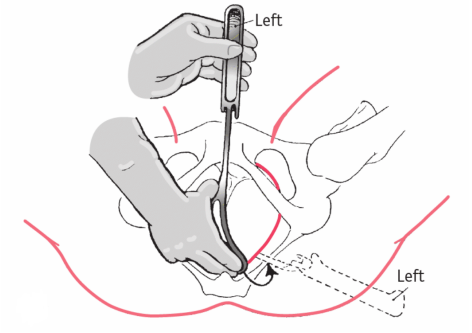

(a) Application of left blade.

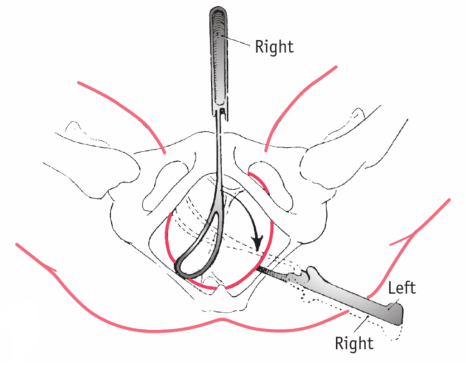

(b) Application of right blade.

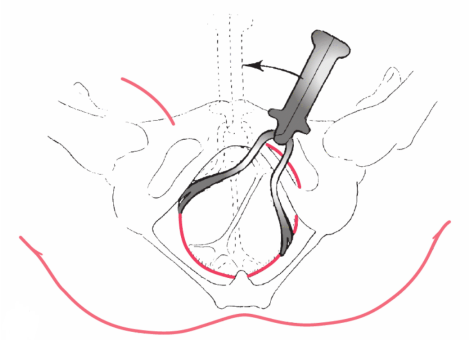

(c) Rotation of forceps.

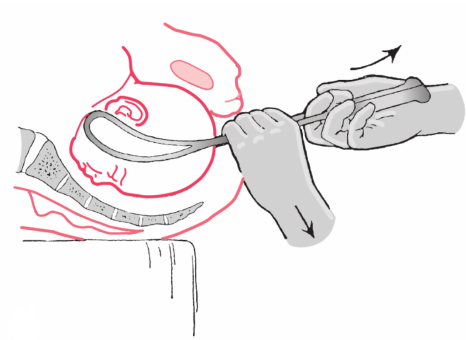

(d) Traction OF forceps.

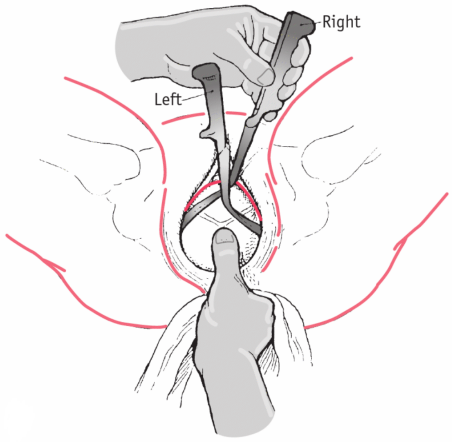

(e) Removal of forceps.

Figure 2.24: Step by step application of Obstetric Forceps (modified from [27]). a) Application of left blade, b) Application of right blade, c) Slight rotation of forceps if required, d) Traction of forceps, e) Removal of forceps.

2.2.7.5 Risks

The use of IVD in a OVD procedures carry a potential health risk for the mother and the baby, where different types of trauma are observed with short-term and long-term morbidity [27, 28, 42]. Some of the complications for both are described below.

- Neonatal
  - Facial or scalp abrasions or bruises.
  - Cephalhaematoma due to the friction of the fetal head and the pelvis or forceps blade.
  - Facial palsy due to the compression of the facial nerve by the forceps blade.
  - Intracranial trauma and haemorrhage.
  - Skull fractures.
- Maternal
  - Vaginal and perineal tears.
  - Haematomas and rectal lacerations.
  - Pelvic floor disorders and long-term pelvic floor morbidity.
  - Post-traumatic stress disorder.
  - Stress urinary incontinence and anal incontinence.

(a) Bruises (taken from [43]).

(b) Cephalhaematoma (taken from [44]).

Figure 2.25: Examples of neonatal complications associated to the use of obstetric forceps in OVD.

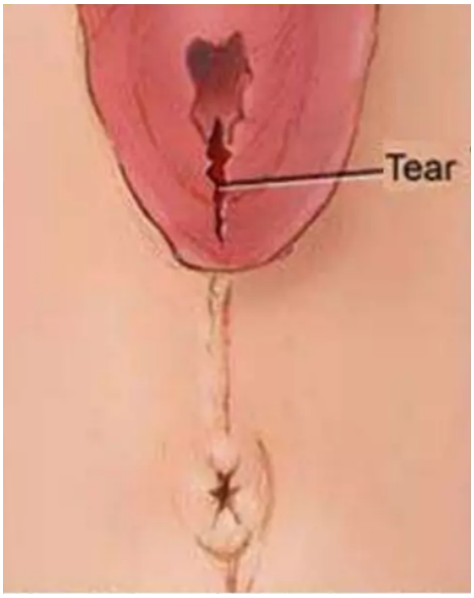

(a) First degree.

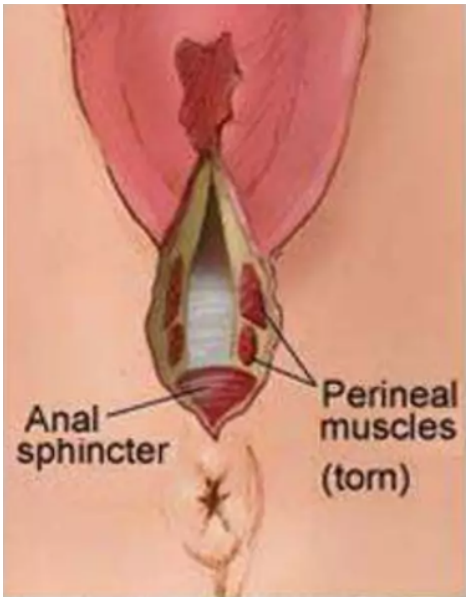

(b) Second degree.

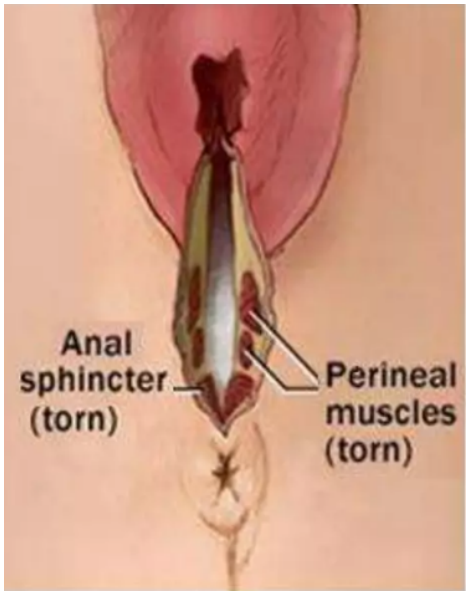

(c) Third degree.

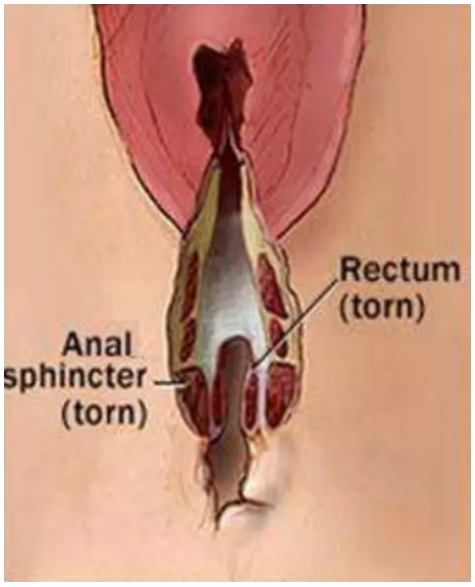

(d) Fourth degree.

Figure 2.26: Maternal complications associated to the use of obstetric forceps in OVD. Lower to greater degrees of perineal tear from left to right and from top to bottom (taken from [45]).

2.3 Literature Review

2.3.1 Childbirth simulations

Although the number of complications in labour and delivery is declining, they are still potentially life threatening and could lead to the death of either the mother or the baby if they are not treated in time by experienced obstetricians. In order to prevent such catastrophic events, obstetric clinicians must keep their skills up to date by performing regular drills in the labour ward [28] or by using childbirth simulators.

For this reason different approaches to simulate childbirth have been researched to assist obstetricians in their training.

Childbirth simulation can be divided in three main categories:

- Mechanical simulations.
- Computer-based simulations.
- Hybrid simulations.

2.3.1.1 Mechanical simulations

In the 18th century in France, the professionalization of the midwife profession took place to train and educate matrons of the countryside who endangered women and babies lives due to ignorance of medical procedures in childbirth. Angélique Marguerite Du Coudray a mistress midwife of Paris who travelled across the country, was in charge to teach theory of childbirth but overall practical exercises carried out on the machine precursor of the childbirth simulator that she invented [46, 47].

Her invention, was a mannequin representing the lower part of a woman anatomy that included the belly, pelvis and upper thighs, a doll representing a new-born baby connected to the placenta by a cord and more accessories (see Figure 2.27).

Figure 2.27: Delivery machine used by Angélique Marguerite Du Coudray in the 18th century in France (taken from [47]).

The lower torso was crafted using fabric, leather, wood, wicker, stuffing and apparently real pelvic bones. It had the birth canal and perineum, and sponges were installed to spurt dyed liquids to simulate blood and amniotic fluid. The newborn was a stuffed doll attached to a placenta by a fabric umbilical cord. A set of twins attached to a placenta, a shrivelled umbilical cord, a crushed infant head, and a model of the reproductive system made of fabric were crafted as well. [48].

Current childbirth simulators are based on the concept of Du Coudray invention, with better materials and characteristics that improved the teaching-learning experience. That is the case of the UK company Limbs & Things® [49], that builds a range of anatomically accurate products like the Birth Simulator PROMPT (see Figure 2.28) [50], which is a mannequin of the lower part of a woman body (similar to the one invented by Du Coudray) with articulated thighs, realistic pelvic floor and improved baby model. This PROMPT can be used to teach Caesarean Section (CS), cervical dilatation, cervical effacement and postpartum hemorrhage among other medical concepts.

Figure 2.28: Childbirth simulator PROMPT (taken from [50]).

Another example of a mechanical birth simulator was presented by Dupuis et al. in 2005 [51]. The BirthSim® simulator, consisted of a fetal mannequin representing a term newborn head equipped with a 6 DoF tracking sensor, a maternal mannequin of a pelvic model, an interface pressure system to simulate the pelvic muscles an a location system consisted of a pneumatic actuator to move the fetal head in the desired position (see Figure 2.29).

Figure 2.29: Demonstration of use of BirthSim®, a mechanical birth simulator used for medical training (taken from [51]).

The purpose of the project was to randomly present to the operator (in this case 32 residents and 25 physicians) 1 of the 11 fetal stations using the fetal head mannequin, then the operators determined the head position and the station by transvaginal assessment. Results shown the comparison between the error rate made by residents and physicians, but the importance of this work resides on the real interaction between obstetricians and the simulator where they can improve their skills and prepare for real cases in the future.

2.3.1.2 Computer-based simulations

In the field of computer-based simulations, the main purpose is to emulate the childbirth behaviour considering different elements such as maternal pelvis shape, pelvis floor and fetus model.

J.-D. Boissonnat and B. Geiger presented their work in 1993 about the simulation of the progress of delivery using a maternal pelvis and a fetal head obtained by Magnetic Resonance Images (MRI) [52]. They used the spacial triangulation (tetrahedrization) method [53] to reconstruct 3D models from tomographic images.

The simulation included only the maternal pelvis obtained from a non-pregnant person and a scaled fetal head obtained from an adult person, any soft tissues were discarded. The main idea was to move the fetal head downwards in discrete steps by applying a force from its centre of gravity, if the head polyhedron penetrates the pelvis polyhedron, a force was calculated and the fetal head was translated or rotated or both to reduce the force to zero (see Figure 2.30).

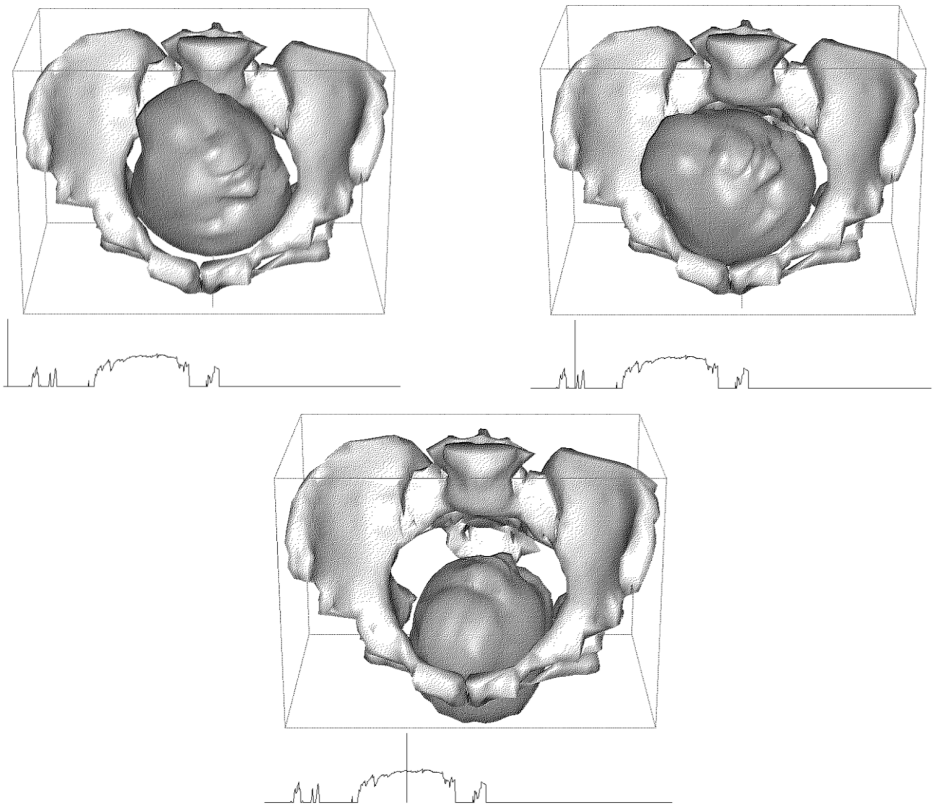

Figure 2.30: Computer-based simulation of the baby head internal rotation during delivery (taken from [52]).

Although results reported that the fetal head followed the cardinal movements during the simulated delivery, it is also reported that the model of the fetal head was artificially produced which impacts directly on the simulation accuracy.

In 2019, Lapeer et al. presented their work about computer-based simulation of childbirth during the second stage of labour, using the Dirichlet-Neumann contact method to calculate the mechanical contact interaction between the maternal pelvis anatomy and the fetal head and total Lagrangian explicit dynamics to calculate soft tissue deformations [54]. The aim of this research was to propel the virtual fetus through the birth canal by applying intra-uterine expulsion forces that affected directly the 3D mesh of the fetus, maternal bony pelvis and pelvic floor muscles (see Figure 2.31).

The simulation started with the fetal head position above the pelvic brim (see Appendix A) upon which the uterine force was applied and updated accordingly to the stage of the delivery; results reported that the different cardinal movements presented during labour were observed as similar to its motions in a real scenario (see Section 2.2.2).

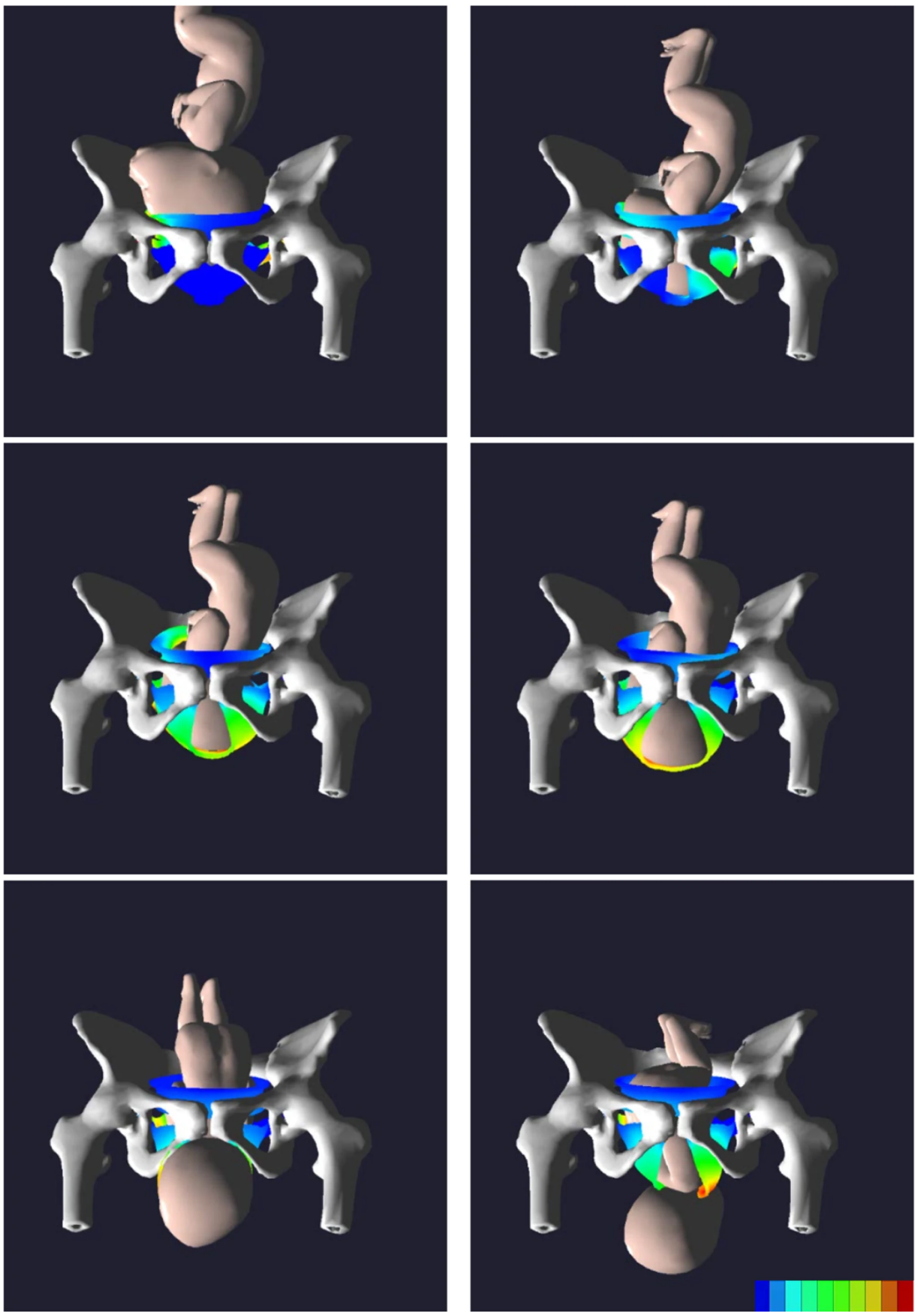

Figure 2.31: Different stages of the cardinal movements during a computer-based childbirth simulation from Lapeer et al. (taken from [54]).

The research of Chuang-Yen et al. published in 2022 [55], investigates the effects of the Vacuum Extractor (VE) on the fetal head when a Operative Vaginal Delivery (OVD) is performed. VEs are used as an alternative over the obstetric forceps as a less invasive instrument for the mother which can cause them perineal laceration (see Section 2.2.7.5), but on the other side, the use of VE can cause scalp wounds, skull fracture or intracranial bleeding.

This research uses Finite Element Analysis (FEA) to simulate the biomechanical effects of different sizes of silicone rubber VEs on the fetal head. This was done by creating 3D models of the VE with different diameters applied on surfaces with different shapes, flat surface, hemispherical ball and fetal head (see Figure 2.32).

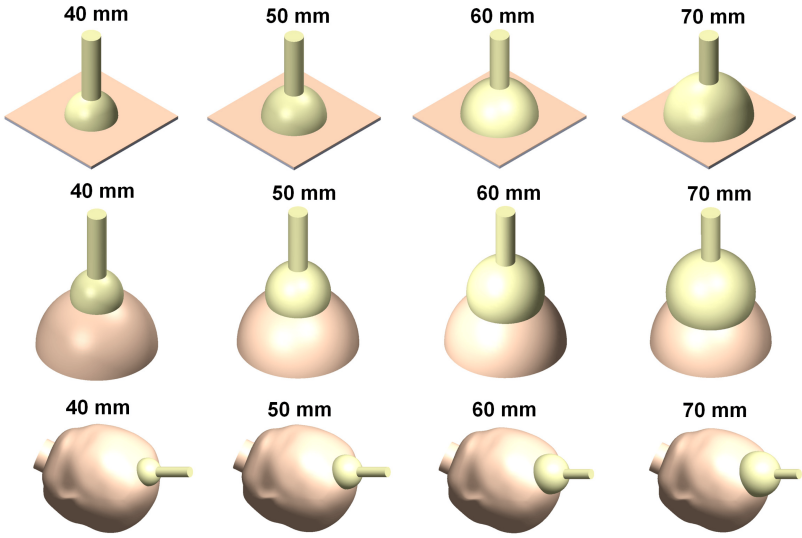

Figure 2.32: Computer-based simulation of Vacuum Extractor models in different sizes acting on flat surface (top), hemispherical ball (middle), and fetal head (bottom) (taken from [55]).

Results of the research, showed that there is a direct relation between the diameter of the suction cup and the reaction force, i.e. the larger the VE, the greater is the reaction force, stress and strain on the surfaces applied (see Figure 2.33 and Figure 2.34).

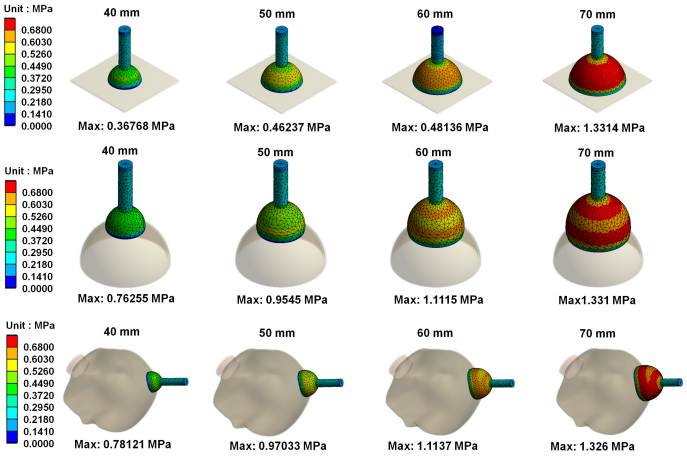

Figure 2.33: Stress distribution on different VEs acting on flat surface (top), hemispherical ball (middle), and fetal head (bottom) (taken from [55]).

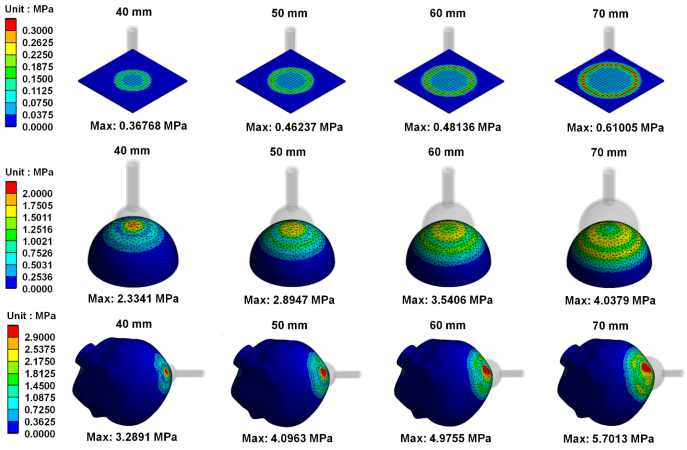

Figure 2.34: Stress distribution on different shapes: flat surface (top), hemispherical ball (middle), and fetal head (bottom) (taken from [55]).

2.3.1.3 Hybrid simulations

Hybrid simulations usually contain a mechanical and a computer-based aspect combined.

In 2004, Lapeer et al. presented their work about a simulation of the Obstetrics Forceps Delivery (OFD) in an augmented environment, where the operator was allowed to manipulate real obstetric forceps blades whilst rotating and extracting a virtual model of a fetus from the birth canal [56].

The aim of their work was to create a childbirth simulation combining AR technology to show a virtual 3D fetus and haptic feedback to manipulate real obstetric forceps in the real world on a virtual fetus. The forceps motions are recorded using passive tracking markers to collect real motion data from the operators and their ability to manipulate the

blades, subsequently data is evaluated in the post-diagnostic assessment on the effect of these manipulations on the fetal head deformation (see Figure 2.35).

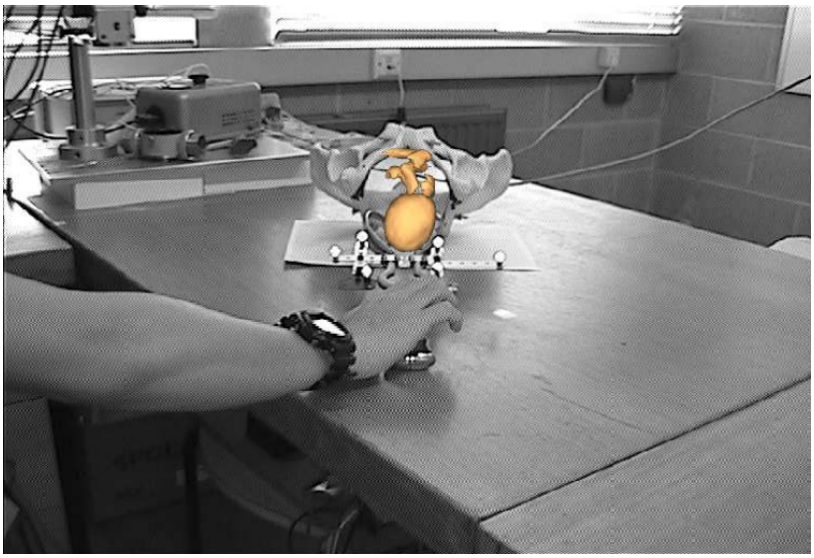

Figure 2.35: Hybrid simulation of the extraction of a virtual 3D fetus model from a real pelvic model using real obstetric forceps (taken from [56]).

Although this research opens the door to create solutions to train doctors using real IVD equipment without performing an invasive procedure such as OVD in a real person, it is also noted that forces individually applied on the obstetric forceps blades within the simulation can not be recorded as no haptic feedback is involved, limiting the capacity to obtain its own data. For training purposes, the lack of feedback from the elements involved such as the virtual 3D fetus model, makes difficult for the trainee to create the muscle memory required for this procedures since the operator is not sensing any reaction force from the model as he/she is just visualizing the outcome in a display.

In 2006 Dupuis et al. published their work about spatial dispersion of forceps blade trajectories between junior and senior obstetricians [57]. New obstetric forceps made from non-magnetic material and with electromagnetic sensors contained in lodges located at the extremities of the shanks, were created to track the forceps placement trajectory.

In order to set the desired fetal station, it was used the BirthSim® childbirth simulator [51] equipped with a dummy fetus that mimics a full-term neonatal head and allows palpation of fontanelles and sutures; an anatomically correct maternal pelvis mannequin that allows palpation of the ischial tuberosity, pubis, sacrum and coccyx; an elastomer that mimics pelvic muscles softer enough to allow palpation of the underlying ischial tuberositys; a pneumatic actuator simulating the fetal spine and allowing the rotation of the fetal back (see Figure 2.36).

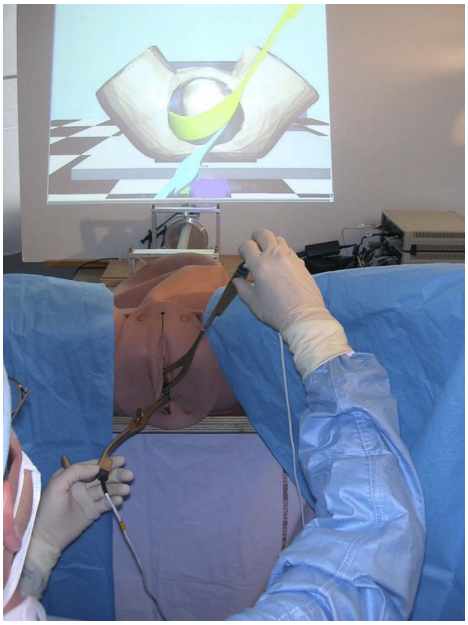

Figure 2.36: Obstetrician inserting bespoke obstetric forceps blades with electromagnetic sensors into the BirthSim® (taken from [57]).

Results presented by Dupuis et al. shown that trajectories depicted by the insertion of forceps blades by junior obstetricians (considered to have less experience) are different in comparison to those performed by senior obstetricians (considered to have more experience). Blades insertion by junior obstetricians tent to create an inconsistent trajectory meanwhile the trajectory depicted by the blade insertion of senior obstetricians is more consistent.

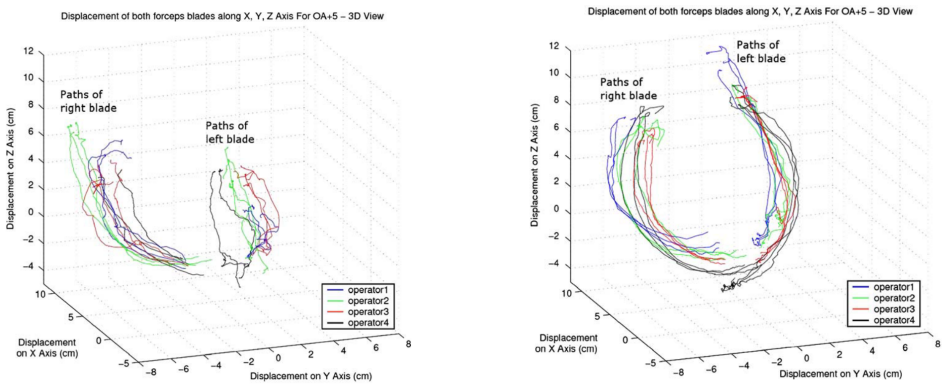

(a) Trajectories performed by junior obstetricians.

(b) Trajectories performed by senior obstetricians.

Figure 2.37: Difference between trajectories performed by junior (left) and senior (right) obstetricians with new bespoke obstetric forceps with electromagnetic sensors (taken from [51]).

2.3.2 Fetal head moulding simulations

Between 2020-2021 from a total of 569,162 birth episodes in England, a number of 63 different delivery complications were recorded by the NHS [9], where approximately 4,000 cases were related with obstructed labour due to malposition and malpresentation of fetus, representing 0.69% of all cases.

In the same period of time, the NHS recorded 58 different birth complications on onset of labour, where approximately 14,000 cases were related with injury to fetal scalp, representing 2.48% of all cases (see Section 2.2.7.5).

Although injuries to the fetal head due to complications in labour and delivery represent a low percentage of cases in England, they are still significant in terms of human lives. The importance of prevention and understanding of the effects that these injuries can cause to the fetal head, are leading this study to expand the knowledge on this topic.

As part of childbirth, Fetal Head Moulding (FHM) is a phenomena that takes place as a result of the interaction between the fetus and the maternal pelvis, when the fetal head changes its shape under the compressing forces of labour to allow it fit the the shape of the birth canal (see Section 2.2.3 for reference) [58].

Excessive moulding carries dangerous consequences for the fetus, ranging from cerebral trauma, psycho-neurological disabilities, cerebral palsy and even death [59].

Research about FHM dates back to the late 1970s, when McPherson and Kriewall studied the material properties of fetal cranial bone when the biomechanics of childbirth process had little research [60]. Their work included 86 specimens of fetal cranial bone obtained from 6 subjects whose gestational age ranged from 52 to 40 weeks, additionally 12 specimens from a 6 years old calvarium was tested for comparison. Fetal cranial bone is a non-homogeneous material, highly curved and with radially oriented fibre patters, characteristics considered in the tests. The aim of the research was to examine the elastic modulus of fetal cranial bone, the relation of gestational age, specimen location and bone fibre orientation influence on the elastic modulus.

Based on their previous work, McPherson and Kriewall performed a Finite Element Analysis (FEA) of the parietal bone of a fetal skull to determine a quantitative description of the deformations of the fetal head. This work was done using a 63 thin shell elements model of the bone, a comparison of scaled models of preterm and term parietal bones were also performed. Results reported deformations qualitatively similar to the ones presented in normal labour and that the preterm parietal bone model exhibited deformations between 2 to 4 times greater than term bone model under the same load distribution [61].

The work of McPherson and Kriewall set the base of later research as the one done by Lapeer in 1999, where he covers in depth research of the fetal head moulding from an engineering perspective, presenting a static, non-linear model of the deformation of a complete fetal skull under the pressure forces exerted by the uterine cervix during the first stage of labour (see Section 2.2.1 for reference), where his model is able to evaluate the head moulding continuously and qualitatively [23].

The 3D fetal skull model used by Lapeer considered shell elements for the thin cranial vault bones with orthotropic properties, the fontanelles and sutures with hyperelastic properties, and the skull base bones with isotropic properties; from which a valid finite element mesh was created.

Since his simulation shown to be sensitive to small changes in the material properties of the elements, causing convergence problems because the higher degree of deformation due to excessive rotations of the fontanelle and sutures; he divided his work in three models described as follows with the results:

- Model using linear geometric behaviour of the deforming skull. Model is fast but presented an over-stiff behaviour.
- Model using non-linear geometry with polynomial regression extrapolation of the displacements when they failed to converge. Deformation of the fetal skull was improved but extrapolated values were unreliable due to the variation result depending on the order of the polynomial and the load applied when the convergence failed.
- Model using non-linear geometry improving elements presenting excessive deformation. Moulding results were compatible with previous obstetric and paediatric studies.

The work of Lapeer improved the assessment of fetal head moulding calculation by using an accurate model of the surface of a complete fetal skull, obtained using laser-scanning of a replica model of the fetal skull (see Figure 2.38).

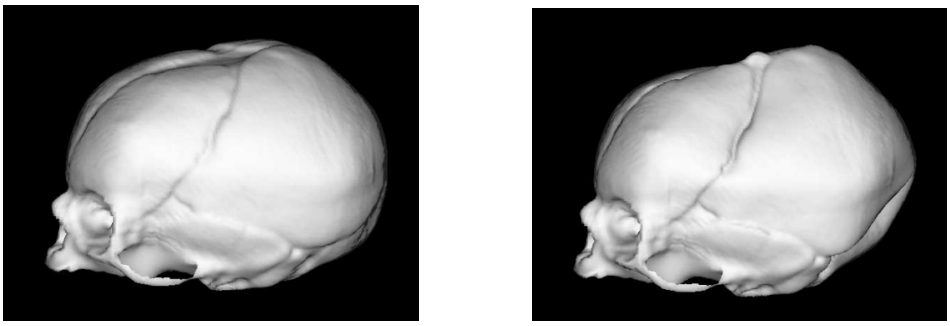

(a) Non-deformed skull. (b) Deformed skull.

Figure 2.38: Virtual fetal skull before (left) and after (right) performing fetal head moulding simulation (taken from [23]).

In 2017, Audinis submitted his Ph.D thesis on Computer-based simulation of the effects of instrumental delivery on the fetal head [62], where he covered the effects of the Obstetric Forceps and VE placement on the fetal head based on a static Finite Element Model (FEMo).

His work enhanced the research done by Lapeer in 1999 [23] by improving the model of the fetal head moulding during the first stage of labour that included the addition of the Hydrostatic Fluid Elements (HFE) to model the Intra-cranial Pressure (ICP), and the simplification and correction of the 3D fetal skull model and by simulating the effect that incorrect placement of Obstetric Forceps and VE has on the fetal head moulding (see Figure 2.39).

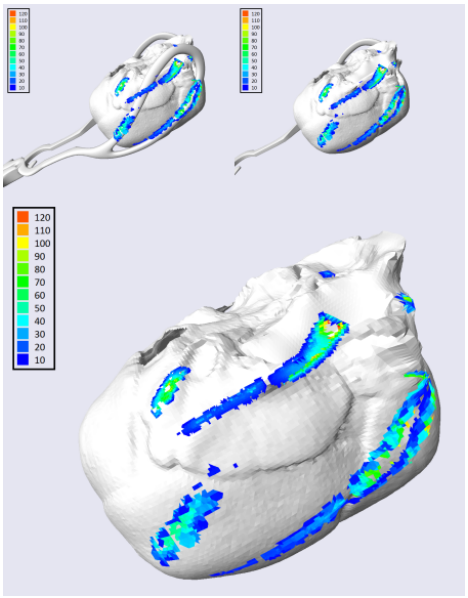

Figure 2.39: Static Finite Element Analysis (SFEA) of obstetric forceps placement on fetal skull by Audinis-2017 (taken from [62])

Some important points to consider is that although forceps blades were used to simulate the compression forces, the latter was applied without the use of the former; i.e. the contact region between the fetal skull and the forceps was marked in the skull and the forces were applied separately. Since this was a static analysis the simulation do not show the changes that the fetal skull is having over time, limiting the visualization of the deformation of the fetal skull surface.

Chapter 3

Methodology

This chapter describes the tools used and methods followed to perform all the tasks involved in the research.

Firstly, the software tools are mentioned as an overview of their purpose and capabilities, and the impact they have in this research.

The computer-based simulation is executed using the software Abaqus®, which will perform finite element analysis, to simulate the mechanical behaviour of the objects when they are interacting with each other. The contact analysis will show how the objects' surfaces behave under different conditions, such as constraints and forces.

A number of steps are needed to prepare the simulation to consider all the conditions under which it will work including the material properties of the objects involved.

3.1 Finite Element Analysis (FEA)

Simulating the effect of the obstetric forceps placement on the fetal head, can be seen as a mechanical problem of a complex and continuous fetal head structure domain in contact with another complex and continuous obstetric forceps structure domain.

In real life, the fetal head can be deformed under the compression forces exerted by the obstetric forceps blades. Modelling the displacement field of complex shapes such as the fetal head using differential equations is impractical. If the domain of this structural problem is discretized into a finite number of subdomains called Finite Elements (FEs), then the displacement field can be approximated by polynomials that are interpolated with respect to points (nodes) located on the boundary or within the elements, and the nodal values are calculated by numerical methods [63, 64, 65, 66].

3.1.1 Stages

The Finite Element Method (FEM) is a numerical method to solve Partial Differential Equations (PDEs), which steps are categorized in three main stages [64]:

- Pre-processing.
- Solution.
- Post-processing.

3.1.1.1 Pre-processing

This is the most important stage where the setup of the analysis takes place and can be broken down as follows:

- Discretization of geometry to transform a continuous problem into a discrete problem that can be solved numerically.
- Selection of elements either first order or second order elements.
- Definition of material properties used by the geometry.
- Definition of physical constraints such as boundary conditions and loads.

Structural equations for every element are created based on these data.

3.1.1.2 Solution

Solves the system of algebraic equations derived at the previous stage.

3.1.1.3 Post-processing

At this stage, the visual representation of the numerical results obtained by the previous stage takes place. Numerical results can involve displacements, stress, strain among many others.

3.1.2 Static and Dynamic FEA

The main characteristic of a Static Finite Element Analysis (SFEA), is that loads are constant and do not change over time.

In order to derive the displacement field for the whole structure in this type of analysis, the stiffness matrix (which contains the geometric and material behaviour information indicating the resistance of the elements to deformation when they are subjected to loading) and the associated element equation for every element should be derived first. This equation correlates the nodal displacements and forces of each individual element as it is shown in Equation 3.1 as follows [65, 64]:

$$[k]\{u\} = \{f\} \tag{3.1}$$

where:

- $[k]$ is the element stiffness matrix.
- $\{u\}$ is the element nodal displacements vector.
- $\{f\}$ is the element nodal forces vector.

The main characteristic of Dynamic Finite Element Analysis (DFEA) is that the loads can change over time.

For dynamic loads or time-varying loads, the mass distribution of the structure produce dynamic effects or inertia forces, therefore the derived matrix equations from Eq. 3.1 should be modified to reflect the mass distribution as follows [65, 64]:

$$[k]\{u\} + [m]\{\ddot{u}\} = \{F\} \tag{3.2}$$

where:

- $[k]$ is the stiffness matrix.
- $\{u\}$ is the element nodal displacements vector.
- $[m]$ is the mass matrix.
- $\{\ddot{u}\}$ is the nodal acceleration vector (second derivative of the displacement).
- $\{f\}$ is the element nodal forces vector.

In the equation above, $\{u\}$, $\{\ddot{u}\}$ and $\{F\}$ are time dependent.

The deformation of a fetal head falls in this category as Fetal Head Moulding (FHM) is a result of the excess of force performed by the obstetric forceps or the birth canal over time.

3.1.3 Numerical metrics

There are different metrics used to measure the output results of the FEA, this research is focused mainly in three metrics as explained in the next sections.

3.1.3.1 Nodal displacement

As mentioned in Section 3.1.2, this metric refers to the computed movement of the model nodes, from their original position to a new position after a load or a boundary condition is applied.

$$u = \{u_x, u_y, u_z\}^T \tag{3.3}$$

Nodal displacement is calculated during FEA as part of solving the stiffness matrix in the equations for static or dynamic analysis (see Equations 3.1 and 3.2).

3.1.3.2 Stress

Stress is defined as the internal force per unit area acting within a solid [65] and describes how internal forces are distributed over a cross-section of the solid subjected to applied loads:

$$\sigma = \frac{F}{A} \tag{3.4}$$

where:

- σ denotes stress (Pa or N/m^2).
- F is the internal force applied (N).
- A is the area (m^2).

In 3D, stress is a second-order tensor that represents the internal force at a point in all directions i.e

$$\sigma = \begin{bmatrix} \sigma_{xx} & \tau_{xy} & \tau_{xz} \\ \tau_{yx} & \sigma_{yy} & \tau_{yz} \\ \tau_{zx} & \tau_{zy} & \sigma_{zz} \end{bmatrix} \tag{3.5}$$

Stress components in Equation 3.5 are depicted in Figure 3.1 and classified as follows:

- **Normal stress:** Force perpendicular (normal) to the surface and it can be represented in vector notation as:
$$\sigma_n = \begin{Bmatrix} \sigma_{xx} & \sigma_{yy} & \sigma_{zz} \end{Bmatrix}^T \tag{3.6}$$
where:
  - σ_{xx}: Normal stress on face perpendicular to x axis in x-direction.
  - σ_{yy}: Normal stress on face perpendicular to y axis in y-direction.
  - σ_{zz}: Normal stress on face perpendicular to z axis in z-direction.
- **Shear stress:** Force parallel (tangential) to the surface and can be represented in vector notation as:
$$\tau = \begin{Bmatrix} \tau_{xy} & \tau_{xz} & \tau_{yx} & \tau_{yz} & \tau_{zx} & \tau_{zy} \end{Bmatrix}^T \tag{3.7}$$
where:
  - τ_{xy}: Shear stress on x face in the y-direction.
  - τ_{xz}: Shear stress on x face in the z-direction.
  - τ_{yx}: Shear stress on y face in the x-direction.
  - τ_{yz}: Shear stress on y face in the z-direction.
  - τ_{zx}: Shear stress on z face in the y-direction.
  - τ_{zy}: Shear stress on z face in the y-direction.

  Due to symmetry of the stress tensor:
$$\tau_{xy} = \tau_{yx}, \tau_{yz} = \tau_{zy}, \tau_{zx} = \tau_{xz} \tag{3.8}$$
  Equation 3.7 can be simplified as follows:
$$\tau = \begin{Bmatrix} \tau_{xy} & \tau_{yz} & \tau_{zx} \end{Bmatrix}^T \tag{3.9}$$

Hence only six components are needed to represent stress at a point as follows:

$$\{\sigma\} = \begin{Bmatrix} \sigma_{xx} & \sigma_{yy} & \sigma_{zz} & \tau_{xy} & \tau_{yz} & \tau_{zx} \end{Bmatrix}^T \tag{3.10}$$

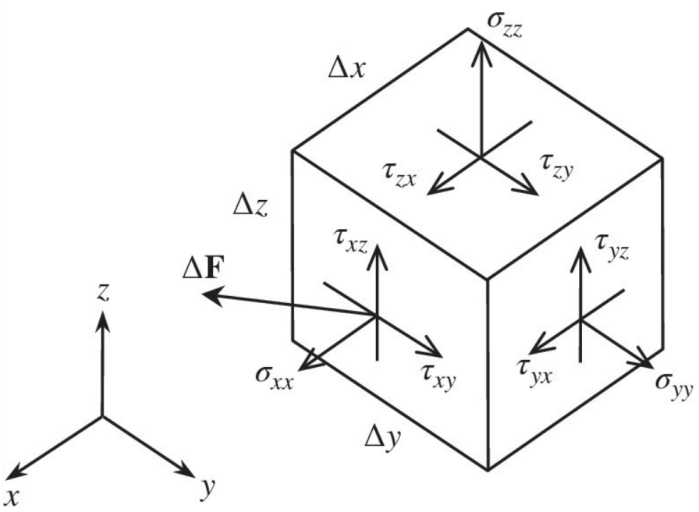

Figure 3.1: Stress components represented in an infinitesimal cube in a Cartesian coordinate system (taken from [65]).

3.1.3.3 Strain

Strain is a quantitative measure of the deformation of a solid, i.e. how much an element stretches, compresses or shears as a direct result of the nodal displacement.

In 3D, strain is a second-order tensor that represents the normal and shear deformations:

$$\varepsilon = \begin{bmatrix} \varepsilon_{xx} & \frac{\gamma_{xy}}{2} & \frac{\gamma_{xz}}{2} \\ \frac{\gamma_{yx}}{2} & \varepsilon_{yy} & \frac{\gamma_{yz}}{2} \\ \frac{\gamma_{zx}}{2} & \frac{\gamma_{zy}}{2} & \varepsilon_{zz} \end{bmatrix} \tag{3.11}$$

Figure 3.2, shows the points P, Q and R of a body before deformation, and the points P', Q' and R' respectively after deformation.

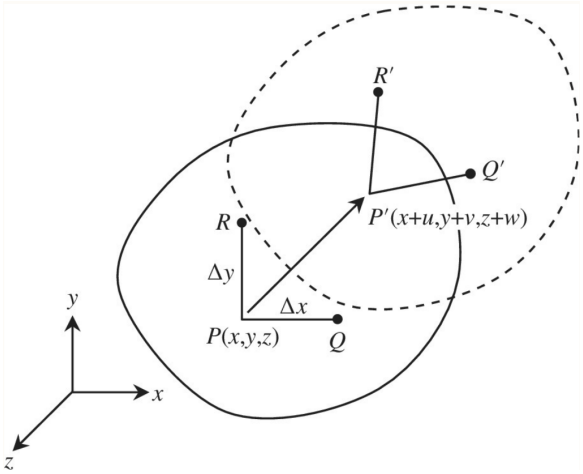

Figure 3.2: Body before and after deformation (taken from [65]).

- **Normal strain:** Under the assumption that strains are small, the normal strain at a point can be defined as the change in length per unit length of an infinitesimal segment originally parallel to the x-axis [65]:

$$\varepsilon_{xx} = \frac{P'Q' - PQ}{PQ} = \frac{\partial u}{\partial x} \tag{3.12}$$

  Similarly, normal strain in the y-direction and z-direction can be derived as:

$$\varepsilon_{yy} = \frac{\partial v}{\partial y} \tag{3.13}$$

$$\varepsilon_{zz} = \frac{\partial w}{\partial z} \tag{3.14}$$

- **Shear strain:** The shear strain, is defined as the change in the angle between a pair of infinitesimal line segments.

  The angle between the segments PQ and $P'Q'$ in the xy plane, can be derived as :

$$\theta_1 = \frac{y_{Q'} - y_Q}{\Delta x} = \frac{\partial v}{\partial x} \tag{3.15}$$

  Similarly, the angle between the segments PR and $P'R'$ is:

$$\theta_2 = \frac{x_{R'} - x_R}{\Delta y} = \frac{\partial u}{\partial y} \tag{3.16}$$

  Hence the shear strain in the xy plane considering Equations 3.15 and 3.16 is defined as:

$$\gamma_{xy} = \theta_1 + \theta_2 = \frac{\partial u}{\partial y} + \frac{\partial v}{\partial x} \tag{3.17}$$

Similarly, we can derive the shear strains in the yz and zx planes as:

$$\gamma_{yz} = \frac{\partial v}{\partial z} + \frac{\partial w}{\partial y} \tag{3.18}$$

$$\gamma_{zx} = \frac{\partial w}{\partial x} + \frac{\partial u}{\partial z} \tag{3.19}$$

Shear strains γ_{xy}, γ_{yz} and γ_{zx}, are called engineering strains. The tensorial shear strains are defined as:

$$\begin{aligned} \varepsilon_{xy} &= \frac{1}{2}\left(\frac{\partial u}{\partial y} + \frac{\partial v}{\partial x}\right) = \frac{\gamma_{xy}}{2} \\ \varepsilon_{yz} &= \frac{1}{2}\left(\frac{\partial v}{\partial z} + \frac{\partial w}{\partial y}\right) = \frac{\gamma_{yz}}{2} \\ \varepsilon_{zx} &= \frac{1}{2}\left(\frac{\partial w}{\partial x} + \frac{\partial u}{\partial z}\right) = \frac{\gamma_{zx}}{2} \end{aligned} \tag{3.20}$$

Therefore, Equation 3.11 can be simplified as:

$$\varepsilon = \begin{bmatrix} \varepsilon_{xx} & \varepsilon_{xy} & \varepsilon_{xz} \\ \varepsilon_{yx} & \varepsilon_{yy} & \varepsilon_{yz} \\ \varepsilon_{zx} & \varepsilon_{zy} & \varepsilon_{zz} \end{bmatrix} \tag{3.21}$$

Considering that $\varepsilon_{ij} = \varepsilon_{ji}$ and $i \neq j$ the strain matrix can be represented as a 3D vector as follows:

$$\{\varepsilon\} = \begin{bmatrix} \varepsilon_{xx} & \varepsilon_{yy} & \varepsilon_{zz} & \varepsilon_{xy} & \varepsilon_{yz} & \varepsilon_{zx} \end{bmatrix}_T \tag{3.22}$$

3.2 Software tools

3.2.1 3D Modeling

The models used in this project were either modified and/or created using software such as Blender® which is a free open source 3D suite, with a great flexibility to model 3D objects [67]; it has an easy to use user interface and a vast amount of online documentation [68]. Version 3.4.1 was used in this research (see Figure 3.3).

Another software tool used to create and modify 3D models was Abaqus® [69] (See Section 3.3).

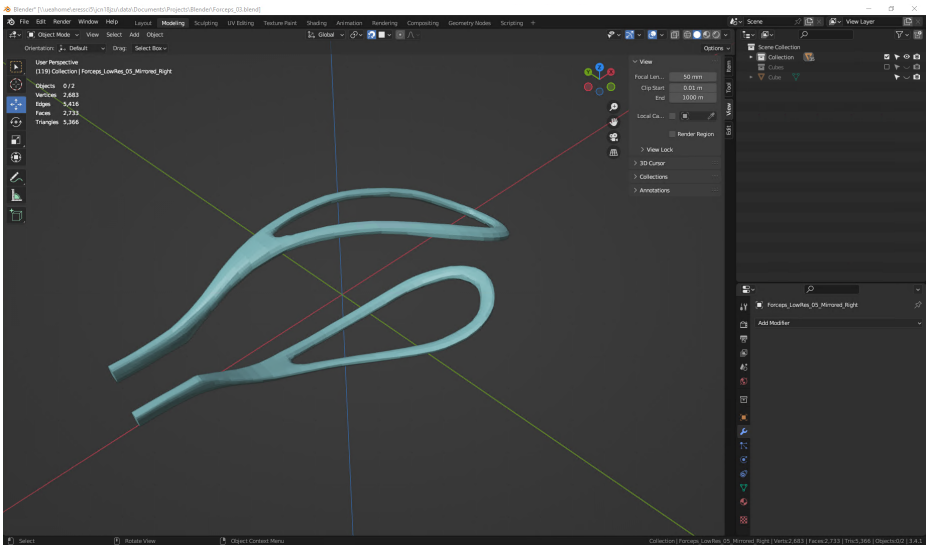

Figure 3.3: Blender® version 3.4.1 user Interface.

3.2.2 Simulation

Abaqus® was used to perform computer-based simulations using FEA. It is a general-purpose finite element-based software that can simulate complex real-world problems such as mechanical, electrical, etc., it can model geometries with different material properties and simulate their structural behaviour [69]. Abaqus® Computer-Aided Engineering (CAE) Version 2021 was used in this research.

3.3 3D Model generation and specification

From a mechanical point of view, childbirth is a complex process where the interaction between maternal pelvis and fetal head is not restricted to just contact between bones but considers different types of elements such as muscles, soft tissues, fluids, etc. An Operative Vaginal Delivery (OVD) puts an extra layer of complexity by adding external elements to the process.

This project will focus on the interaction between the *obstetric forceps* and the *fetal head* when a OVD is performed. The interaction of either the fetus or the obstetric forceps with the maternal pelvic tissues are not considered, only the effects of the forceps on the fetal head.

3.3.1 3D Obstetrics forceps

3.3.1.1 Model approximation

An initial simplification of the obstetric forceps was created using a pair of geometric curved plates to validate the basic motions performed by the real Obstetric Forceps (see Figure 3.4).

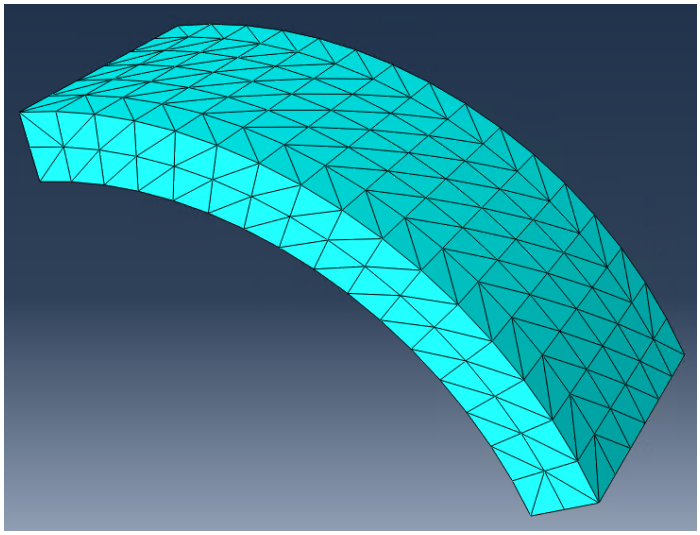

Figure 3.4: Geometric curved plate as a minimal representation of the obstetric forceps.

This minimal representation contains a lower number of elements and nodes (see Table 3.1) compared with the models used in later simulations, making the processing time of the simulation shorter.

Feature	**Count**
Nodes	416
Elements	1504
Type	Solid (C3D4)

Table 3.1: Mesh information of simplified geometric curved plate.

3.3.1.2 Initial model

This research considered the same 3D obstetric forceps that were used in the work of Lapeer 2014 et al. [70], which is a 3D representation of the Neville-Barnes forceps with Simpson's handles (see Figure 3.5). Table 3.2 shows detail information about the number of nodes and elements contained in the model.

Feature	**Count**
Nodes	1734
Elements	3468

Table 3.2: Mesh information of original 3D forceps [70].

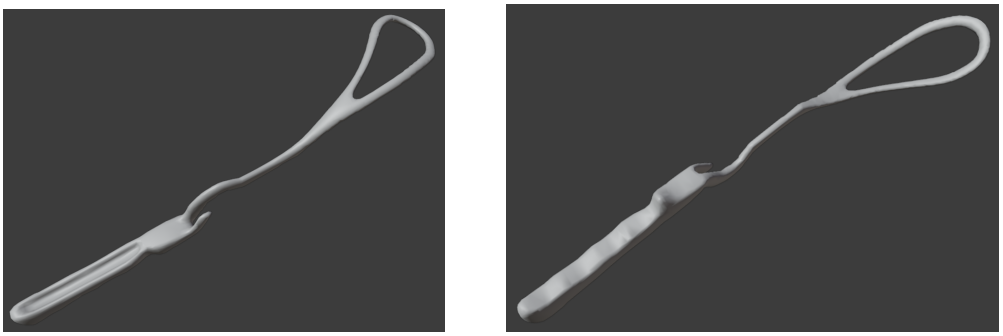

(a) Top view. (b) Bottom view.

Figure 3.5: Top (a) and bottom (b) views of original 3D obstetrics forceps model [70].

This 3D model was not entirely suitable for the simulation, the lack of smoothness added converge problems and the excess of mesh added unnecessary elements to process. For this reason, a new mesh was needed to consider only the relevant parts of the obstetric forceps for the simulation (see Section 3.3.1.3).

3.3.1.3 Proposed 3D model

This research proposes a new 3D model of the obstetric forceps where the handles and lock parts were removed, keeping only the shanks and blades. Figure 3.6 shows the comparison between the initial and the proposed 3D model; Figures 3.6a and 3.6b display the top and bottom views respectively of the initial 3D model, where the handles are visible, such as the internal bezel, fingers guard, and lock. Figures 3.6c and 3.6d display the top and bottom views respectively of the proposed 3D model, where the handles and locks were removed.

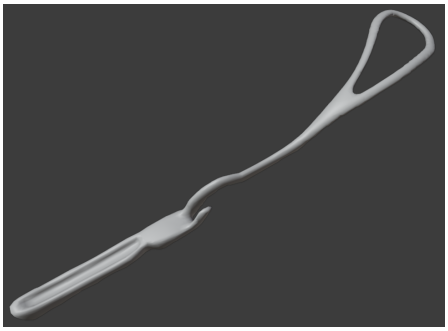

(a) Initial model - top view.

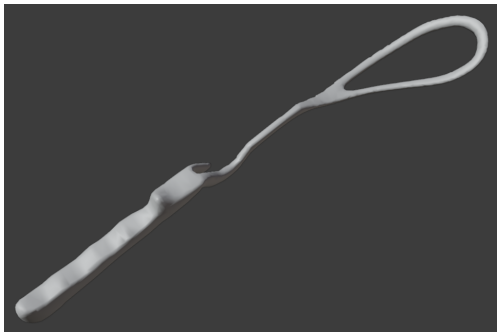

(b) Initial model - bottom view.

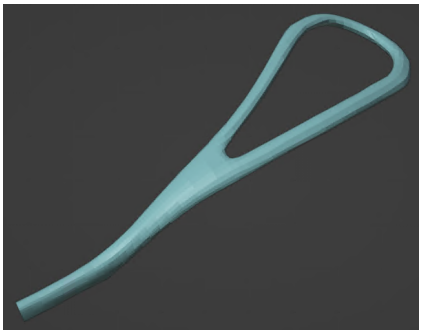

(c) Proposed model - top view.

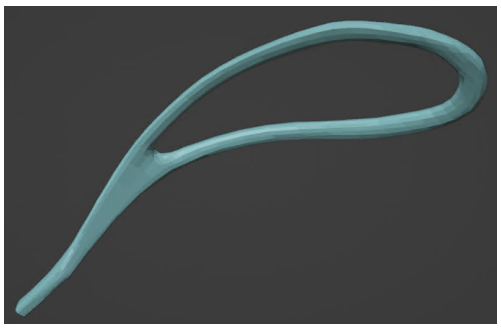

(d) Proposed model - bottom view.

Figure 3.6: Obstetric forceps comparison between initial 3D model (top) and proposed 3D model (bottom).

Figure 3.7, shows the final version of the proposed 3D forceps model. As it can be seen, the model is reduced to consider only the blades which is the part that is in contact with the baby head during childbirth.

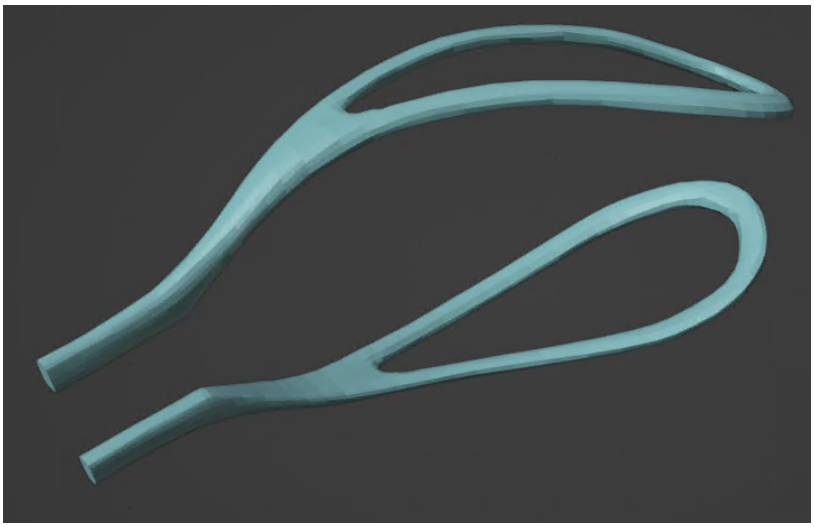

Figure 3.7: Final proposed version of 3D obstetric forceps model without handles.

3D Object	Count of Nodes	Count of Elements	Element Type
Initial			
Left blade	1737	3468	-
Proposed			
Left blade	1752	6250	Solid (C3D4)
Right blade	1744	6209	Solid (C3D4)

Table 3.3: Mesh information comparison between original and proposed 3D obstetric forceps.

The mesh information comparison between meshes contemplating the number of nodes and elements, between the initial and the final proposed version of the obstetric forceps blades is described in Table 3.3.

3.3.1.4 Material properties

The material properties of the obstetric forceps were defined as steel, described in Table 3.4.

Description	Value
Young's modulus	209 GPa
Poisson's ratio	0.3
Mass density	7800 kg/m^3
Material type	Elastic Isotropic

Table 3.4: Steel material properties.

3.3.2 3D Fetal head model

3.3.2.1 Model approximation

A simplification of the Fetal Head (FeH) or Baby Head (BH) was made using a 3D model of a geometric Sphere (SPH) which served as a faster way to validate the effects of the Obstetric Forceps on the FeH or Baby Head (BH).

Meshes of a geometric sphere with different number of elements were created (see Figure 3.8) and defined as follows:

- SPH_1 - Coarse mesh.
- SPH_2 - Medium mesh
- SPH_3 - Fine mesh.

- SPH_4 - Finer mesh.

Each sphere has a diameter of 10cm or 0.1m, this is:

$$d_{SPH_1} = d_{SPH_2} = d_{SPH_3} = d_{SPH_4} = 0.1\text{m} \tag{3.23}$$

where:

- d_{SPH_1} is the diameter of SPH_1.
- d_{SPH_2} is the diameter of SPH_2.
- d_{SPH_3} is the diameter of SPH_3.
- d_{SPH_4} is the diameter of SPH_4.

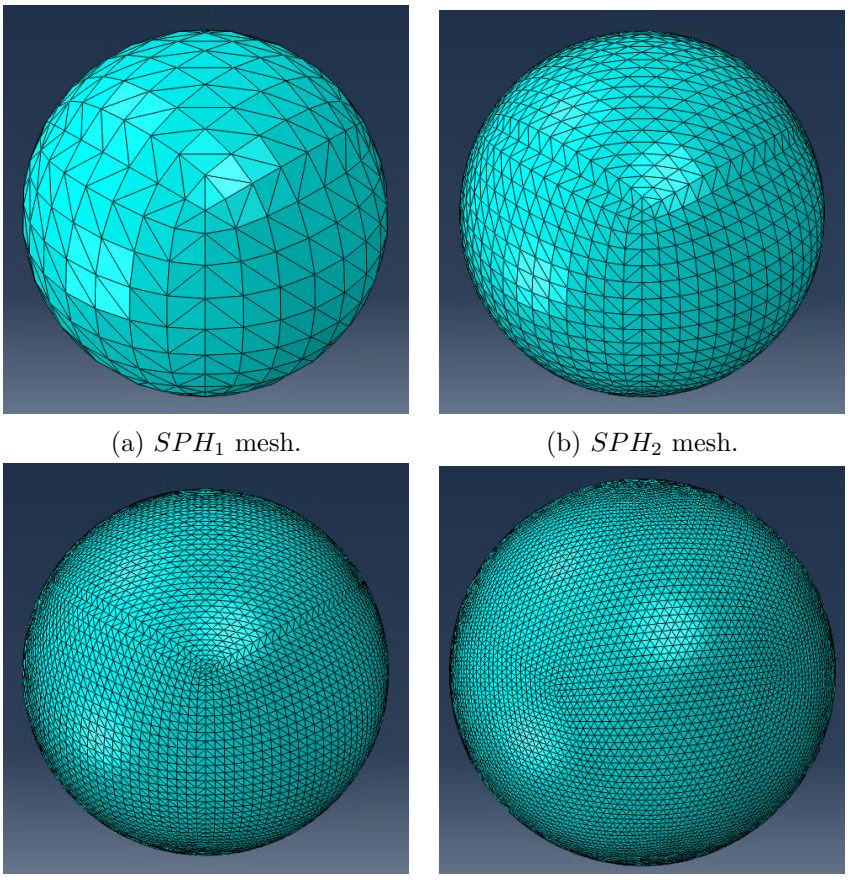

(a) SPH_1 mesh. (b) SPH_2 mesh.

(c) SPH_3 mesh. (d) SPH_4 mesh.

Figure 3.8: Different mesh refinements of the geometric sphere classified as coarse (Figure 3.8a), medium (Figure 3.8b), fine (Figure 3.8c) and finer (Figure 3.8d) according to the number of elements they contain (see Table 3.5).

Table 3.5, shows the number of nodes, elements and the element type of the different mesh refinements of the geometric sphere.

Mesh	Feature	Count
SPH_1	Nodes	386
	Elements	768
	Type	Shell (S3)
SPH_2	Nodes	1,538
	Elements	3,072
	Type	Shell (S3)
SPH_3	Nodes	6,146
	Elements	12,288
	Type	Shell (S3)
SPH_4	Nodes	10,242
	Elements	20,480
	Type	Shell (S3)

Table 3.5: Geometric spheres mesh information.

3.3.2.2 Initial model

The 3D FeH model or BH used in this research, was obtained from the laser scan of a baby head mannequin (see Figure 3.9). Table 3.6, shows the mesh information of the 3D model.

Figure 3.9: Original 3D model of baby head obtained from a laser scan.

Feature	Count
Nodes	99,994
Elements	200,000

Table 3.6: Original 3D fetal head mesh information (number of nodes and number of elements).

For purposes of the simulation, this original fine mesh represents a challenge in terms of processing time, due to the large number of nodes and elements it has. Considering this, a coarse mesh is considered to solve this issue modifying the original 3D model to the current needs of the research.

3.3.2.3 Proposed 3D Geometry

Due to the high number of elements in the original 3D FeH model, different with different number of elements were created (see Figure 3.10) and defined as follows:

- FeH_1 - Coarse mesh.
- FeH_2 - Medium mesh.
- FeH_3 - Fine mesh.

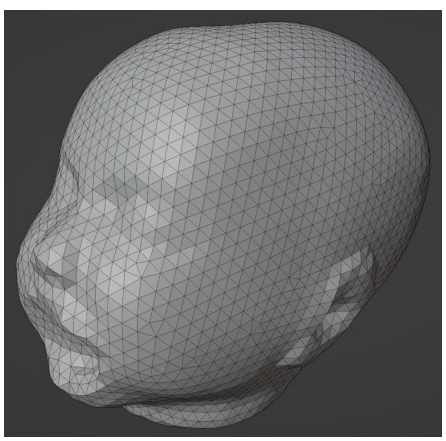

(a) FeH_1 mesh.

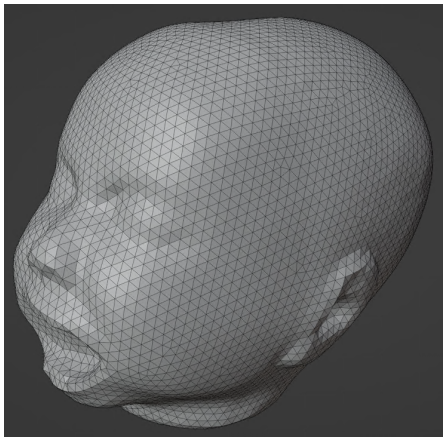

(b) FeH_2 mesh.

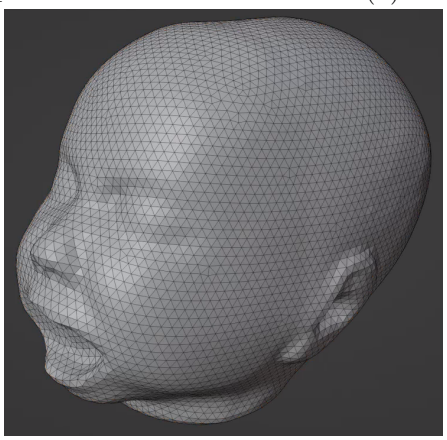

(c) FeH_3 mesh.

Figure 3.10: Different mesh refinements of the fetal head classified as coarse (Figure 3.10a), medium (Figure 3.10b) and fine (Figure 3.10c).

Table 3.7, shows the number of nodes and elements of the different fetal head meshes.

Mesh	Feature	Count
FeH_1	Nodes	3489
	Elements	6974
	Type	Shell (S3)
FeH_2	Nodes	6576
	Elements	13148
	Type	Shell (S3)
FeH_3	Nodes	8482
	Elements	16960
	Type	Shell (S3)

Table 3.7: Information of different Fetal Head (FeH) meshes refinement.

Features like fontanelles and sutures were required to get a better representation of the fetal head mechanical structure, features that were added to the previous set of meshes by projecting them from a fetal skull model, as a result a new set of Improved Fetal Head (IFeH) meshes were created (see Figure 3.11) and defined as follows:

- $IFeH_1$ - Improved coarse mesh.
- $IFeH_2$ - Improved medium mesh.
- $IFeH_3$ - Improved fine mesh.

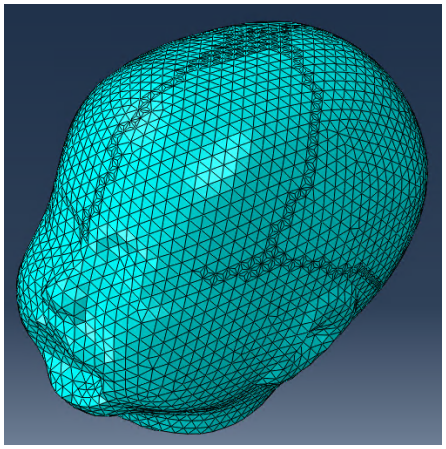

(a) $IFeH_1$ mesh.

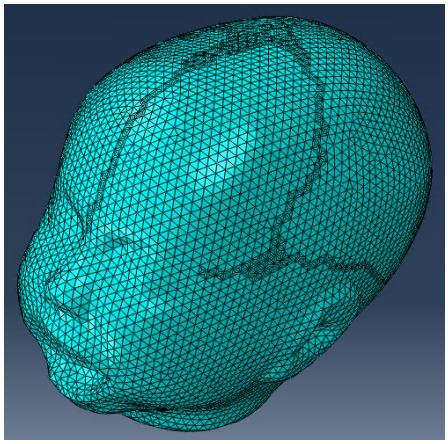

(b) $IFeH_2$ mesh.

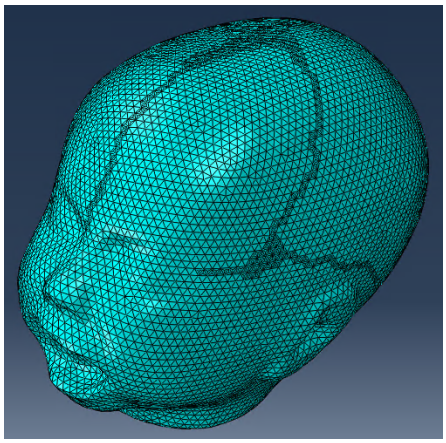

(c) $IFeH_3$ mesh.

Figure 3.11: Different mesh refinements of the Improved Fetal Head (IFeH) model with fontanelles and sutures classified as coarse (Figure 3.11a), medium (Figure 3.11b) and fine (Figure 3.11c).

Table 3.8, shows the new count of nodes and elements for the modified meshes.

Mesh	Feature	Count
$IFeH_1$	Nodes	3956
	Elements	7908
	Type	Shell (S3)
$IFeH_2$	Nodes	7325
	Elements	14646
	Type	Shell (S3)
$IFeH_3$	Nodes	9373
	Elements	18742
	Type	Shell (S3)

Table 3.8: Information of different Improved Fetal Head (IFeH) meshes refinement.

3.3.2.4 Material properties

With the addition of fontanelles and sutures, the fetal head was divided in different regions (see Section 2.2.3) which are grouped in three different material properties (taken from [60]):

- Fontanelles and sutures: Specified as hyperelastic isotropic material with the following properties:
  - Thickness: 0.75 mm (0.00075 m)
  - Mass density: 1000 kg/m^3
  - Material type: Hyperelastic
  - Strain energy potential: Mooney-Rivlin with parameters defined in Table 3.9 as follows:

Coefficient	Value
C_{10}	1.18 MPa
C_{01}	0.295 MPa
D_1	0 Pa

Table 3.9: Mooney-Rivlin parameters, where C_{01} and C_{10} describe the shear behavior of the material and D_1 introduce compressibility (set to zero if the material is fully incompressible).

- Cranial bone: This material was specified as an elastic lamina material with the following properties:
  - Thickness: 0.75 mm (0.00075 m)
  - Mass density: 1200 kg/m^3

– Material type: Elastic lamina with parameters defined in Table 3.10 as follows:

Coefficient	Value
E_1	3.86 GPa
E_2	965 MPa
Nu_{12}	0.22
G_{12}	1.582 GPa
G_{13}	1.582 GPa
G_{23}	1.582 GPa

Table 3.10: Bone material properties, E_1 and E_2 are Young's modulus referring to elastic modulus parallel and perpendicular to the bone fiber respectively; G_{12} is the in-plane shear modulus, G_{13} is the out-of-plane shear modulus and G_{23} is the transverse out-of-plane shear modulus; Nu_{12} is Poisson's ratio.

In this case the lamina material is assumed to be very thin, hence the through-thickness normal stress and strain is considered to be negligible therefore E_3 modulus is not considered.

On the other side, shear modulus G_13 and G_23 are still important even though E_3 is not considered because it can occur transverse shear deformation.

- Base bone: This material was specified as elastic lamina material similar but thicker than the cranial bone with the following properties:
  - Thickness: 2 mm (0.002 m)
  - Mass density: 1200 kg/m^3
  - Material type: Elastic lamina with the same parameters defined in Table 3.10 for cranial bone.

3.4 Computer-based Simulations

A number of different experiments were considered to simulate the behaviour of the effect of obstetric forceps placement on the fetal head, which are explained in this section.

All simulations were performed using a PC machine with the next specifications:

Feature	Value
Operative System	Windows 10 Enterprise
Processor	Intel Core i7-4790K @ 4.00GHz
RAM	32.0 GB

Table 3.11: Technical specifications of PC machine were simulations were performed.

3.4.1 Simulation steps

In real life, the obstetric forceps blades are inserted one by one inside the birth canal on each side of the fetal head (see Section 2.2.7.4), whilst they are held by the obstetrician to prevent the blades to slide out of the canal or move from the desired position.

The process to insert the blades and placed them in the correct position before they are closed and locked, and before to perform the extraction of the baby from the mother is not considered in this research.

This simulation only considers the initial, close and pull steps, hence the next assumptions are made:

- The process to insert the blades and placed them in the correct position is assumed hence not performed.
- Only the contact interaction between the blades and the baby head is considered. No other interaction is performed.
- Blades are placed as close as possible to the 3D mesh of the fetal head without touching each other to give room between a **no contact state** and a **contact state**.

3.4.1.1 Initial step

The **initial step** or **initial state** refers to the state where the simulation has not started yet i.e. when $t = 0$, but the conditions are set such as:

- Initial position and location of right and left forceps blades.
- Initial position and location of baby head.
- Modelling constraints.
- Boundary conditions.

3.4.1.2 Close step

The aim of this step is to simulate the effect of the obstetric forceps on the fetal head when the obstetrician is closing and locking the blades around the fetal head.

This step begins when the obstetric forceps blades, Forceps Left Blade (FLB), Forceps Right Blade (FRB) and the Baby Head (BH) are in the **no contact state** or **initial state**, i.e.

$$\begin{aligned} FLB(x, y, z) &= (x_{1_0}, y_{1_0}, z_{1_0}) \\ FRB(x, y, z) &= (x_{2_0}, y_{2_0}, z_{2_0}) \\ BH(x, y, z) &= (x_{3_0}, y_{3_0}, z_{3_0}) \end{aligned} \tag{3.24}$$

Where:

- $FLB(x, y, z)$ is the position of the forceps left blade.
- $FRB(x, y, z)$ is the position of the forceps right blade.

- $BH(x, y, z)$ is the position of the baby head.
- $x_{i_0}, y_{i_0}, z_{i_0}$ where $i = 1...3$, is the initial position of each model.
- Taken the screen as a reference, we consider x, y and z axis as follows:
  - x is the horizontal axis (red).
  - y is the vertical axis (green).
  - z is the axis (blue) perpendicular to x and y.

Then the obstetric forceps move towards the fetal head to enter the **contact state**. The displacement of the obstetric forceps blades in this step is defined as:

$$\begin{aligned} 0 <= u_{FLB_x} <= u_{FB_{max_x}} \\ 0 <= u_{FRB_x} <= u_{FB_{max_x}} \end{aligned} \tag{3.25}$$

Where:

- u_{FLB_x} is the displacement of the forceps left blade on the x component.
- u_{FRB_x} is the displacement of the forceps right blade on the x component.
- $u_{FB_{max_x}}$ is the maximum displacement of the forceps blades on the x component.

When the displacement of the Forceps Blades (FB) (both FLB and FRB) reaches the maximum displacement $u_{FB_{max_x}}$, it stops the motion of the blades which ends the close step before to continue with the pull step. The **contact state** does not end when the step finishes.

3.4.1.3 Pull step

The pull step aim is to simulate the effect of the obstetric forceps on the fetal head when the obstetrician has already secured the baby head with the forceps and is pulling the blades to move the baby head out of the birth canal.

This step begins when the close step has been completed and reached the point where:

$$\begin{aligned} u_{FLB_x} = u_{FB_{max_x}} \\ u_{FRB_x} = u_{FB_{max_x}} \end{aligned} \tag{3.26}$$

The displacement of the obstetric forceps blades in this step is happening on the z axis and defined as:

$$\begin{aligned} 0 <= u_{FLB_z} <= u_{FB_{max_z}} \\ 0 <= u_{FRB_z} <= u_{FB_{max_z}} \end{aligned} \tag{3.27}$$

The maximum displacement of the blades in the pull step is set to stop the motion of the blades hence end the step. This is when we reach the point when:

$$\begin{aligned} u_{FLB_z} = u_{FB_{max_z}} \\ u_{FRB_z} = u_{FB_{max_z}} \end{aligned} \tag{3.28}$$

Chapter 4

Experiments

Contact problems are challenging from a FEM perspective since they may not converge and/or give unexpected results. For that reason, this research approach was to build the simulation by incrementally adding complexity to it, starting from simple 3D models to make proof of concept and then move to more complex models.

This chapter explains the path followed in this research to improve over each experiment, from the creation of the first simplified simulation through a number of different experiments up to the final simulation.

4.1 Spheres in contact with curved plates

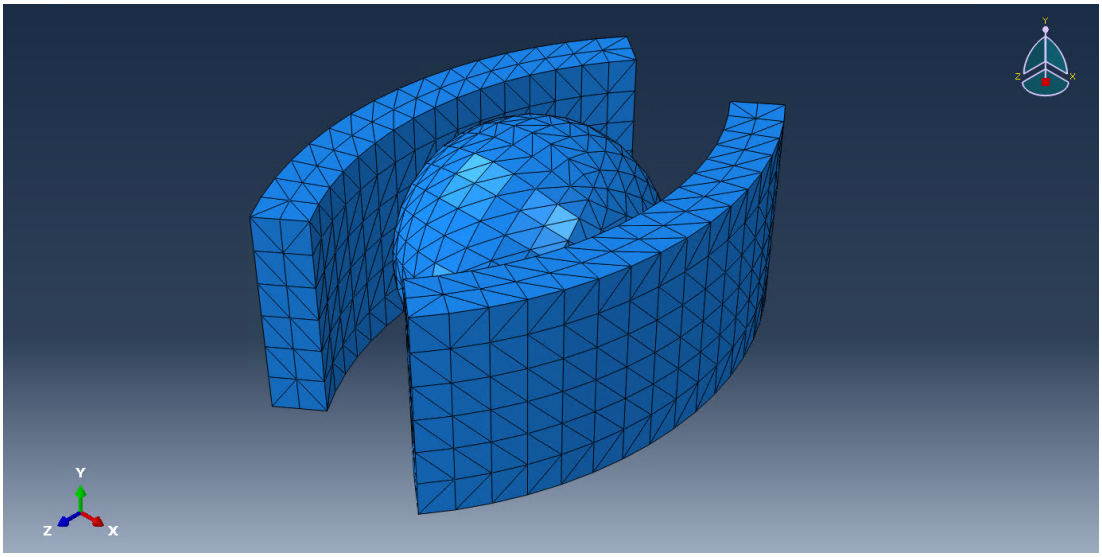

Figure 4.1: Sphere in contact with curved plates simulation.

The aim of this experiment, is to simulate the obstetric forceps-baby head behavior when the close step is performed (see Section 3.4.1.2).

Since each blade of the obstetrics forceps has a specific and complex shape, they were simplified using the geometry shape of a curved plate (see Figure 3.4 in Section 3.3.1.1). At the same time the fetal head was simplified using the geometric shape of a sphere with different number of elements (see Figure 3.8 in Section 3.3.2.1).

Figure 4.1 shows the assembly of the sphere and the pair of cubes in the initial step of the simulation in the Abaqus® environment.

4.1.1 Experiment setup

This section describe the specific steps followed to setup the FEM for the simulation.

4.1.1.1 Sphere model

Spheres are divided in two regions (see Figure 4.2), one that represents the anterior fontanelle and other the cranial bone as described in Section 2.2.3, hence they have two different material properties as described in Section 3.3.2.4. These regions also define contact surfaces that can interact with other surfaces like the curved plates.

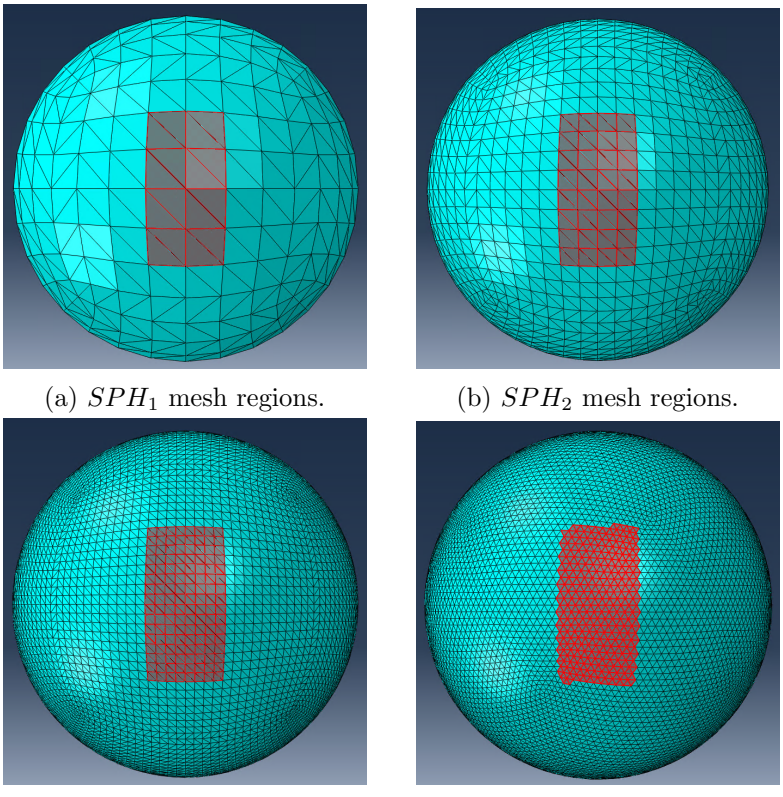

(a) SPH_1 mesh regions. (b) SPH_2 mesh regions.

(c) SPH_3 mesh regions. (d) SPH_4 mesh regions.

Figure 4.2: Representation of anterior fontanelle (red) and cranial bone (turquoise) regions on sphere meshes with different count of elements from lower (SPH_1) to higher (SPH_4).

A second region definition was created representing the posterior fontanelle. This change modified the cranial bone region as it is shown in Figure 4.3. These new regions also represent contact surfaces in the analysis that can interact with the curved plates.

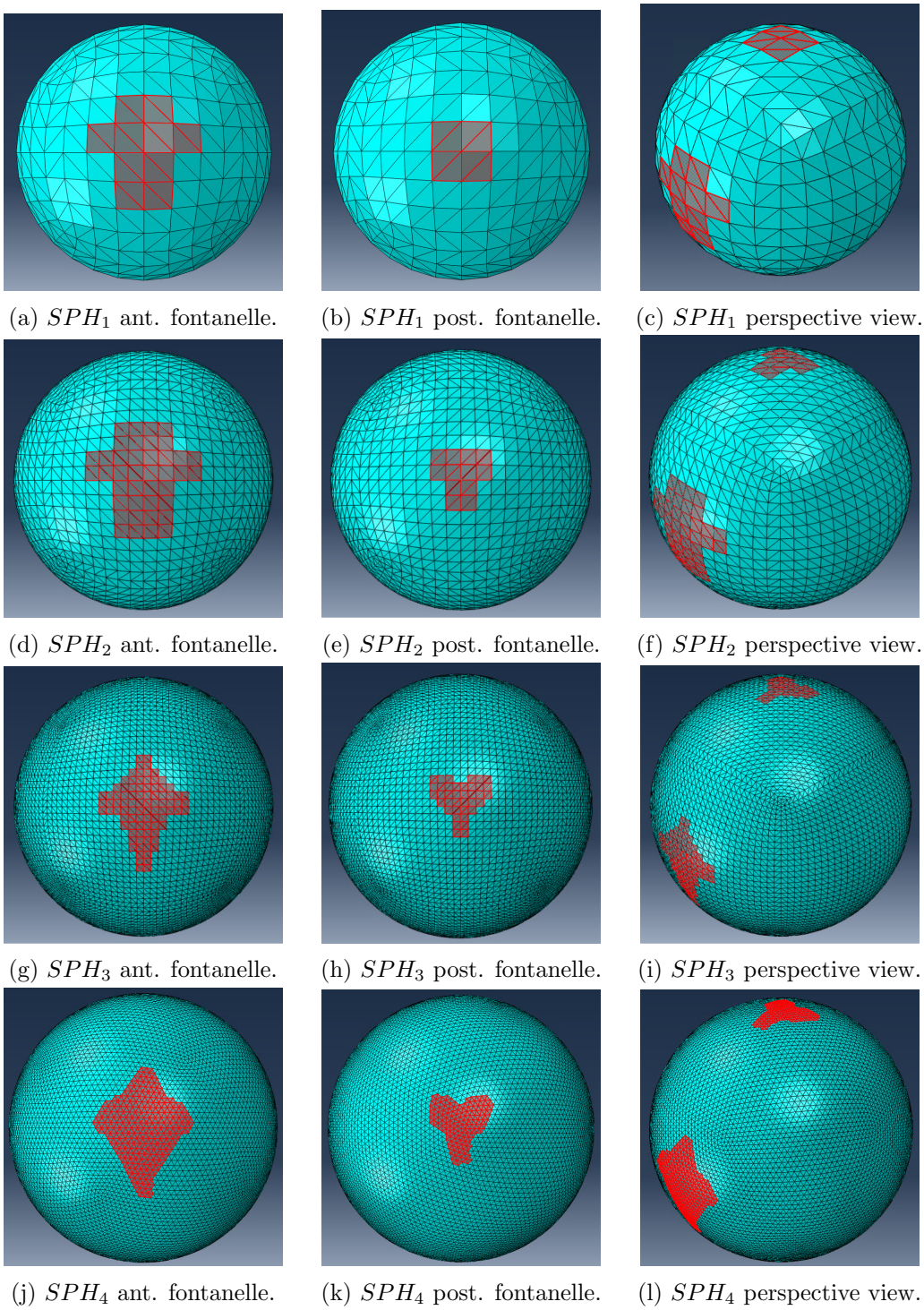

(a) SPH_1 ant. fontanelle. (b) SPH_1 post. fontanelle. (c) SPH_1 perspective view.

(d) SPH_2 ant. fontanelle. (e) SPH_2 post. fontanelle. (f) SPH_2 perspective view.

(g) SPH_3 ant. fontanelle. (h) SPH_3 post. fontanelle. (i) SPH_3 perspective view.

(j) SPH_4 ant. fontanelle. (k) SPH_4 post. fontanelle. (l) SPH_4 perspective view.

Figure 4.3: Improved regions of sphere meshes: anterior fontanelle (left column) and posterior fontanelle (mid column) in red, cranial bone in turquoise. Perspective of both fontanelles (right column). Meshes with different count of elements from lower SPH_1 on top, to higher SPH_4 bottom.

4.1.1.2 Blades model

The inner face of each blade or curved plate mesh is defined as the contact surface that will interact with the sphere as defined in Figure 4.4.

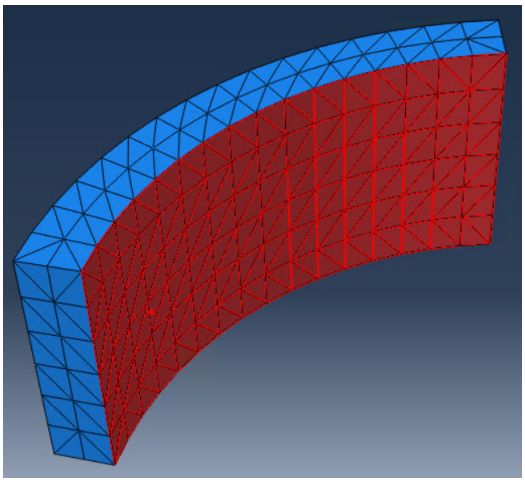

Figure 4.4: Obstetric forceps blade mesh simplification with contact surface definition in red.

4.1.1.3 Steps

All experiments start with an **Initial Step** where the initial conditions of the experiments are set at $t = 0$ (see Section 3.4.1.1).

The initial position of the 3D models is defined as follows based on their volume centroid[1]:

$$\begin{aligned} FLB(x, y, z) &= (-0.05, 0, 0) \\ FRB(x, y, z) &= (0.05, 0, 0) \\ SPH(x, y, z) &= (0, 0, 0) \end{aligned} \tag{4.1}$$

The second step considered in this experiment is the **Close step** as described in Section 3.4.1.2, which considers different analysis depending on the boundary conditions specified in the experiment (see Section 4.1.1.6).

4.1.1.4 Interactions

According to the regions defined previously for the curved plates in Section 4.1.1.2 and the spheres in Section Section 4.1.1.1, this analysis considers the following contact interactions between them (see Figure 4.5):

- LB-SPH: Internal surface of Left Blade (LB) in contact with the Sphere (SPH) cranial bone region.

[1] All values are defined in meters (m).

- RB-SPH: Internal surface of Right Blade (RB) in contact with the Sphere (SPH) cranial bone region

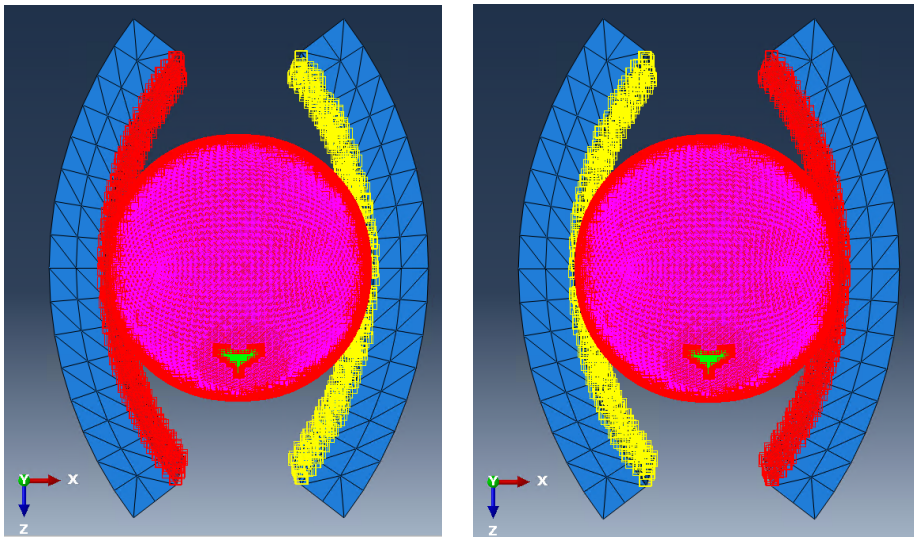

(a) LB-SPH contact interaction. (b) RB-SPH contact interaction.

Figure 4.5: Contact interactions between curved plates and sphere (red surface in both meshes). Figure 4.5a shows the interaction between the left blade and sphere, Figure 4.5b shows the interaction between the right blade and sphere respectively.

In this experiment, there is no direct interaction between fontanelles and curved plates.

4.1.1.5 Loads

This experiment does not apply explicit loads on the blades as it is commonly used in Contact Mechanics [71], instead a constant velocity boundary condition is applied to move the curved plates towards the sphere without applying a direct force. This method allows us to control the amount of displacement to perform over the blades.

4.1.1.6 Boundary Conditions (BCs)

Each mesh contains a set of nodes that will help to apply the Boundary Conditions (BCs) needed in the **Initial** and **Close** steps for the analysis. Node sets are defined as follows (see Figure 4.6):

- Left Blade Constraint (LB_C).
- Right Blade Constraint (RB_C).
- Sphere Constraint (SPH_C).

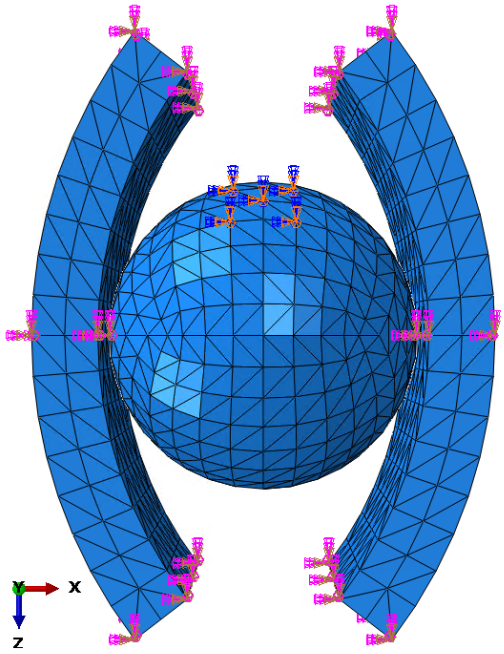

Figure 4.6: Set of nodes defining the BCs in the FEA for LB_C (pink points in left block), SPH_C (blue and orange points in the sphere in the middle) and RB_C (pink points in right block).

The BCs applied to the set of nodes per mesh per step are described in Table 4.1.

Set	**Step**	
	Initial	**Close**
LB_C	Fixed position	Allows displacement in x axis
LB_C	No velocity	Constant velocity on x axis at $1mm/s$
RB_C	Fixed position	Allows displacement in x axis
RB_C	No velocity	Constant velocity on x axis at $1mm/s$
SPH_C	Encastre[2]	Propagated[3]

Table 4.1: BCs applied in the sphere in contact with curved plates analysis in the **Initial** and **Close** steps.

4.1.2 Experimental results with anterior fontanelle only

This section outlines the results obtained in the current spheres in contact with curved plates experiment.

[2]There is no motion at all, no translations and no rotations.
[3]The BC applied in the previous step in used in the current one.

Table 4.2 shows the nodal displacement in x axis (U_x) and the nodal displacement magnitude U, for every sphere when both FLB_x and FRB_x have been translated towards the sphere, this is:

$$\begin{aligned} FLB(x,y,z) &= (-0.050 + a, 0, 0) \\ FRB(x,y,z) &= (0.050 - a, 0, 0) \end{aligned} \tag{4.2}$$

where a is the displacement of the blades performed in the **Close Step** at $1mm$, $2mm$ and $3mm$.

Close step	**Mesh**	U_x	U
$1mm$	SPH_1	$-1.232e^{-03}$	$9.547e^{-04}$
	SPH_2	$-1.681e^{-03}$	$5.213e^{-04}$
	SPH_3	$-1.908e^{-03}$	$8.136e^{-04}$
	SPH_4	$-1.820e^{-03}$	$8.962e^{-04}$
$2mm$	SPH_1	$-2.459e^{-03}$	$1.572e^{-03}$
	SPH_2	$-4.393e^{-03}$	$1.443e^{-03}$
	SPH_3	$-4.443e^{-03}$	$1.555e^{-03}$
	SPH_4	$-4.426e^{-03}$	$1.569e^{-03}$
$3mm$	SPH_1	$-4.359e^{-03}$	$1.476e^{-03}$
	SPH_2	$-6.757e^{-03}$	$2.706e^{-03}$
	SPH_3	$-6.640e^{-03}$	$2.638e^{-03}$
	SPH_4	$-6.457e^{-03}$	$2.573e^{-03}$

Table 4.2: Nodal displacement in x axis (U_x in m) and nodal displacement magnitude (U in m) of sphere in contact with curved plates analysis when LB_C and RB_C performed a 1mm, 2mm and 3mm translation in the x axis towards the sphere.

Figures 4.7 and 4.8 show the nodal displacement in x axis (U_x) and nodal displacement magnitude (U) results of the spheres in contact with curved plates, when curved plates FLB_x and FRB_x have been translated $1mm$ towards the sphere, Figures 4.9 and 4.10 when curved plates have been translated $2mm$, and Figures 4.11 and 4.12 when curved plates have been translated $3mm$. U_x shows the displacement regions in x axis and U shows the displacements regions in all affected axis during the forceps-spheres contact analysis.

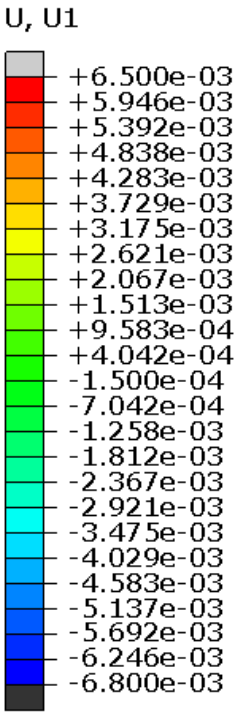

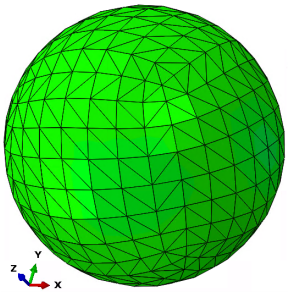

(a) SPH_1 anterior left sagittal view.

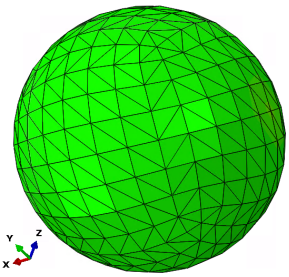

(b) SPH_1 posterior right sagittal view.

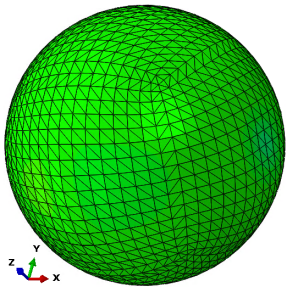

(c) SPH_2 anterior left sagittal view.

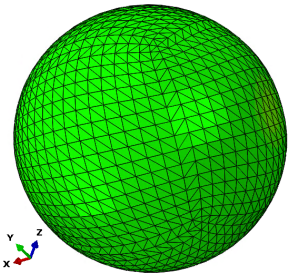

(d) SPH_2 posterior right sagittal view.

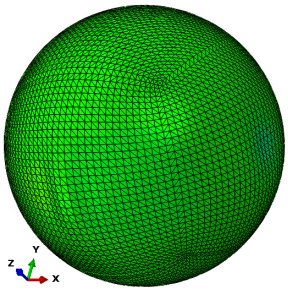

(e) SPH_3 anterior left sagittal view.

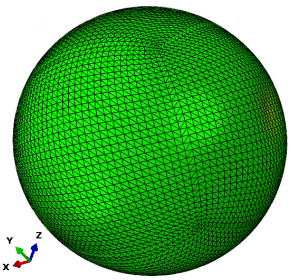

(f) SPH_3 posterior right sagittal view.

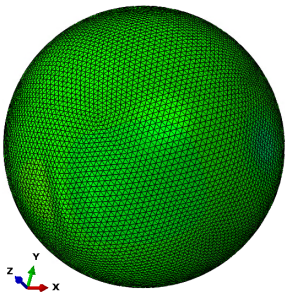

(g) SPH_4 anterior left sagittal view.

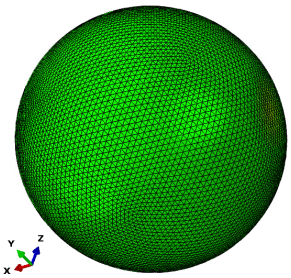

(h) SPH_4 posterior right sagittal view.

Figure 4.7: Nodal displacement in x axis (U_x) result in spheres models when $FLB_x = FRB_x = 1$mm

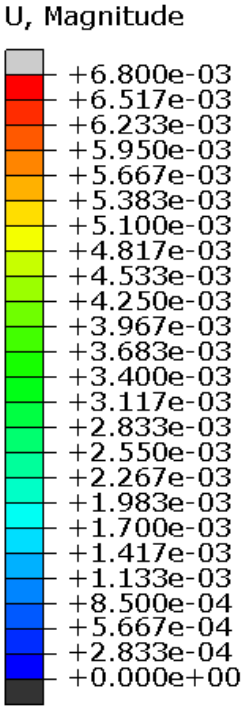

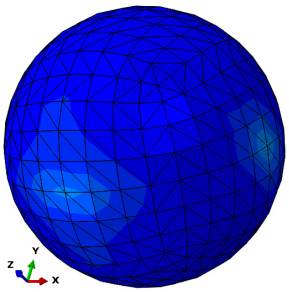

(a) SPH_1 anterior left sagittal view.

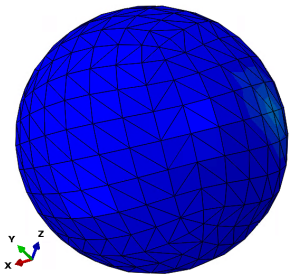

(b) SPH_1 posterior right sagittal view.

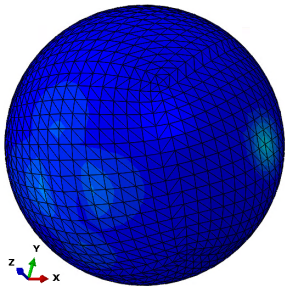

(c) SPH_2 anterior left sagittal view.

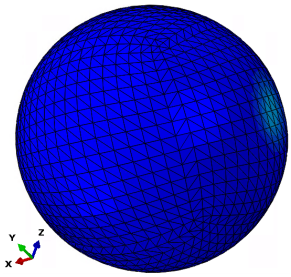

(d) SPH_2 posterior right sagittal view.

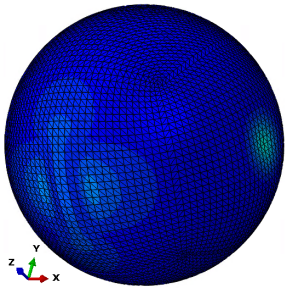

(e) SPH_3 anterior left sagittal view.

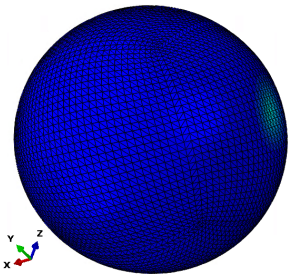

(f) SPH_3 posterior right sagittal view.

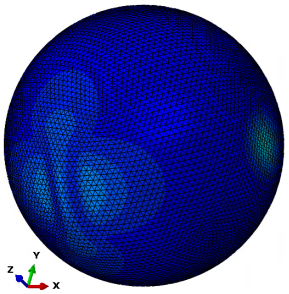

(g) SPH_4 anterior left sagittal view.

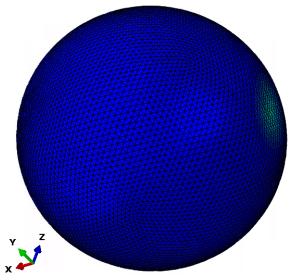

(h) SPH_4 posterior right sagittal view.

Figure 4.8: Nodal displacement magnitude (U) result in spheres models when $FLB_x = FRB_x = 1$mm

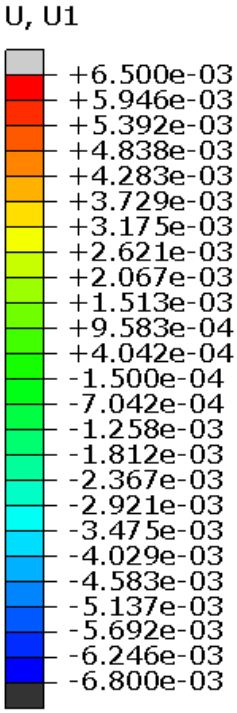

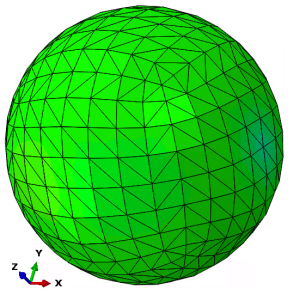

(a) SPH_1 anterior left sagittal view.

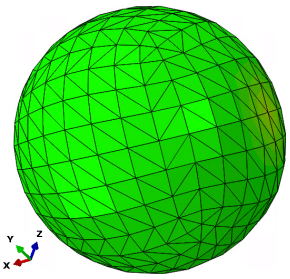

(b) SPH_1 posterior right sagittal view.

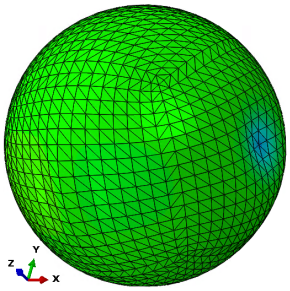

(c) SPH_2 anterior left sagittal view.

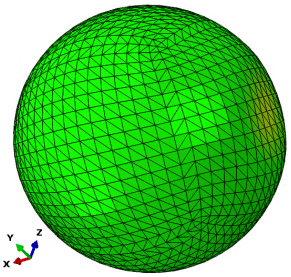

(d) SPH_2 posterior right sagittal view.

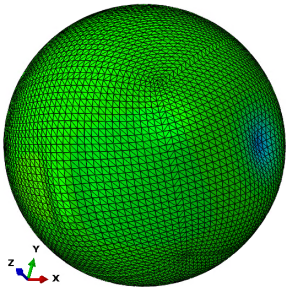

(e) SPH_3 anterior left sagittal view.

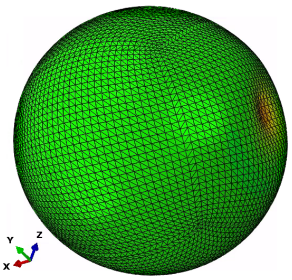

(f) SPH_3 posterior right sagittal view.

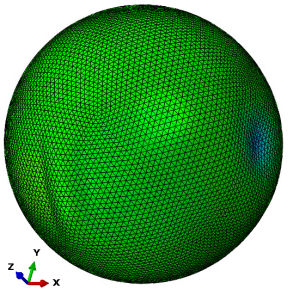

(g) SPH_4 anterior left sagittal view.

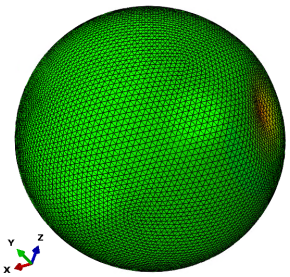

(h) SPH_4 posterior right sagittal view.

Figure 4.9: Nodal displacement in x axis (U_x) result in spheres models when $FLB_x = FRB_x = 2$mm

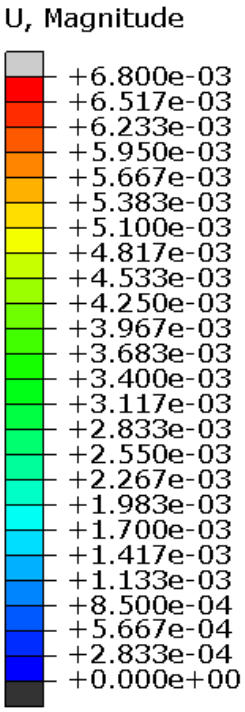

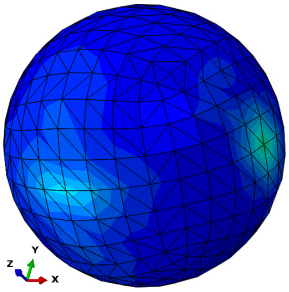

(a) SPH_1 anterior left sagittal view.

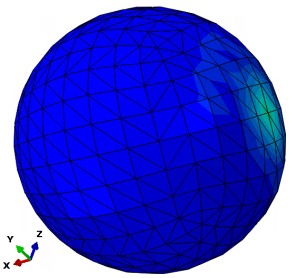

(b) SPH_1 posterior right sagittal view.

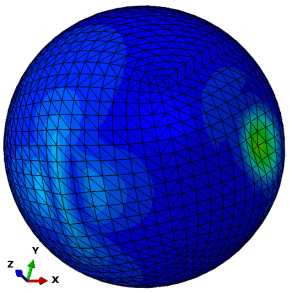

(c) SPH_2 anterior left sagittal view.

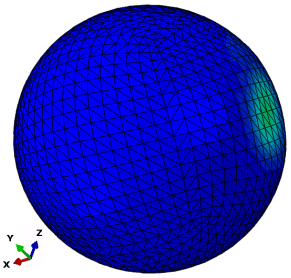

(d) SPH_2 posterior right sagittal view.

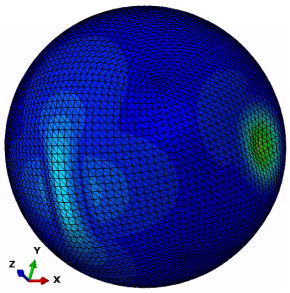

(e) SPH_3 anterior left sagittal view.

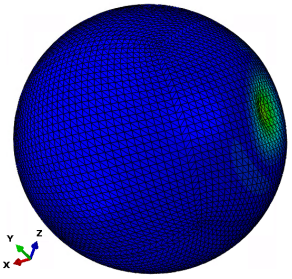

(f) SPH_3 posterior right sagittal view.

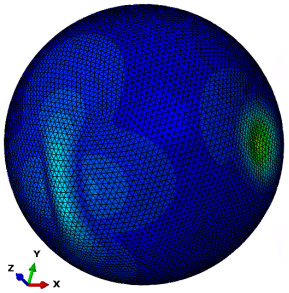

(g) SPH_4 anterior left sagittal view.

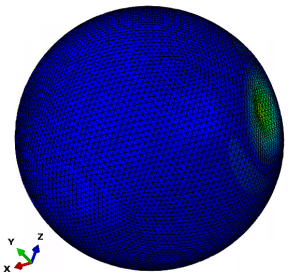

(h) SPH_4 posterior right sagittal view.

Figure 4.10: Nodal displacement magnitude (U) result in spheres models when $FLB_x = FRB_x = 2$mm

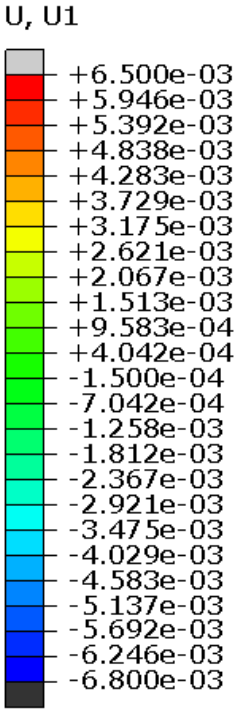

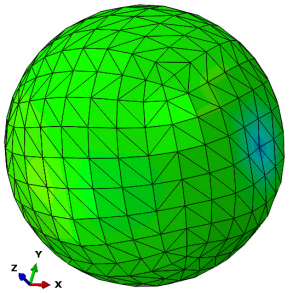

(a) SPH_1 anterior left sagittal view.

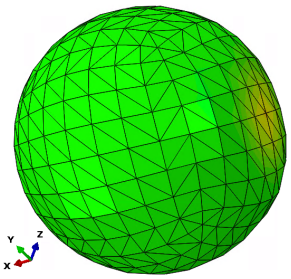

(b) SPH_1 posterior right sagittal view.

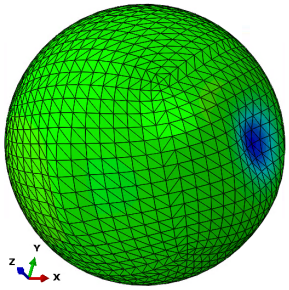

(c) SPH_2 anterior left sagittal view.

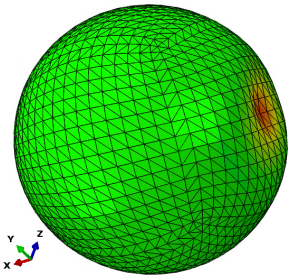

(d) SPH_2 posterior right sagittal view.

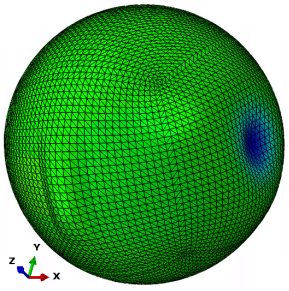

(e) SPH_3 anterior left sagittal view.

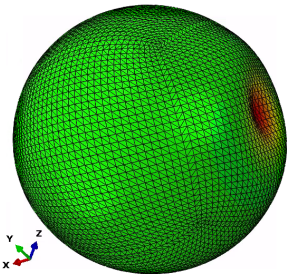

(f) SPH_3 posterior right sagittal view.

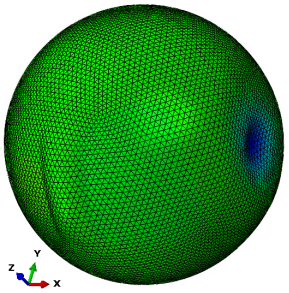

(g) SPH_4 anterior left sagittal view.

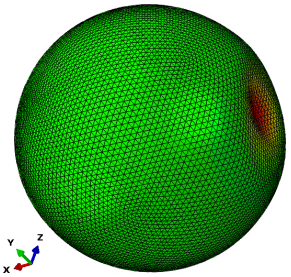

(h) SPH_4 posterior right sagittal view.

Figure 4.11: Nodal displacement in x axis (U_x) result in spheres models when $FLB_x = FRB_x = 3$mm

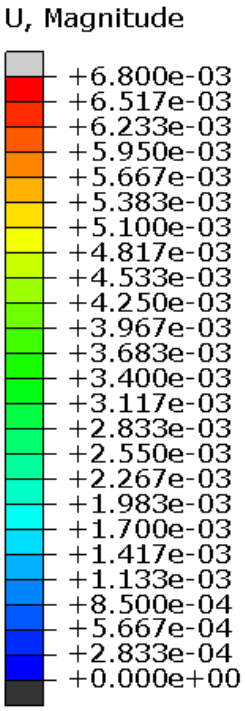

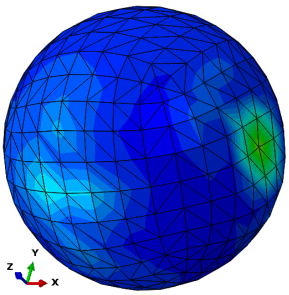

(a) SPH_1 anterior left sagittal view.

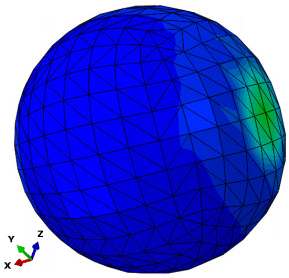

(b) SPH_1 posterior right sagittal view.

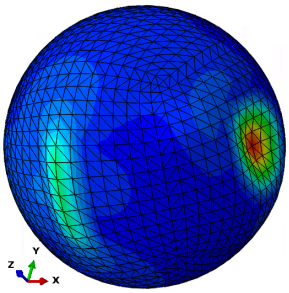

(c) SPH_2 anterior left sagittal view.

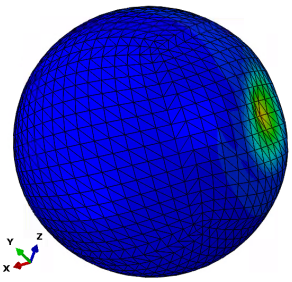

(d) SPH_2 posterior right sagittal view.

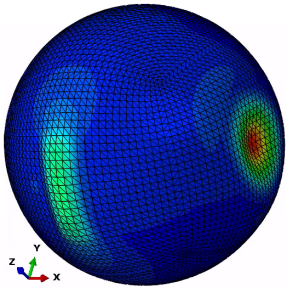

(e) SPH_3 anterior left sagittal view.

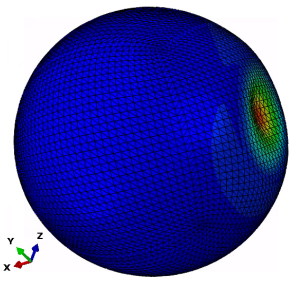

(f) SPH_3 posterior right sagittal view.

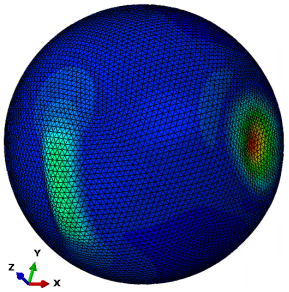

(g) SPH_4 anterior left sagittal view.

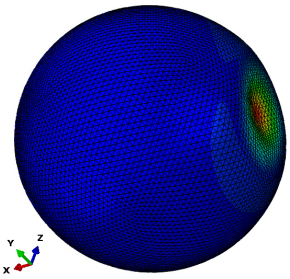

(h) SPH_4 posterior right sagittal view.

Figure 4.12: Nodal displacement magnitude (U) result in spheres models when $FLB_x = FRB_x = 3$mm

4.1.3 Experimental results with anterior and posterior fontanelles

The results presented in this section considers the implementation of an improvement version of the fontanelle region by adding the posterior fontanelle (in contrast with the previous results), this improvement also modifies the region representing the cranial bone.

Nodal displacement in x axis (U_x) and the nodal displacement magnitude (U), for every sphere when both FLB_x and FRB_x have been translated towards the sphere $3mm$ (see Eq. 4.2) are shown in Table 4.3:

Close step	Mesh	U_x	U
$3mm$	SPH_1	$-4.332e^{-03}$	$2.242e^{-04}$
	SPH_2	$-6.719e^{-03}$	$2.873e^{-03}$
	SPH_3	$-6.603e^{-03}$	$2.331e^{-03}$
	SPH_4	$-6.453e^{-03}$	$2.611e^{-03}$

Table 4.3: Nodal displacement in x axis (U_x in m) and nodal displacement magnitude (U in m) of sphere with improved fontanelles in contact with curved plates analysis when LB_C and RB_C performed a 3mm translation in the x axis towards the sphere.

Figures 4.13 and 4.14 show the nodal displacement in x axis (U_x) and nodal displacement magnitude (U) results of the spheres with improved fontanelles in contact with curved plates when FLB_x and FRB_x have been translated $3mm$ towards the sphere.

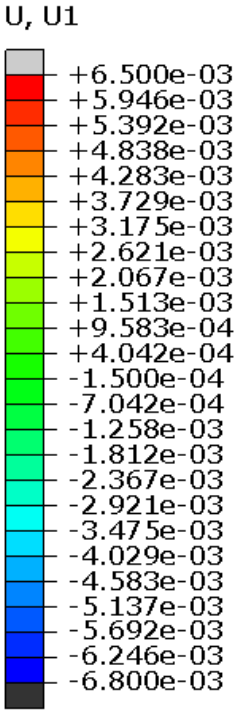

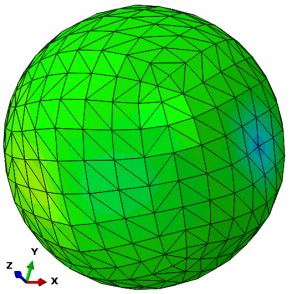

(a) SPH_1 anterior left sagittal view.

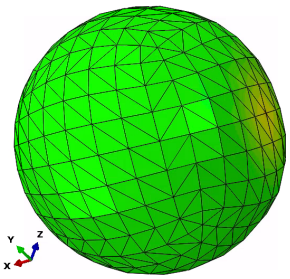

(b) SPH_1 posterior right sagittal view.

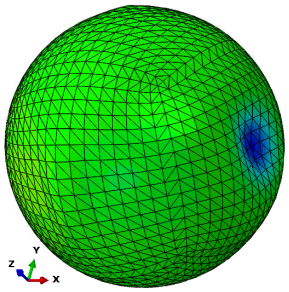

(c) SPH_2 anterior left sagittal view.

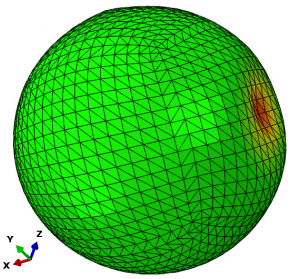

(d) SPH_2 posterior right sagittal view.

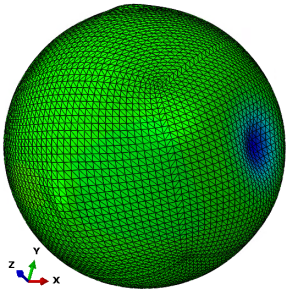

(e) SPH_3 anterior left sagittal view.

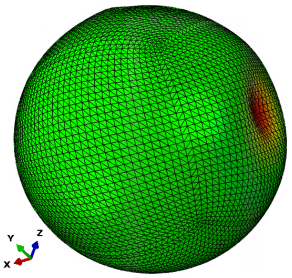

(f) SPH_3 posterior right sagittal view.

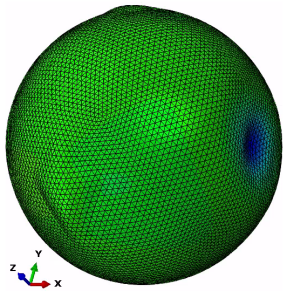

(g) SPH_4 anterior left sagittal view.

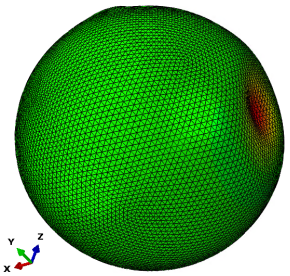

(h) SPH_4 posterior right sagittal view.

Figure 4.13: Nodal displacement in x axis (U_x) result in spheres models when $FLB_x = FRB_x = 3$mm

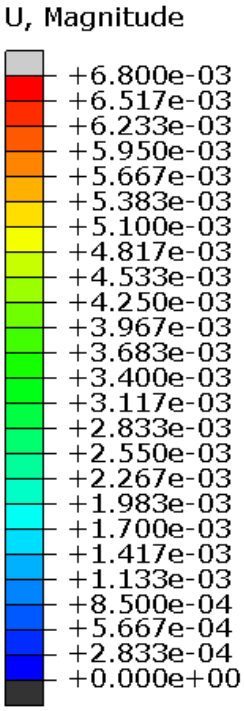

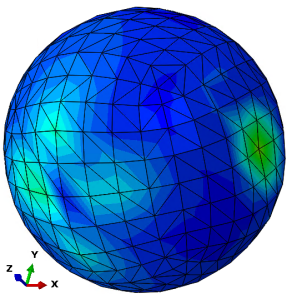

(a) SPH_1 anterior left sagittal view.

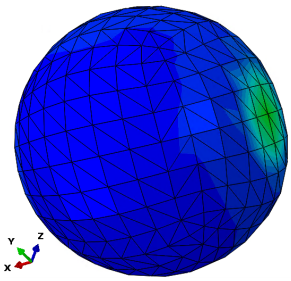

(b) SPH_1 posterior right sagittal view.

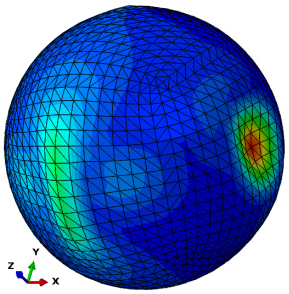

(c) SPH_2 anterior left sagittal view.

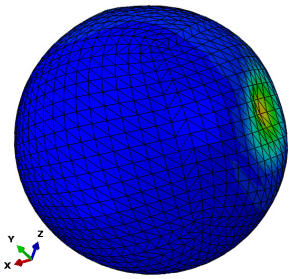

(d) SPH_2 posterior right sagittal view.

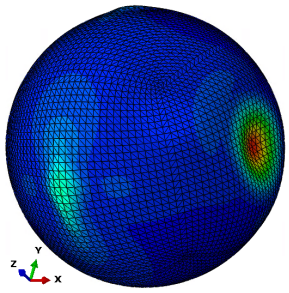

(e) SPH_3 anterior left sagittal view.

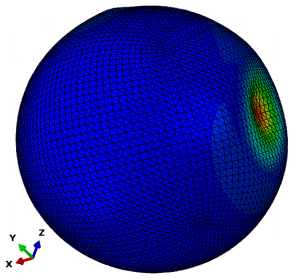

(f) SPH_3 posterior right sagittal view.

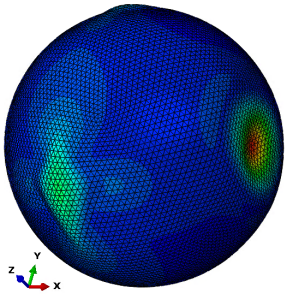

(g) SPH_4 anterior left sagittal view.

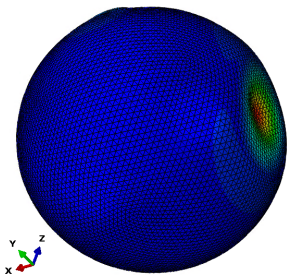

(h) SPH_4 posterior right sagittal view.

Figure 4.14: Nodal displacement magnitude (U) result in spheres models when $FLB_x = FRB_x = 3$mm

4.1.4 Discussion

4.1.4.1 Anterior fontanelle only

From Table 4.2 we made the following observations:

- The maximum displacements in the x direction, U_x, increase with increasing closing steps ranging from $1mm$ to $3mm$ respectively. This is also clear in the Figures 4.7, 4.9 and 4.11, e.g. SPH_4 has a nodal displacement of $\sim 2mm$ at a closing step of $1mm$ and $\sim 6.5mm$ at a closing step of $3mm$.

- Within each closing step, the maximum displacements in the x direction, U_x, also increase with increasing mesh sizes, e.g considering a closing step of $3mm$ (see Figure 4.11) there is a difference of $\sim 2mm$ between the nodal displacement of SPH_1 of $\sim 4.4mm$ and SPH_4 of $\sim 6.5mm$.

- When assessing the nodal displacement magnitude of the center of the anterior fontanelle, U, the average displacement increases with increasing closing steps but within each closing step the increasing trend with increasing meshes is not there and does not appear to follow a clear pattern either at least from the values in the Table 4.2. However when looking at figures 4.8, 4.10 and 4.12 we clearly observe different nodal displacement patterns of the anterior fontanelle as the mesh size increases. This implies that, as expected, finer meshes provide more reliable nodal displacement patterns. Another phenomenon that presents itself is the volume conservation. Indeed the deformation of the anterior fontanelle will be affected by the overall lateral deformation of $\sim 6.4mm$ that is clearly visible in Figure 4.12 for the highest closing step of $3mm$ and the finest mesh.

4.1.4.2 Anterior and posterior fontanelle

From Table 4.3 we made the following observations:

- When comparing U_x for each of the four meshes for the $3mm$ closing step with the equivalent results in Table 4.2, we noticed that there is a clear difference between SPH_1 and SPH_2 of about $\sim 2.3mm$, but the differences from SPH_2 to SPH_4 are neglible.

- When comparing U for each of the four meshes for the $3mm$ closing step there are discrepancies that require us to look at the figures for further explanation.

- Comparing the finest meshes in Figures 4.12 and 4.14 we observe that the overall nodal displacement area of the anterior fontanelle is concentrated in a rectangular shape region in the former that in the latter. This is again due to volume conservation as some of the previous bulging deformation of the anterior fontanelle is now present in the posterior fontanelle.

4.1.4.3 Summary

The basic experiments have shown the importance of increasing the number of elements in the meshes to improve the accuracy of the deformation fields of crucial anatomical locations including the anterior fontanelle and the lateral part of the fetal head, here represented as a sphere.

The necking of the mesh at the lateral part of the sphere is a commonly known phenomenon when laterally compressing for example a thin plastic ball, which validates the realism of the experiments. At the same time we observe that the necking of the mesh (captured as Ux) is practically the same in both experiments at a closing step of $3mm$, where results of the anterior fontanelle only is $-6.457e^{-03}m$ and the anterior and posterior fontanelle is $-6.453e^{-03}m$ with a difference between them of $-4.0e^{-06}m$.

The addition of the posterior fontanelle adds further realism to the overall deformation of the anterior fontanelle.

4.2 Curved plates traction on spheres

The aim of this experiment is to simulate the obstetric forceps-baby head behaviour when the **Pull Step** is performed (see Section 3.4.1.3).

4.2.1 Experimental setup

4.2.1.1 Models

Previous curved plates and spheres models are considered in this experiment as they were specified in Section 4.1.1.

4.2.1.2 Steps

This part of the analysis assumes that the **Initial Step** and **Close Step** have already been performed (see Section 4.1.1.3), hence it should consider the different cases of displacements performed in the **Close Step**.

Pull Step is described in Section 3.4.1.3.

4.2.1.3 Interactions

The interactions between the curved plates and the spheres as described is the Spheres in contact with curved plate experiment (see Section 4.1.1.4) is kept in this experiment as well.

4.2.1.4 Loads

Similar to previous experiment, there are not specific loads applied over the curved blades, instead a constant velocity boundary condition is applied on each curved plate to move them in the z axis direction.

4.2.1.5 BCs

The BCs applied in the **Pull Step** (see Table 4.4), consider the same node sets specified in the previous step (see Section 4.1.1.6).

Set	**Pull Step**
LB_C	Allows translation in z axis
LB_C	Constant velocity on z axis at $1cm/s$
RB_C	Allows translation in z axis
RB_C	Constant velocity on z axis at $1cm/s$
SPH_C	Propagated

Table 4.4: BCs applied to the set of nodes in the **Pull** step in the curved plates traction on spheres analysis.

4.2.2 Experimental results with anterior fontanelle only

This section outlines the results obtained in the current curved plates traction on spheres experiment performed over the sphere meshes with anterior fontanelle only.

Table 4.5 shows the nodal displacement in x axis (U_x) and the nodal displacement magnitude (U), for every sphere when both FLB_z and FRB_z have been translated in the z axis, this is:

$$\begin{aligned} FLB(x, y, z) &= (0, 0, 0.01) \\ FRB(x, y, z) &= (0, 0, 0.01) \end{aligned} \tag{4.3}$$

after the **Close Step** has been performed.

Close step	**Pull step**	**Mesh**	U_x	U
$1mm$	$1cm$	SPH_1	$-1.576e^{-03}$	$4.239e^{-03}$
		SPH_2	$-2.305e^{-03}$	$4.192e^{-03}$
		SPH_3	$-2.314e^{-03}$	$4.930e^{-03}$
		SPH_4	$-2.575e^{-03}$	$5.361e^{-03}$
$2mm$	$1cm$	SPH_1	$-3.315e^{-03}$	$5.545e^{-03}$
		SPH_2	$-5.275e^{-03}$	$5.862e^{-03}$
		SPH_3	$-5.139e^{-03}$	$6.372e^{-03}$
		SPH_4	$-4.930e^{-03}$	$6.905e^{-03}$
$3mm$	$1cm$	SPH_1	$-7.362e^{-03}$	$5.833e^{-03}$
		SPH_2	$-7.382e^{-03}$	$7.351e^{-03}$
		SPH_3	$-7.364e^{-03}$	$7.822e^{-03}$
		SPH_4	$-6.893e^{-03}$	$8.096e^{-03}$

Table 4.5: Nodal displacement in x axis (U_x in m) and nodal displacement magnitude (U in m) of curved plates traction on spheres analysis when LB_C and RB_C performed a 1cm translation in the z axis after the close step was performed for $1mm$, $2mm$, and $3mm$ in the x axis.

Figures 4.15 and 4.16 show the nodal displacement in x axis (U_x) and nodal displacement magnitude (U) results of curved plates traction on spheres when curved plates FLB_x and FRB_x have been translated $1mm$ in the x axis and FLB_z and FRB_z have been translated $1cm$ in the z axis, Figures 4.17 and 4.18 when curved plates have been translated $2mm$ towards the sphere and FLB_z and FRB_z have been translated $1cm$ in the z axis, and Figures 4.19 and 4.20 when curved plates have been translated $3mm$ towards the sphere and FLB_z and FRB_z have been translated $1cm$ in the z axis.

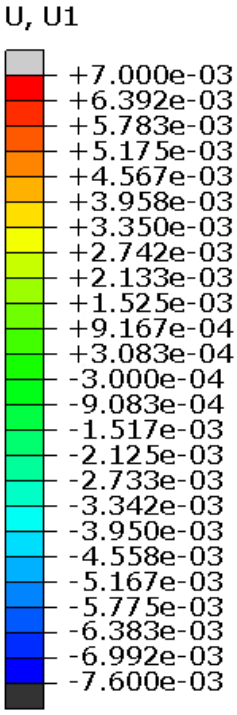

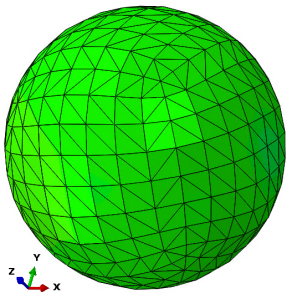

(a) SPH_1 anterior left sagittal view.

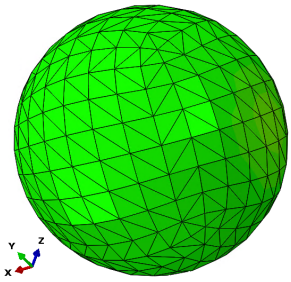

(b) SPH_1 posterior right sagittal view.

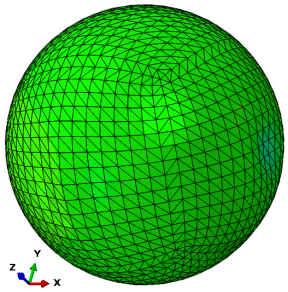

(c) SPH_2 anterior left sagittal view.

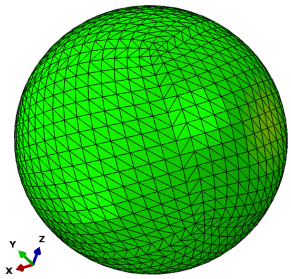

(d) SPH_2 posterior right sagittal view.

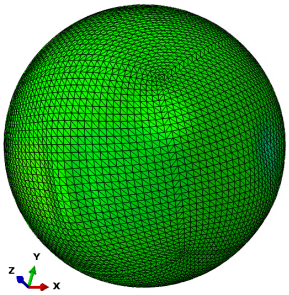

(e) SPH_3 anterior left sagittal view.

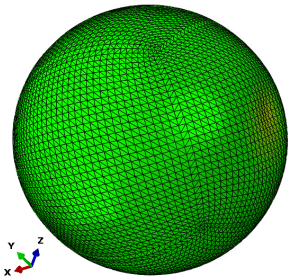

(f) SPH_3 posterior right sagittal view.

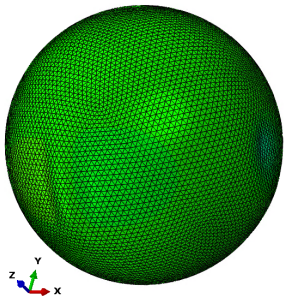

(g) SPH_4 anterior left sagittal view.

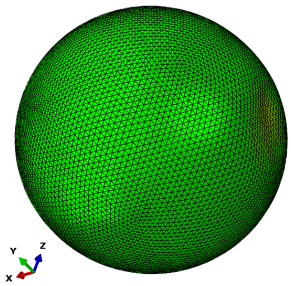

(h) SPH_4 posterior right sagittal view.

Figure 4.15: Nodal displacement in x axis (U_x) result in spheres models when $FLB_x = FRB_x = 1$mm and $FLB_z = FRB_z = 1$cm

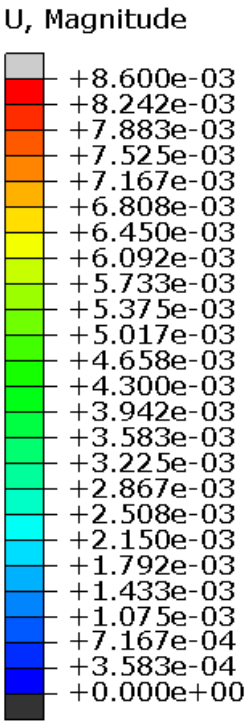

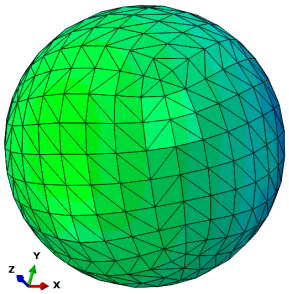

(a) SPH_1 anterior left sagittal view.

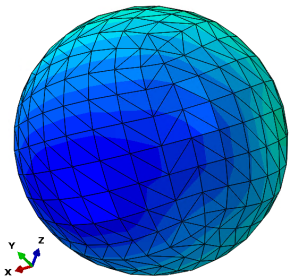

(b) SPH_1 posterior right sagittal view.

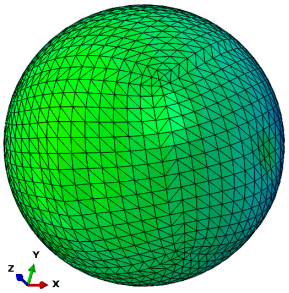

(c) SPH_2 anterior left sagittal view.

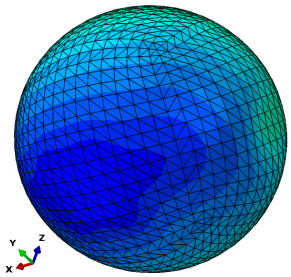

(d) SPH_2 posterior right sagittal view.

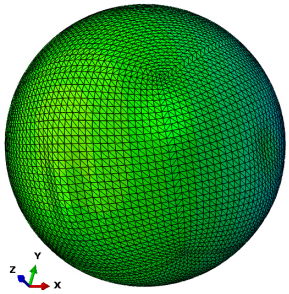

(e) SPH_3 anterior left sagittal view.

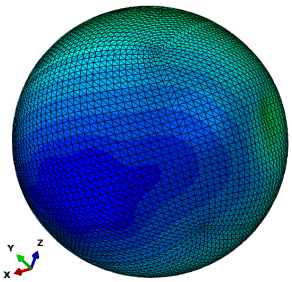

(f) SPH_3 posterior right sagittal view.

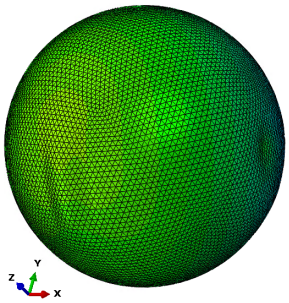

(g) SPH_4 anterior left sagittal view.

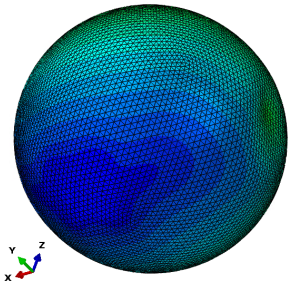

(h) SPH_4 posterior right sagittal view.

Figure 4.16: Nodal displacement magnitude (U) result in spheres models when $FLB_x = FRB_x = 1\text{mm}$ and $FLB_z = FRB_z = 1\text{cm}$

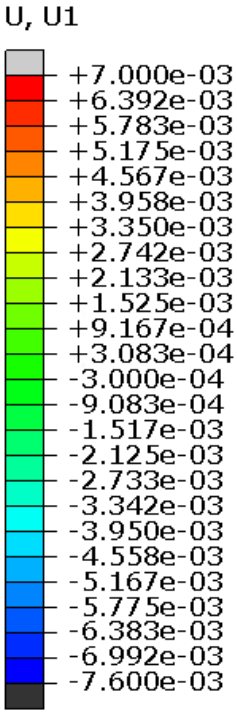

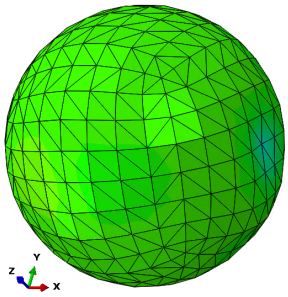

(a) SPH_1 anterior left sagittal view.

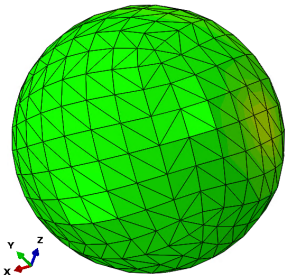

(b) SPH_1 posterior right sagittal view.

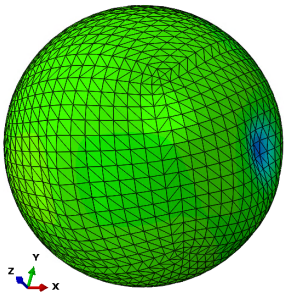

(c) SPH_2 anterior left sagittal view.

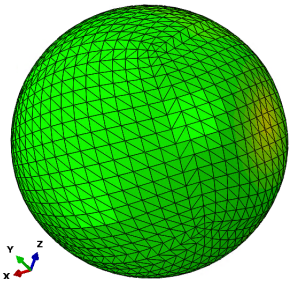

(d) SPH_2 posterior right sagittal view.

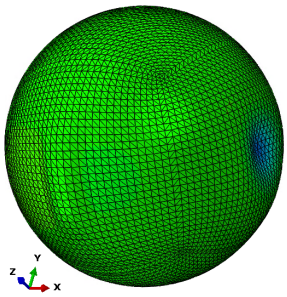

(e) SPH_3 anterior left sagittal view.

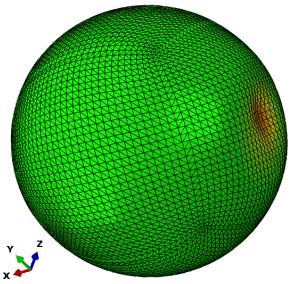

(f) SPH_3 posterior right sagittal view.

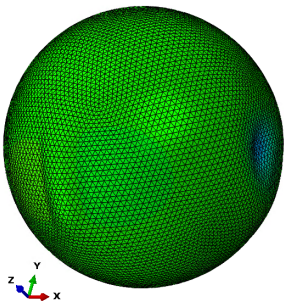

(g) SPH_4 anterior left sagittal view.

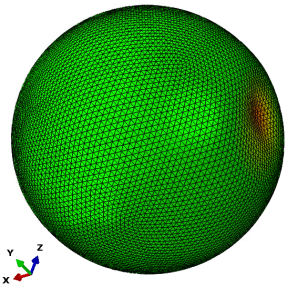

(h) SPH_4 posterior right sagittal view.

Figure 4.17: Nodal displacement in x axis (U_x) result in spheres models when $FLB_x = FRB_x = 2$mm and $FLB_z = FRB_z = 1$cm

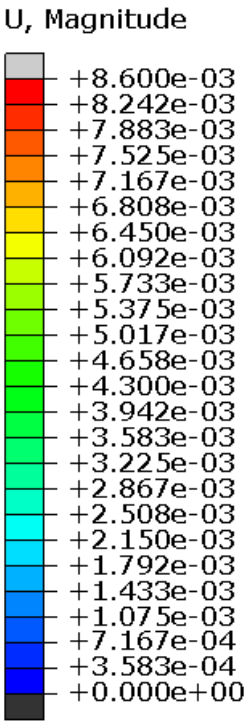

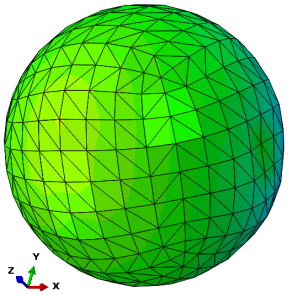

(a) SPH_1 anterior left sagittal view.

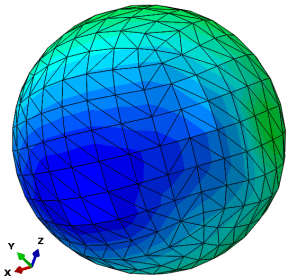

(b) SPH_1 posterior right sagittal view.

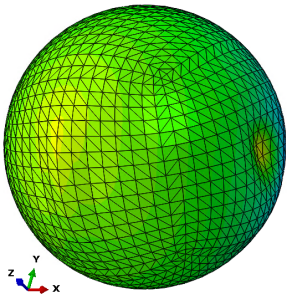

(c) SPH_2 anterior left sagittal view.

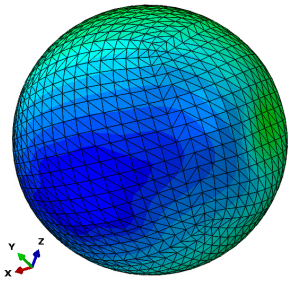

(d) SPH_2 posterior right sagittal view.

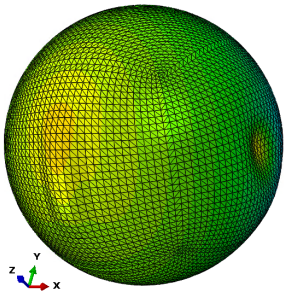

(e) SPH_3 anterior left sagittal view.

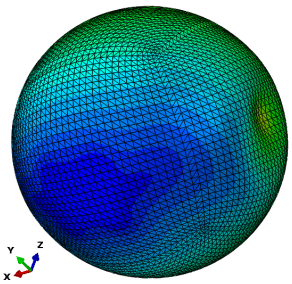

(f) SPH_3 posterior right sagittal view.

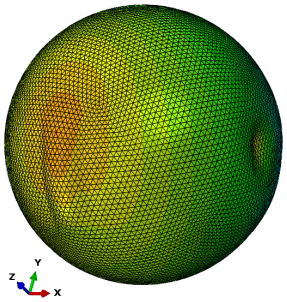

(g) SPH_4 anterior left sagittal view.

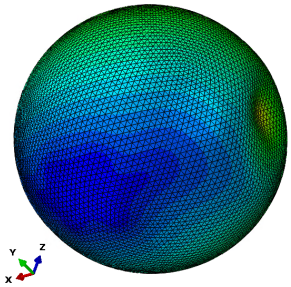

(h) SPH_4 posterior right sagittal view.

Figure 4.18: Nodal displacement magnitude (U) result in spheres models when $FLB_x = FRB_x = 2$mm and $FLB_z = FRB_z = 1$cm

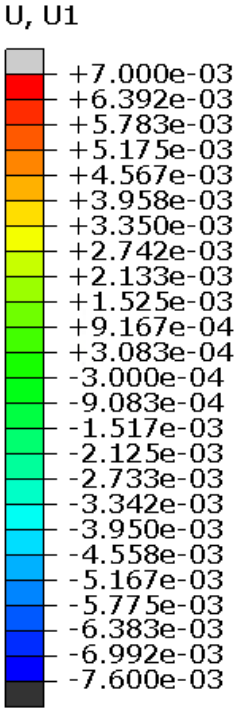

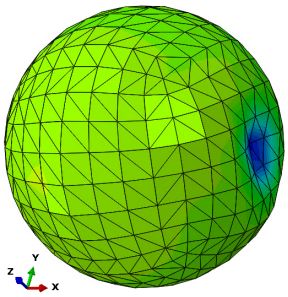

(a) SPH_1 anterior left sagittal view.

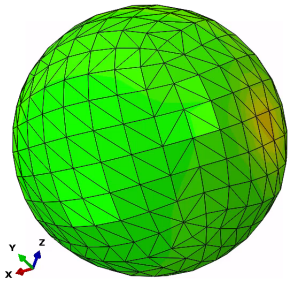

(b) SPH_1 posterior right sagittal view.

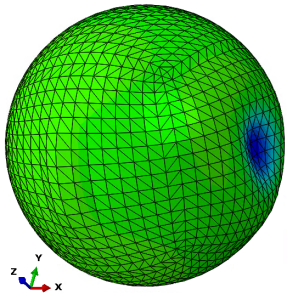

(c) SPH_2 anterior left sagittal view.

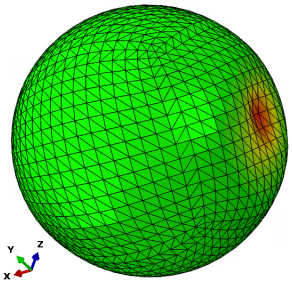

(d) SPH_2 posterior right sagittal view.

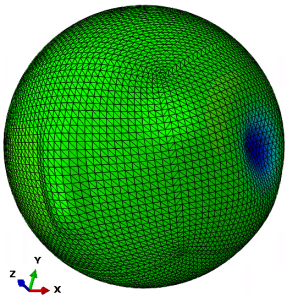

(e) SPH_3 anterior left sagittal view.

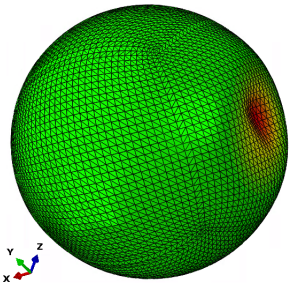

(f) SPH_3 posterior right sagittal view.

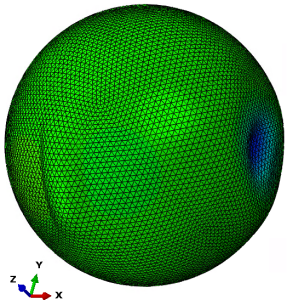

(g) SPH_4 anterior left sagittal view.

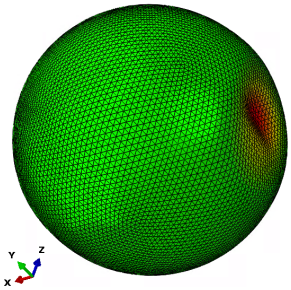

(h) SPH_4 posterior right sagittal view.

Figure 4.19: Nodal displacement in x axis (U_x) result in spheres models when $FLB_x = FRB_x = 3$mm and $FLB_z = FRB_z = 1$cm

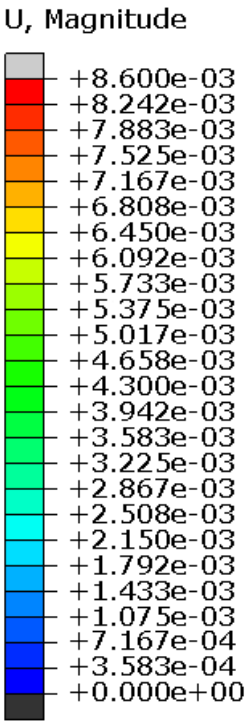

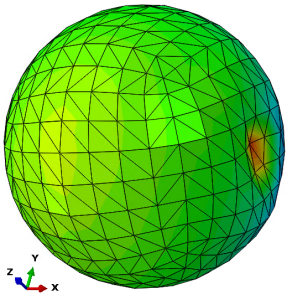

(a) SPH_1 anterior left sagittal view.

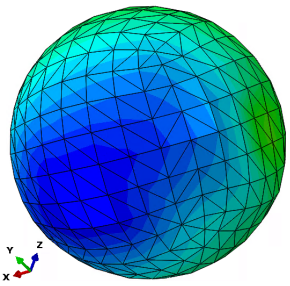

(b) SPH_1 posterior right sagittal view.

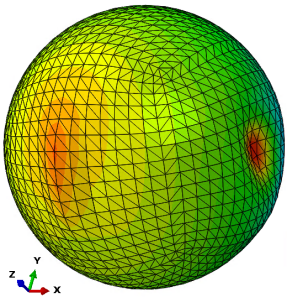

(c) SPH_2 anterior left sagittal view.

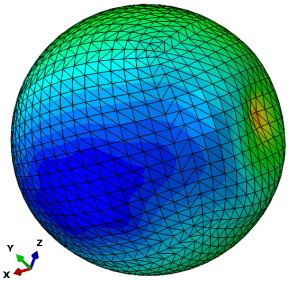

(d) SPH_2 posterior right sagittal view.

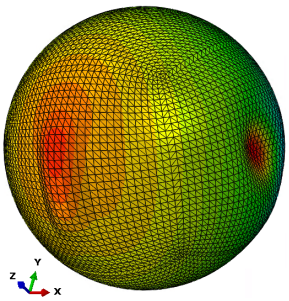

(e) SPH_3 anterior left sagittal view.

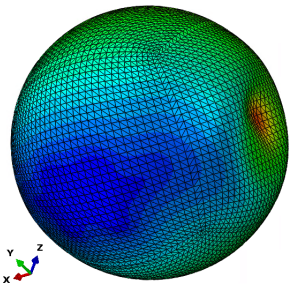

(f) SPH_3 posterior right sagittal view.

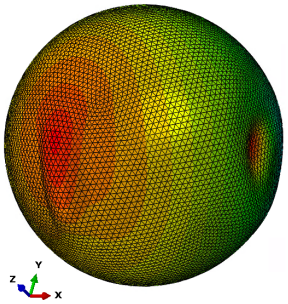

(g) SPH_4 anterior left sagittal view.

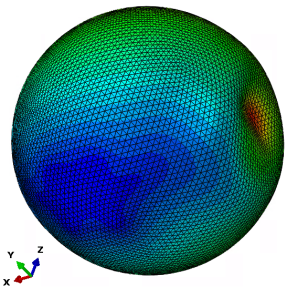

(h) SPH_4 posterior right sagittal view.

Figure 4.20: Nodal displacement magnitude (U) result in spheres models when $FLB_x = FRB_x = 3$mm and $FLB_z = FRB_z = 1$cm

4.2.3 Experimental results with anterior and posterior fontanelle

This section outlines the results obtained in the current curved plates traction on spheres experiment with improved fontanelles.

Table 4.6 shows the nodal displacement in x axis (U_x) and the nodal displacement magnitude (U), for every sphere when both FLB_z and FRB_z have been translated $1cm$ in the z (see Eq. 4.3) after the **Close Step** of $3mm$ has been performed.

Close step	Pull Step	Mesh	U_x	U
$3mm$	$1cm$	SPH_1	$-7.368e^{-03}$	$5.891e^{-03}$
		SPH_2	$-7.289e^{-03}$	$7.106e^{-03}$
		SPH_3	$-7.315e^{-03}$	$7.625e^{-03}$
		SPH_4	$-6.882e^{-03}$	$8.103e^{-03}$

Table 4.6: Nodal displacement in x axis (U_x in m) and nodal displacement magnitude (U in m) of sphere with improved fontanelles in curved plates traction on spheres analysis when LB_C and RB_C performed a 3mm translation in the x axis towards the sphere and 1cm in the z axis.

Figures 4.21 and 4.22 show the nodal displacement in x axis (U_x) and nodal displacement magnitude (U) results of the curved plates traction on spheres when FLB_z and FRB_z have been translated $1cm$ in the z after the **Close Step** of $3mm$ has been performed.

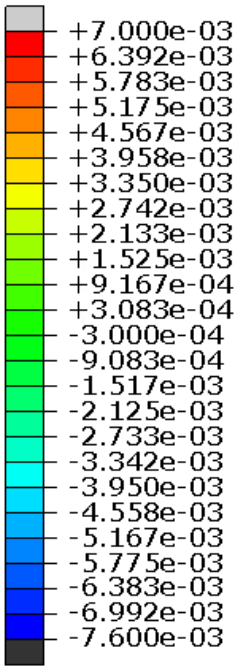

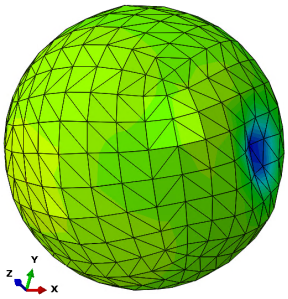

(a) SPH_1 anterior left sagittal view.

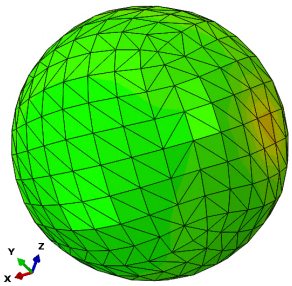

(b) SPH_1 posterior right sagittal view.

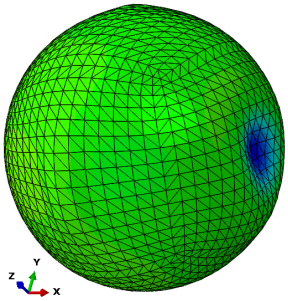

(c) SPH_2 anterior left sagittal view.

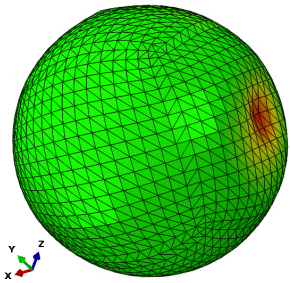

(d) SPH_2 posterior right sagittal view.

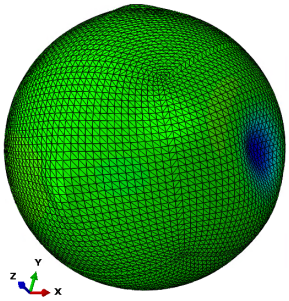

(e) SPH_3 anterior left sagittal view.

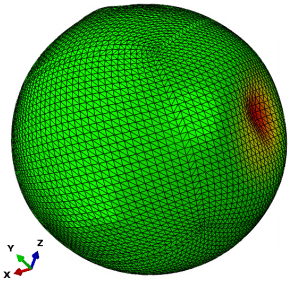

(f) SPH_3 posterior right sagittal view.

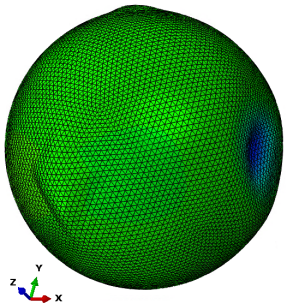

(g) SPH_4 anterior left sagittal view.

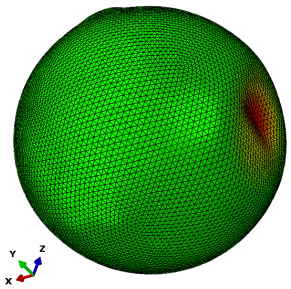

(h) SPH_4 posterior right sagittal view.

Figure 4.21: Nodal displacement in x axis (U_x) result in spheres models when $FLB_x = FRB_x$ = 3mm and $FLB_z = FRB_z$ = 1cm in curved plates traction on spheres with improved fontanelles

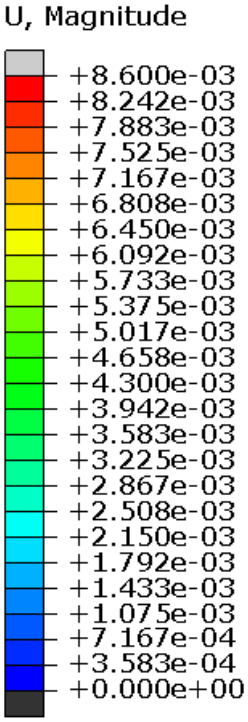

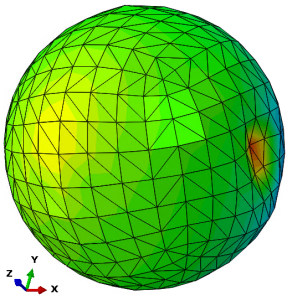

(a) SPH_1 anterior left sagittal view.

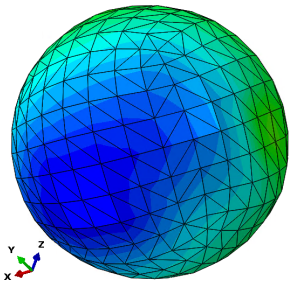

(b) SPH_1 posterior right sagittal view.

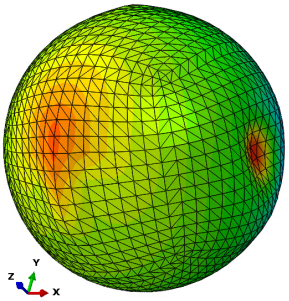

(c) SPH_2 anterior left sagittal view.

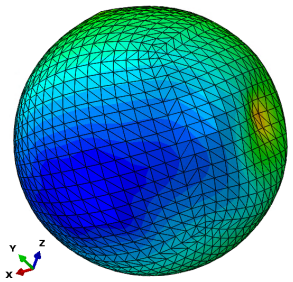

(d) SPH_2 posterior right sagittal view.

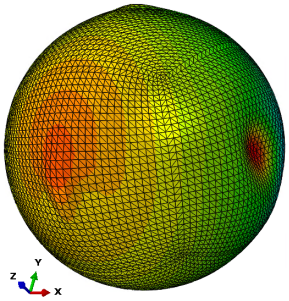

(e) SPH_3 anterior left sagittal view.

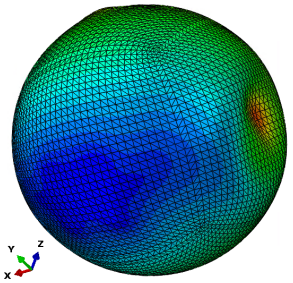

(f) SPH_3 posterior right sagittal view.

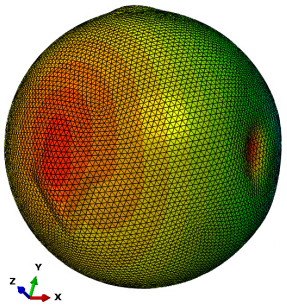

(g) SPH_4 anterior left sagittal view.

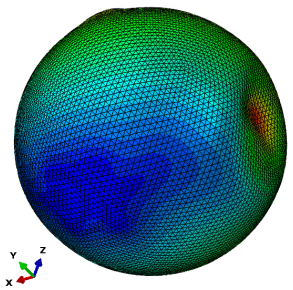

(h) SPH_4 posterior right sagittal view.

Figure 4.22: Nodal displacement magnitude (U) result in spheres models when $FLB_x = FRB_x$ = 3mm and $FLB_z = FRB_z$ = 1cm in curved plates traction on spheres with improved fontanelles

4.2.4 Discussion

4.2.4.1 Anterior fontanelle only

From Table 4.5 we made the following observations:

- The nodal displacements in the x direction, U_x, increase with increasing closing steps ranging from $1mm$ to $3mm$ respectively. This is also clear in the Figures 4.15, 4.17 and 4.19, e.g SPH_4 has a nodal displacement of $-2.575e^{-03}m$ at a closing step of $1mm$ that increased to $-6.893e^{-03}m$ at a closing step of $3mm$.

- Within each closing step, the nodal displacements in the x direction, U_x, increase between the coarsest and the next refined meshes, but we noticed a decrement in SPH_3 and SPH_4 when the close step is $2mm$ and $3mm$ respect to SPH_2 in the same close step states.

- When assessing the nodal displacement of the center of the anterior fontanelle, U, the average displacement increases with increasing closing steps. Within each closing step the differences in U are more consistent than in the contact only experiments (see Table 4.2). These are also substantially higher than in the contact only experiments which is to be expected, e.g. SPH_4 at the closing step of $3mm$ in the contact only experiment has a nodal displacement magnitude U of $2.573e^{-03}m$, whilst in this experiment is $8.096e^{-03}m$ at the same closing step.

- When comparing U_x between contact and traction, and contact only experiments, we observed that these are also higher in the former. This is due to the shear effect caused by the traction. In contrast with U, the nodal displacement in x direction, U_x in the contact only experiments compared with the contact and traction experiments, is very marginal, e.g. SPH_4 at the closing step of $3mm$ in the contact only experiment has a value of U_x of $-6.457e^{-03}m$, whilst in this experiment is $-6.893e^{-03}m$ at the same closing step, with a difference between them of only $0.435^{-03}m$.

4.2.4.2 Anterior and posterior fontanelle

From Table 4.6 we made the following observations:

- In contrast with the contact only experiments, the effect of adding the posterior fontanelle in the contact and traction experiment seems to be very marginal where, both U_x and U deformations are only marginal different to the anterior fontanelle only experiment, e.g. SPH_4 at the closing step of $3mm$ in the anterior fontanelle experiment has a value of U_x and U of $-6.893e^{-03}m$ and $8.096e^{-03}m$ respectively, whilst adding the posterior fontanelle they are $-6.882e^{-03}m$ and $8.103e^{03}$ respectively at the same closing step (see Tables 4.5 and 4.6).

- In Figures 4.20 (U anterior fontanelle only) and 4.22 (U anterior and posterior fontanelle) we observe that the nodal displacement area of the anterior fontanelle is largely similar however there is a clear difference in the area of the posterior fontanelle, where it is bulging (top of sphere). This makes sense when traction is added as it would

have more effect on the anterior fontanelle, which is aligned with the line of traction unlike the posterior fontanelle which lies remote of the line of traction.

- The maximum value of the nodal displacement magnitude U in the anterior fontanelle only results is $8.096e^{03}m$ and in the anterior and posterior fontanelles result is $8.103e^{03}m$, which reveals that the nodal displacement is slightly higher in the latter experiment.

4.2.4.3 Summary

The addition of traction shows increased deformation of the anterior fontanelle due to being in line with the traction and also increased lateral deformation due to the shear effect.

This concludes the experiments using simplified head models and forceps models that have shown the importance of mesh refinement and the correct modeling of the head to forceps contact, resulting in realistic deformations.

4.3 Mesh convergence test

In previous experiments we have used the geometric shape of a sphere as a basic approximation of a fetal head, as it has been observed in the results from Table 4.2 when the closing step is set to $1mm$, the finer the mesh the more accurate the result is.

Past experiments have used four different levels of mesh refinement as stated in Table 3.5 which gave different levels of nodal displacement in the x axis (Ux), this can be seen in Table 4.7:

Mesh	**# Elements**	U_x
SPH_1	768	$-1.232e^{-03}$
SPH_2	3072	$-1.681e^{-03}$
SPH_3	12288	$-1.908e^{-03}$
SPH_4	20480	$-1.820e^{-03}$

Table 4.7: Relationship between mesh refinement (number of elements) and nodal displacement in x axis (U_x) in the spheres in contact with curved plates at a closing step of $1mm$.

For the correctness of the FEA, a convergence test based on mesh size is performed where the nodal displacement in the x axis (U_x) is used as observation index of the convergence. The mesh sizes of the convergence test are SPH_1 with 768 elements, SPH_2 with 3,072 elements, SPH_3 with 12,288 elements and SPH_4 with 20,480 elements as previously mentioned in Table 4.7.

As it can be seen in the blue line in the chart from Figure 4.23, an increment of the nodal displacement (U_x) is noticed from mesh SPH_1 to mesh SPH_2 and then from mesh SPH_2 to mesh SPH_3, but not from mesh SPH_3 to SPH_4 where a decrease is observed.

An extrapolation of the converged values is done using curve fitting to estimate the theoretical U_x values (red line in the chart).

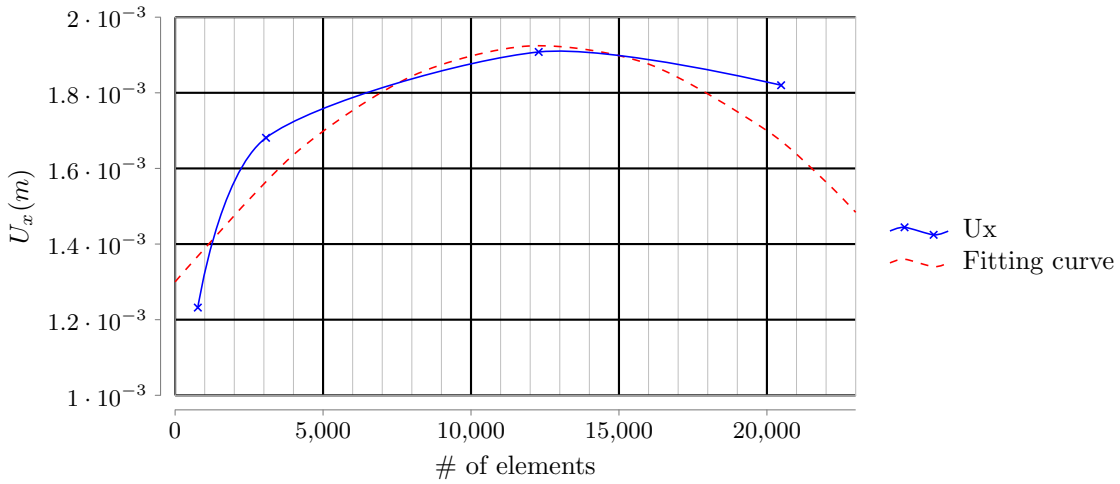

Figure 4.23: Nodal displacement in x axis (U_x) vs mesh size relationship (blue) and polynomial fitting curve (red).

From the chart we can assume that a mesh with $\sim$ 13000 elements is suffice to perform further analysis. This is relevant for the next experiments using the fetal head, where three different meshes are used (see Table 3.8) to perform the different experiments and where the finer mesh contains $18,742$ elements, higher than the minimum $13,000$ elements needed to achieve mesh convergence and have a solution independent of the mesh size.

4.4 Fetal head in contact with forceps

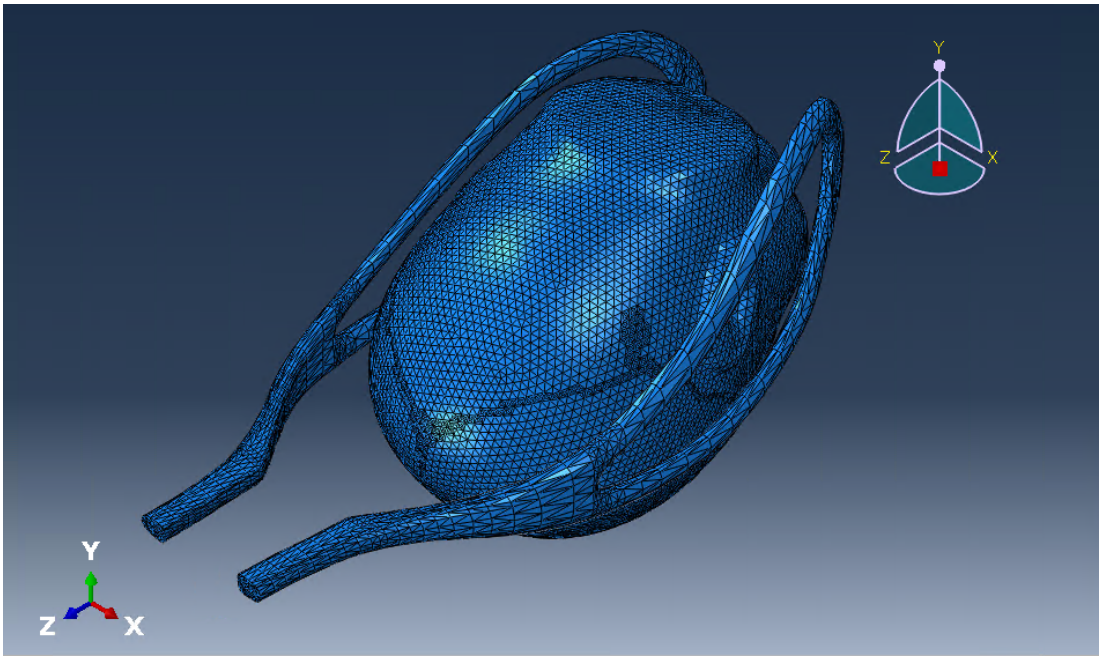

Figure 4.24: Fetal head in contact with obstetric forceps simulation.

The aim of this experiment is to simulate the Baby Head (BH) in contact with obstetric forceps behavior when the **Close Step** is performed (see Section 3.4.1.2).

In contrast with previous experiments, this experiment use the 3D model of real obstetric forceps blades and the 3D model of a real BH mannequin both obtained by laser scan.

This experiment simulates a more realistic behavior of the **Close Step** when the baby head is compressed by obstetric forceps compared with its counterpart simulated with spheres and curved plates as it was explained in Section 4.1.

4.4.1 Experimental setup

4.4.1.1 Baby head model

The BH model used in this experiment is the improved fetal head model described in Section 3.3.2.3 and defined as IFeH.

This improved fetal head model considers different regions that represent sutures, fontanelles, cranial bones and base bone (see Sections 2.2.3.1, 2.2.3.2 and 2.2.3 for reference) that exist in a real baby head structure. Each region has a different material property except the sutures and fontanelles that share the same material; all material properties are defined in Section 3.3.2.4.

Figure 4.25, 4.26, 4.27 and 4.28 show the suture, fontanelle, cranial bones and base bone regions respectively around the different IFeH meshes.

Each region in the different IFeHs, represents a contact surface that can interact with other surfaces like the obstetric forceps.

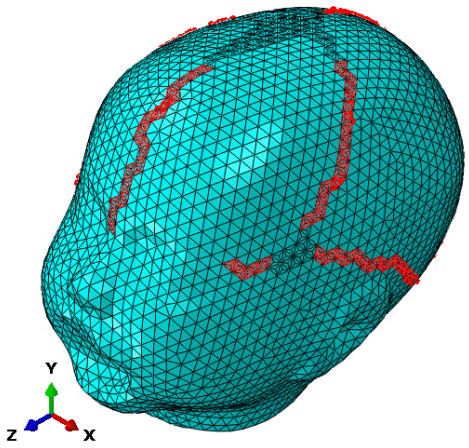

(a) $IFeH_1$ sutures anterior-left sagittal view.

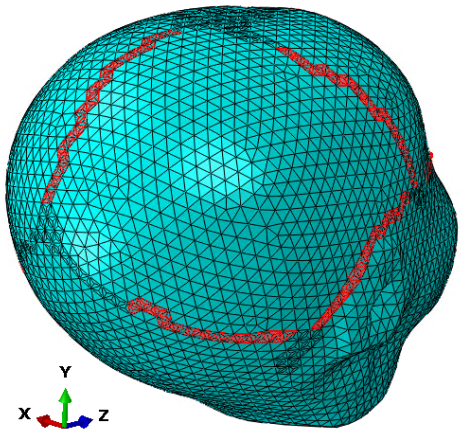

(b) $IFeH_1$ sutures posterior right sagittal view.

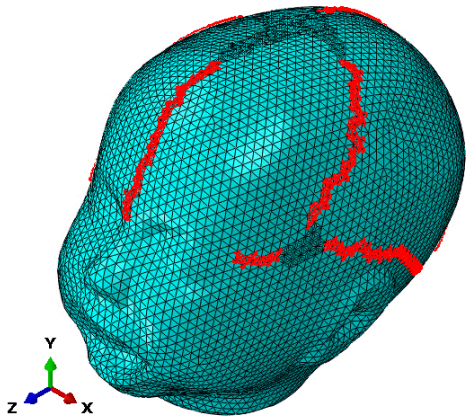

(c) $IFeH_2$ sutures anterior left sagittal view.

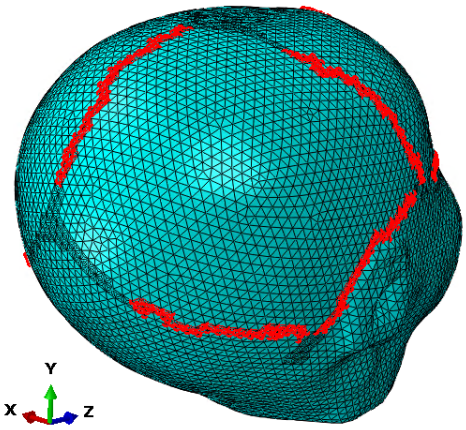

(d) $IFeH_2$ sutures posterior right sagittal view.

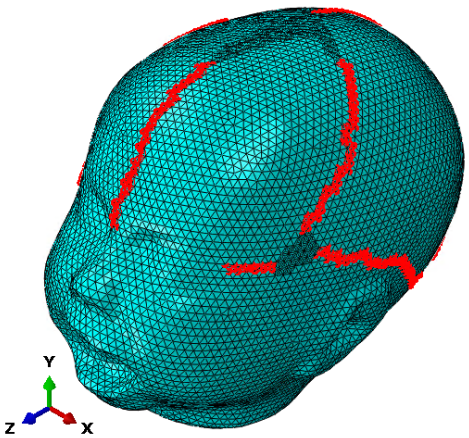

(e) $IFeH_3$ sutures anterior left sagittal view.

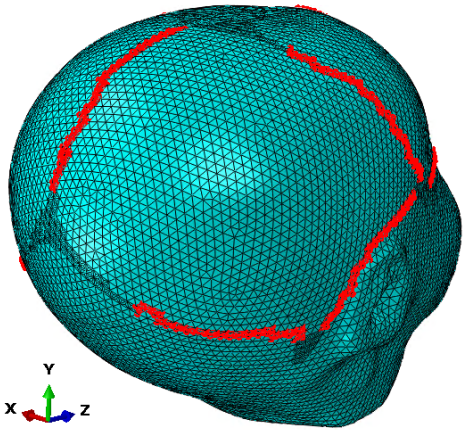

(f) $IFeH_3$ sutures posterior right sagittal view.

Figure 4.25: Different IFeH meshes with suture regions in red.

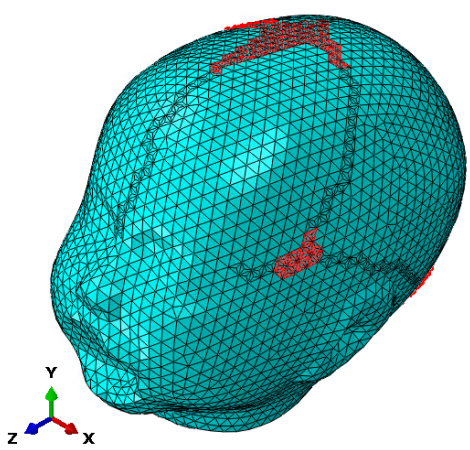

(a) $IFeH_1$ fontanelles anterior-left sagittal view.

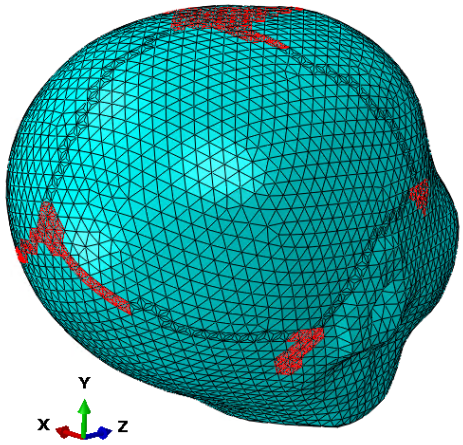

(b) $IFeH_1$ fontanelles posterior-right sagittal view.

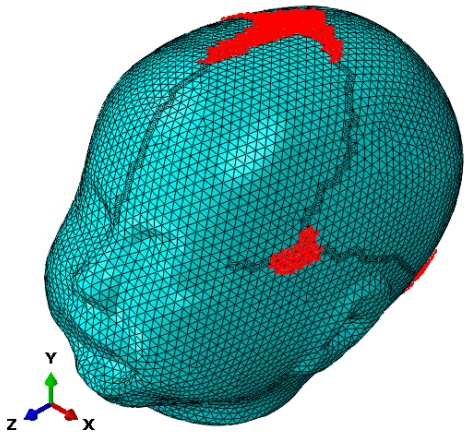

(c) $IFeH_2$ fontanelles anterior-left sagittal view.

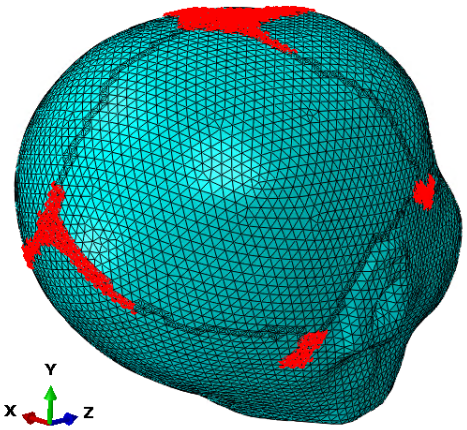

(d) $IFeH_2$ fontanelles posterior-right sagittal view.

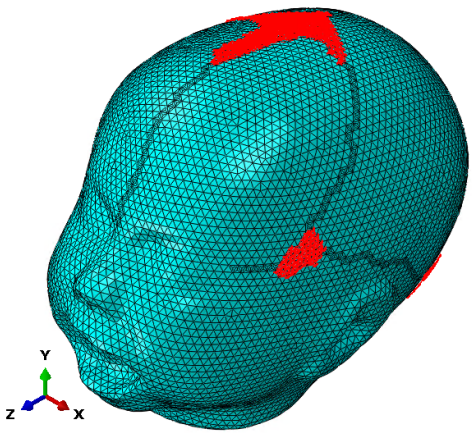

(e) $IFeH_3$ fontanelles anterior-left sagittal view.

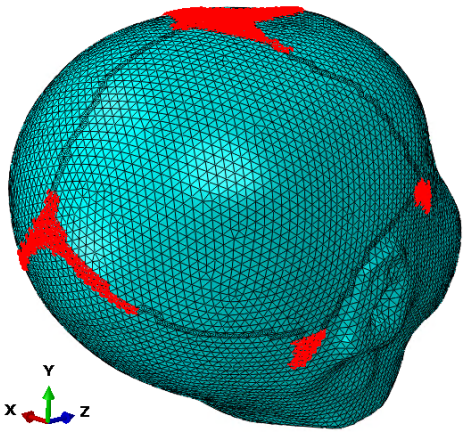

(f) $IFeH_3$ fontanelles posterior-right sagittal view.

Figure 4.26: Different IFeH meshes with fontanelle regions in red.

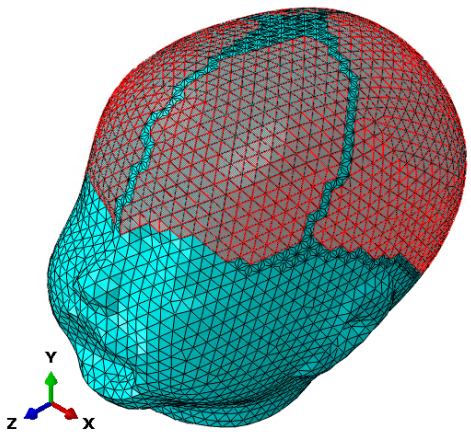

(a) $IFeH_1$ cranial bones anterior-left sagittal view.

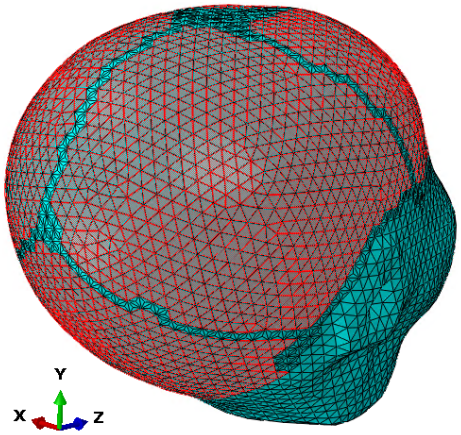

(b) $IFeH_1$ cranial bones posterior-right sagittal view.

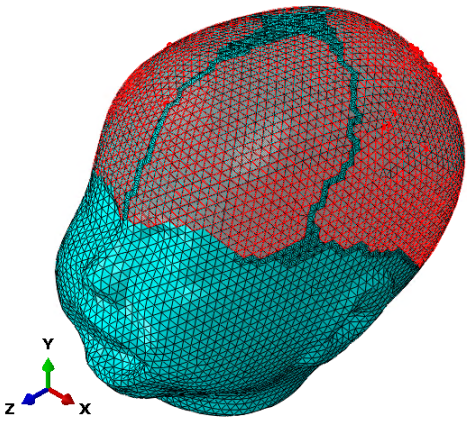

(c) $IFeH_2$ cranial bones anterior-left sagittal view.

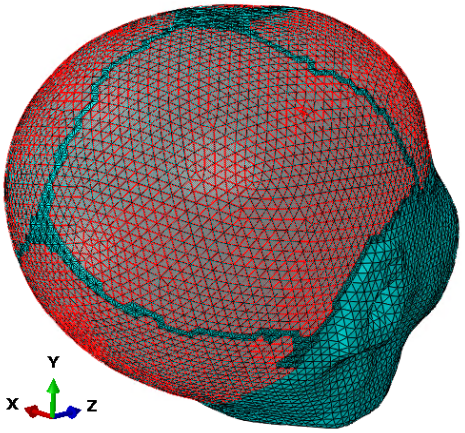

(d) $IFeH_2$ cranial bones posterior-right sagittal view.

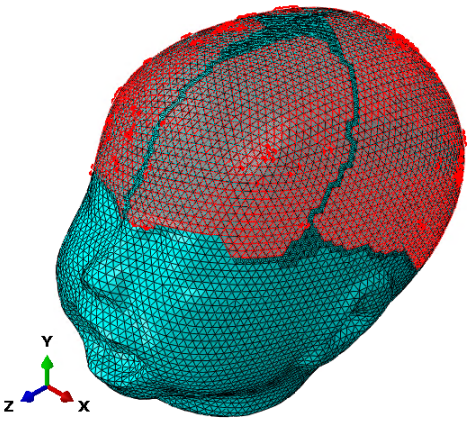

(e) $IFeH_3$ cranial bones anterior-left sagittal view.

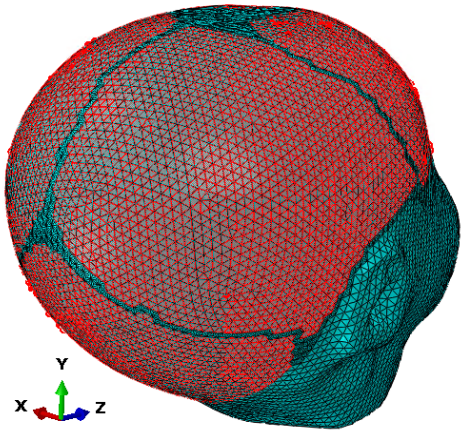

(f) $IFeH_3$ cranial bones posterior-right sagittal view.

Figure 4.27: Different IFeH meshes with cranial bone regions in red.

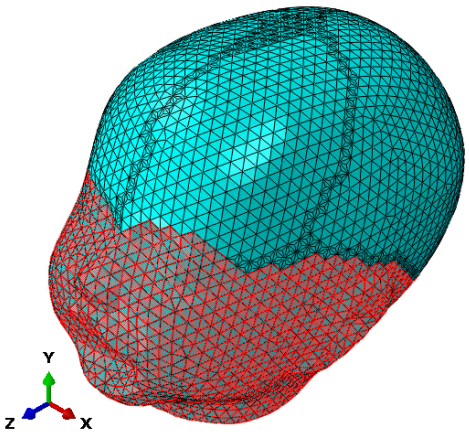

(a) $IFeH_1$ base bone anterior-left sagittal view.

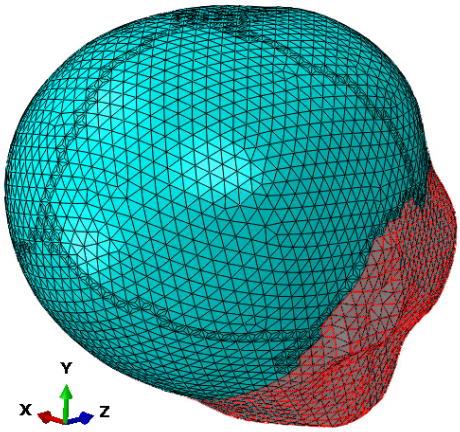

(b) $IFeH_1$ base bone posterior-right sagittal view.

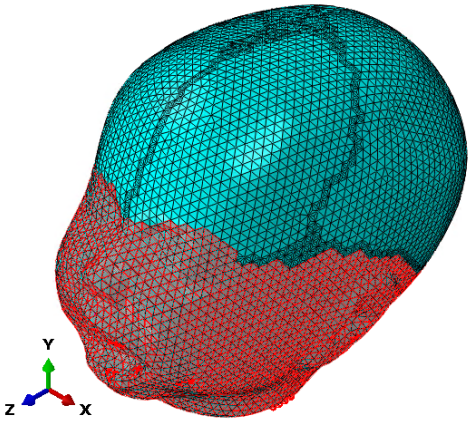

(c) $IFeH_2$ base bone anterior-left sagittal view.

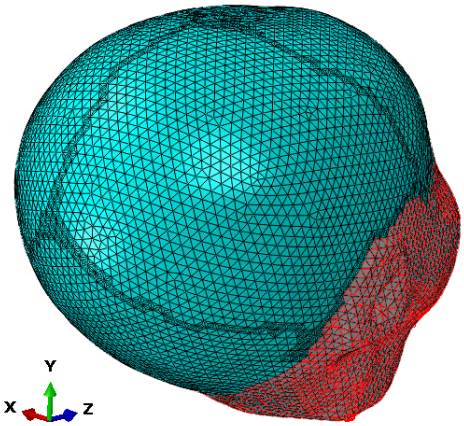

(d) $IFeH_2$ base bone posterior-right sagittal view.

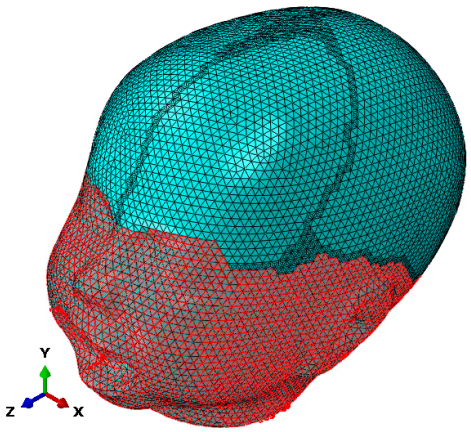

(e) $IFeH_3$ base bone anterior-left sagittal view.

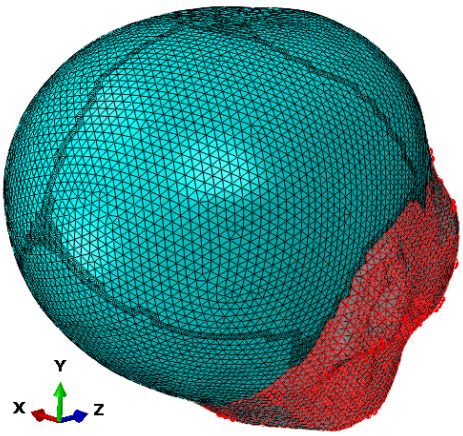

(f) $IFeH_3$ base bone posterior-right sagittal view.

Figure 4.28: Different IFeH meshes with base bone region in red.

4.4.1.2 Obstetric forceps model

The final version of the proposed 3D obstetric forceps model as described in Section 3.3.1.3 contains a Forceps Left Blade (FLB) and a Forceps Right Blade (FRB) which material property is specified in Section 3.3.1.4. Each blade represents a single region that contains a contact surface located in the internal face of the forceps blade as it is shown in Figure 4.29.

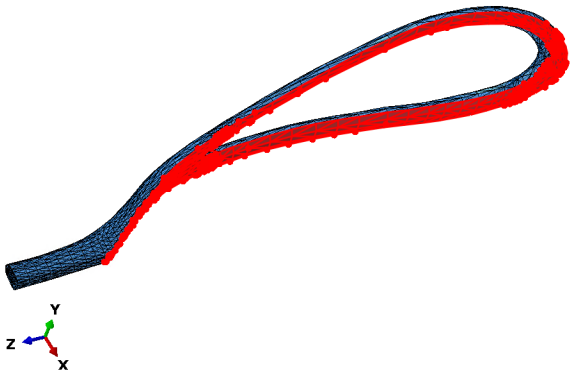

Figure 4.29: Obstetric forceps right blade with internal surface definition in red.

4.4.1.3 Steps

In the **Initial Step**, the initial position of the models is defined as follows[4]:

$$\begin{aligned} FRB(x,y,z) &= (-0.0335, -0.00514, 0.01) \\ FLB(x,y,z) &= (0.0375, -0.004, 0.00978) \\ IFeH(x,y,z) &= (0.00182, -0.005, 0) \end{aligned} \tag{4.4}$$

The simulation starts with the execution of the **Close Step** as described in Section 3.4.1.2, which considers different analysis depending on the boundary conditions specified in the experiment.

4.4.1.4 Interactions

According to the initial positions of the FLB, FRB and IFeH models, the next interactions are defined (see Section 2.2.3 for reference about anatomy of fetal head):

- FRB interacts with:
  - Right mastoid fontanelle.
  - Right parietal bone.
  - Right squamosal suture.
  - Base bone.

[4] All values are defined in meters (m).

- FLB interacts with:
  - Left mastoid fontanelle.
  - Left parietal bone.
  - Left squamosal suture.
  - Base bone.

Figure 4.30a and Figure 4.30b show the surfaces defined in the fetal head (as mentioned previously) that interact with the Forceps Right Blade (FRB) and Forceps Left Blade (FLB) respectively.

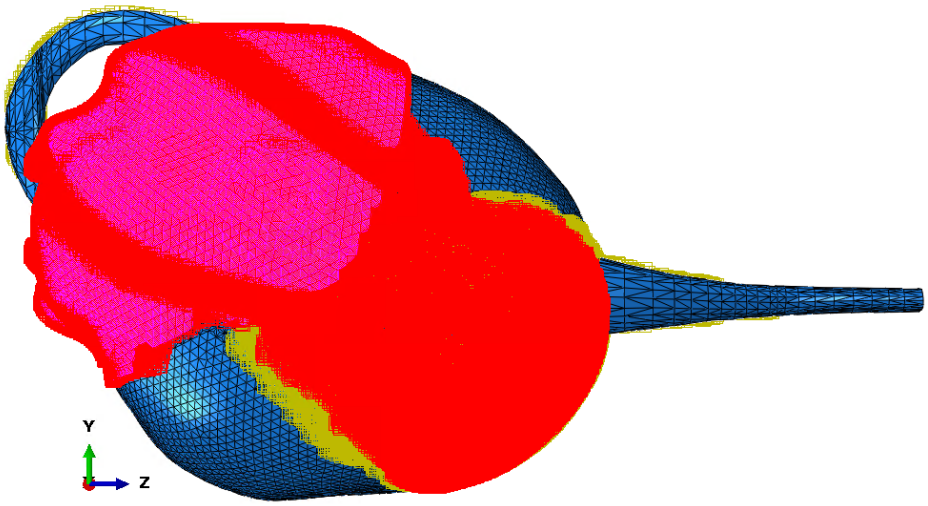

(a) FRB interactions with IFeH.

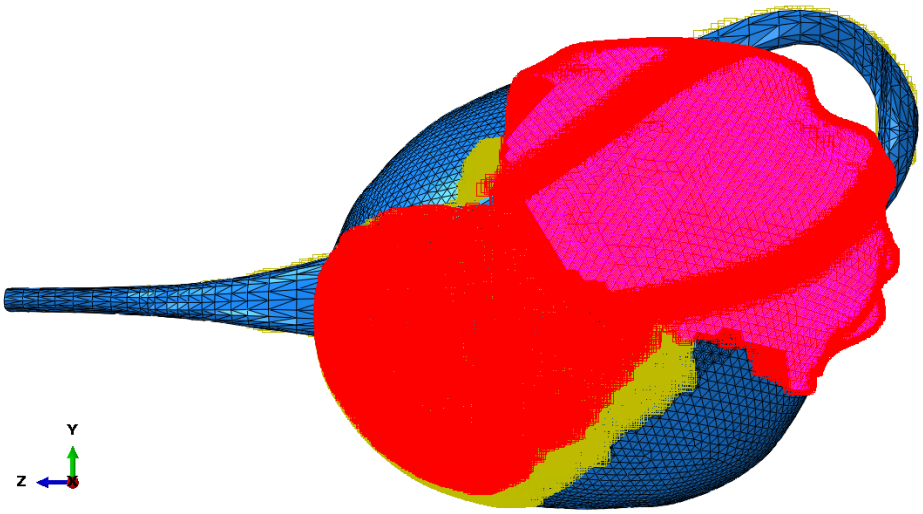

(b) FLB interactions with IFeH.

Figure 4.30: LB and RB interactions with IFeH regions (pink and red).

4.4.1.5 Loads

Similar to previous experiments, this experiment does not apply explicit loads over the obstetric forceps blades, instead a constant velocity boundary condition is applied to move them. This approach allows to control the amount of displacement to perform over the blades.

4.4.1.6 Boundary Conditions (BCs)

Similar to the BCs defined in the experiment described in section 4.1, in this experiment a set of nodes for each model is created where the BCs are applied (see Figure 4.31). Node sets are defined as follows:

- Left Blade Constraint (LB_C).
- Right Blade Constraint (RB_C).
- Improved Fetal Head Constraint (IFeHC).

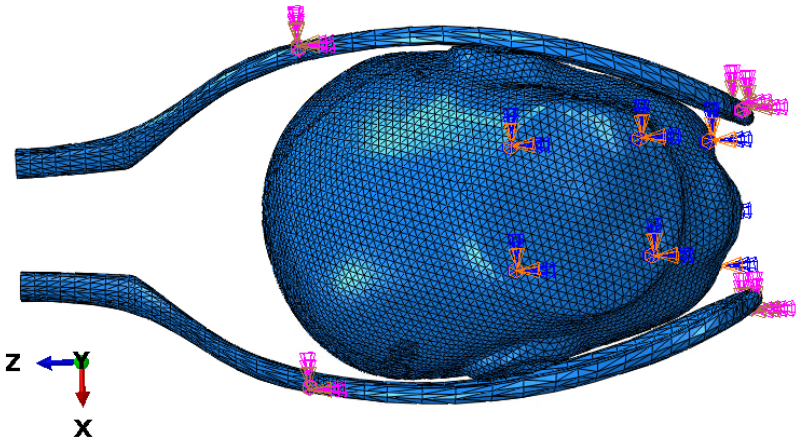

Figure 4.31: Set of nodes (pink and blue with orange points) defining the BCs in the FEA for RB_C, IFeHC and LB_C.

Table 4.8 describes the BCs applied to each set of nodes per step.

Set	Step	
	Initial	**Close**
LB_C	Fixed position	Allows displacement in x axis
LB_C	No velocity	Constant velocity on x axis at $1mm/s$
RB_C	Fixed position	Allows displacement in x axis
RB_C	No velocity	Constant velocity on x axis at $1mm/s$
IFeHC	Encastre	Propagated

Table 4.8: BCs applied to set of nodes in the **Initial** and **Close** steps in the fetal head in contact with forceps analysis.

4.4.2 Experimental results

This section outlines the results obtained in the current fetal head in contact with forceps experiment.

Table 4.9 shows the nodal displacement over the x axis (U_x) and the nodal displacement magnitude (U), for every fetal head mesh when both FLB_x and FRB_x have been translated towards the sphere, this is:

$$\begin{aligned} FLB(x,y,z) &= (-0.0335 + b, 0, 0) \\ FRB(x,y,z) &= (0.0365 - b, 0, 0) \end{aligned} \tag{4.5}$$

where b is the displacement of the blades performed in the **Close Step** at $1mm$ and $2mm$.

Close step	Mesh	U_x	U
$1mm$	$IFeH_1$	$1.385e^{-03}$	$1.152e^{-03}$
	$IFeH_2$	$1.387e^{-03}$	$1.162e^{-03}$
	$IFeH_3$	$1.094e^{-03}$	$1.136e^{-03}$
$2mm$	$IFeH_1$	$1.993e^{-03}$	$1.780e^{-03}$
	$IFeH_2$	$2.117e^{-03}$	$1.776e^{-03}$
	$IFeH_3$	$1.743e^{-03}$	$1.831e^{-03}$

Table 4.9: Nodal displacement over the x axis (U_x in m) and nodal displacement magnitude (U in m) of the fetal head in contact with forceps analysis when LB_C and RB_C performed a 1mm and 2mm translation in the x axis towards the sphere.

Figures 4.32 and 4.33 show the nodal displacement over the x axis (U_x) and nodal displacement magnitude (U) results of the fetal head in contact with forceps when forceps blades FLB_x and FRB_x have been translated $1mm$ towards the IFeH, at the same time Figures 4.34 and 4.35 when FLB_x and FRB_x have been translated $2mm$ towards the IFeH.

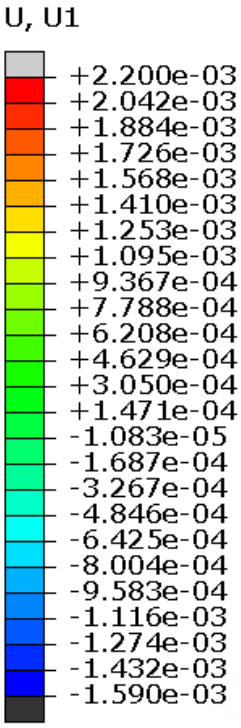

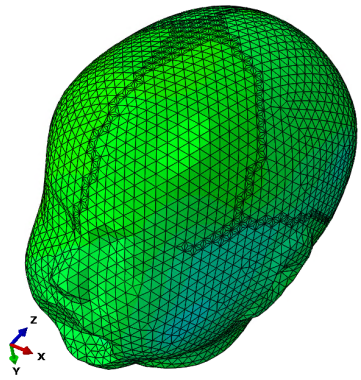

(a) $IFeH_1$ anterior left sagittal view.

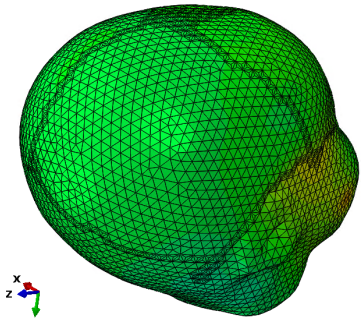

(b) $IFeH_1$ posterior right sagittal view.

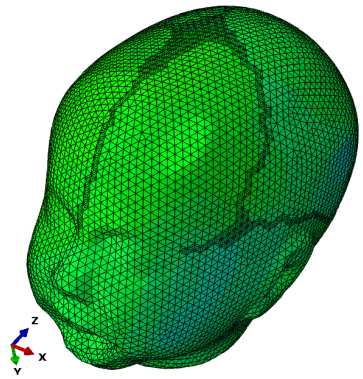

(c) $IFeH_2$ anterior left sagittal view.

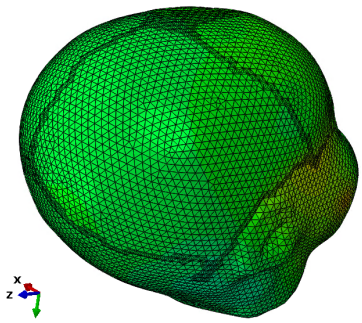

(d) $IFeH_2$ posterior right sagittal view.

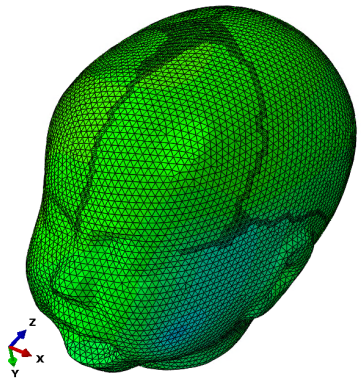

(e) $IFeH_3$ anterior left sagittal view.

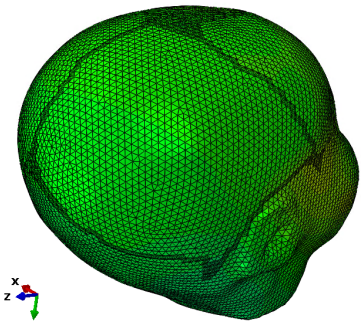

(f) $IFeH_3$ posterior right sagittal view.

Figure 4.32: Nodal displacement results over the x axis (U_x) in IFeH models when $FLB_x = FRB_x = 1$mm

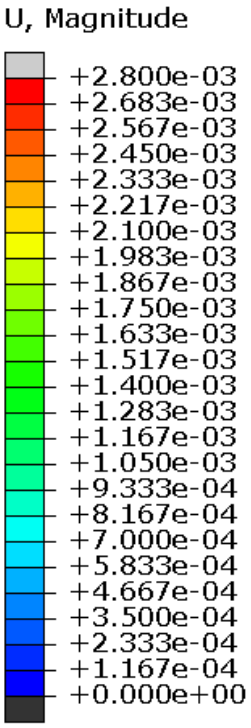

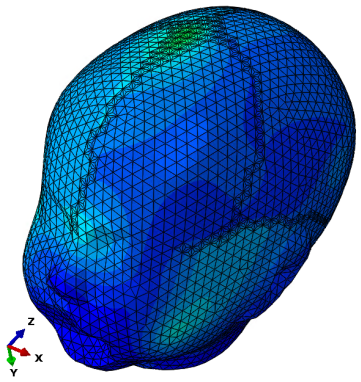

(a) $IFeH_1$ anterior left sagittal view.

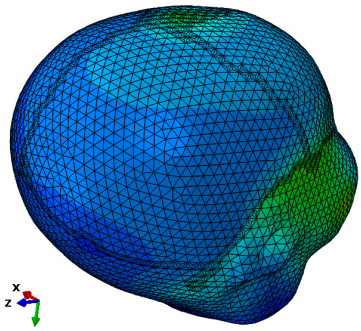

(b) $IFeH_1$ posterior right sagittal view.

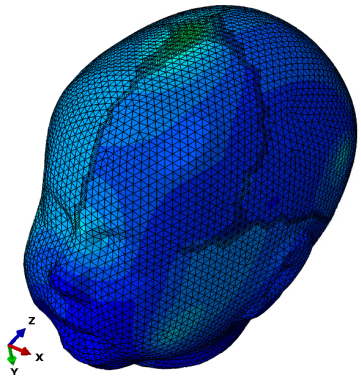

(c) $IFeH_2$ anterior left sagittal view.

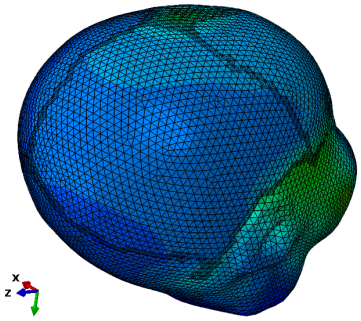

(d) $IFeH_2$ posterior right sagittal view.

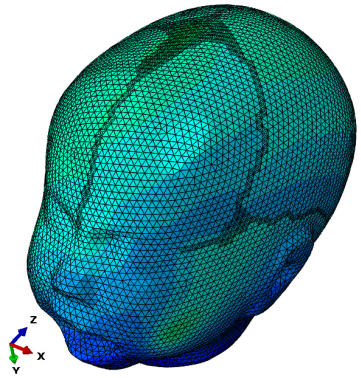

(e) $IFeH_3$ anterior left sagittal view.

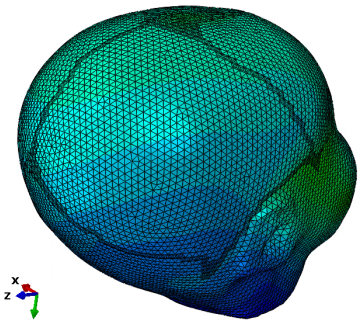

(f) $IFeH_3$ posterior right sagittal view.

Figure 4.33: Nodal displacement magnitude (U) results in IFeH models when $FLB_x = FRB_x = 1$mm

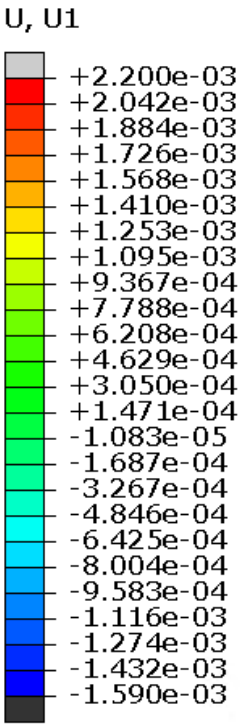

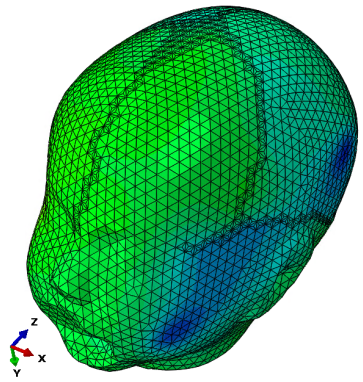

(a) $IFeH_1$ anterior left sagittal view.

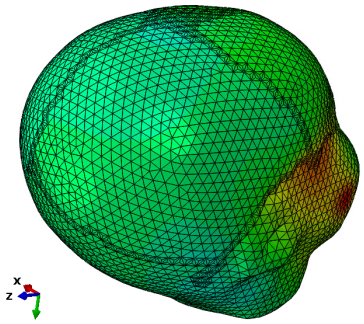

(b) $IFeH_1$ posterior right sagittal view.

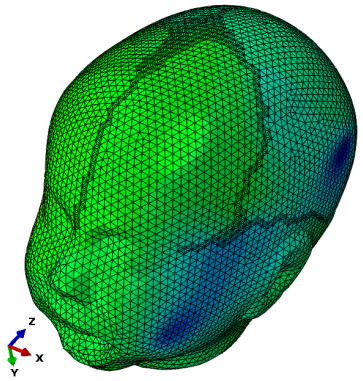

(c) $IFeH_2$ anterior left sagittal view.

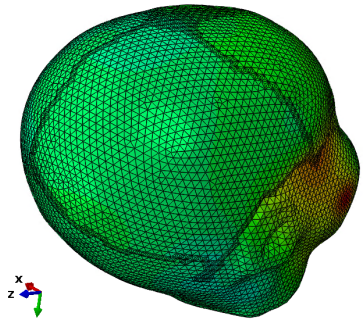

(d) $IFeH_2$ posterior right sagittal view.

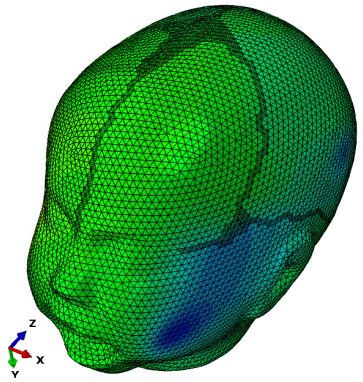

(e) $IFeH_3$ anterior left sagittal view.

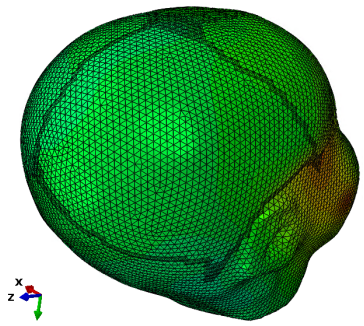

(f) $IFeH_3$ posterior right sagittal view.

Figure 4.34: Nodal displacement results over the x axis (U_x) in IFeH models when $FLB_x = FRB_x = 2$mm

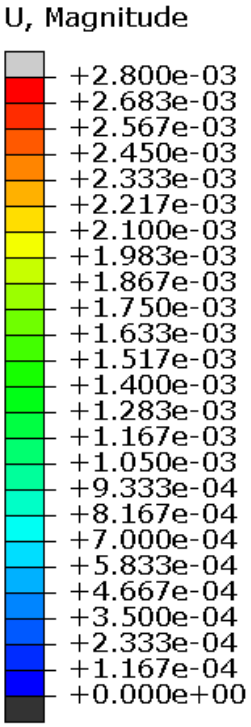

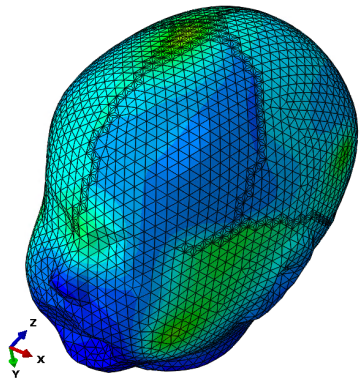

(a) $IFeH_1$ anterior left sagittal view.

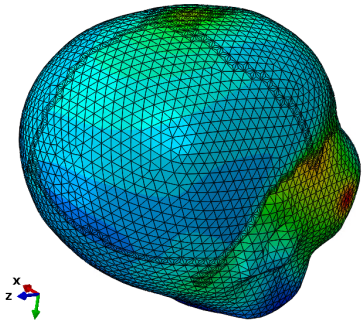

(b) $IFeH_1$ posterior right sagittal view.

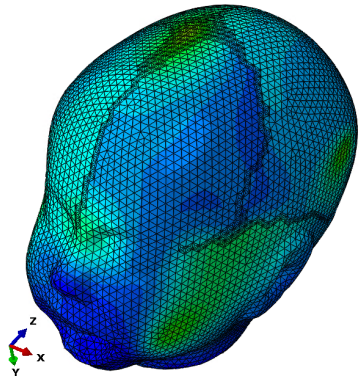

(c) $IFeH_2$ anterior left sagittal view.

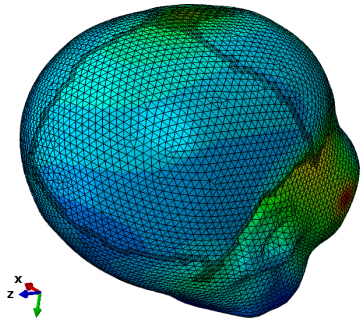

(d) $IFeH_2$ posterior right sagittal view.

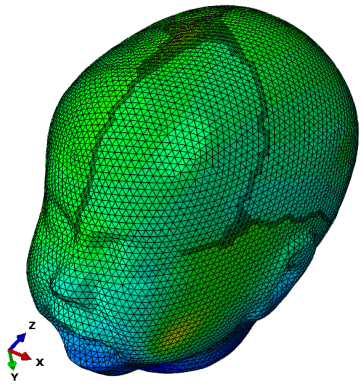

(e) $IFeH_3$ anterior left sagittal view.

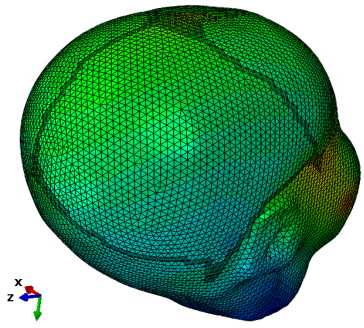

(f) $IFeH_3$ posterior right sagittal view.

Figure 4.35: Nodal displacement magnitude (U) results in IFeH models when $FLB_x = FRB_x = 2$mm

4.4.3 Discussion

- From Table 4.9 we observe:
  - Nodal displacement in the x direction o lateral side, U_x, and nodal displacement magnitude in the anterior fontanelle, U, increase with increasing closing step.
  - Based on the sphere experiments and the complex nature of the fetal head, even the coarsest mesh for the latter is substantially finer than the former equivalent mesh. Indeed the coarsest fetal head mesh is almost $8K$ elements compared with the coarsest sphere mesh containing 768 elements.
  - This is why the difference in U_x and U across the three different IFeH meshes are marginal.
- It is observed that the nodal displacement in the x direction U_x at the closing steps of $1mm$ and $2mm$ is similar across the difference meshes, however the $IFeH_3$ mesh present a lower value compared to the coarsest meshes.
- From Figures 4.32 and 4.34, it is clear that the finer the mesh the more detailed deformation patterns in crucial regions where the forceps is applied, is observed.
- The importance of mesh refinement becomes more apparent as the finest mesh shows more accurate patterns of the nodal displacement magnitude U depicted in Figures 4.33 and 4.35 at closing steps of $1mm$ and $2mm$ respectively.

4.5 Forceps traction on fetal head

The aim of this experiment is to simulate the obstetric forceps-baby head behaviour when the **Pull Step** is performed (see Section 3.4.1.3).

4.5.1 Experimental setup

4.5.1.1 Models

Previous obstetric forceps and baby head models are considered in this experiment as they were specified in Sections 4.4.1.2 and 4.4.1.1 respectively.

4.5.1.2 Steps

This analysis assumes that the **Initial Step** and **Close Step** have already been performed (see Section 4.4.1.3), hence the different cases of displacements performed in the **Close Step** are considered. The **Pull Step** is described in Section 3.4.1.3.

4.5.1.3 Interactions

The interactions between the obstetric forceps and improved fetal head as described in the previous experiment (see Section 4.4.1.4) is considered in this experiment as well.

4.5.1.4 Loads

Similar to previous experiment, there are no explicit loads applied for this experiment, instead a constant velocity boundary condition is applied the different set of nodes of LB_C and RB_C to move the obstetric forceps blades.

4.5.1.5 BCs

The BCs applied in this step (see Table 4.10), consider the same node sets specified in the previous step (see Section 4.4.1.6).

Set	**Pull Step**
LB_C	Allows translation in z axis
LB_C	Constant velocity on x axis at $1mm/0.1s$
RB_C	Allows translation in z axis
RB_C	Constant velocity on x axis at $1mm/0.1s$
IFeHC	Propagated

Table 4.10: BCs applied to the set of nodes in the **Pull** step in the forceps traction on fetal head analysis.

4.5.2 Experimental results

This sections outlines the results obtained in the current forceps traction on fetal head experiment.

Table 4.11 shows the nodal displacement over the x axis (U_x) and the nodal displacement magnitude (U), for every fetal head when both FLB_z and FRB_z have been translated $2mm$ in the z axis (see Eq. 4.6) after the **Close Step** of $1mm$ and $2mm$ have been performed.

$$\begin{aligned} FLB(x, y, z) &= (0, 0, 0.002) \\ FRB(x, y, z) &= (0, 0, 0.002) \end{aligned} \tag{4.6}$$

Close step	Pull step	Mesh	U_x	U
$1mm$	$2mm$	$IFeH_1$	$2.073e^{-03}$	$1.619e^{-03}$
		$IFeH_2$	$2.071e^{-03}$	$1.668e^{-03}$
		$IFeH_3$	$1.246e^{-03}$	$3.971e^{-03}$
$2mm$	$2mm$	$IFeH_1$	$2.895e^{-03}$	$2.180e^{-03}$
		$IFeH_2$	$2.792e^{-03}$	$2.223e^{-03}$
		$IFeH_3$	$1.942e^{-03}$	$4.825e^{-03}$

Table 4.11: Nodal displacement in x axis (U_x in m) and nodal displacement magnitude (U in m) of forceps traction on fetal head analysis when LB_C and RB_C performed a 2mm translation in the z axis after the close step was performed for 1mm and 2mm in the x axis.

Figures 4.36 and 4.37 show the nodal displacement over the x axis (U_x) and nodal displacement magnitude (U) results of the forceps traction on fetal head when forceps blades FLB_x and FRB_x have been translated $1mm$ towards the IFeH and FLB_z and FRB_z have been translated $2mm$ in the z axis, at the same time Figures 4.38 and 4.39 when FLB_x and FRB_x have been translated $2mm$ towards the IFeH and FLB_z and FRB_z have been translated $2mm$ in the z axis.

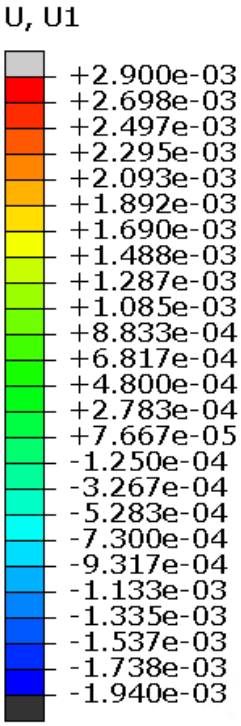

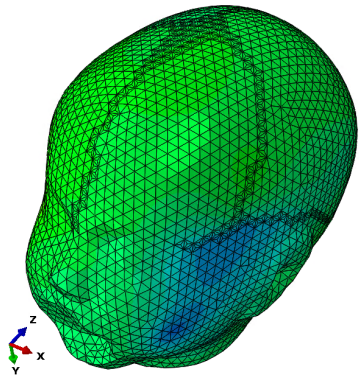

(a) $IFeH_1$ anterior left sagittal view.

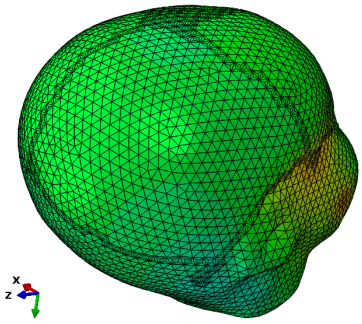

(b) $IFeH_1$ posterior right sagittal view.

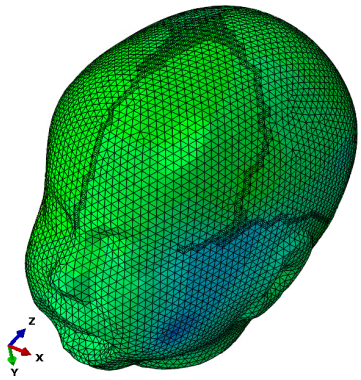

(c) $IFeH_2$ anterior left sagittal view.

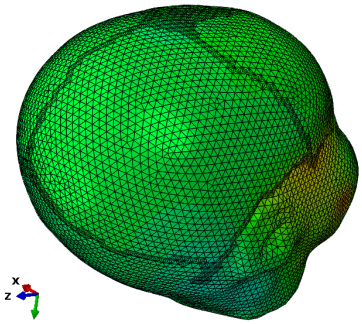

(d) $IFeH_2$ posterior right sagittal view.

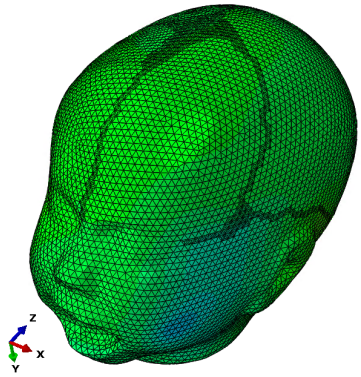

(e) $IFeH_3$ anterior left sagittal view.

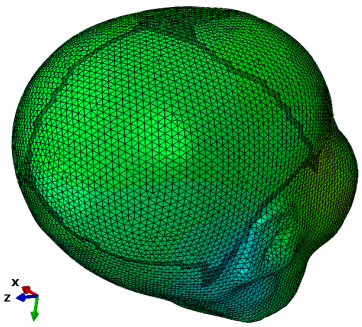

(f) $IFeH_3$ posterior right sagittal view.

Figure 4.36: Nodal displacement results over the x axis (U_x) in IFeH models when $FLB_x = FRB_x = 1$mm and $FLB_z = FRB_z = 2$mm

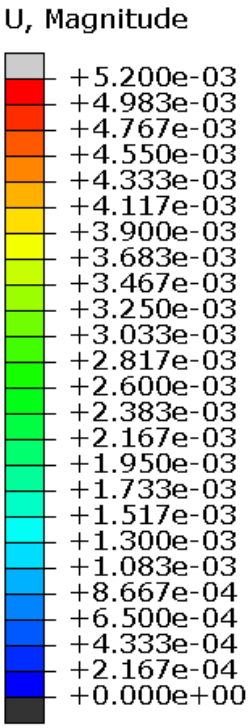

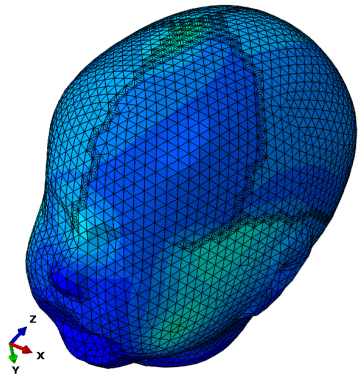

(a) $IFeH_1$ anterior left sagittal view.

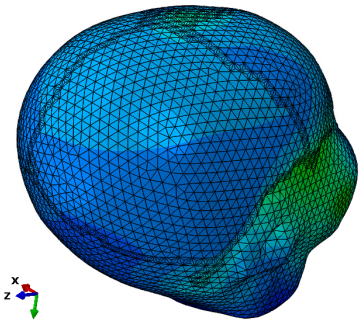

(b) $IFeH_1$ posterior right sagittal view.

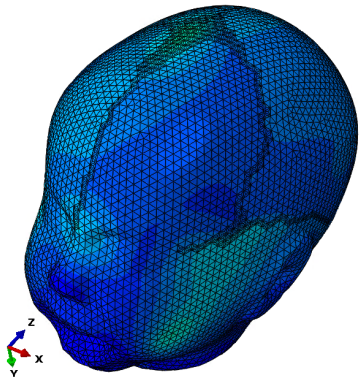

(c) $IFeH_2$ anterior left sagittal view.

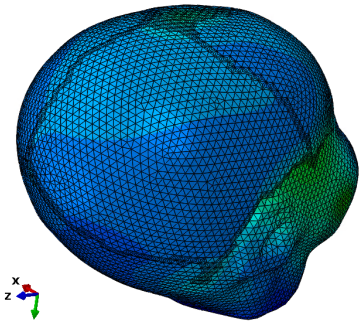

(d) $IFeH_2$ posterior right sagittal view.

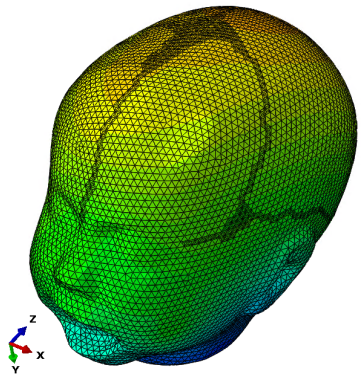

(e) $IFeH_3$ anterior left sagittal view.

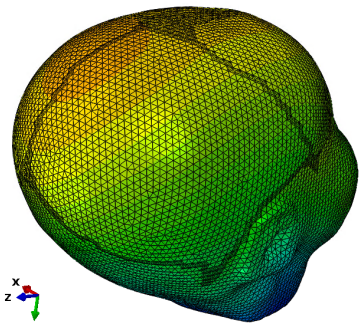

(f) $IFeH_3$ posterior right sagittal view.

Figure 4.37: Nodal displacement magnitude result (U) in IFeH models when $FLB_x = FRB_x = 1\text{mm}$ and $FLB_z = FRB_z = 2\text{mm}$

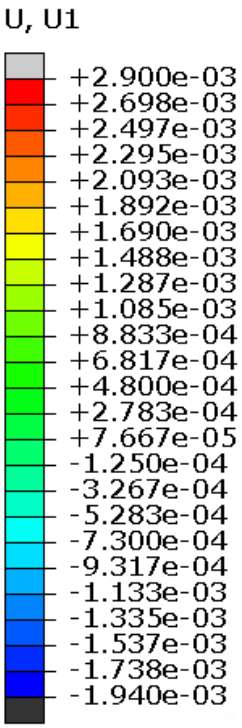

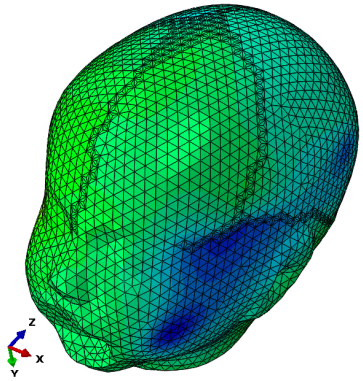

(a) $IFeH_1$ anterior left sagittal view.

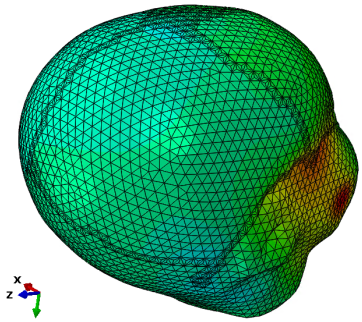

(b) $IFeH_1$ posterior right sagittal view.

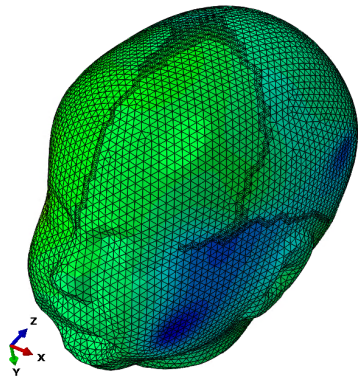

(c) $IFeH_2$ anterior left sagittal view.

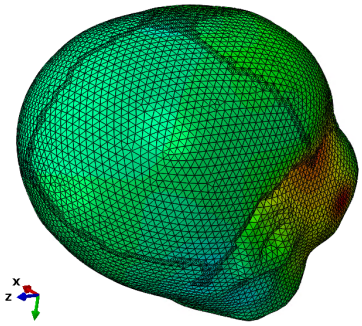

(d) $IFeH_2$ posterior right sagittal view.

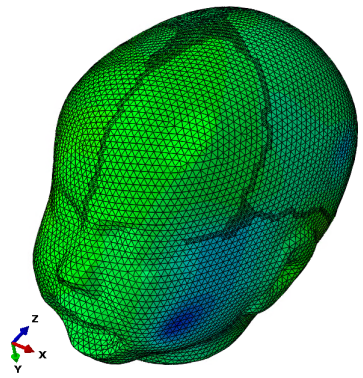

(e) $IFeH_3$ anterior left sagittal view.

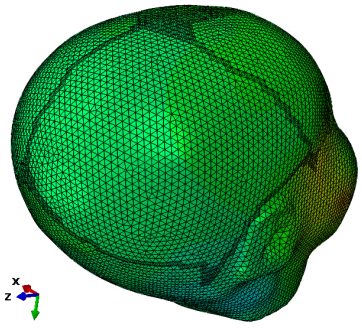

(f) $IFeH_3$ posterior right sagittal view.

Figure 4.38: Nodal displacement results over the x axis (U_x) in IFeH when $FLB_x = FRB_x =$ 2mm and $FLB_z = FRB_z =$ 2mm

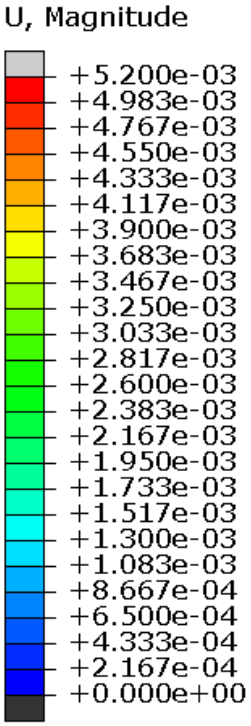

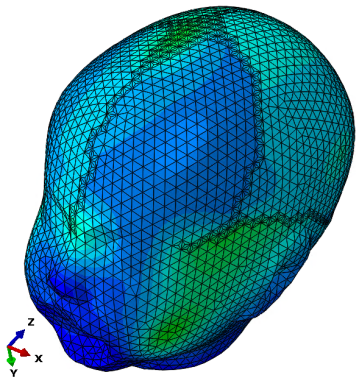

(a) $IFeH_1$ anterior left sagittal view.

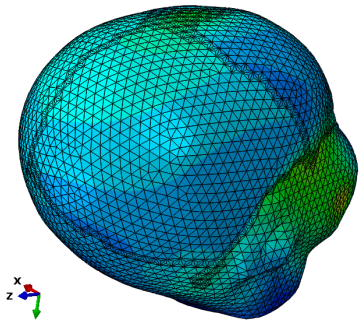

(b) $IFeH_1$ posterior right sagittal view.

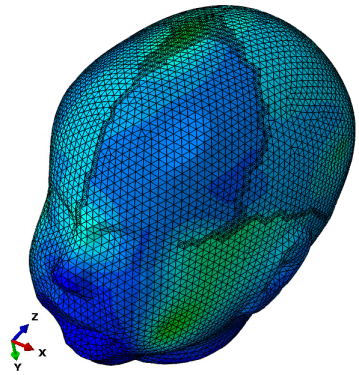

(c) $IFeH_2$ anterior left sagittal view.

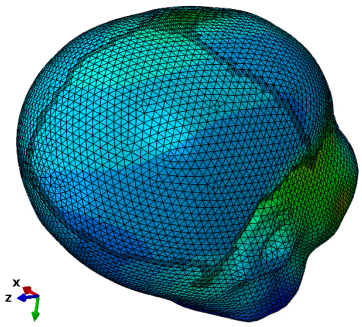

(d) $IFeH_2$ posterior right sagittal view.

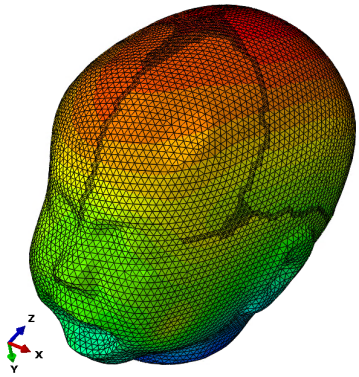

(e) $IFeH_3$ anterior left sagittal view.

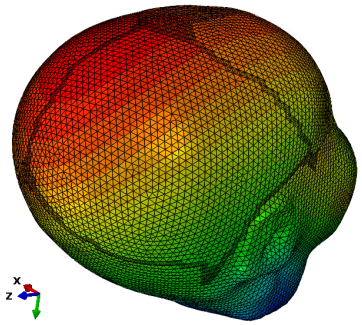

(f) $IFeH_3$ posterior right sagittal view.

Figure 4.39: Nodal displacement magnitude result (U) in IFeH when $FLB_x = FRB_x =$ 2mm and $FLB_z = FRB_z =$ 2mm

In terms of stresses, Table 4.12 shows the maximum values of the von Mises stress (S) and Shear stress ($S12$), for every fetal head when both FLB_x and FRB_x have been translated $2mm$ in the z axis after the **Close Step** of $1mm$ and $2mm$ have been performed.

Close step	Pull step	Mesh	S	$S12$
$1mm$	$2mm$	$IFeH_1$	$2.685e^{+08}$	$9.219e^{+07}$
		$IFeH_2$	$1.612e^{+08}$	$8.073e^{+07}$
		$IFeH_3$	$1.242e^{+08}$	$6.285e^{+07}$
$2mm$	$2mm$	$IFeH_1$	$4.032e^{+08}$	$1.219e^{+08}$
		$IFeH_2$	$3.875e^{+08}$	$1.172e^{+08}$
		$IFeH_3$	$2.090e^{+08}$	$7.551e^{+07}$

Table 4.12: Maximum values of von Mises stress (S in N/m^2) and Shear stress ($S12$ in N/m^2) of forceps traction on fetal head analysis when LB_C and RB_C performed a 2mm translation in the z axis after the close step was performed for 1mm and 2mm in the x axis.

Figures 4.40 and 4.41 show the von Mises stress (S in N/m^2) and Shear stress ($S12$ in N/m^2) results of the forceps traction on fetal head when forceps blades FLB_x and FRB_x have been translated $1mm$ towards the IFeH and FLB_z and FRB_z have been translated $2mm$ in the z axis, at the same time Figures 4.42 and 4.43 when FLB_x and FRB_x have been translated $2mm$ towards the IFeH and FLB_z and FRB_z have been translated $2mm$ in the z axis.

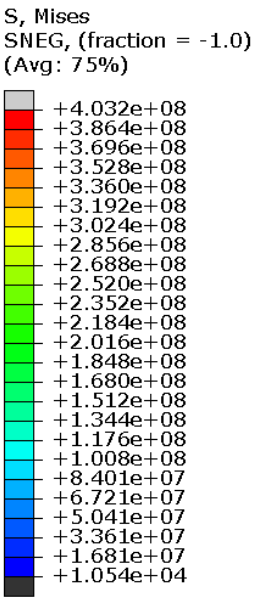

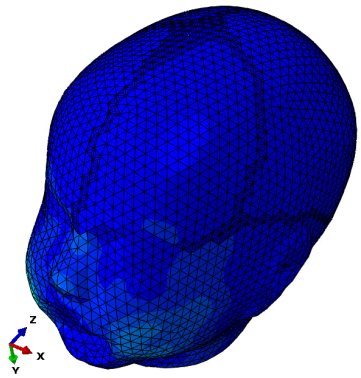

(a) $IFeH_1$ anterior left sagittal view.

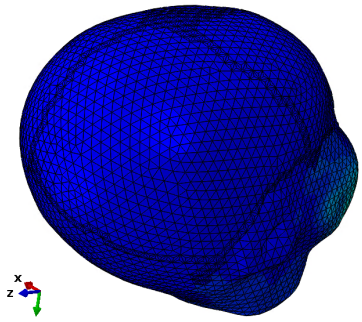

(b) $IFeH_1$ posterior right sagittal view.

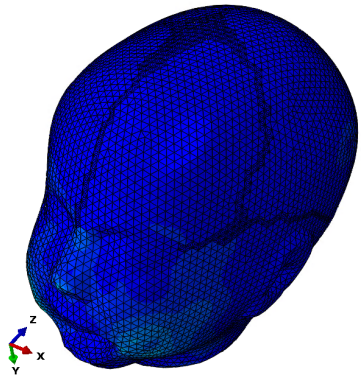

(c) $IFeH_2$ anterior left sagittal view.

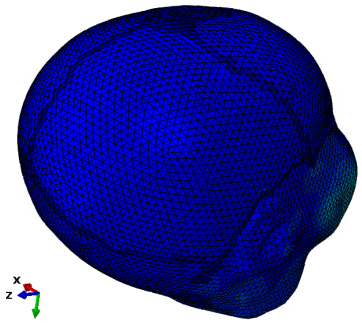

(d) $IFeH_2$ posterior right sagittal view.

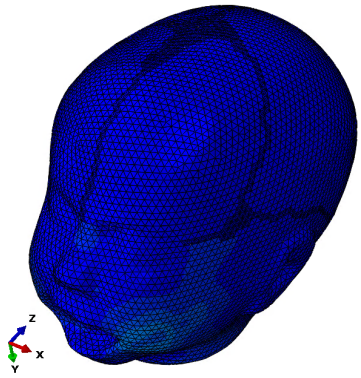

(e) $IFeH_3$ anterior left sagittal view.

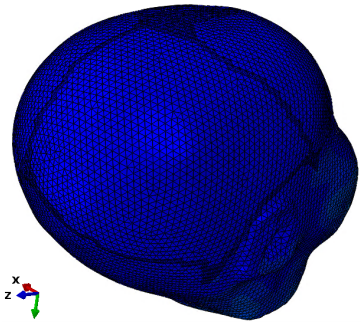

(f) $IFeH_3$ posterior right sagittal view.

Figure 4.40: Nodal stress (S) result in IFeH models when $FLB_x = FRB_x = 1$mm and $FLB_z = FRB_z = 2$mm

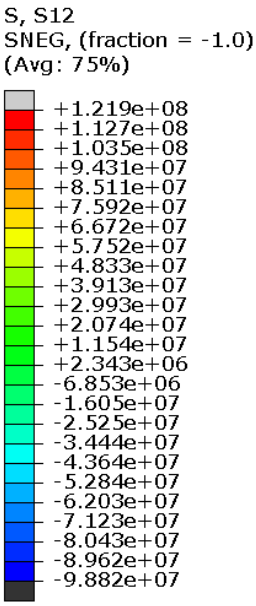

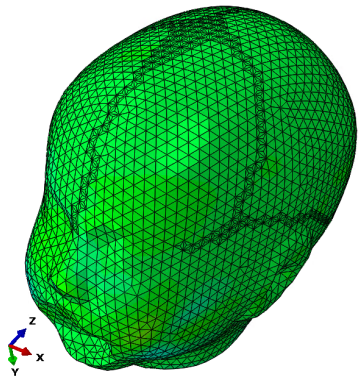

(a) $IFeH_1$ anterior left sagittal view.

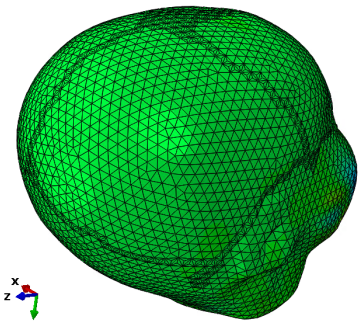

(b) $IFeH_1$ posterior right sagittal view.

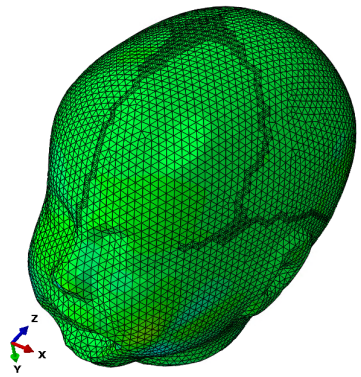

(c) $IFeH_2$ anterior left sagittal view.

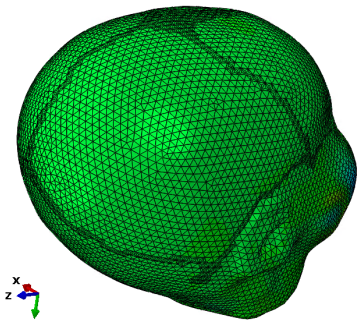

(d) $IFeH_2$ posterior right sagittal view.

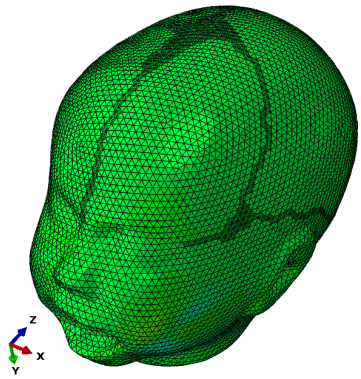

(e) $IFeH_3$ anterior left sagittal view.

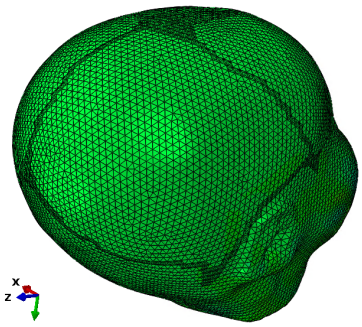

(f) $IFeH_3$ posterior right sagittal view.

Figure 4.41: Shear stress ($S12$) result in IFeH models when $FLB_x = FRB_x = 1$mm and $FLB_z = FRB_z = 2$mm

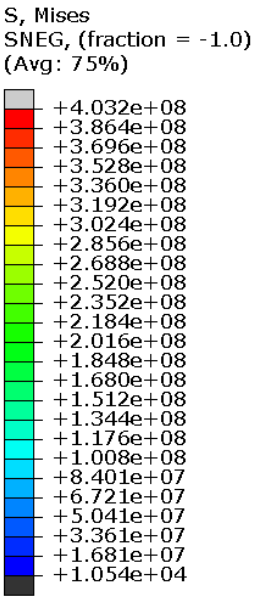

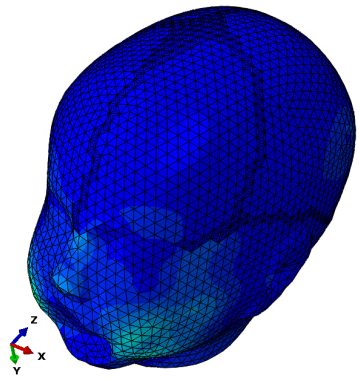

(a) $IFeH_1$ anterior left sagittal view.

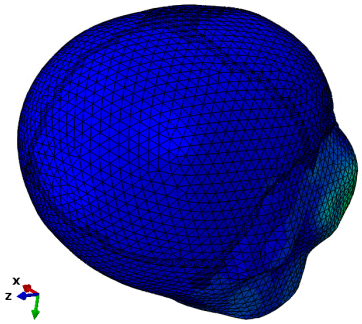

(b) $IFeH_1$ posterior right sagittal view.

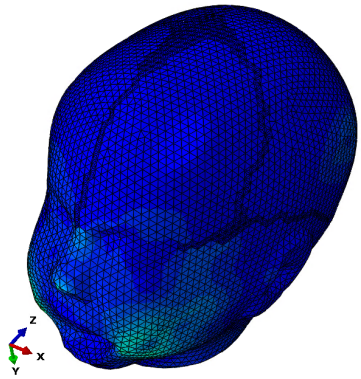

(c) $IFeH_2$ anterior left sagittal view.

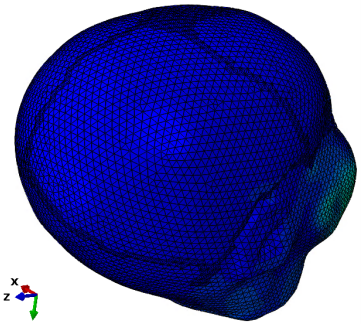

(d) $IFeH_2$ posterior right sagittal view.

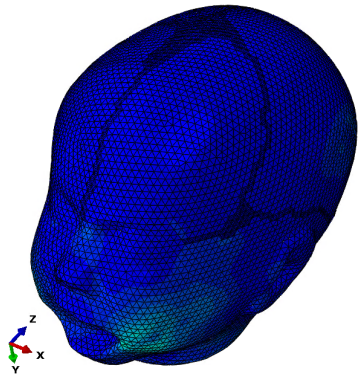

(e) $IFeH_3$ anterior left sagittal view.

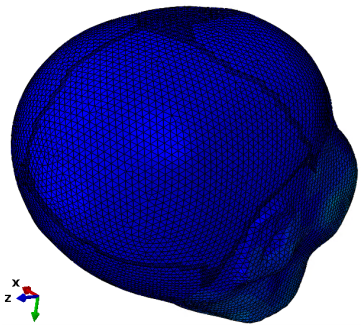

(f) $IFeH_3$ posterior right sagittal view.

Figure 4.42: Nodal stress (S) result in IFeH models when $FLB_x = FRB_x = 2$mm and $FLB_z = FRB_z = 2$mm

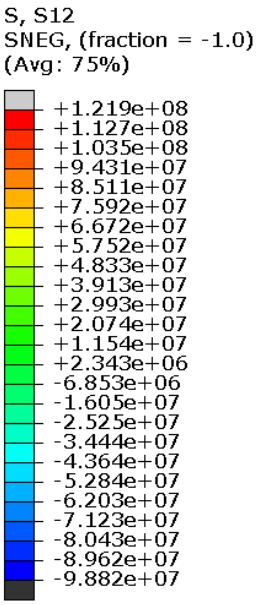

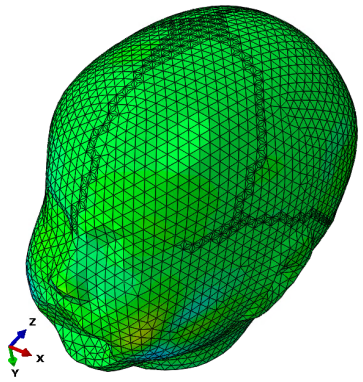

(a) $IFeH_1$ anterior left sagittal view.

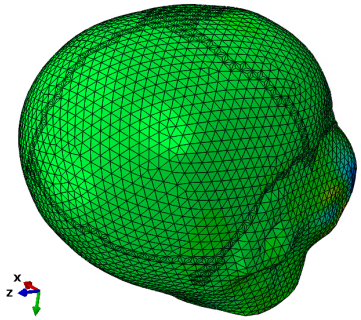

(b) $IFeH_1$ posterior right sagittal view.

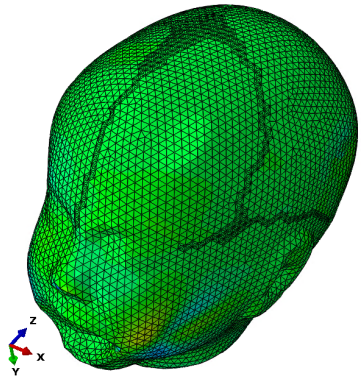

(c) $IFeH_2$ anterior left sagittal view.

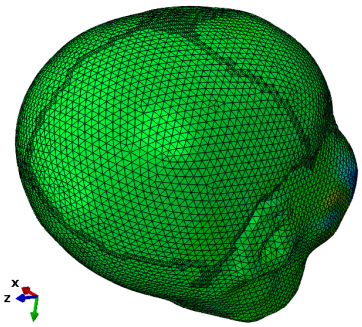

(d) $IFeH_2$ posterior right sagittal view.

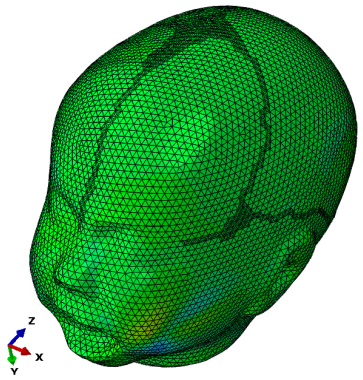

(e) $IFeH_3$ anterior left sagittal view.

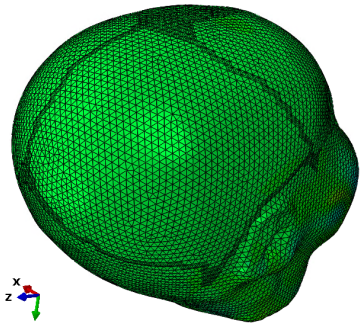

(f) $IFeH_3$ posterior right sagittal view.

Figure 4.43: Shear stress ($S12$) result in IFeH models when $FLB_x = FRB_x = 2$mm and $FLB_z = FRB_z = 2$mm

4.5.3 Discussion

- From Table 4.11 we observe:
  - Nodal displacement in the x direction or lateral side, U_x, and nodal displacement magnitude in the anterior fontanelle, U, increase with increasing closing step.
  - With increasing mesh complexity U_x decreases and U increases.
- It is observed that the nodal displacement in the x direction U_x in the two coarsest meshes ($IFeH_1$ and $IFeH_2$) at the closing step of $1mm$ and $2mm$ is overestimated, this can be seen in Figure 4.36 and more clearly in Figure 4.38 respectively. The displacement area of U_x depicted in the region between the temporal and the mandible bones in both sides of the head is larger in the coarsest meshes but significantly smaller in the finest mesh. This is due to overestimating the shear effect from the forceps traction. This can also be observed in Figures 4.41 and 4.43 showing the shear stress S_{12} on all meshes, and noticing that the shear stress area is reduced the finer the mesh.
- From Figures 4.37 and 4.39 showing the nodal displacement magnitude U at closing steps of $1mm$ and $2mm$ respectively, it is clear that the finer mesh $IFeH_3$ better captures the large displacement of the anterior fontanelle area which is completely subjected to the forceps traction displacement (remember that the fetal neck is encastred so will show zero displacement). The nodal displacement difference from $IFeH_1$ to $IFeH_2$ is neglible at either closing step of $1mm$ and $2mm$ with an approximate displacement of $1.6e^{-03}m$ and $2.2e^{-03}m$ respectively, but a clear difference of more than $2mm$ between $IFeH_2$ and $IFeH_3$ in each closing step is observed.
- From Table 4.12 we observe that the von Mises stress S and Shear stress $S12$ decrease as increasing mesh complexity, but increase as the IFeH is under more compression due to the higher translation of the blades towards it.
- From Figures 4.40 and 4.42, it is observed that increasing mesh complexity, the area of the von Mises Stress S is reduced at the same time that the maximum value, i.e. at a closing step of $1mm$, $IFeH_1$ has a maximum Mises value of $2.685e^{+08}$ and $IFeH_3$ a value of $1.242e^{+08}$, at a closing step of $2mm$, $IFeH_1$ has a value of $4.032e^{+08}$ and $IFeH_3$ a value of $2.090e^{+08}$. This is due to the overestimation in the coarsest meshes.
- It is observed from Figure 4.41 and more clearly in Figure 4.43, an overestimation of the area and maximum values of the Shear stress $S12$ in the coarsest meshes. At a closing step of $1mm$, $IFeH_1$ has a maximum Shear stress value of $9.219e^{+07}$ and $IFeH_3$ a value of $6.285e^{+07}$, meanwhile at a closing step of $2mm$, $IFeH_1$ has a value of $1.219e^{+08}$ and $IFeH_3$ a value of $7.551e^{+07}$.

4.6 Rotated fetal head in contact with forceps

The aim of this experiment is to simulate the obstetric forceps-baby head behaviour when the baby head presents an internal rotation at the time the **Close Step** is performed (see Section 3.4.1.2).

4.6.1 Experimental setup

4.6.1.1 Models

Previous obstetric forceps and baby head models are considered in this experiment as they were specified in Sections 4.4.1.2 and 4.4.1.1 respectively.

4.6.1.2 Steps

In the **Initial Step**, the initial position of the models is defined as follows[5]:

$$\begin{aligned} FRB(x,y,z) &= (-0.035, -0.00514, 0.01) \\ FLB(x,y,z) &= (0.036, -0.004, 0.00978) \\ IFeH(x,y,z) &= (0.00183, -0.005, 0.0212) \end{aligned} \tag{4.7}$$

Additionally the baby head is rotated -10 degrees in the z axis.

The simulation starts with the execution of the **Close Step** as described in Section 3.4.1.2, which considers different analysis depending on the boundary conditions specified in the experiment.

4.6.1.3 Interactions

The interactions between the obstetric forceps and improved fetal head described in Section 4.4.1.4 are considered in this experiment as well.

4.6.1.4 Loads

Similar to previous experiments, this experiment does not apply explicit loads over the obstetric forceps blades, instead a constant velocity boundary condition is applied to move them. This approach allows to control the amount of displacement to perform over the blades.

4.6.1.5 BCs

The same BCs defined in Section 4.4.1.6 are used in this experiment.

[5] All values are defined in meters (m).

4.6.2 Experimental results

This section outlines the results obtained in the current experiment rotated fetal head in contact with forceps experiment.

Table 4.13 shows the nodal displacement in x axis (U_x) and the nodal displacement magnitude (U), for every fetal head mesh when both FLB_x and FRB_x have been translated $2mm$ towards the IFeH, this is:

$$\begin{aligned} FRB(x, y, z) &= (-0.033, -0.00514, 0.01) \\ FLB(x, y, z) &= (0.034, -0.004, 0.00978) \end{aligned} \tag{4.8}$$

Close step	Mesh	U_x	U_y	U_z	U
$2mm$	$IFeH_1$	$-2.107e^{-03}$	$-1.445e^{-03}$	$1.603e^{-03}$	$2.659e^{-03}$
	$IFeH_2$	$-2.105e^{-03}$	$-1.410e^{-03}$	$1.519e^{-03}$	$2.603e^{-03}$
	$IFeH_3$	$-2.363e^{-03}$	$-1.710e^{-03}$	$1.773e^{-03}$	$2.966e^{-03}$

Table 4.13: Nodal displacement in x axis (U_x in m), in y axis (U_y in m), in z axis (U_z in m) and nodal displacement magnitude (U in m) of the rotated fetal head in contact with forceps analysis when LB_C and RB_C performed a 2mm translation in the x axis towards the IFeH.

Figures 4.44, 4.45, 4.46 and 4.47 show the nodal displacement over the x, y and z axis (U_x, U_y and U_z) and nodal displacement magnitude (U) results respectively of the rotated fetal head in contact with forceps when forceps blades FLB_x and FRB_x have been translated $2mm$ towards the IFeH.

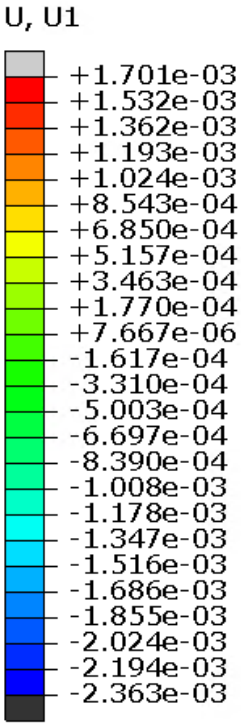

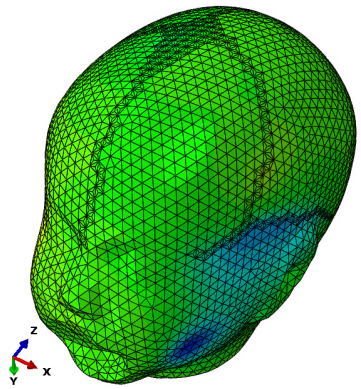

(a) $IFeH_1$ anterior left sagittal view.

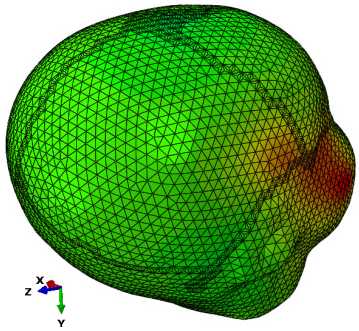

(b) $IFeH_1$ posterior right sagittal view.

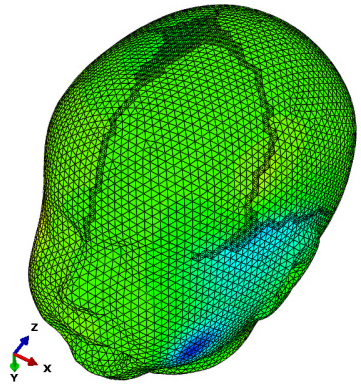

(c) $IFeH_2$ anterior left sagittal view.

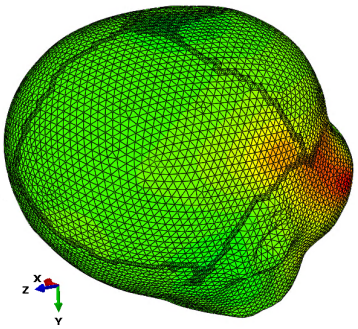

(d) $IFeH_2$ posterior right sagittal view.

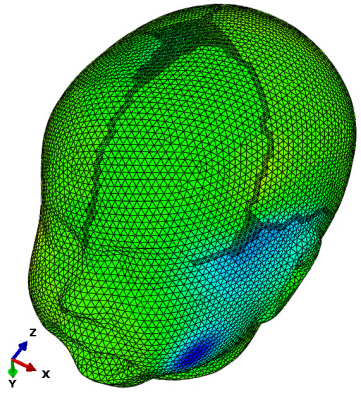

(e) $IFeH_3$ anterior left sagittal view.

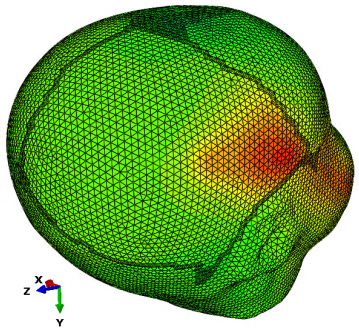

(f) $IFeH_3$ posterior right sagittal view.

Figure 4.44: Nodal displacement over the x axis (U_x) result in IFeH models when $FLB_x = FRB_x = 2$mm

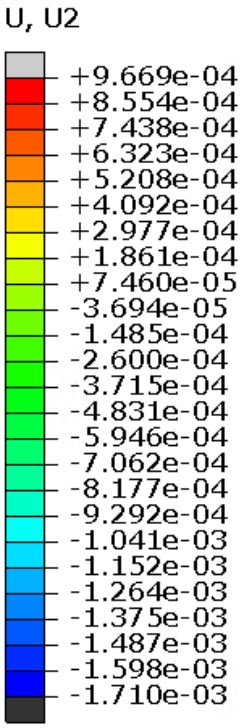

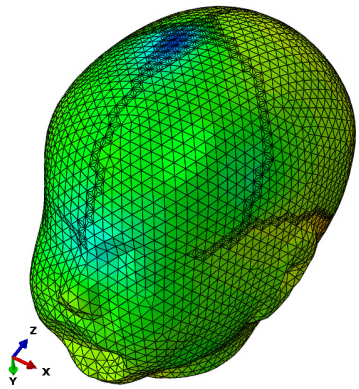

(a) $IFeH_1$ anterior left sagittal view.

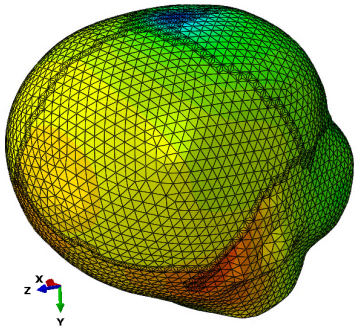

(b) $IFeH_1$ posterior right sagittal view.

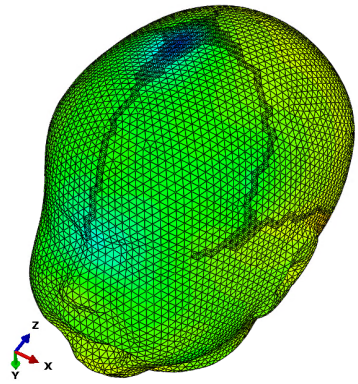

(c) $IFeH_2$ anterior left sagittal view.

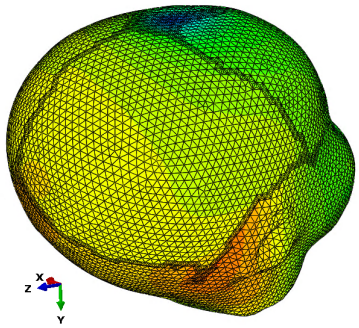

(d) $IFeH_2$ posterior right sagittal view.

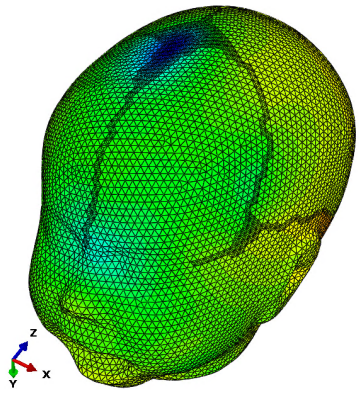

(e) $IFeH_3$ anterior left sagittal view.

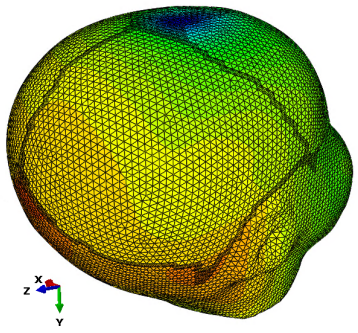

(f) $IFeH_3$ posterior right sagittal view.

Figure 4.45: Nodal displacement over the y axis (U_y) result in IFeH models when $FLB_x = FRB_x = 2$mm

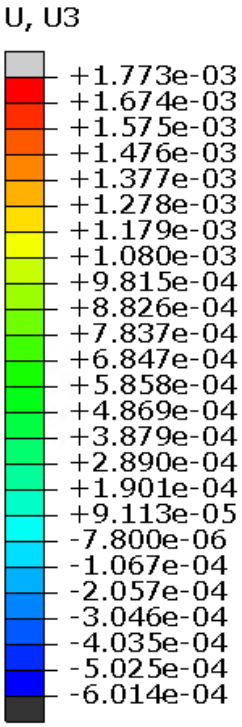

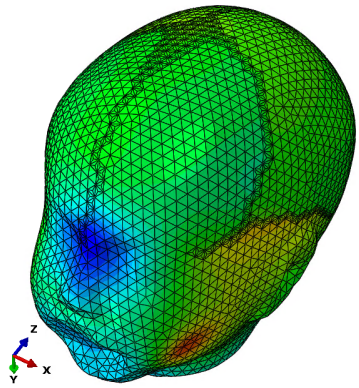

(a) $IFeH_1$ anterior left sagittal view.

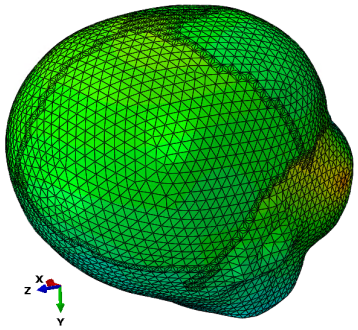

(b) $IFeH_1$ posterior right sagittal view.

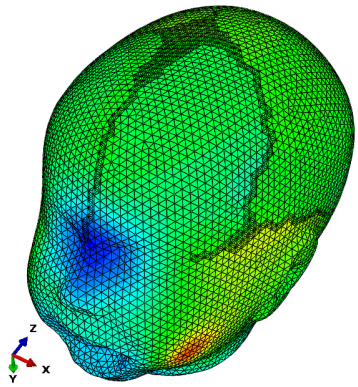

(c) $IFeH_2$ anterior left sagittal view.

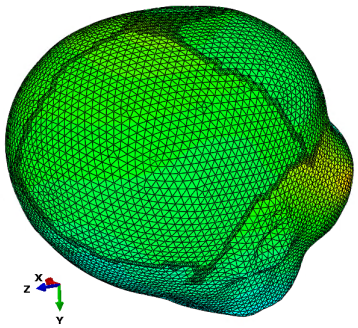

(d) $IFeH_2$ posterior right sagittal view.

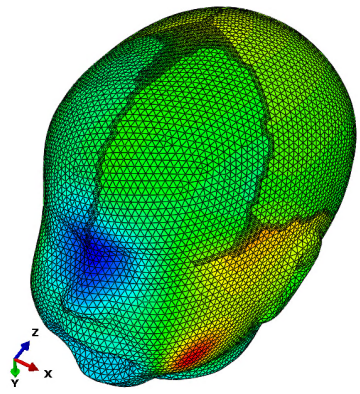

(e) $IFeH_3$ anterior left sagittal view.

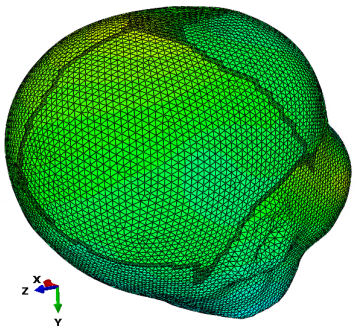

(f) $IFeH_3$ posterior right sagittal view.

Figure 4.46: Nodal displacement over the z axis (U_z) result in IFeH models when $FLB_x = FRB_x = 2$mm

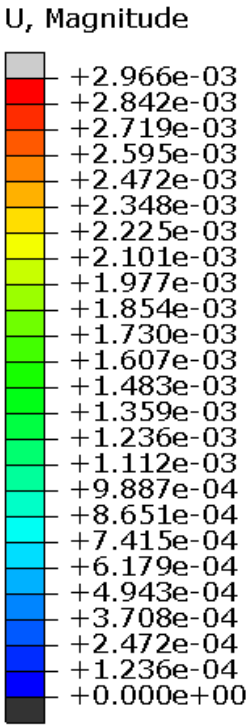

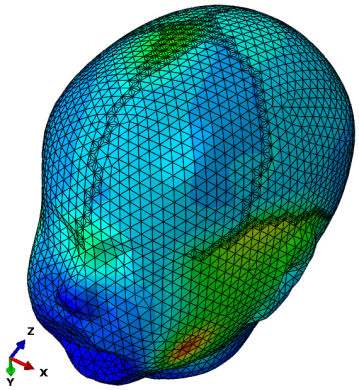

(a) $IFeH_1$ anterior left sagittal view.

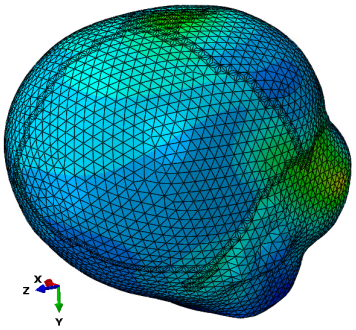

(b) $IFeH_1$ posterior right sagittal view.

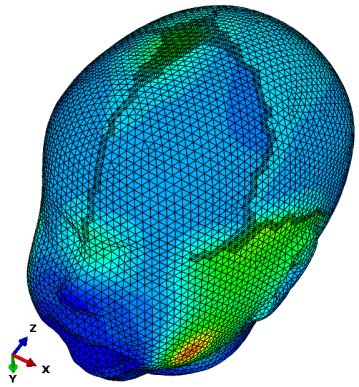

(c) $IFeH_2$ anterior left sagittal view.

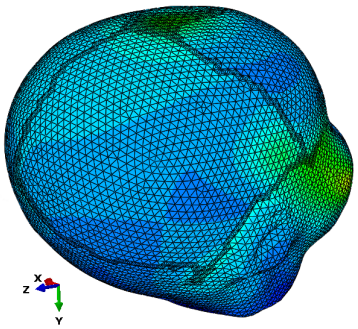

(d) $IFeH_2$ posterior right sagittal view.

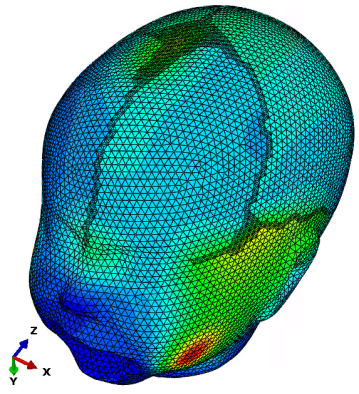

(e) $IFeH_3$ anterior left sagittal view.

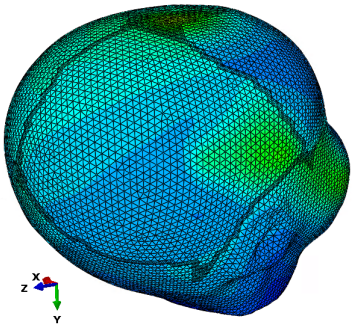

(f) $IFeH_3$ posterior right sagittal view.

Figure 4.47: Nodal displacement magnitude (U) result in IFeH models when $FLB_x = FRB_x = 2$mm

4.6.3 Discussion

- From Table 4.13 we observe:
  - With increasing mesh complexity both U_x and U_y are similar for the two coarser meshes but higher for the finest mesh.
  - The nodal displacement U_z and nodal displacement magnitude U decrease from $IFeH_1$ to $IFeH_2$, but increase again from $IFeH_2$ to $IFeH_3$.
- In Figure 4.44, we can see that $IFeH_1$ and $IFeH_2$ meshes underestimate the nodal displacement area U_x on the left and right side of the head between the temporal and mandible bones. It is clear in the posterior right sagittal view that the nodal displacement area in the temporal bone which value $\sim 1.7mm$ is bigger in $IFeH_3$ than the other two meshes.
- Is it observed in Figure 4.45 that $IFeH_1$ and $IFeH_2$ underestimated the nodal displacement area U_y in the anterior fontanelle (blue zone at the top of the head), where $IFeH_3$ shows a bigger concentration of the displacement with a value of $-1.710e^{-03}m$ compared to the coarsest meshes.
- In Figure 4.46, it is observed that the nodal displacement U_z is concentrated in the mandible bone having its maximum value in the $IFeH_3$ with a value of $1.773e^{-03}m$.
- It is observed in Figure 4.47, that the nodal displacement magnitude U was underestimated in the coarsest meshes, at the same time we can see similar nodal displacement patterns between the different meshes but the importance of mesh refinement becomes relevant as the finest mesh shows more accurate displacement areas with higher values, e.g. the area in the mandible bone in the $IFeH_3$ mesh has a nodal displacement magnitude of $\sim 2.9mm$ meanwhile the $IFeH_1$ mesh has a nodal displacement magnitude of $\sim 2.6mm$.

4.7 Forceps traction on rotated fetal head

The aim of this experiment is to simulate the obstetric forceps-rotated baby head behaviour when the **Pull Step** is performed (see Section 3.4.1.3).

4.7.1 Experimental setup

4.7.1.1 Models

Previous obstetric forceps and baby head models are considered in this experiment as they were specified in Sections 4.4.1.2 and 4.4.1.1 respectively.

4.7.1.2 Steps

This analysis assumes that the **Initial Step** and **Close Step** have already been performed (see Section 4.6.1.2), hence the displacement performed in the **Close Step** is considered (see Eq. 4.9).

Pull Step is described in Section 3.4.1.3.

$$\begin{aligned} FRB(x,y,z) &= (-0.033, -0.00514, 0.01) \\ FLB(x,y,z) &= (0.034, -0.004, 0.00978) \\ IFeH(x,y,z) &= (0.00183, -0.005, 0.0212) \end{aligned} \tag{4.9}$$

4.7.1.3 Interactions

The interactions between the obstetric forceps and improved fetal head described in Section 4.4.1.4 are considered in this experiment as well.

4.7.1.4 Loads

Similar to previous experiments, this experiment does not apply explicit loads over the obstetric forceps blades, instead a constant velocity boundary condition is applied to move them. This approach allows to control the amount of displacement to perform over the blades.

4.7.1.5 BCs

The BCs applied in this step (see Table 4.14), consider the same node sets specified in the previous step (see Section 4.6.1.5).

Set	**Pull Step**
LB_C	Allows translation in z axis
LB_C	Constant velocity on x axis at $1mm/0.2s$
RB_C	Allows translation in z axis
RB_C	Constant velocity on x axis at $1mm/0.2s$
IFeHC	Propagated

Table 4.14: BCs applied to the set of nodes in the **Pull** step in the forceps traction on rotated fetal head analysis.

4.7.2 Experimental results

This section outlines the results obtained in the current forceps traction on rotated fetal head experiment.

Table 4.15 shows the nodal displacement over the x axis (U_x) and the nodal displacement magnitude (U), for every fetal head mesh when both FLB_z and FRB_z have been translated $2mm$ in the z axis after the **Close Step** of $2mm$ has been performed (see Eq. 4.10).

$$\begin{aligned} FRB(x,y,z) &= (-0.033, -0.00514, 0.012) \\ FLB(x,y,z) &= (0.034, -0.004, 0.01178) \end{aligned} \tag{4.10}$$

Close step	Pull step	Mesh	U_x	U_y	U_z	U	CPU time
$2mm$	$2mm$	$IFeH_1$	$-2.755e^{-03}$	$-1.764e^{-03}$	$2.301e^{-03}$	$3.708e^{-03}$	$3.1e^{+04}$
		$IFeH_2$	$-2.784e^{-03}$	$-1.731e^{-03}$	$2.201e^{-03}$	$3.577e^{-03}$	$1.3e^{+05}$
		$IFeH_3$	$-3.043e^{-03}$	$-1.935e^{-03}$	$2.505e^{-03}$	$3.965e^{-03}$	$2.7e^{+05}$

Table 4.15: Nodal displacement over the x axis (U_x in m), the y axis (U_y in m), the z axis (U_z in m) and nodal displacement magnitude (U in m) of the forceps traction on rotated fetal head analysis when LB_C and RB_C performed a 2mm translation in the z axis over the IFeH. CPU time is in seconds on an Intel(R) Core(TM) i9-14900K, 3.20 GHz CPU with 96 GB RAM.

Figures 4.48, 4.49, 4.50 and 4.51 show the nodal displacement in x, y and z axis and nodal displacement magnitude (U) results respectively of the forceps traction on rotated fetal head when FLB_x and FRB_x have been translated $2mm$ towards the IFeH and FLB_z and FRB_z have been translated $2mm$ in the z axis.

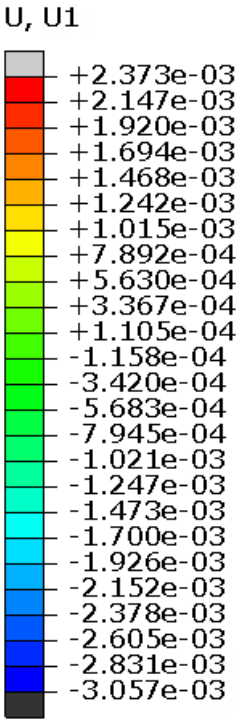

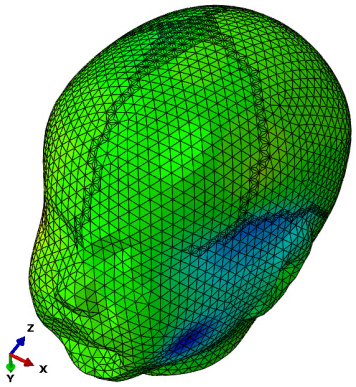

(a) $IFeH_1$ anterior left sagittal view.

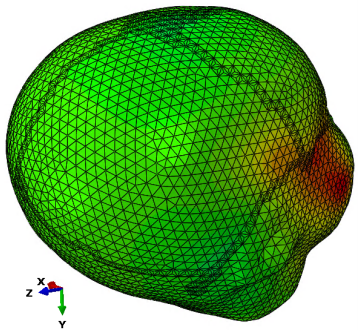

(b) $IFeH_1$ posterior right sagittal view.

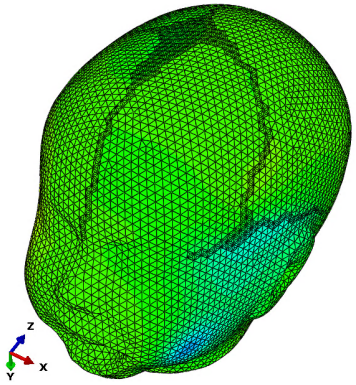

(c) $IFeH_2$ anterior left sagittal view.

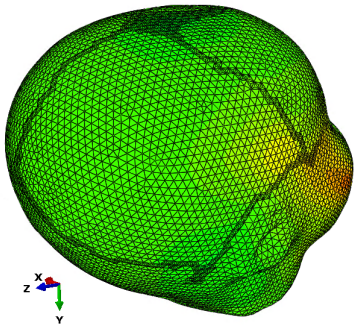

(d) $IFeH_2$ posterior right sagittal view.

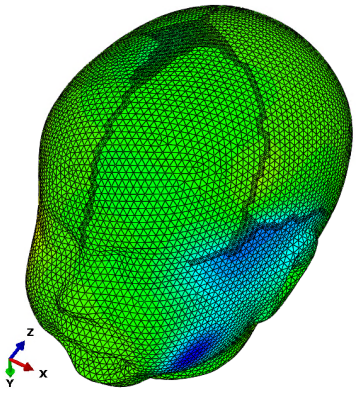

(e) $IFeH_3$ anterior left sagittal view.

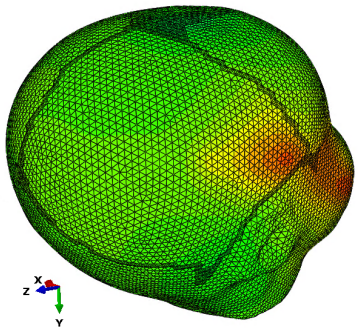

(f) $IFeH_3$ posterior right sagittal view.

Figure 4.48: Nodal displacement over the x axis (U_x) result in IFeH models when $FLB_x = FRB_x = 2\text{mm}$ and $FLB_z = FRB_z = 2\text{mm}$

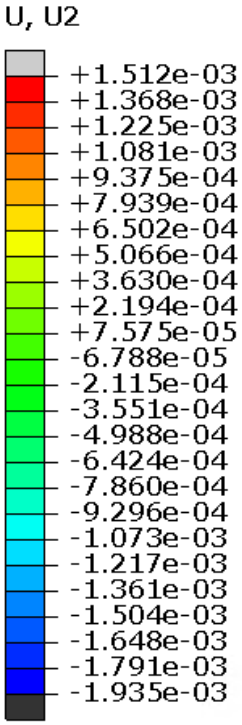

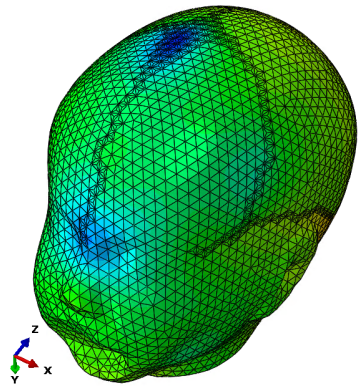

(a) $IFeH_1$ anterior left sagittal view.

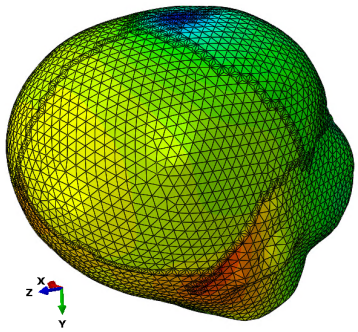

(b) $IFeH_1$ posterior right sagittal view.

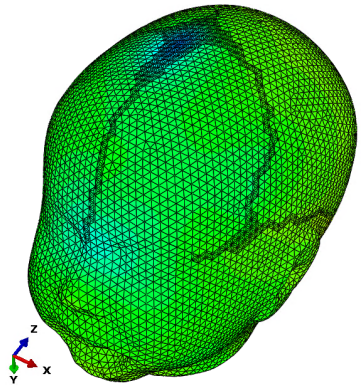

(c) $IFeH_2$ anterior left sagittal view.

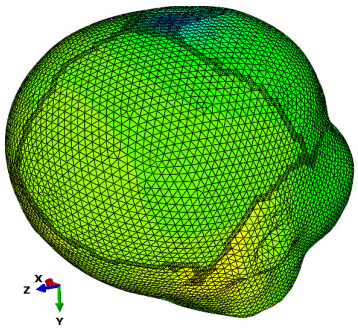

(d) $IFeH_2$ posterior right sagittal view.

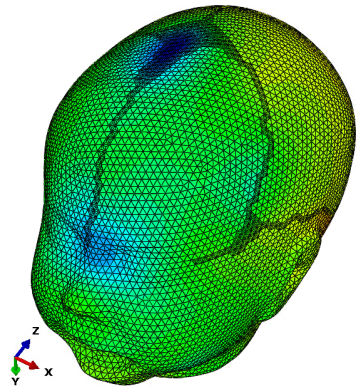

(e) $IFeH_3$ anterior left sagittal view.

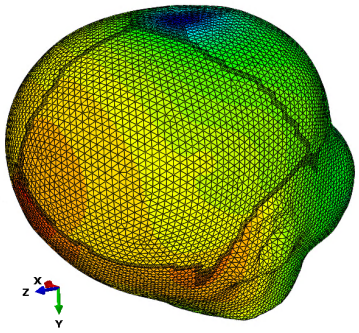

(f) $IFeH_3$ posterior right sagittal view.

Figure 4.49: Nodal displacement over the y axis (U_y) result in IFeH models when $FLB_x = FRB_x = 2\text{mm}$ and $FLB_z = FRB_z = 2\text{mm}$

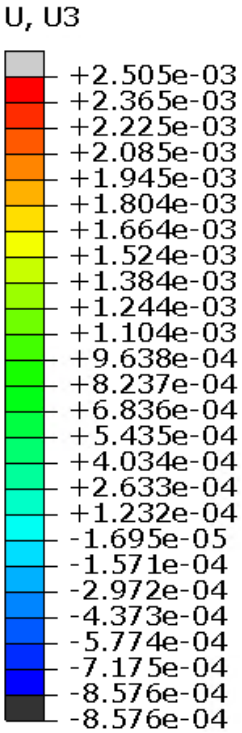

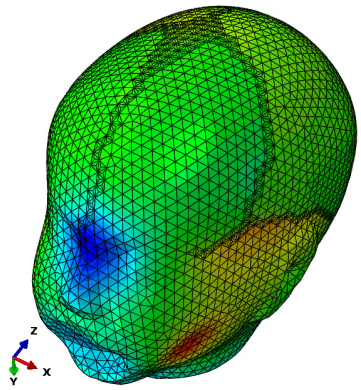

(a) $IFeH_1$ anterior left sagittal view.

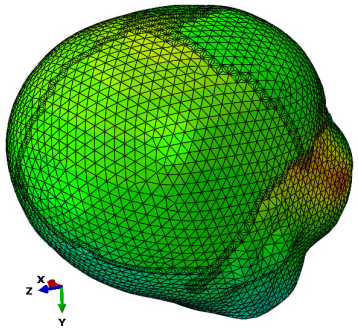

(b) $IFeH_1$ posterior right sagittal view.

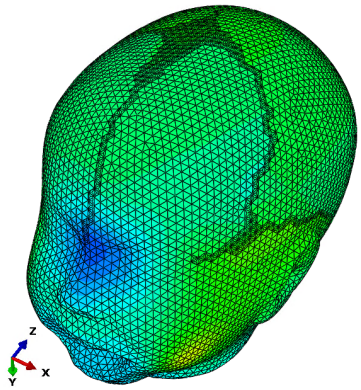

(c) $IFeH_2$ anterior left sagittal view.

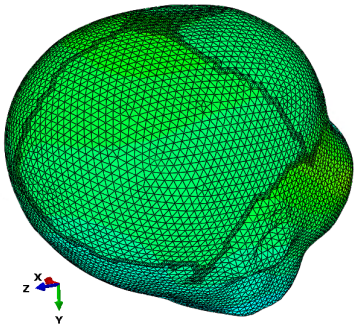

(d) $IFeH_2$ posterior right sagittal view.

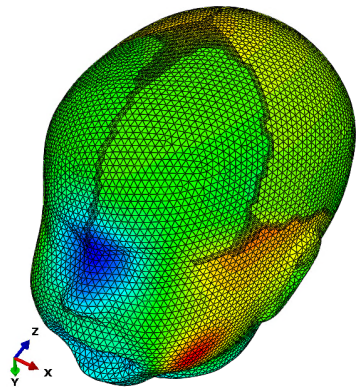

(e) $IFeH_3$ anterior left sagittal view.

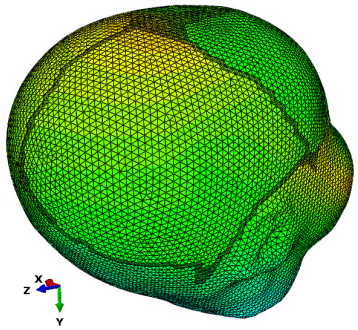

(f) $IFeH_3$ posterior right sagittal view.

Figure 4.50: Nodal displacement over the z axis (U_z) result in IFeH models when $FLB_x = FRB_x = 2\text{mm}$ and $FLB_z = FRB_z = 2\text{mm}$

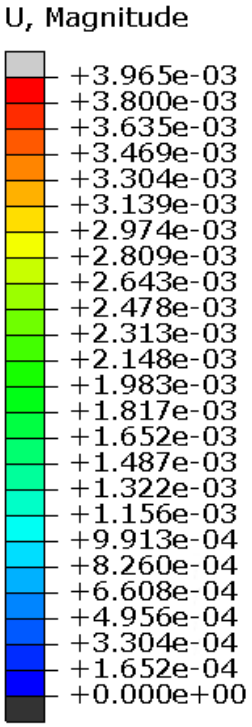

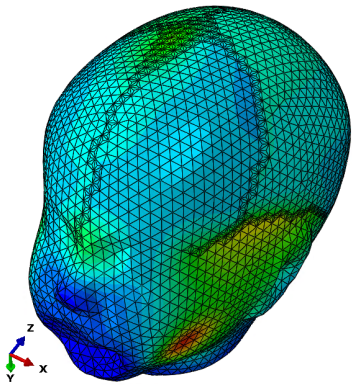

(a) $IFeH_1$ anterior left sagittal view.

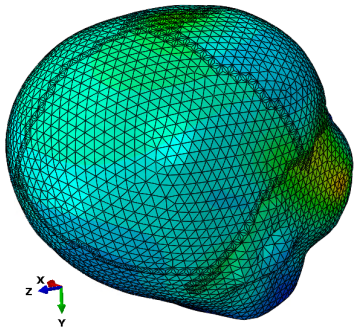

(b) $IFeH_1$ posterior right sagittal view.

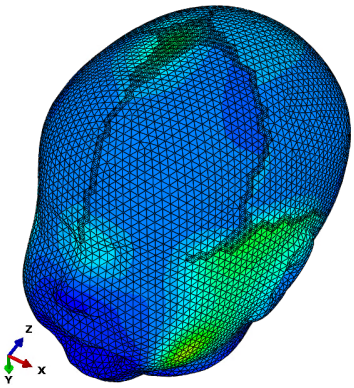

(c) $IFeH_2$ anterior left sagittal view.

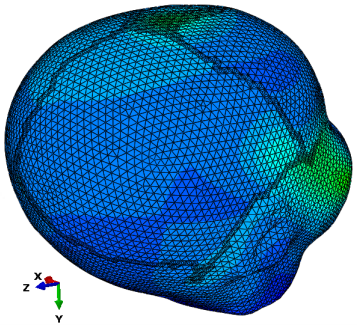

(d) $IFeH_2$ posterior right sagittal view.

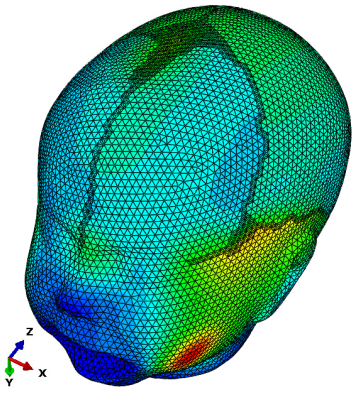

(e) $IFeH_3$ anterior left sagittal view.

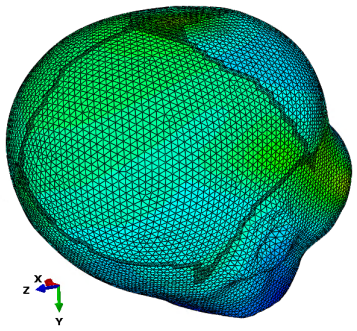

(f) $IFeH_3$ posterior right sagittal view.

Figure 4.51: Nodal displacement magnitude (U) result in IFeH models when $FLB_x = FRB_x = 2\text{mm}$ and $FLB_z = FRB_z = 2\text{mm}$

The maximum values of the vom Mises stress (S) and Shear stress ($S12$) for every fetal head when FLB_x and FRB_x have been translated $2mm$ in the z axis after the **Close Step** of $2mm$ have been performed, are shown in the next Table:

Close step	Pull step	Mesh	S	$S12$
$2mm$	$2mm$	$IFeH_1$	$1.853e^{+08}$	$8.044e^{+07}$
		$IFeH_2$	$2.715e^{+08}$	$8.299e^{+07}$
		$IFeH_3$	$2.792e^{+08}$	$9.096e^{+07}$

Table 4.16: Maximum values of von Mises stress (S in N/m^2) and Shear stress ($S12$ in N/m^2) of forceps traction on rotated fetal head analysis when LB_C and RB_C performed a 2mm translation in the z axis after the close step was performed for 2mm in the x axis.

Figures 4.52 and 4.53 show the von Mises stress (S in N/m^2) and Shear stress ($S12$ in N/m^2) results of the forceps traction on rotated fetal head when FLB_x and FRB_x have been translated $2mm$ towards the IFeH and FLB_z and FRB_z have been translated $2mm$ in the z axis.

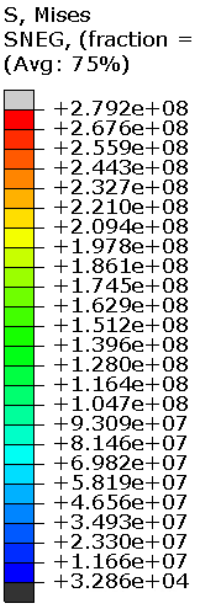

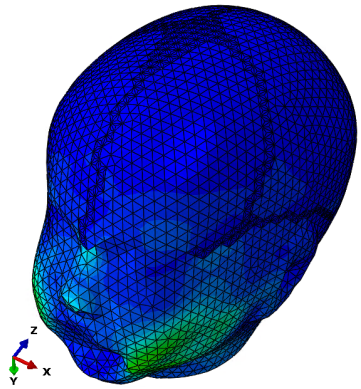

(a) $IFeH_1$ anterior left sagittal view.

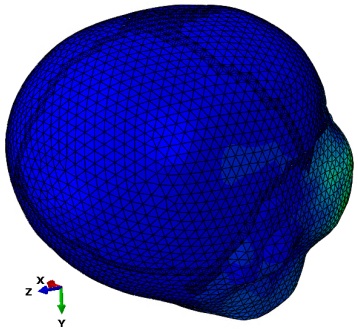

(b) $IFeH_1$ posterior right sagittal view.

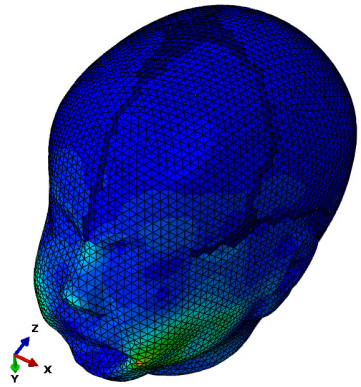

(c) $IFeH_2$ anterior left sagittal view.

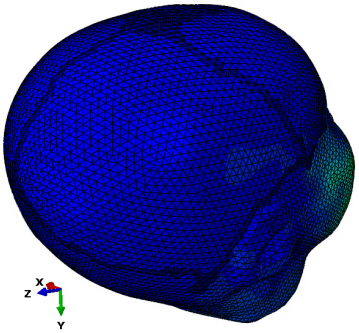

(d) $IFeH_2$ posterior right sagittal view.

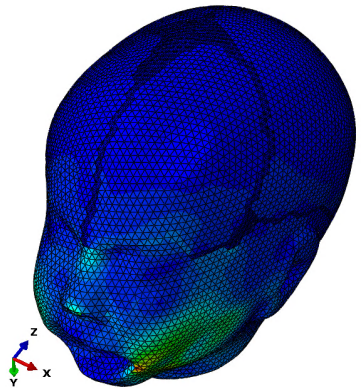

(e) $IFeH_3$ anterior left sagittal view.

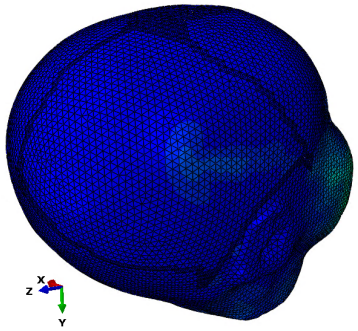

(f) $IFeH_3$ posterior right sagittal view.

Figure 4.52: Nodal stress (S) result in IFeH models when $FLB_x = FRB_x = 2$mm and $FLB_z = FRB_z = 2$mm

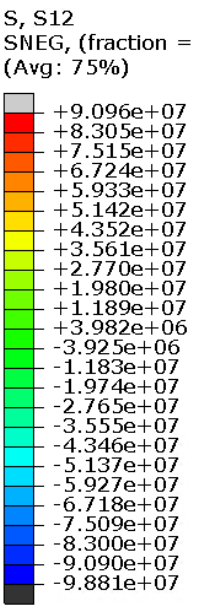

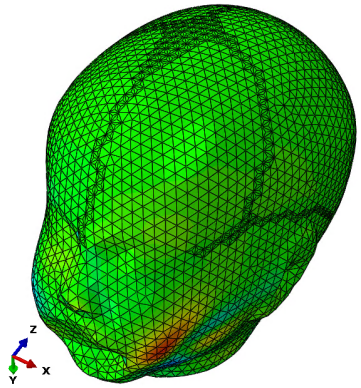

(a) $IFeH_1$ anterior left sagittal view.

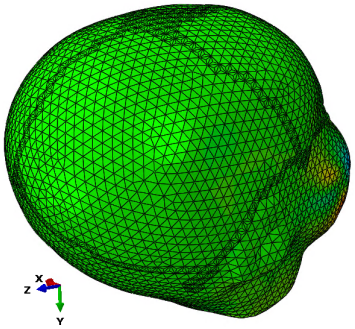

(b) $IFeH_1$ posterior right sagittal view.

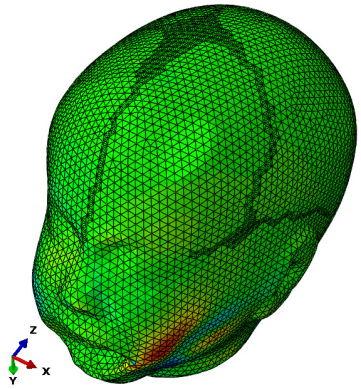

(c) $IFeH_2$ anterior left sagittal view.

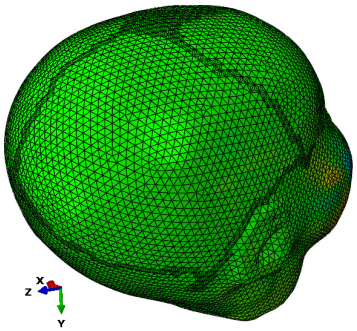

(d) $IFeH_2$ posterior right sagittal view.

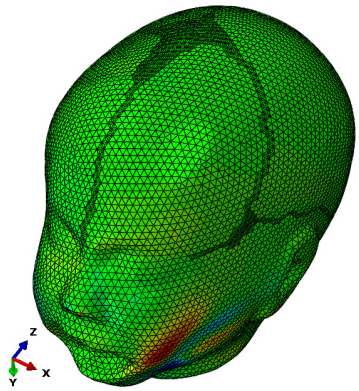

(e) $IFeH_3$ anterior left sagittal view.

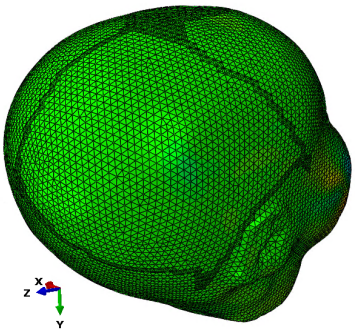

(f) $IFeH_3$ posterior right sagittal view.

Figure 4.53: Shear stress ($S12$) result in IFeH models when $FLB_x = FRB_x = 2$mm and $FLB_z = FRB_z = 2$mm

4.7.3 Discussion

- From Table 4.15 we observe:
  - U_x displacements marginally increase by increasing mesh complexity from $IFeH_1$ to $IFeH_2$, but it is seem a higher change from $IFeH_2$ to $IFeH_3$.
  - Nodal displacement in the y axis U_y increases by increasing mesh complexity, although it is observed a drop in the displacement from $IFeH_1$ to $IFeH_2$, but an increment from $IFeH_2$ to $IFeH_3$.
  - Nodal displacement in the z axis U_z has a similar behaviour as U_y.
  - Nodal displacement magnitude U follows the same behaviour as U_y and U_z, where the nodal displacement magnitude increases by increasing mesh complexity.
- It is observed in Figure 4.48 that the nodal displacement in the x axis U_x in both sides of the $IFeH$ is better captured in $IFeH_3$ mesh, showing a bigger and more accurate area of displacement. $IFeH_1$ and $IFeH_2$ meshes show an underestimated and smaller area of the nodal displacement between the temporal bone and mandible bone, where the maximum displacement were $-2.755e^{-03}m$ and $-2.784e^{-03}m$ respectively compared to $IFeH_3$ with a value of $-3.043e^{-03}m$.
- The nodal displacement in the y axis U_y can be seen in Figure 4.49, where the coarsest meshes underestimate the displacement in the anterior fontanelle, posterior fontanelle, and the region behind the ears. The maximum displacement presented in $IFeH_3$ with a value of $-1.935e^{-03}m$ is marginal compared to $IFeH_1$ with a value of $-1.764e^{-03}m$ and a difference of $0.171mm$ and $IFeH_2$ with a maximum displacement of $-1.731e^{-03}$ and a difference of $0.203mm$, both differences respect to the finest mesh.
- It is observed that the displacement in the z axis U_z shown in Figure 4.50, follows a similar behaviour as the displacements in the other two axes, where the regions of displacements are underestimated in the anterior fontanelle and the region between the temporal bone and the mandible bone. The maximum displacement presented in $IFeH_3$ with a value of $2.505e^{-03}m$ is marginal compared to $IFeH_1$ with a value of $2.301e^{-03}m$ and a difference of $0.203mm$ and $IFeH_2$ with a value of $2.201e^{-03}m$ and a difference of $0.303mm$, both differences respect to the finest mesh.
- Figure 4.51 shows the nodal displacement magnitude U for every fetal head model. Here it is observed that the coarsest meshes underestimated the nodal displacement magnitude compared to the finest mesh $IFeH_3$. The maximum displacement of $IFeH_1$ is $3.708e^{-03}m$ and $IFeH_2$ is $3.577e^{-03}m$ compared to the displacement presented in $IFeH_3$ of $3.965e^{-03}m$. A second observation shows that the displacement regions change between models, being the finest mesh the most accurate of them.
- From Table 4.16, we observe that both the von Mises stress S and the Shear stress $S12$ increase by increasing the mesh complexity.
- It is observed in Figure 4.52, that the von Mises stress regions in the different $IFeH$ models, increase when the mesh complexity is increased. The coarsest meshes underestimated the fetal head deformation, e.g. $IFeH_1$ presented a maximum stress value

of $1.853e^{+08}N/m^2$, $IFeH_2$ a value of $2.715e^{+08}N/m^2$ and the finest mesh $IFeH_3$ a value of $2.792e^{+08}N/m^2$, where the highest stress in presented in the area on the mandible bone.

- Figure 4.53 shows the Shear stress $S12$ for every $IFeH$ model. The stress regions follow a similar behaviour as the Von Mises Stress, where the Shear stress in underestimated in the coarsest meshes, although it is observed that the stress regions are not far different between the coarsest meshes $IFeH_1$ with a stress value of $8.044e^{+07}N/m^2$, $IFeH_2$ with a value of $8.299e^{+07}N/m^2$ and the finest mesh $IFeH_3$ with a value of $9.096e^{+07}N/m^2$.

4.8 Comparing not rotated and rotated forceps application

This section compares the results of the forceps effect on the fetal head when performing a symmetric and an asymmetric forceps placement over the finer mesh ($IFeH_3$), when both FLB_x and FRB_x have been translated $2mm$ towards the IFeH and FLB_z and FRB_z have been translated $2mm$ in the z axis.

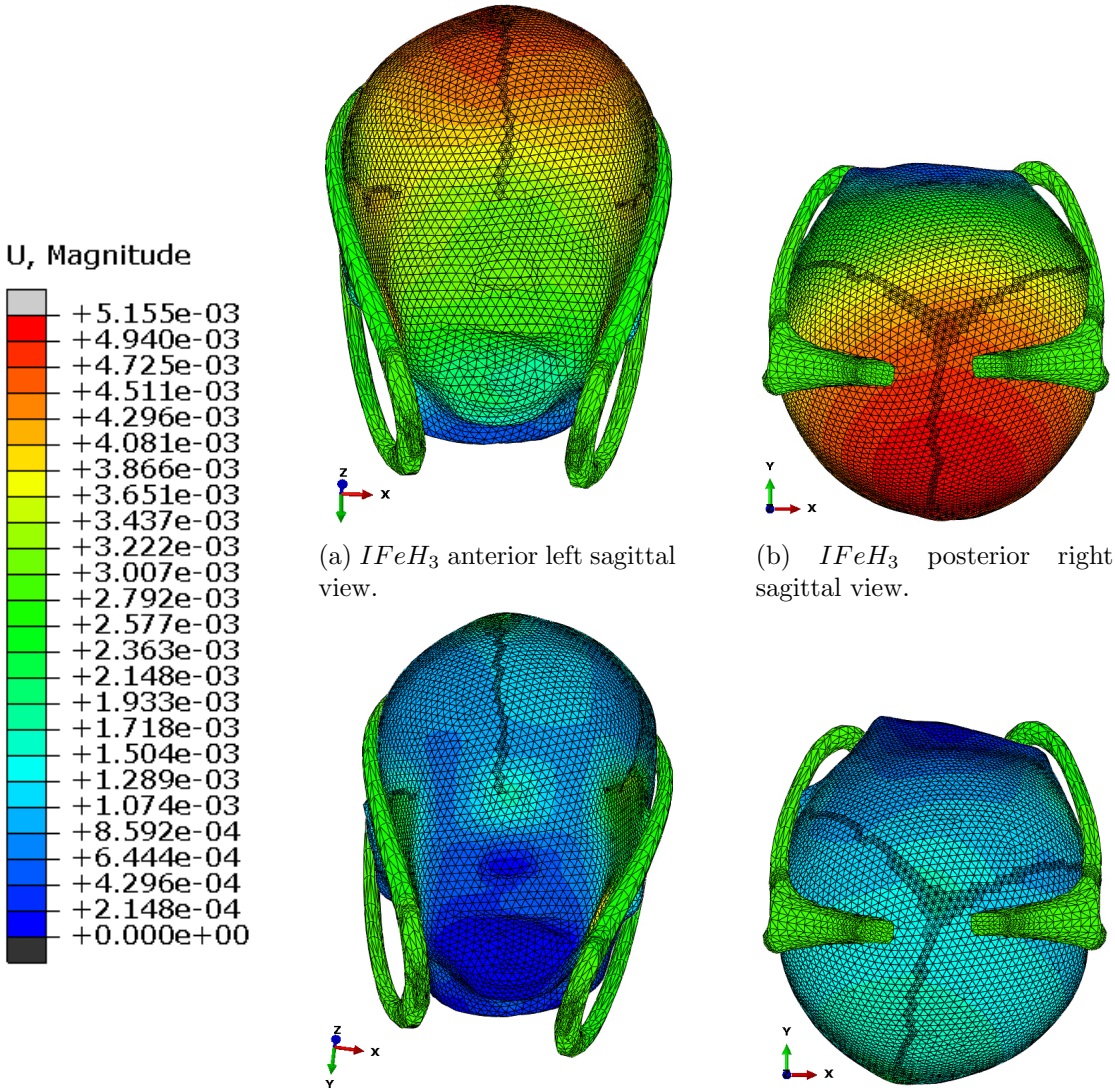

(a) $IFeH_3$ anterior left sagittal view.

(b) $IFeH_3$ posterior right sagittal view.

(c) $IFeH_3$ anterior left sagittal view.

(d) $IFeH_3$ posterior right sagittal view.

Figure 4.54: Comparing nodal displacement magnitude (U in m) for symmetric (top) and asymmetric (bottom) placements respectively.

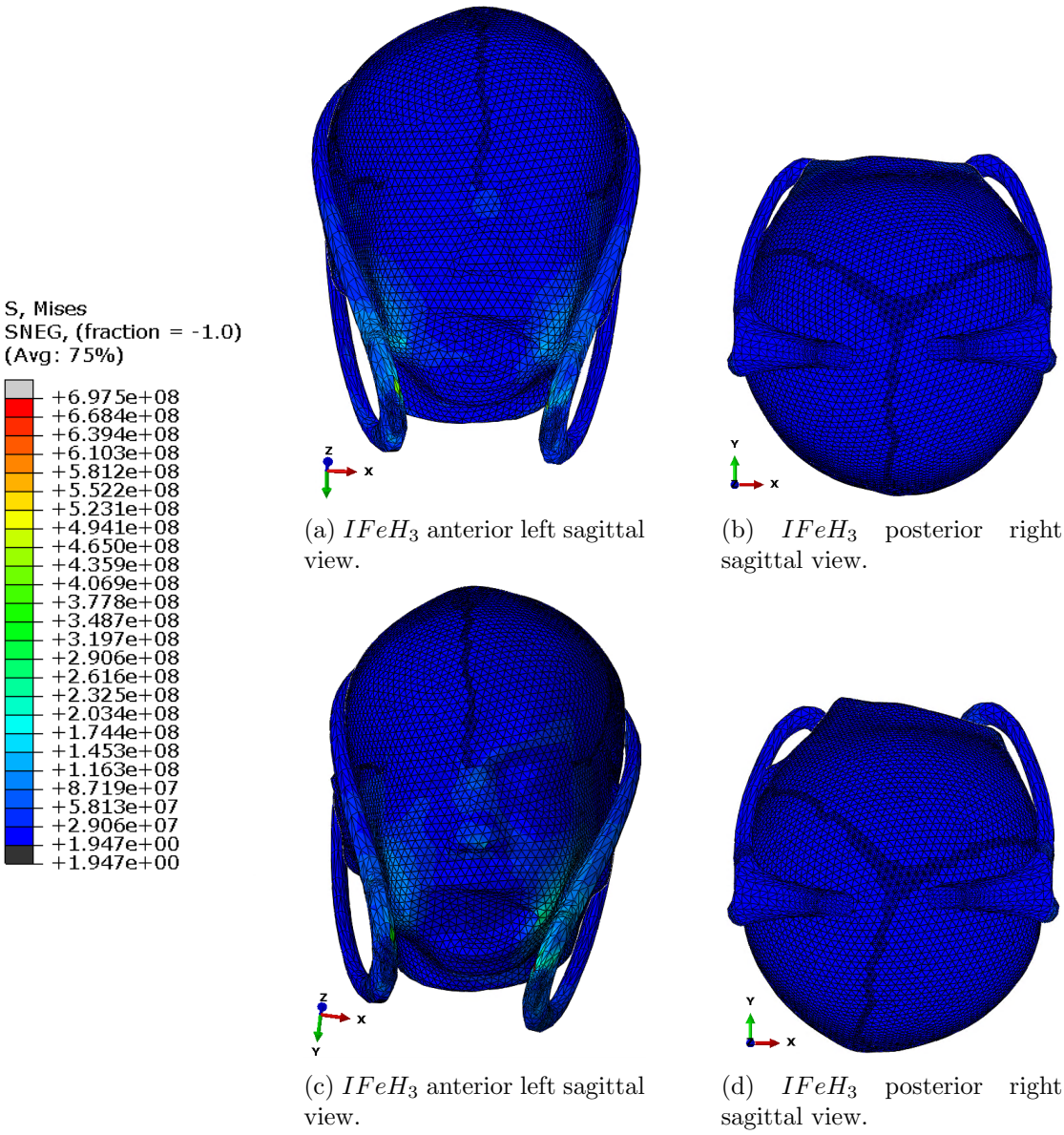

(a) $IFeH_3$ anterior left sagittal view.

(b) $IFeH_3$ posterior right sagittal view.

(c) $IFeH_3$ anterior left sagittal view.

(d) $IFeH_3$ posterior right sagittal view.

Figure 4.55: Comparing von Mises stress (S in N/m^2) for symmetric (top) and asymmetric (bottom) placements respectively.

Figure 4.54 shows the overall nodal displacement fields (scaled by magnification factor 2.0) for the symmetric (non rotated) and symmetric (rotated) forceps placements respectively.

It is clear that the nodal displacement concentrated at the top region of the head (anterior fontanelle) is higher for the symmetric placement ($\sim 5mm$), due to better contact between the forceps blades and the fetal head compared to the asymmetric placement ($\sim 3.9mm$).

However, the contact area between the blade and the fetal head is bigger in the asymmetric placement.

Figure 4.55 shows the von Mises stress (S) for the same configurations. The stresses are generally low across the fetal scalp but high in the contact regions. In this Figure, it is clearer that the area affected by the stress in both sides of the fetal face is bigger in the asymmetric placement.

The stress performed over the mandible bone in the right side of the image in the asymmetric placement is higher ($\sim 2.8e^{+08}\ N/m^2$) compared to the stress performed in the same region in the symmetric placement ($\sim 2.0e^{+08}\ N/m^2$)

Finally, CPU processing times for the more complex asymmetric analysis increase with mesh complexity from $3.1e^{+04}$ seconds to $2.7e^{+05}$ seconds (see Table 4.15).

Chapter 5

Conclusion

The aim of this research was to contribute to a better understanding of the compression and traction effect of the obstetric forceps placement on the fetal head, where the application and traction stages of the forceps procedure were analyzed.

This work improves on the work done by Audinis [62] by replacing the Static Finite Element Analysis (SFEA) with a Dynamic Finite Element Analysis (DFEA). Also by providing a more realistic fetal head model (which shape is closer to a real fetal head) and a smooth model of the obstetric forceps, a quasi-static analysis with contact constraints could be performed. The closing and traction of the forceps were then simulated to resemble a real forceps application.

To assess the importance of various experimental parameters we conducted experiments with simplified models first, by replacing the fetal head with a sphere and the forceps with curved plates. We added synthetic anterior and later, posterior fontanelles to the sphere. The closing and tractions steps were performed at constant velocities which allowed us:

- To assess the importance of mesh refinement
- To assess the ABAQUS general contact procedure used to simulate the contact constraints between sphere/plates (head/forceps). All experiments used a constant velocity Boundary Condition to move the plates/forceps instead of explicit loads as it is commonly used.

All these experiments were successful, i.e. showing more accuracy for finer models, realistic contact interaction and realistic "bulging" of the anterior and posterior fontanelles in agreement with intracranial volume conservation.

Based on these findings we then performed experiments on a realistic fetal head model and models of a real Neville-Barnes forceps. We compared a symmetric (non-rotated or "correct") forceps placement against an asymmetric placement caused by an incomplete internal rotation (by 10 degrees). As before, the importance of mesh refinement was shown. More importantly, the asymmetric placement showed distinctly larger nodal displacements near the temporal bone, i.e. the near the forceps to head contact area. This is a phenomenon that is observed in real scenarios [57].

5.1 Future work

5.1.1 Motion approximation

In a real OVD scenario where the Obstetric Forceps is used, the procedure involves placing the forceps blades one by one (right blade then lock in left), close them around the fetal head, pull and then scoop to help the fetus out of the birth canal. Due to the complexity of this procedure, this research is focused only in the simulation of the close and pull stages.

The velocity at which the obstetricians perform the procedure regardless of the amount of force required, is intermittent but smooth and gentle. We have resorted to a constant velocity based approach due to the difficulty of estimating the relatively low net forces on the fetal scalp despite the traction force being relatively high but largely reduced by the resistance of soft tissues. The only way to successfully use standard dynamic analysis with forces requires all maternal soft tissues, i.e. pelvic floor muscles and bony pelvis to be included, at cost of significantly increased complexity.

5.1.2 Soft tissues consideration

The fetal head structure is a compound of different layers of different materials where each of them has a specific purpose.

In the work of Audinis in 2017 [62], he described that considering soft tissues in the analysis of the fetal head moulding as a consequence of the placement of the forceps on the fetal skull would not alter the results. For a static analysis this is correct, but not for a dynamic analysis, as the latter depends on friction and damping from the contact interaction between the obstetric forceps blades and the fetal head, as well as the absence of pelvic floor muscles (as outlined in the previous section).

Soft tissues such as skin provide an extra layer of protection, from an engineering and mechanical point of view, it also adds strength to the structure of the fetal head when encased in it. Although it was discarded in this work, it could affect the final results.

Since the skin is a loose thus allowing movement, it could be affected by the obstetric forceps motions which is an area of research in itself. Indeed, skin lacerations are quite common following asymmetrical (incorrectly) application of the forceps blades.

As it was described in the experiments chapter, the obstetric forceps blades position over the baby head and the baby head position, play an important role to determine the way in which the mesh nodes are displaced. From a mechanical and anatomical point of view, it affects the way the head bones are moving, e.i. closing the obstetric forceps in a lower position would have a different outcome compare to closing the forceps is a higher position.

The importance of the insertion of the blades matters.

5.1.3 Fetal head model improvement

Although a 3D model of the fetal head was used in this research making a better approximation of the space occupied by the fetal head within the obstetrics forceps blades and the interaction between them, the representation of internal structures of the fetal head like the skull and brain represent a challenge.

In this research, a fetal skull with fontanelles and sutures was initially considered, but then discarded and replaced by a fetal head model that had more realistic compliance with the obstetric forceps blades. A fetal skull model has a better definition of bones, sutures and fontanelles but the interaction with obstetric forceps is less realistic due to the lack of soft tissues around it. Our current fetal head model considered a projection of bones, sutures and fontanelles from the fetal skull which can be considered less ideal but works better to demonstrate the interaction it has with the obstetric forceps.

A better model of the baby head would include a fair representation of the fetal skull with bones, fontanelles and sutures definitions inside the baby head. This way the fetal head interaction with forceps would be preserved and additionally the indirect interaction with the skull and forceps will be present as well.

5.1.4 Blades position

The interaction between the fetal head and obstetric forceps blades is highly dependant of blades position respect the head, i.e. considering the blades being at each side of the fetal head, if they are moved slightly up or down, the effect on the baby head and fontanelles change in terms of nodal displacement.

Simulating these cases can support the fact that the correct blades placement impact directly the fetal head bony structure, and show which positions affect more or less the fetal head.

Since the simulation of the birth canal is out of the scope of this research, it was noticed that if there is a slightly incorrect forceps placement on the baby head, during the close and pull step it is visible how the baby head slides towards the center of the forceps or performs rotations with respect to the neck area which is the point attached to the body. This is assumed to happen because the head is fitting according to the space between the forceps blades, without considering the birth canal. If the birth canal is considered and the baby head is already touching its walls this behaviour can be minimized due to the almost non existent space between the baby head and the birth canal.

Appendix A

Anatomy of Maternal Pelvis

From a general point of view, the pelvis supports the upper body and enables movement in an upright posture, at the same time that it transmits and distributes the weight to the lower limbs. On the other side, from a female point of view, it also works as a protective bony structure for the reproductive organs, bladder and rectum [17].

During pregnancy, the female pelvis suffers a series of subtle changes in its composition, shape, plane of inclination and dimensions, these changes help the female skeleton to support the fetus weight through out of all the pregnancy process and childbirth.

The maternal pelvis consists of four pelvic bones [17, 4, 14]:

- **Sacrum:** It consists of five fused vertebrae and is concave in its anterior surface. It articulates at its upper segment with the ilium, at its lower segment with the coccyx, and laterally with the sacrospinous and sacrotuberous ligaments.
- **Coccyx:** Triangular-shaped bone composed of three to five vertebrae. It articulates with the lower end of the sacrum, where a joint is formed or in some cases the bones are fused with no joint.
- **Two innominates:** These bones are composed of three regions:
  - **Ilium:** It is the upper part of the innominate bone and articulates with the sacrum.
  - **Ischium:** It is an L-shaped bone which connects to the ilium posteriorly and to the pubis anteriorly.
  - **Pubis:** It has two arms called *rami* and it forms the anterior portion of the pelvis.

Figure A.1, shows the maternal pelvis bones, and their position respect of each other.

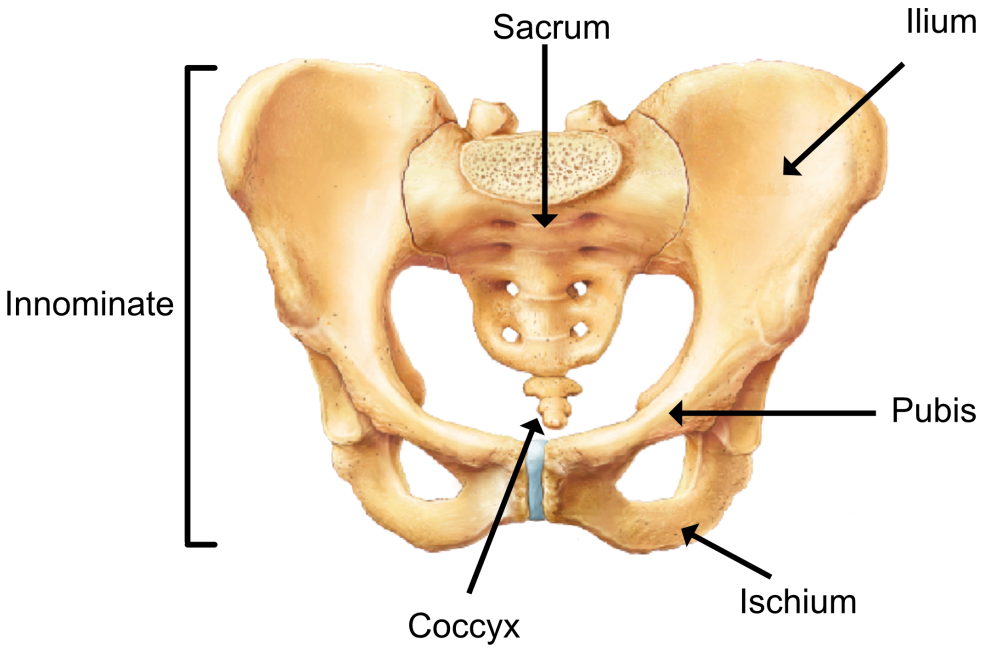

Figure A.1: Anteroposterior view of the maternal pelvis bones (modified from [5]).

The pelvis, is a three-dimensional structure that has to be large enough to allow the fetus head to go through the **pelvis brim**, which is a continuous oval ridge that runs from the pubic crest anteriorly, the line of the innominate bone laterally and the sacral promontory posteriorly (see Figure A.2).

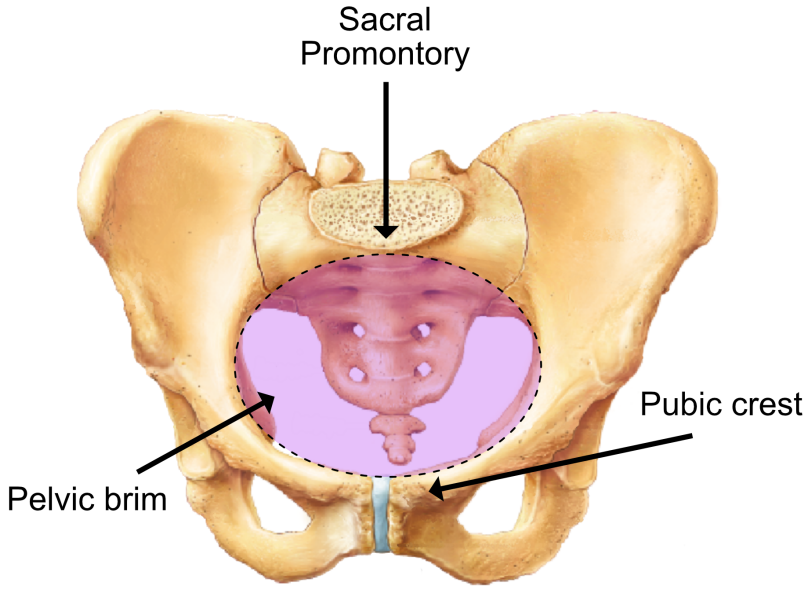

Figure A.2: Anteroposterior view of the pelvic brim (modified from [5]).

The pelvis is dived in two regions:

- **False pelvis:** Its function is to support the pregnant uterus. It is located above the pelvic brim, limited by the lumbar vertebrae posteriorly, the iliac fosa bilaterally and the abdomen wall anteriorly.
- **True pelvis:** It is the inferior region to the pelvic brim, surrounded by the sacrum and coccyx posteriorly and the ischuim bilaterally and pubis anteriorly.

Figure A.3, shows the regions that belongs to the false and true pelves. The false pelvis is highlighted in light red and the true pelvis in light blue.

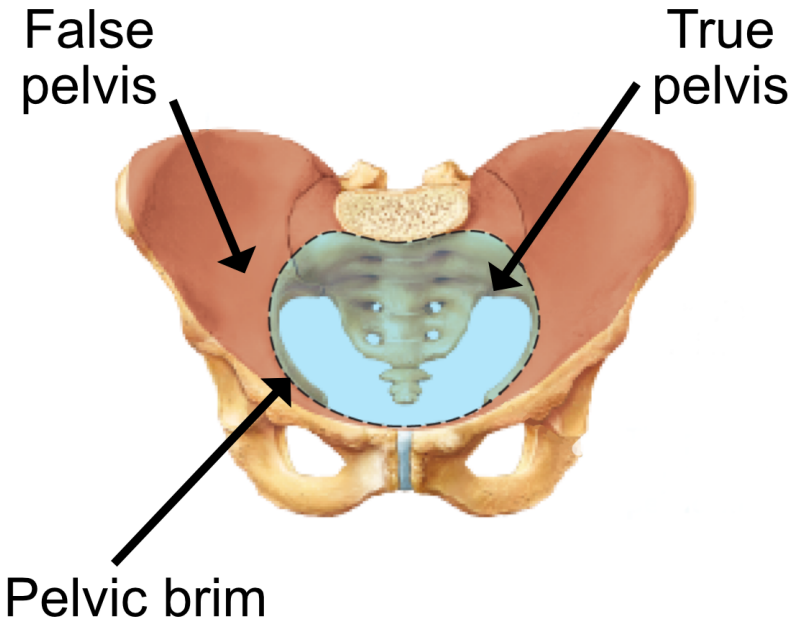

Figure A.3: Anteroposterior view of the false and true pelves (modified from [5]).

A.1 Pelvic measurements

The most significant part of the maternal pelvis is the *true pelvis*, through which the fetal head negotiates passage. This bony structure create a passage that is divided in three regions, inlet, cavity and outlet.

Figure A.4, shows the different regions in the true pelvis; inlet is the cavity upper limit, cavity region highlighted in light purple, outlet is the lower limit of the cavity.

When there is a cephalic presentation, as the fetus head is descending from the inlet, passing through the cavity to the outlet, it is depicting a curve called **curve of carus**, which is the path that the presenting part follows until expulsion.

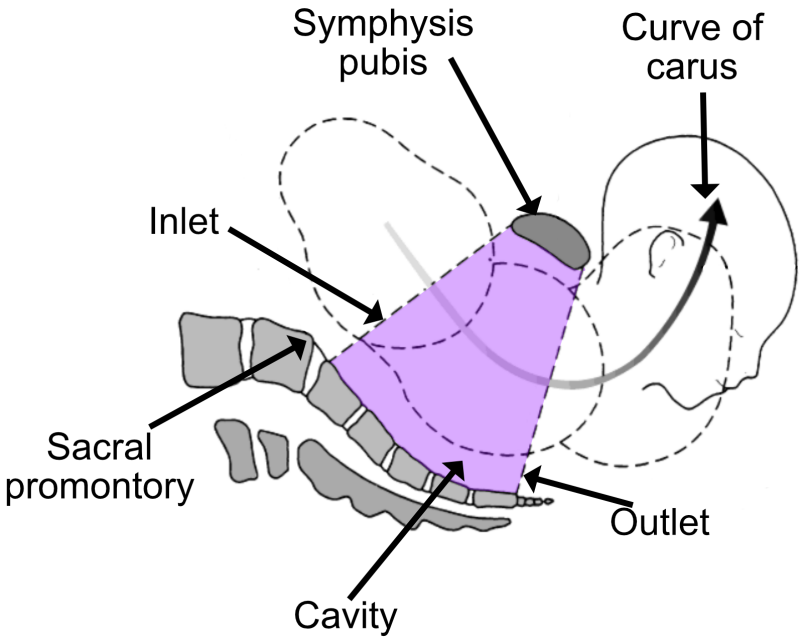

Figure A.4: Sagittal view of the pelvis regions (modified from [72]).

A.1.1 Pelvic inlet

The pelvis brim is the *inlet* plane (see Figure A.3) where the fetal head or the presenting part enters to the **true pelvis** in the transverse position. The *inlet* diameters are described as follows:

- **Anteroposterior:** It is measured from the upper inner border of the symphysis pubis to the sacral promontory, and it is approximately 11 cm long.
- **Two Obliques:** The right and left diameters are measured from the sacroiliac joint to the iliopectineal eminence, and they are approximately 12 cm long.
- **Transverse:** It is the longest diameter, measured from the widest points on the iliopectineal lines, and it is approximately 13 cm long.

Figure A.5, shows a superior view of the pelvic inlet diameters.

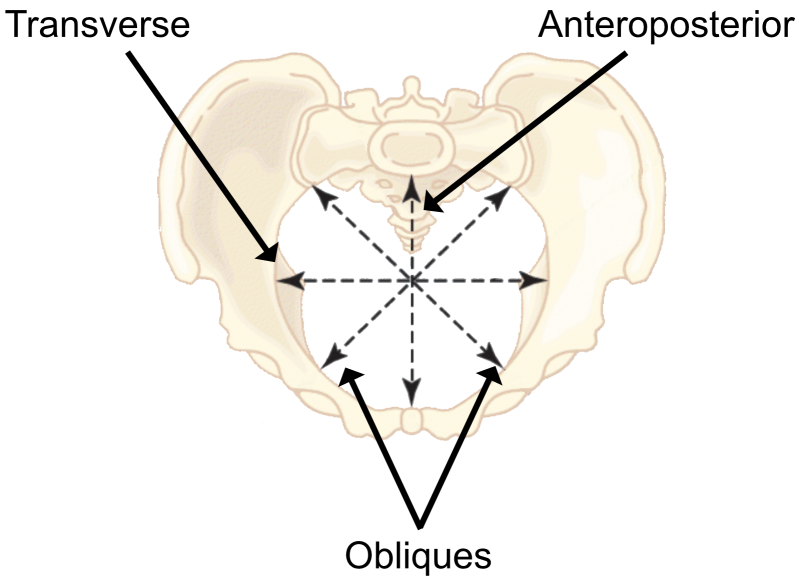

Figure A.5: Superior view of the pelvis inlet diameters(modified from [14]).

A.1.2 Pelvic cavity

Pelvic cavity: This region extends from the inlet to the outlet of the pelvis, and is designed to facilitate the descend and rotation of the fetus (presenting part). Usually it has a circular shape in a gynecoid pelvis, and from an anteroposterior view, it is shallow at the front and deep at the back. The *cavity* diameters are described as follows:

- **Anteroposterior:** It is measured from the inner border of the symphysis pubis to bottom part of the curve of the sacrum, and it is approximately 12 cm long.
- **Two Obliques:** The right and left diameters are measured from the sacroiliac joint to a mid point between the upper and lower pubic rami, and they are approximately 12 cm long.
- **Transverse:** It is measured from the right to the left ischial spines, and it is approximately 12 cm long.

A.1.3 Pelvic outlet

Pelvic outlet: It has a diamond shape which boundaries are the tip of the coccyx posteriorly and the

- **Anteroposterior:** It is measured from the lower border of the symphysis pubis to the sacrococcygeal joint, and it is approximately 13 cm long.
- **Two Obliques:** The right and left diameters are measured from the sacrospinous ligaments to the obturator foramen, and they are approximately 12 cm long.
- **Transverse:** It is measured from the right to the left ischial spines, and it is approximately 11 cm long.

Figure A.6, shows an inferior view of the pelvic outlet diameters.

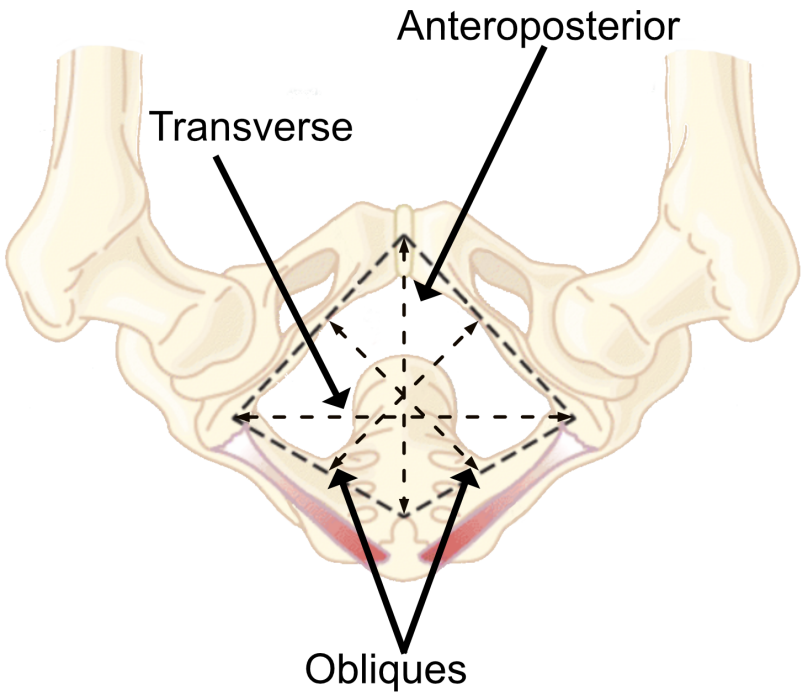

Figure A.6: Inferior view of the pelvis outlet diameters (modified from [14]).

A.1.4 Pelvic shapes

The shape of the pelvis can be classified in 4 different groups (see Figure A.7):

- **Gynecoid**: This is the most common type of pelvic shape found in approximately 50% of women. It has a round inlet, straight walls, average prominence ischial spines and a well curved sacrum. Subpubic arch with an angle between 85-90 degrees and a large sacrospinous notch [14, 24].
- **Android**: Although this is the most common type of pelvic shape between males, it is found in less than 30% of women. It has a triangular inlet, convergent walls, prominent spines and a shallow sacral curve. Narrow subpubic arch with and angle between 60-75 degrees and a long narrow sacrospinous notch [14, 24].
- **Anthropoid**: I is found in approximately 20% of women. It has a long narrow oval inlet, walls that do not converge, not prominent ischial spines and usually a posterior inclination of the sacrum. Narrow subpubic arch with an angle of more than 90 degrees and small sacrospinous notch [14, 24].
- **Platypelloid**: It is found in 3% of women. It has an oval inlet, straight and divergent walls and a posterior inclination of a flat sacrum. A wide subpubic arch with more than 90 degrees and a long small sacrospinous notch [14, 24].

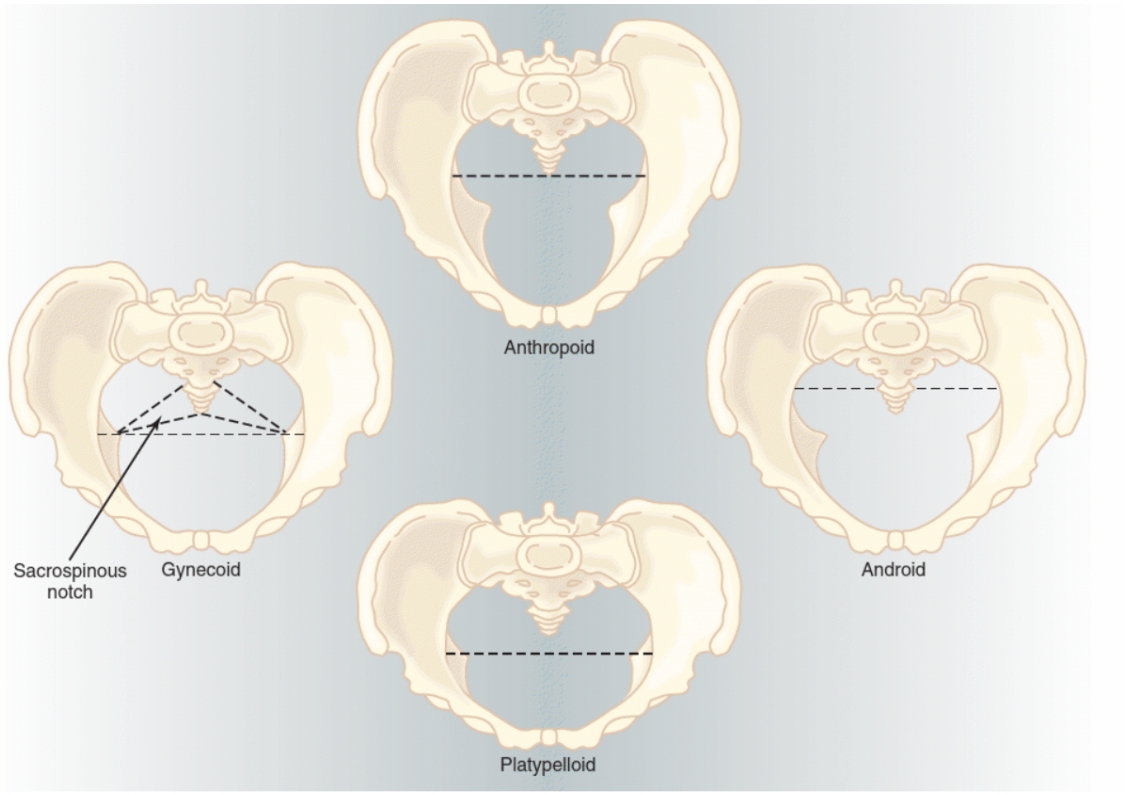

Figure A.7: Basic pelvic shapes (taken from [14]).

Appendix B

3D forceps model simplification

B.1 Original model

The 3D obstetric forceps model (see Fig. B.2) used in the work of *Lapeer 2014 et. al* [70], was obtained from a real Neville-Barnes type with Simpsons handles (see Figure B.1).

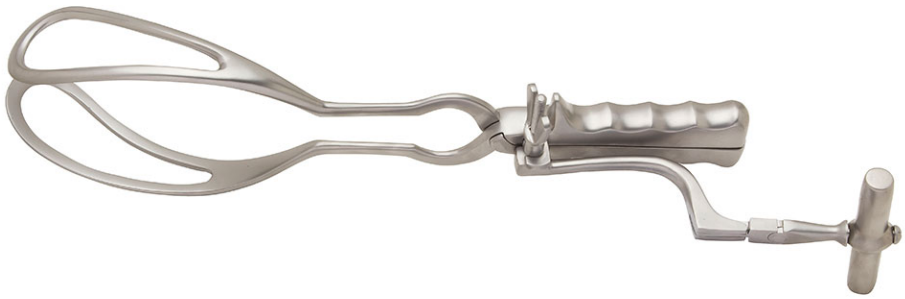

Figure B.1: Neville-Barnes obstetric forceps with simpsons handles.

Table B.1, shows the individual blades weight of the stainless steel Neville-Barnes obstetric forceps type with Simpsons handles. Due to the left blade having an extra piece to attach the traction handle, there is a weight difference between them.

Blade	**Weight (kg)**
Left	0.350
Right	0.333

Table B.1: Weight of individual obstetric forces blades.

Table B.2, shows the different measurements obtained from the forceps:

Measure	Value	
	cm	m
Length of blades	15	0.15
Distance between blade tips	2.3	0.023
Maximum blade separation	8.2	0.082
Pelvic radius curvature	17.5	0.175
Shanks length	8.5	0.085

Table B.2: Different measurements of the obstetric forceps.

Figure B.2, shows different views of the original 3D model, and as it can be seen in the images, this model has the lock, finger guards, the bezel in the internal face of the handles and in the external face of the handles the fingers guide design.

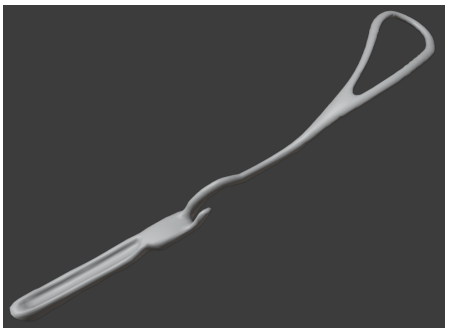

(a) Top left view

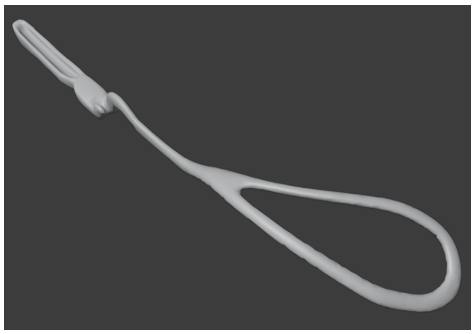

(b) Top right view

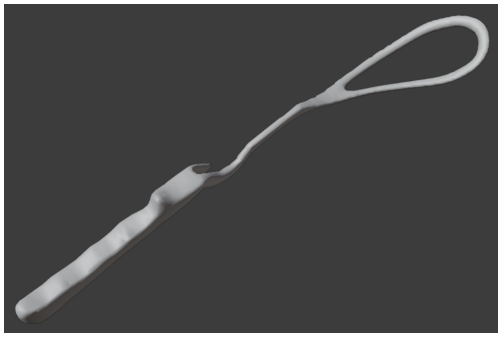

(c) Bottom left view

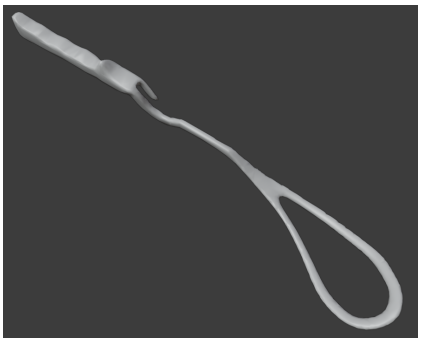

(d) Bottom right view

Figure B.2: Different views from original 3D forceps model.

Due to the nature of this project and to ease the execution of the simulations, the original 3D obstetric forceps model was modified from simplifying the handle and lock to completely remove part of the handles. These changes were done using the software Blender® [67].

B.2 New mesh creation

In order to perform a better simulation with a smooth surface in the blades, a new mesh was created, this is due to the original 3D forceps surface was not as smooth as it was expected (see Figure B.3), as the internal surface of the blades and the edges of the whole model have nodes at a different high level than the nodes in the surrounding area, creating little spikes that could affect the simulation.

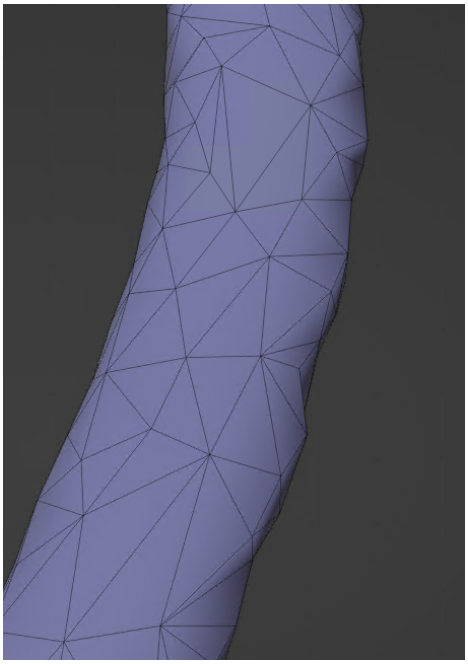

Figure B.3: Section of original obstetric forceps blade mesh.

Firstly, a manual approach was done to modify the nodes with problems, but it was time consuming and the result was not good enough to be used. Then it was decided to create a new mesh using the current one as base, through the retopology process.

B.2.1 Retopology

The original 3D model of the obstetric forceps presented a certain degree of deformation and its mesh was not uniform (see Figure B.3). The goal of this step was to create a new uniform mesh without the current problems in the blade nodes.

This process simplify current meshes, to make them cleaner and easier to manipulate [73]. Although the process can be done automatically, a manual sculpting approach was chosen to smooth certain areas of the blades.

By using retopology, a new mesh is created by placing little patches, in this case quads (rectangles) on top of all the current mesh surface.

Figure B.4a shows the original model with a non uniform mesh and Figure B.4b shows the new mesh with the uniform mesh after retopology.

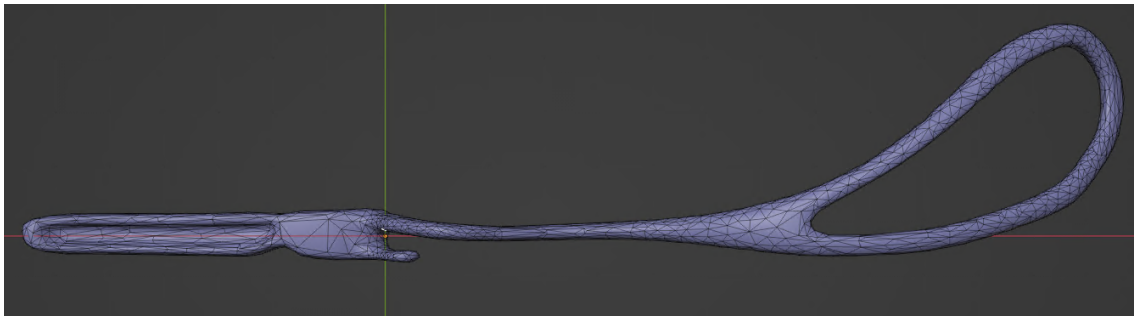

(a) Original mesh, before retopology.

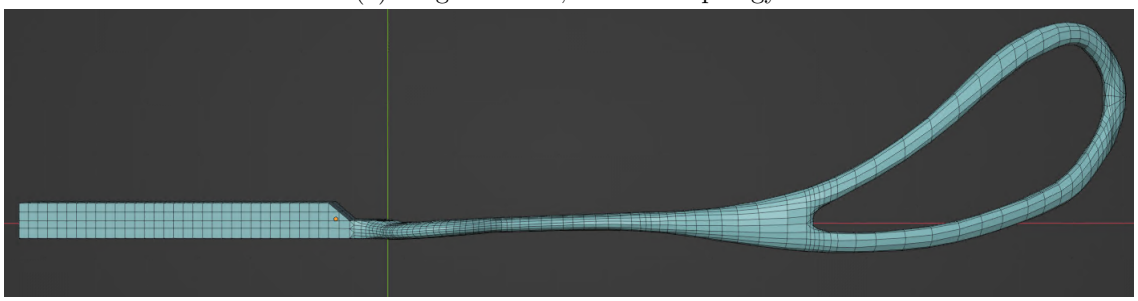

(b) New mesh, after retopology.

Figure B.4: Comparison between original 3d model mesh (top) and new mesh after retopology (bottom).

B.3 Handles simplified

On this step, a new version of the 3D model was created by modifying some of the features of the handles to create a more basic shape:

- **Handles**: The shape of the handles was modified to create a rectangular cube, where all sides are flat. This change impacted directly over the volume of the handles, reducing them as a result.
- **Finger guards**: This feature was removed completely from the handles (since it is not relevant for the simulation), to let them be flat in all sides as mentioned previously.
- **Lock**: Removed from each handle to simplify them and keep flat sides.
- **Shanks**: They are not tilt to the middle of the handles any more, and are completely parallel and aligned from each other.

Figure B.5, shows the final result after this changes were performed. Notice that in this version, the handles have the same thickness as the shanks, being less ticker than the original handles.

These changes help to keep the handles in constant contact but as it can be seen in Figure B.6, this can only be use considering that the blades have been already closed. Performing the close stage with this version is only possible by adding additional constraints to prevent the blades to slide.

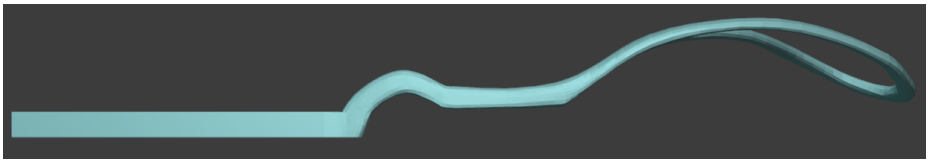

Figure B.5: Obstetric forceps blade with handle simplified.

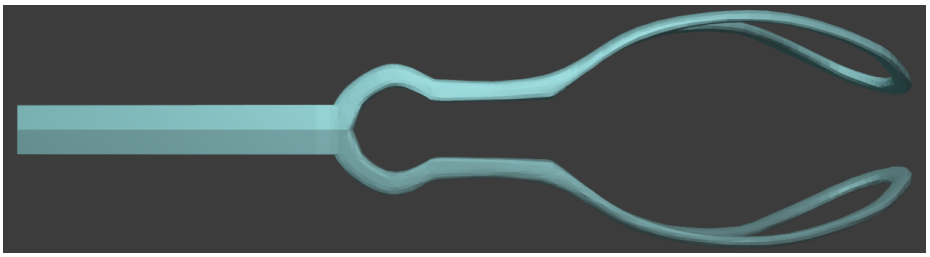

Figure B.6: Obstetric forceps blades with handle modified side by side.

B.4 Hinge with pin

A second version of the 3D forceps was created, where the same features of the handles were removed, such as the finger guards, and the lock; the handles were reshaped as more thicker rectangular cubes compare with the previous version, the tilt and crossing shanks design was kept, letting them to cross each other.

Figure B.7, shows the 3D model after performing the changes mentioned. Note that the shanks do not have the hole in the middle just yet.

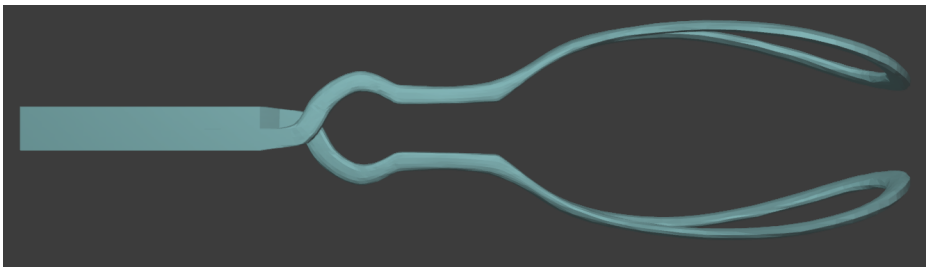

Figure B.7: Forceps without pin.

The inclination in the shanks helped to create the hinge mechanism, along with a hole in the intersection of the shanks and the middle line between the handless. The use of the pin inserted in the shanks hole lets the blades to perform rotations around it.

The hinge and the pin create a scissors alike mechanism that helps to rotate the forceps blades independently in order to open or close them if necessary. With this approach, the closing motion of the blades over the fetus head can be simulated manipulating the handles only and hold the position before to perform the pulling motion.

Figure B.8, shows the model after creating the hole in the shanks.

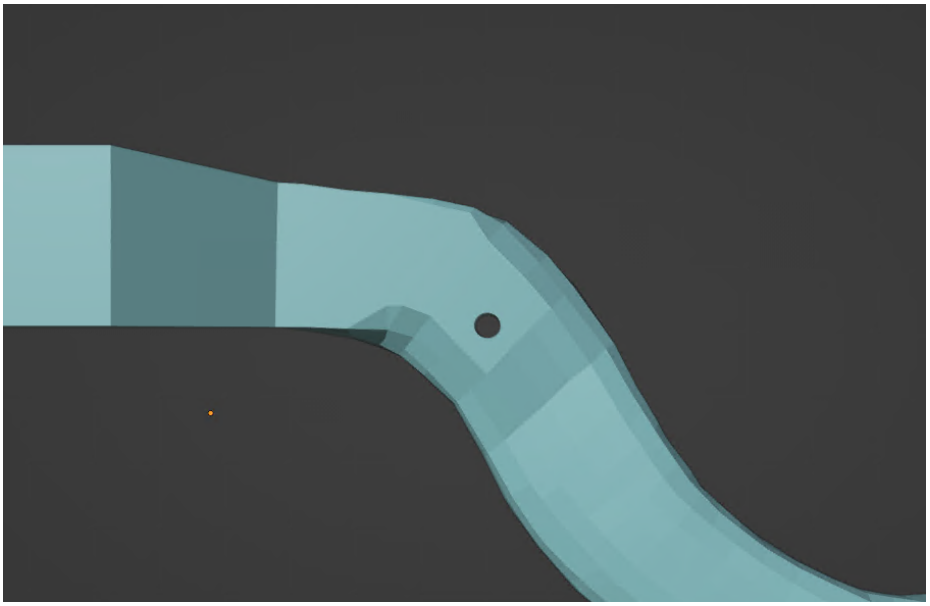

Figure B.8: Left blade shank with hole.

Figure B.9, shows the final version of the obstetric forceps with the hinge mechanism after all changes were done. As it can be seen, the mayor difference between this version and the original, is the handles shape.

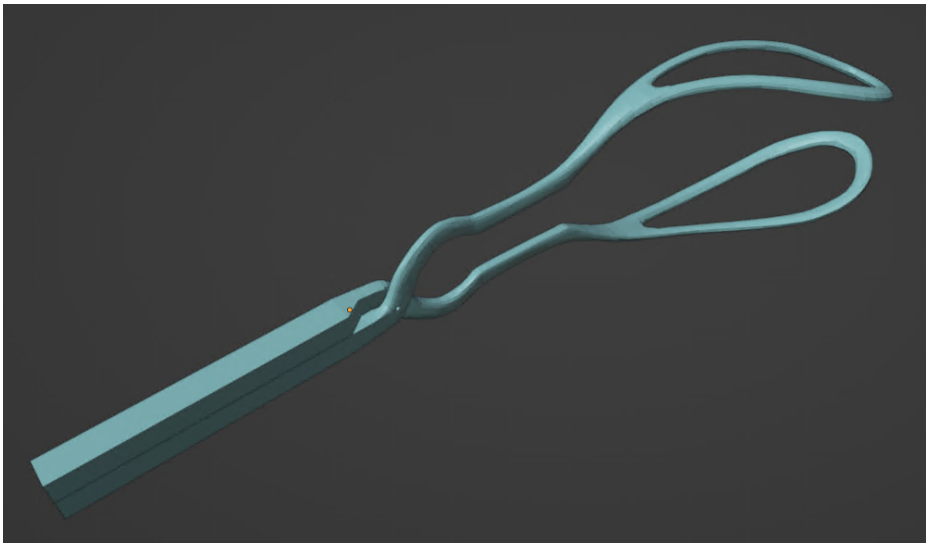

Figure B.9: Obstetric forceps with hinge mechanism.

B.5 Blades without handles

Previous version with the hinge mechanism (see Section B.4), a number of different contact interactions were added, such as the hole-pin contact, internal surface of handles contact and internal surface of shanks contact, making the simulation more robust but also more expensive computational wise.

This new version of the obstetric forceps was created to avoid these unnecessary contact interactions and focus only in the contact interaction between the obstetric forceps blades and the bay head.

Hence, it was decided to remove the handles and shanks from the obstetric forceps as well as the pin (see Figure B.10), along with all the contact interactions created between them.

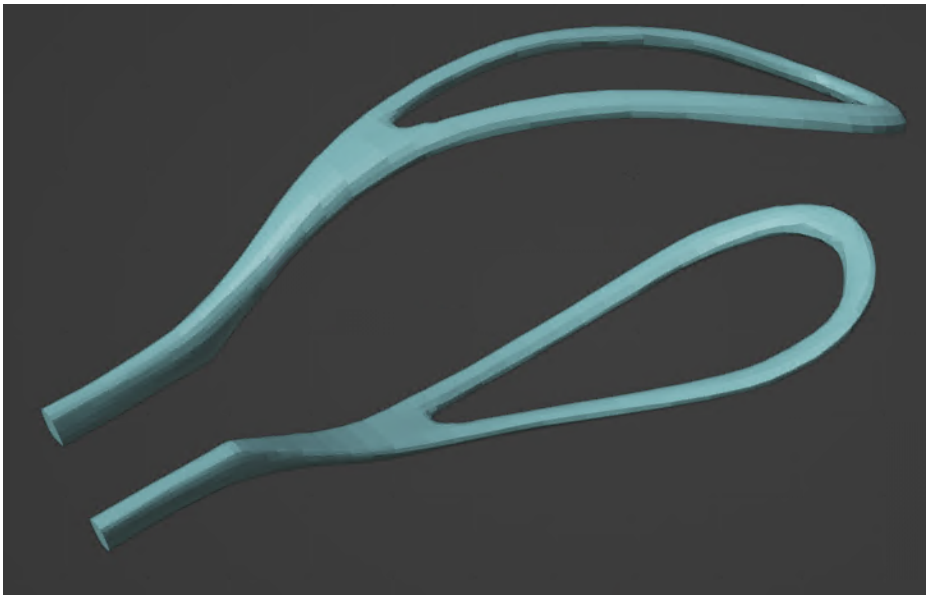

Figure B.10: Obstetric forceps 3D model with handles and shanks removed.

As well as in the previous version, this version also suffered changes in volume as it can be seen in Table B.3. There is a more significant difference in volume between the original mesh and the modified meshes in both pieces of Software about %17. The reason behind this, is because the modified meshes have a simpler handle design, which does not consider the lock system, the fingers guard neither the fingers guide.

Version	**Blade**	**Volume**
	Original	0.0000348 m^3
Hinge mechanism	Left	0.0000288 m^3
	Right	0.0000288 m^3
No handles	Left	0.0000113 m^3
	Right	0.0000113 m^3

Table B.3: Forceps versions and the difference in volumes.

Appendix C

Abaqus input file format

In Abaqus®, every 3D object also called **part** has a definition based on the number of **nodes** (or vertices), and the number of **faces** (or elements) it has, these definitions are contained in a plain text file called "input file" with extension **.inp**[1] [74].

C.1 Syntax elements

The file is divided in a number of sections, where different options are defined; the text in Listing 1, shows an extract of the materials definition taken from an Abaqus® input file.

```
1  ** MATERIALS
2  **
3  *Material, name=Steel
4  *Density
5  7800.,
```

Listing 1: Material definition, text extracted from Abaqus input file.

Lets consider this text to explain the following elements:

- *Comment lines*: Text lines to add comments, they start with two stars (**) and are ignored by Abaqus®.

  For example:

  ** MATERIALS (line 1-2).

- *Keyword lines*: Text line defining an option and often have parameters.

  If the keyword is defining an option, then the first character must be a star (*), if parameters are given, they must be separated by a comma (,).

  For example:

[1] Although the lines in the text file must follow certain syntax rules, the explanation about all these rules are out of the scope of this thesis. We are interested in the file content more than how the file is created. Please refer to the Abaqus® documentation for more details [74].

*Material, name=Steel (line 3).

where:

  - The option defined is: *Material.
  - The parameter defined is: , name=Steel.

- *Data lines*: Text lines containing numeric or alphanumeric entries, according to the keyword description. All data is separated by commas, it can contain one or more lines.

  For example:

  *Density (line 4)

  7800., (line 5).

  where:

  - The option defined is: *Density
  - The data entry is: 7800.,

C.2 Sections

The input file contains several sections, where each of them defines different options in the simulation. For our purposes, we are only interested in two sections of the file:

- Node
- Element

C.2.1 Node

The node section is defined inside the **part** option, and it defines the coordinates of all nodes or vertices contained in the part.

Lets consider the next text in Listing 2, extracted from an input file.

```
1  ** PARTS
2  **
3  *Part, name=Left_Part
4  *Node
5      1, -0.130291998, 0.00263100001, -0.00284800003
6      2, -0.130291998, 0.00263100001, -0.00153799995
7      ...
```

Listing 2: Part nodes definition, text extracted from Abaqus input file.

The part option is set and named "Left_Part" in line 3 as follows: *Part, name=Left_Part Then, in line 4, the "Node" option is set, following with the coordinates for each node (line 5-6).

In the file, every node is defined with the following format:
Node Number, X coordinate, Y coordinate, Z coordinate
In this case, the first node is defined as follows:

- Node number: 1
- X coordinate: -0.130291998
- Y coordinate: 0.00263100001
- Z coordinate: -0.00284800003

The same will happen with the subsequent nodes.

C.2.2 Element

The element sections is defined inside the **part** option, and it defines how the elements or faces are formed in the part. This definition will depend on the type of element.

Lets consider the text shown in Listing 3, extracted from an input file.

```
1  *Element, type=C3D10
2      1,  4400, 4401, 4402, 4403, 7864, 7863, 7862, 7866, 7865, 7867
3      2,  4400, 4404, 4405, 4401, 7870, 7869, 7868, 7864, 7871, 7872
4      ...
```

Listing 3: Part element definition, text extracted from Abaqus input file.

Here, the element option is set in line 1, along with the type parameter set to C3D10, which is defining a continuum tetrahedron element with 10 nodes [75][2].

The elements are defined in lines 2-3.

Every element has the next format:
Element Number, Node 1, Node 2, Node 3, Node 4, Mid node 1, Mid node 2, Mid node 3, Mid node 4, Mid node 5, Mid node 6
Where:

- Element Number: Refers to the number of the element in the part, since a part can contain hundreds or thousands of elements, the input file have to define every one of them.
- Nodes: In this case, we have four nodes defined in the element, this is because they are forming a tetrahedron, if we go back to Section F.1, we can see Figure F.1 representing a tetrahedron formed by four nodes **a**, **b**, **c**, and **d**.

[2] Abaqus® handles different types of elements; depending on its family, degrees of freedom (which is directly related to the element family), number of nodes, formulation and integration. Please refers to the Abaqus® documentation for more information [75]

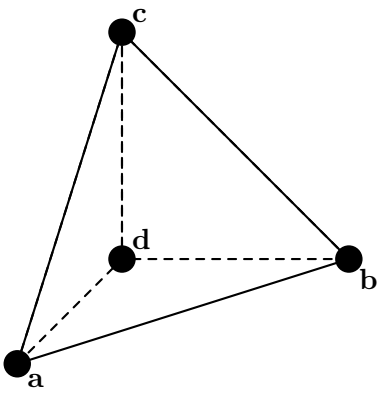

Figure F.1: Geometric figure of a tetrahedron.

- Mid nodes: They are the mid points between a node pair (or edge). Since the tetrahedron has six edges, then it will have six mid nodes.
  Figure C.1, shows the four nodes in black (**a**, **b**, **c**, and **d**) and the six mid nodes in blue (**r**, **s**, **t**, **x**, **y**, and **z**).

  For example, the mid node **r**, is between the node pair **a** and **b**.

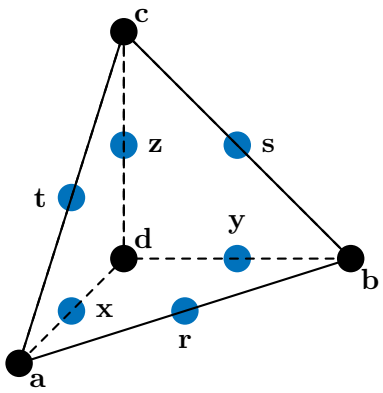

Figure C.1: Tetrahedron with nodes and mid nodes in edges.

Appendix D

OBJ file format

Object files or OBJ, are plain text files that define the geometry of 3D objects and other objects properties such as texture, color, normals, render attributes, etc. This file format can also be used to transfer geometric data back and forth between different applications [76].

D.1 Syntax elements

The file is divided in different sections, and each section is well defined by keywords followed by the value or set of values. Listing 4, shows an extract of the obj file created in Blender® from the original blade 3D model.

Lets consider the extract to explain the next elements:

- *Comment lines*: Text lines to add comments, they start with (#), they are ignored by Blender® when an obj file is imported.

  For example:

  # Blender v2.93.5 OBJ File: ” (line 1-2).

  Here, we can see that the line starts with the # keyword, hence all following text is considered a comment.

- *Keyword lines*: Text line defining a section or group of data. The keyword is the first character or series of characters in the line.

  For example:

  o 01_Forceps_Original (line 3).

  where:

  - o: Represents the keyword

- *Values*: Text lines containing the value(s) of the keyword. They come after the keyword and it can be a set of numeric values, a single numeric value, a string or a combination of them. All values are blank space-separated.

  For example:

```
1   # Blender v2.93.5 OBJ File: ''
2   # www.blender.org
3   o 01_Forceps_Original
4   v -0.122903 -0.020278 -0.003920
5   v -0.124895 -0.016976 -0.002479
6   v -0.124421 -0.015930 -0.003795
7   v -0.121596 -0.016769 -0.005362
8   ...
9   vt 1.000000 0.375000
10  vt 1.000000 0.375000
11  vt 1.000000 0.375000
12  vt 1.000000 0.375000
13  ...
14  vn -0.6013 -0.6205 -0.5034
15  vn -0.9221 -0.3203 -0.2171
16  vn -0.7143 -0.1658 -0.6799
17  vn -0.3897 -0.1084 -0.9146
18  ...
19  f 1/1/1 2/2/2 3/3/3
20  f 1/1/1 3/3/3 4/4/4
21  f 2/2/2 5/5/5 6/6/6
22  f 7/7/7 6/6/6 5/5/5
23  ...
```

Listing 4: Extract of a OBJ file from the original 3D model of the obstetric blade.

o 01_Forceps_Original (line 3).

v -0.122903 -0.020278 -0.003920 (line 4).

f 1/1/1 2/2/2 3/3/3 (line 19).

where:

- In line 3, we have the string value 01_Forceps_Original after the keyword o.
- In line 4, we have a set of three numeric values separated by blank spaces -0.122903 -0.020278 -0.003920 after the keyword v.
- In line 9, we have a set of triplets separated by blank spaces 1/1/1 2/2/2 3/3/3, but the values in each triples is separated by the / symbol. All the values are defined after the keyword f.

D.2 Sections

Among the relevant information in the file format, we are going to describe five sections that are more important for our purposes[1], because they define the 3D geometry surface of the objects contained in the file, although only two of them are used for file format conversion from OBJ to INP (See Section E for a detailed description of the process):

- Object name.
- Vertex.
- Vertex texture coordinate.
- Vertex normal.
- Face.

D.2.1 Object name

This section sets the name of the 3D object inside the obj file. Each object name definition line starts with the keyword "o". Lets see the next extract from our example in Listing 4 :
o 01_Forceps_Original (line 3).
where:

- o: Is the keyword used to define the 3D object name.
- 01_Forceps_Original: Is the 3D object name. It can be any text.

D.2.2 Vertex

It sets all the vertices position in three dimensions, in the format (x, y, z), being each point a float point number.

Each vertex definition line starts with the keyword "v", and only contains coordinates information. Although there is not a vertex identifier as such defined, every vertex definition line represents a different vertex for the object specified.

For example:
v -0.122903 -0.020278 -0.003920 (line 5).
v -0.124895 -0.016976 -0.002479 (line 6).

As we can see in the example, we have two vertex definitions, each of them starting with the keyword "v", after that, it follows the three dimension coordinate, every element in the line is separated by blank spaces.

This is the first section that is important for the file conversion process.

[1]The other sections are not described here since they are not used in this project and are out of the scope of the research (please refer to [76] and [77] for more information about the other sections).

D.2.3 Vertex texture coordinate

This section defines two floating point numbers (u, v), used to determine how to paint the three-dimensional pixels from a 2D texture map. The vertex texture line is defined with the keyword "vt".

For example:
vt 1.000000 0.375000 (line 9).
where:

- vt: Is the keyword for the vertex texture line.
- 1.000000 0.375000: Are the coordinates u, v in 2D.

D.2.4 Vertex normal

Vector describing the direction of the normal in the three-dimensional space. It uses three floating point numbers defined as "i", "j" and "k".

Each vertex normal definition line starts with the keyword "vn".
For example:
vn -0.6013 -0.6205 -0.5034 (line 14).
where:

- vn: Is the keyword defining the vertex normal.
- -0.6013 -0.6205 -0.5034: Are the set of i, j, k values defining the normal vector.

D.2.5 Face

This sections groups triples of numbers to specify vertex data: geometric vertex, texture vertex, and vertex normal, that are separated by slashes (/). The triples are separated by blank spaces. These group of triples form the geometric shape of the face (triangle, quadrilateral, or polygon). The face line definition starts with the keyword "f".

For example:
f 1/1/1 2/2/2 3/3/3 (line19)
where:

- f: Is the keyword defining the face.
- 1/1/1 2/2/2 3/3/3: Are the sets of triples defining the vertex data in the format v/vt/vn v/vt/vn v/vt/vn.

This is the second section that is important for the file conversion process.

Appendix E

File conversions

All 3D models created in Blender® are stored inside the .BLEND file format, which contains the information of every model such as vertex coordinates, face vertices, normals direction of faces, vertices per model, etc. Since the file has a proprietary format, this data cannot be used outside the software. For this reason, it has to be converted into a suitable format that can be used inside Abaqus® that also uses its own .INP format.

Since there is not a direct way to extract the data from one suite and use it in the other, we have to perform this conversion externally in two steps:

- Create OBJ file from Blender® model.
- Convert OBJ file into Abaqus® INP file.

E.1 Create OBJ file

Blender® has different options to export the 3D models created in the suite to other formats such as: Collada [78, 79], Alembic [80, 81], Universal Scene Description (USD) [82, 83], Grease Pencil as Scalable Vector Graphics (SVG) [84, 85], Grease Pencil as Portable Document Format (PDF) [86, 87], Stereolithography (STL) [88, 89] and Wavefront [77, 76] (see Blender® manual for more details [68]).

Since the information required for Abaqus® to create parts, consist of all the vertices coordinates in the 3D objects, normals and the group of vertices per face, disregarding any other data such as texture or lights; we choose to use the OBJ file format to export the data as its simplicity fulfills this project's needs (See Appendix D for more information about the file format).

The Wavefront OBJ (.obj) format, constitutes plain text containing geometry objects (vertex coordinates, normals), texture data, vertex and texture groups.

E.2 Create INP file

Once we have created the .OBJ file, the next step is to convert it into an .INP file. These two files contain similar information related to vertices and faces, but they do not share the same format, and because of that, we have to use an external tool to approach that goal.

E.2.1 Automatic conversion

In this research, a program using the programming language C# has been created using Microsoft Visual Studio 2017® to perform the file conversion. It can read one or more .OBJ files at the same time to add the 3D models into a single .INP file.

The program starts reading the .OBJ file to be processed line by line; it validates the initial character in every line to identify what kind of section is defined (either vertex or face, as they are the relevant sections to create the .INP file, see Section D.2), hence create the respective object in the program. Once it has read all the elements from the section, it writes the output to the .INP file, and this process is repeated for the next section.

Algorithm 1, shows the complete logic used in the program.

Algorithm 1 INP File Creation

```
1: procedure READS AN OBJ FILE TO CREATE AN INP FILE
Require: Valid .OBJ file name as source and .INP file name as destination
Ensure: INP is created from source data
2:     Sets variables
3:     Opens source file fin in read mode
4:     Creates and opens destination file fout in write mode
5:     Creates tmpVertex as a new Vertex object
6:     Creates tmpFace as a new Face object
7:     Sets vertexCounter = 0
8:     Sets faceCounter = 0
9:     Sets faceNum = 0
10:
11:    // Writes the INP file header
12:    Write to fout file: "**"
13:    Write to fout file: "*PART, NAME = PartName"
14:    Write to fout file: "*NODE, NSET = NodeSetName"
15:    while (line = fin.ReadLine()) != null do
16:        textArr = create array by splitting line by blank spaces
17:        // Validates vertex data
18:        if textArr[0] == "v" then
19:            vertexCounter++
20:            tmpVertex.id = vertexCounter
21:            tmpVertex.x = textArr[1]
22:            tmpVertex.y = textArr[2]
23:            tmpVertex.z = textArr[3]
24:            Write tmpVertex data to fout file in the next order: id, x, y, z
25:        else
26:            // Validates face data
27:            if textArr[0] == "f" then
28:                // Sets the faces type
```

```
29:                 if textArr.Length = 4 && faceNum != 3 then
30:                     faceNum = 3
31:                     Write to fout file:
32:                     "*ELEMENT, ELSET = ElementSetName3, TYPE = S3R"
33:                 else
34:                     if textArr.Length = 5 && faceNum != 4 then
35:                         faceNum = 4
36:                         Write to fout file:
37:                         "*ELEMENT, ELSET = ElementSetName4, TYPE = S4R"
38:                     else
39:                         if textArr.Length > 5 then
40:                             continue
41:                         end if
42:                     end if
43:                 end if
44:                 faceCounter++
45:                 tmpFace.id = faceCounter
46:                 Write to fout file: "{tmpFace.id}"
47:                 i = 1
48:                 Creates facesArr
49:                 while (i < textArr.Length) do
50:                     j = 0
51:                     // Iterate over the text to extract the face numbers in every triplet
52:                     while (textArr[i][j] != "/") do
53:                         Add textArr[i][j] to facesArr
54:                         j++
55:                     end while
56:                     // Iterates over the array to extract all its elements
57:                     Write to fout file: ",{faceArr}"
58:                     i++
59:                 end while
60:                 Write to fout file: "\n"
61:             else
62:                 // Any other character is ignored
63:                 continue
64:             end if
65:         end if
66:     end while
67:     Write to fout file: "*END PART"
68:     Close fin file
69:     Close fout file
70: end procedure
```

E.2.2 Classes definition

The program was created using the Object Oriented Programming (OOP) paradigm to facilitate its development and future maintenance. The next three classes were created to perform the file conversion:

- Vertex.
- Face.
- File processing.

The file Program.cs (see Listing 5), is the main file to be executed, it creates the objects and calls the method to perform the file conversion process.

```
1  class Program
2  {
3      static void Main(string[] args)
4      {
5          // Example of two obj files merged into one inp file
6          FileOut.CombObj2inp("../file1.obj", "../file2.obj",
7              "../outFile.inp", "AssemblyName",
8              "part1", "nodeSetName1", "elementsSetName1",
9              "part2", "nodeSetName2", "elementsSetName2");
10     }
11 }
```

Listing 5: C# code from Program.cs

This code is performing the next:

- Create main class (line 1).
- Defines the "Main" method of the class (line 3).
- Calls the method "CombObj2inp" from the object "FileOut" (line 6).

  This method receives a series of parameters that define two obj input files and the output inp file, needed to perform the file conversion.

E.2.2.1 Vertex

The Vertex class has the next definition:

- Attributes:
  - id: Vertex identifier.
  - x: Vertex 3d x coordinate.
  - y: Vertex 3d y coordinate.

  - z: Vertex 3d z coordinate.

- Methods:
  - None.

E.2.2.2 Face

The Face class has the next definition:

- Attributes:
  - id: Face identifier.
  - vert: List of vertex objects that form the face.
- Methods:
  - None.

E.2.2.3 FileProcessing

The FileProcessing class has the next definition:

- Attributes:
  - None.
- Methods:
  - Obj2Inp: Convert one obj file into an inp file, setting the heading of the file and the nodes and elements sets.
  - CombineObj: Combines up to two obj files into a single inp file.
  - CombineInpAssembly: Creates the assembly section of the inp file.

E.2.3 Class diagram

The program class diagram is shown in Figure E.1:

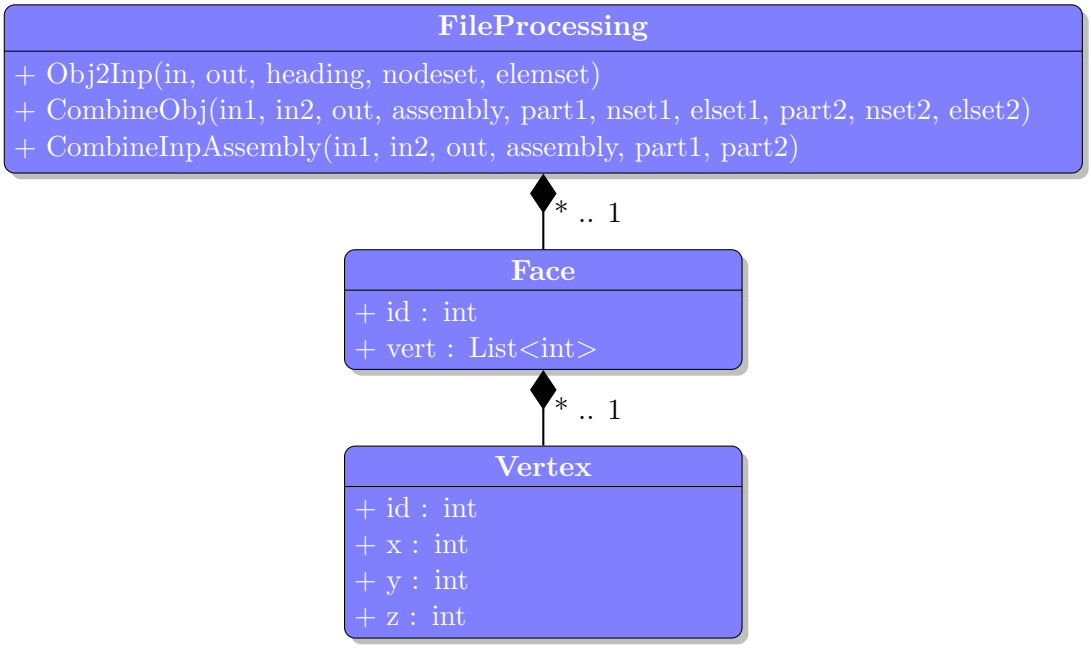

Figure E.1: File conversion class diagram.

Appendix F

Volume Calculation of 3D Objects

F.1 Mathematical definition

The 3D solid objects in the simulation are formed from a set of tetrahedrons or triangular pyramids (see Figure F.1), and each of these 3D objects can contain hundreds or even thousands of these tetrahedrons with different sizes.

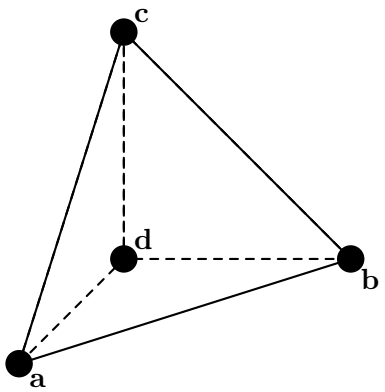

Figure F.1: Geometric figure of a tetrahedron and its vertices.

Each tetrahedron is formed by four points or vertices, and six edges; we can calculate its volume knowing the coordinates of each of these points using Equation F.1:

$$V = \frac{|(\mathbf{a} - \mathbf{d}) \cdot ((\mathbf{b} - \mathbf{d}) \times (\mathbf{c} - \mathbf{d}))|}{6} \tag{F.1}$$

where **a**, **b**, **c**, **d** are tetrahedron 3D vertices defined as follows:

- $\mathbf{a} = (a_1, a_2, a_3)$
- $\mathbf{b} = (b_1, b_2, b_3)$
- $\mathbf{c} = (c_1, c_2, c_3)$
- $\mathbf{d} = (d_1, d_2, d_3)$

In order to calculate the total volume V_T of the 3D object, it is necessary to calculate the volume V of each tetrahedron contained in the object individually, thus we can isolate each tetrahedron and assume than one of its coordinates reside in the origin O of the coordinate system, if we consider vertex $\mathbf{d}$ to be in O, then $\mathbf{d} = 0$ (see Figure F.2).

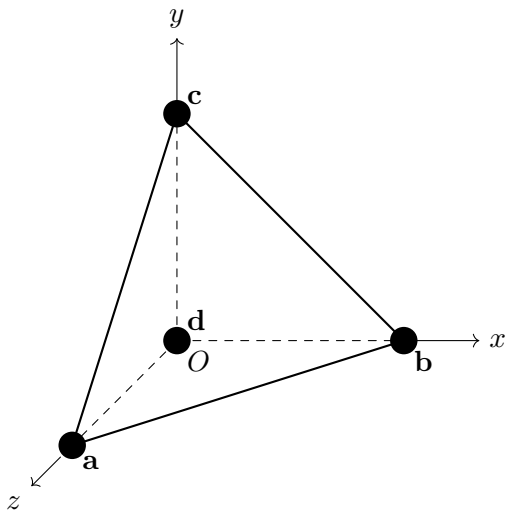

Figure F.2: Tetrahedron with vertex $\mathbf{d}$ on origin O

.

Then Equation F.1 can be reduced to:

$$V = \frac{|(\mathbf{a}) \cdot (\mathbf{b} \times \mathbf{c})|}{6} \tag{F.2}$$

And the total volume V_T of the object can be expressed as:

$$V_T = \sum_{i=1}^{n} V_i \tag{F.3}$$

where:

- i is the individual tetrahedron analyzed.
- n represents the total number of tetrahedrons contained in the 3D object.
- V_i is the volume of each individual tetrahedron contained in the 3D object.

F.2 Automatic calculation

A computer program using the programming language Python, was created to read data from the Node and Element sections in the Abaqus® input file, and then calculate the total volume of the parts contained in the file. The purpose of this program is, to compare the 3D objects volume before and after a simulation; since the volume should not change, it has to be the same in both cases.

The process is divided in two steps.

- Read data from file.
- Volume calculation.

F.2.1 Read data from file

Firstly, an input file is passed to the program to be open, then the program will read every line in the file and consider only the ones that are important and disregard the ones we do not need.

Only the Node and Element sections are considered for every part in the file, in that specific order; due to the Element section depends on the Node section.

The program has a flag called file_stage, which will help to set the stage where the system is. It starts reading the lines until we find the one with the text ** PARTS (see Line 1 in Listings 2), which means that the Parts section starts there, nothing is done there.

It keeps reading the next lines, if a comment line is found, it will be disregarded until it finds the line with the text * Part; the same line contains the name of the part as a parameter (see Line 3 in Listing 2), for example , name=Left_Part; which will be saved in the attribute name in the Part object. The flag file_stage is set to PART.

The next line, should contain the text * Node, if so, the program will set the flag to NODE, and the subsequent lines are the entries for every node. There is a node entry per line, and each of them are saved in the Node list contained in the Part object.

The process continues until a line containing text * Element is found, then the flag file_stage is set to ELEMENT, and the subsequent lines are the entries for every element, one entry per line, and each entry is saved in the Element list contained in the Part object.

If the text * is found while reading element entries, the flag file_stage is set to OTHER and all lines after that are disregarded.

Once the text * End Part is found, the process to read data from file terminates.

Once the data has been successfully read from the input file, the Model object has part objects in the part list. See Algorithm 2 for more details.

F.2.2 Volume calculation

The second step of the program will iterate over the part list to obtain the volume per part, which will calculate the volume of every element or tetrahedron in the part (see Equation F.2 in Section F.1), and then sum them up to obtain the total volume of the part (see Equation F.3 in Section F.1).

See Algorithm 3 for more details.

F.2.3 Classes definition

We use the OOP paradigm to create the program, which makes it more modular and easier to maintain. A total of five classes were created, following the same objects definitions in Abaqus®, which make it transparent for the user to have the same objects names. The main.py file, is the main file to be executed, and it creates the objects to be used, and calculates the volume of the parts defined in the input file passed to the system. The code of the main.py file is shown in Listing 6.

```python
"""
Program to calculate the volume of 3D objects defined in
Abaqus input file.
"""
from src.Model import Model

model = Model()

model.process_file("InputFiles/08_01_Gravity.inp")

if len(model.parts) > 0:
    tot_volume = 0.0
    for part in model.parts:
        tot_volume = tot_volume + part.calculate_volume()
        print(f"Part: {part.name}, volume: {part.volume}")

    print(f"Total volume: {tot_volume}")
```

Listing 6: Python code from main.py file.

Here we explain each code line:

- In Line 5, the program is adding the Model package to be used.
- Line 7, creates the Model object as model.
- Line 9, passes the Input file name and path.
- Line 11-17, validates if a part was found, if so, proceed to calculate the volume of each part and print the result.

F.2.4 Model

The Model class has the next definition:

- Attributes:
  - file_data: Contains the data from the input file.
  - parts: Is a list Part objects.
- Methods:
  - process_file: Reads Abaqus input file to extract parts data.

F.2.5 Part

The Part class has the next definition:

- Attributes:

  - name: Part name.
  - nodes: Is a list Node objects.
  - elements: Is a list of Element objects.
  - volume: Part volume.
- Methods:
  - calculate_volume: Calculates part volume based on the sum of each element volume.

F.2.6 Node

The Node class has the next definition:

- Attributes:
  - id: Node id.
- Methods:
  - None.

This class inherits from Point3D class.

F.2.7 Element

The Element class has the next definition:

- Attributes:
  - id: Element id.
  - node1: Node 1 id.
  - node2: Node 2 id.
  - node3: Node 3 id.
  - node4: Node 4 id.
- Methods:
  - None.

F.2.8 Point3D

The Point3D class has the next definition:

- Attributes:
  - x: X coordinate.
  - y: Y coordinate.
  - x: Z coordinate.
- Methods:
  - None.

F.2.9 Class diagram

The program class diagram is show in Figure F.3:

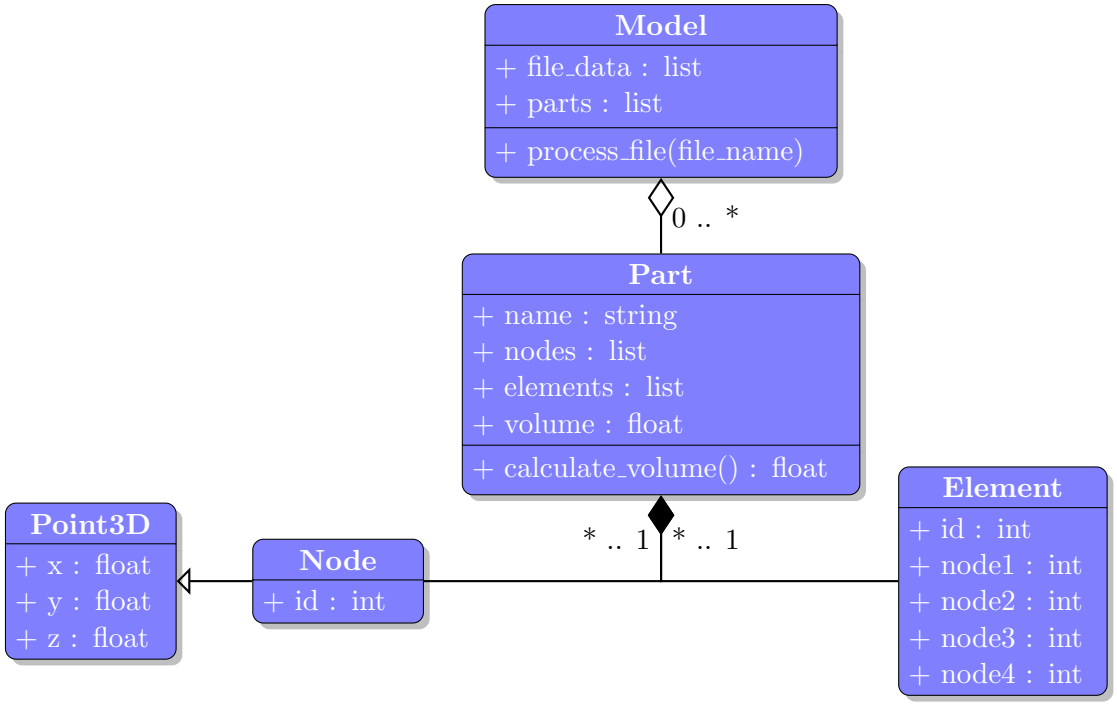

Figure F.3: Class diagram of the program to perform Volume Calculation of 3D objects.

Algorithm 2 Process file

```
1: procedure PROCESS INPUT FILE
Require: Abaqus .inp file
Ensure: Nodes and Elements have been extracted
2:     file_data = file.open
3:     if file_data is not empty then
4:         file_lines = file_data.read_lines
5:         if file_lines.len > 0  then
6:             for line in file_lines do
7:                 if "*Part" in line then
8:                     file_stage = PART
9:                     Create part object
10:                    Get part name and assign it to part
11:                    continue
12:                end if
13:                if "*Node" in line and file_stage is PART then
14:                    file_stage = NODE
15:                    continue
16:                end if
17:                if "*Element" in line and file_stage is NODE then
18:                    file_stage = ELEMENT
19:                    continue
20:                end if
21:                if file_stage is NODE then
22:                    Get coordinates
23:                    Add coordinates to Node object
24:                    Add node to part node list
25:                    continue
26:                end if
27:                if file_stage is ELEMENT then
28:                    if "*" in line then
29:                        file_stage = OTHER
30:                        continue
31:                    else
32:                        Get element data
33:                        Add data to Element object
34:                        Add element to part element list
35:                    end if
36:                end if
37:            end for
38:        end if
39:    end if
40: end procedure
```

Algorithm 3 Volume calculation

```
1: procedure CALCULATES PART'S VOLUME
Require: Nodes and elements
Ensure: Total volume was calculated
2:     if len(nodes) > 0 and len(elements) > 0 then
3:         tot_volume = 0.0
4:         for element in elements do
5:             Get element nodes p, q, r,s
6:             Move p node to origin
7:             Recalculate nodes coordinates for q, r, and s
8:             Calculate tetrahedron volume
9:             Sum up tetrahedron volume to tot_volume
10:        end for
11:        return tot_volume
12:    end if
13: end procedure
```

References

[1] Merriam-Webster. *Merriam-Webster Dictionary*. 2023. URL: https://www.merriam-webster.com/ (visited on 29th April 2023) (cit. on pp. xx, xxii).

[2] The free dictionary. *Farlex Partner Medical Dictionary*. 2023. URL: https://medical-dictionary.thefreedictionary.com (visited on 29th April 2023) (cit. on p. xx).

[3] Neville F. Hacker, Joseph C. Gambone and Calvin J. Hobel. *Essentials of Obstetrics and Gynecology*. 6th. Elsevier, 2016. ISBN: 978-1-4557-7558-3 (cit. on p. xx).

[4] Sophie Eleanor Kay and Charlotte Jean Sandhu. *Crash Course Obstetrics and Gyneacology*. 4th. Elsevier, 2019. ISBN: 978-0-7020-7347-2. URL: https://www.elsevier.com/books/crash-course-obstetrics-and-gynaecology/datta/978-0-7020-7347-2 (visited on 8th August 2022) (cit. on pp. xx, 4, 11, 14, 18 sqq., 152).

[5] Elaine Marieb and Katja Hoehn. *Human Anatomy and Physiology*. 11th. Pearson Education Limited, 2018. ISBN: 978-1-2922-6085-3 (cit. on pp. xx, 153 sq.).

[6] Andrea Nelson and Katherine Greene. *Medical Terminology for Healthcare Professions*. University of West Florida Pressbooks, 2021. URL: https://pressbooks.uwf.edu/medicalterminology/ (visited on 24th May 2023) (cit. on p. xx).

[7] *Concise Medical Dictionary*. 8th ed. Oxford University Press, January 2010. ISBN: 9780199557141. DOI: 10.1093/acref/9780199557141.001.0001. URL: http://www.oxfordreference.com/view/10.1093/acref/9780199557141.001.0001/acref-9780199557141 (cit. on p. xx).

[8] Cleveland Clinic. *Health Library*. 2024. URL: https://my.clevelandclinic.org/health (visited on 30th July 2024) (cit. on p. xx).

[9] NHS. *NHS Maternity Statistics, England - 2020-21*. 2021. URL: https://digital.nhs.uk/data-and-information/publications/statistical/nhs-maternity-statistics/2020-21 (visited on 1st October 2022) (cit. on pp. 1, 24 sq., 44).

[10] World Heatlh Organization. *Number of births*. 2023. URL: https://platform.who.int/data/maternal-newborn-child-adolescent-ageing (visited on 28th April 2023) (cit. on p. 1).

[11] The Royal College of Obstetricians and Gynaecologists - RCOG. *Assisted Vaginal Birth (ventouse or forceps)*. 2020. URL: https://www.rcog.org.uk/for-the-public/browse-all-patient-information-leaflets/assisted-vaginal-birth-ventouse-or-forceps/ (visited on 6th October 2022) (cit. on p. 1).

[12] Melissa S Wong. 'Forceps delivery: Contemporary tips for a classic obstetric tool'. In: *Contemporary OB/GYN* 64.12 (2019), pp. 14–17. URL: https://cdn.sanity.io/files/0vv8moc6/contobgyn/71290dc8a84e334f940f89c3fbbd901d680de3b5.pdf/OBGYN1219-ezine.pdf (cit. on pp. 1, 27).

[13] D J Murphy et al. 'Assisted Vaginal Birth'. In: *BJOG: An International Journal of Obstetrics and Gynaecology* 127 (9 August 2020), e70–e112. ISSN: 1470-0328. DOI: https://doi.org/10.1111/1471-0528.16092. URL: https://obgyn.onlinelibrary.wiley.com/doi/abs/10.1111/1471-0528.16092 (visited on 6th October 2022) (cit. on pp. 1, 24, 26, 30).

[14] Calvin J. Hobel and Mark Zakowski. 'Normal Labor, Delivery, and Postpartum Care'. In: *Essentials of Obstetrics and Gynecology*. 6th. Elsevier, 2016. Chap. 8, pp. 96–124. ISBN: 978-1-4557-7558-3 (cit. on pp. 4, 7, 10 sqq., 16 sq., 152, 156 sqq.).

[15] Calvin J. Hobel and Amy R. Lamb. 'Uterine Contractility and Dystocia'. In: *Essentials of Obstetrics and Gynecology*. 6th. Elsevier, 2016, pp. 147–154. ISBN: 978-1-4557-7558-3 (cit. on p. 4).

[16] Denis Walsh. 'Care in the first stage of labour'. In: 14th. Elsevier Health Sciences UK, 2011. ISBN: 978-0-7020-3105-2 (cit. on pp. 4 sqq., 9).

[17] Sue Macdonald and Julia Magill-Cuerden. *Mayes' Midwifery*. 14th. Elsevier Health Sciences UK, 2011. ISBN: 978-0-7020-3105-2 (cit. on pp. 4, 152).

[18] C. J. Arthuis, F. Perrotin and E. G. Simon. 'Fetal head station: myth of ACOG classification'. In: *Ultrasound in Obstetrics and Gynecology* 49 (2 February 2017), pp. 280–280. ISSN: 09607692. DOI: 10.1002/uog.17292 (cit. on p. 6).

[19] Kimberlee Carter and Marie Rutherford. *Building a Medical Terminology Foundation*. Open Education Resource, May 2023 (cit. on p. 7).

[20] Soo Downe. 'Care in the second stage of labour'. In: 14th. Elsevier Health Sciences UK, 2011. ISBN: 978-0-7020-3105-2 (cit. on p. 7).

[21] Abdelmonem A. Hegazy and Mohammad A. Hegazy. 'Newborns' Cranial Vault: Clinical Anatomy and Authors' Perspective'. In: *International Journal of Human Anatomy* 1 (2 July 2018). Ed. by Ismail Malkoc, pp. 21–25. ISSN: 25772279. DOI: 10.14302/issn.2577-2279.ijha-18-2179. URL: https://openaccesspub.org/ijha/article/789 (cit. on p. 10).

[22] R.J. Lapeer and R.W. Prager. 'Fetal head moulding: finite element analysis of a fetal skull subjected to uterine pressures during the first stage of labour'. In: *Journal of Biomechanics* 34.9 (September 2001), pp. 1125–1133. ISSN: 00219290. DOI: 10.1016/S0021-9290(01)00070-7. URL: https://linkinghub.elsevier.com/retrieve/pii/S0021929001000707 (cit. on p. 10).

[23] Rudy Jacques Lapeer. 'A biomechanical model of foetal head moulding'. PhD thesis. University of Cambridge, 1999 (cit. on pp. 11, 44 sq.).

[24] Barbara Burden and M Susan Sapsed. 'The fetal skull'. In: *Mayes' Midwifery*. 14th. Elsevier Health Sciences UK, 2011. Chap. 30. ISBN: 978-0-7020-3105-2 (cit. on pp. 14, 157).

[25] Kuldip K. Bharj and Anne Marie Henshaw. 'Confirming pregnancy and care of the pregnant woman'. In: 14th. Elsevier Health Sciences UK, 2011. ISBN: 978-0-7020-3105-2 (cit. on pp. 17, 19 sqq.).

[26] Charles R. B. Beckmann et al. *Obstetrics and Gynecology*. 5th. Lippincott Williams and Wilkins, 2006. ISBN: 9780781758062 (cit. on p. 20).

[27] Stephanie Meakin. 'Procedures in obstetrics'. In: 14th. Elsevier Health Sciences UK, 2011. ISBN: 978-0-7020-3105-2 (cit. on pp. 24, 27, 30, 32 sq.).

[28] Eckhart J. Buchmann, William Stones and Niranjan Thomas. 'Preventing deaths from complications of labour and delivery'. In: *Best Practice and Research Clinical Obstetrics and Gynaecology* 36 (October 2016), pp. 103–115. ISSN: 15216934. DOI: 10.1016/j.bpobgyn.2016.05.012. URL: https://linkinghub.elsevier.com/retrieve/pii/S1521693416300384 (cit. on pp. 24, 33, 35).

[29] Abdul-Qader T. Ismail et al. 'Obstetric forceps dimensions and the newborn head biometry: Time for an update'. In: *European Journal of Obstetrics and Gynecology and Reproductive Biology* 256 (January 2021), pp. 270–273. ISSN: 03012115. DOI: 10.1016/j.ejogrb.2020.11.046 (cit. on pp. 24 sq.).

[30] Committee of Obstetrics Practice. 'Approaches to Limit Intervention During Labor and Birth'. In: *ACOG Committee Opinion* 133 (2 February 2019) (cit. on p. 25).

[31] Calvin J. Hobel. 'Obstetric procedures'. In: 6th. Elsevier, 2016. ISBN: 978-1-4557-7558-3 (cit. on pp. 25 sqq.).

[32] P. M Dunn. 'The Chamberlen family (1560-1728) and obstetric forceps'. In: *Archives of Disease in Childhood - Fetal and Neonatal Edition* 81 (3 November 1999), F232–F234. ISSN: 1359-2998. DOI: 10.1136/fn.81.3.F232 (cit. on p. 25).

[33] Sukhera Sheikh, Inithan Ganesaratnam and Haider Jan. 'The birth of forceps'. In: *JRSM Short Reports* 4 (7 July 2013), pp. 1–4. ISSN: 2042-5333. DOI: 10.1177/2042533313478412 (cit. on pp. 25 sq.).

[34] Sarah Gutema. *Death and Delivery: The History of Obstetric Forceps*. 2019. URL: https://histsci152vp.wordpress.com/2019/10/14/death-and-delivery-the-history-of-obstetric-forceps/ (visited on 29th April 2023) (cit. on p. 25).

[35] Frank Forster. 'Robert Barnes and His Obstetric Forceps'. In: *The Australian and New Zealand Journal of Obstetrics and Gynaecology* 11 (3 August 1971), pp. 139–147. ISSN: 0004-8666. DOI: 10.1111/j.1479-828X.1971.tb00468.x (cit. on p. 25).

[36] Surgical Dynamics Ltd. *Surgical Dynamics*. 2023. URL: https://www.surgicaldynamics.co.uk (visited on 20th May 2023) (cit. on pp. 25 sq.).

[37] Alexander Oboh. *Force Limiting Obstetric Forceps for Instrumental vagina Delivery*. 2016. URL: https://www.hra.nhs.uk/planning-and-improving-research/application-summaries/research-summaries/force-limiting-obstetric-forceps-for-instrumental-vagina-delivery/ (cit. on p. 26).

[38] BioMed Central Ltd. *BMC*. 2023 (cit. on p. 26).

[39] Ismael Ortega. *Pulling forces involved with forceps delivery and its association with maternal injury during birth*. August 2019. URL: https://www.isrctn.com/ISRCTN18126471?q=&filters=recruitmentCountry:Spain&sort=&offset=9&totalResults=630&page=1&pageSize=10&searchType=basic-search (cit. on p. 26).

[40] Obgynkey. *Operative Vaginal Delivery*. 2023. URL: https://obgynkey.com/operative-vaginal-delivery-7/ (cit. on pp. 26, 28, 30).

[41] Richard Hayman. 'Instrumental vaginal delivery'. In: *Current Obstetrics and Gynaecology* 15 (2 April 2005), pp. 87–96. ISSN: 09575847. DOI: 10.1016/j.curobgyn.2004.12.001 (cit. on p. 30).

[42] Paul Defoort. 'Instrumental Delivery: The Obstetric Perspective'. In: 1st. Mac Keith Press, 1994. ISBN: 9780521451499 (cit. on p. 33).

[43] RR School Of Nursing. *Forceps Marks Photos*. April 2023. URL: https://www.rrnursingschool.biz/newborns/info-iup.html (visited on 26th May 2023) (cit. on p. 33).

[44] Quizlet. 'Newborn Skin findings'. In: (2023). URL: https://quizlet.com/121938681/newborn-skin-findings-flash-cards/ (visited on 26th May 2023) (cit. on p. 33).

[45] Shrooti Shah. *Episiotomy*. April 2015. URL: https://www.slideshare.net/Shrootishah/episiotomy-47180736 (visited on 26th May 2023) (cit. on p. 34).

[46] Muséum national d'Histoire naturelle. *Mannequin pédagogique d'accouchement*. July 2024. URL: https://www.mnhn.fr/fr/mannequin-pedagogique-d-accouchement (visited on 30th July 2024) (cit. on p. 35).

[47] Christian Du Brulle. *Accouche! l'ulb revisite la natalité*. February 2019. URL: https://dailyscience.be/28/02/2019/accouche-lulb-revisite-la-natalite/ (visited on 30th July 2024) (cit. on p. 35).

[48] Olivia Campbell. *How a French midwife solved a public health crisis*. March 2020. URL: https://daily.jstor.org/how-a-french-midwife-solved-a-public-health-crisis/ (visited on 30th July 2024) (cit. on p. 36).

[49] Margot Cooper. *Limbs and things*. URL: https://limbsandthings.com/uk (visited on 30th July 2024) (cit. on p. 36).

[50] Lings and Things. *Birthing Simulator PROMPT Flex - Standard*. URL: https://limbsandthings.com/uk/products/80100/80100-birthing-simulator-prompt-flex-standard-light-skin-tone?cat=ranges&subcat=prompt-flex (visited on 30th July 2024) (cit. on p. 36).

[51] Olivier Dupuis et al. 'Birth simulator: Reliability of transvaginal assessment of fetal head station as defined by the American College of Obstetricians and Gynecologists classification'. In: *American Journal of Obstetrics and Gynecology* 192 (3 March 2005), pp. 868–874. ISSN: 00029378. DOI: 10.1016/j.ajog.2004.09.028. URL: https://www.sciencedirect.com/science/article/pii/S0002937804010488 (visited on 29th July 2024) (cit. on pp. 36 sq., 42 sq.).

[52] J.-D. Boissonnat and B. Geiger. '3D simulation of delivery'. In: *Proceedings Visualization '93*. IEEE Comput. Soc. Press, pp. 416–419. ISBN: 0-8186-3940-7. DOI: 10.1109/VISUAL.1993.398903 (cit. on pp. 37 sq.).

[53] Jean-Daniel Boissonnat and Bernhard Geiger. 'Three-dimensional reconstruction of complex shapes based on the Delaunay triangulation'. In: ed. by Raj S. Acharya and Dmitry B. Goldgof. July 1993, pp. 964–975. DOI: 10.1117/12.148710 (cit. on p. 37).

[54] Rudy Lapeer et al. 'A computer-based simulation of childbirth using the partial Dirichlet-Neumann contact method with total Lagrangian explicit dynamics on the GPU'. In: *Biomechanics and Modeling in Mechanobiology* 18 (3 June 2019), pp. 681–700. ISSN: 1617-7959. DOI: 10.1007/s10237-018-01109-x (cit. on pp. 38 sq.).

[55] Chuang-Yen Huang et al. 'Investigating the Effects of Different Sizes of Silicone Rubber Vacuum Extractors during the Course of Delivery on the Fetal Head: A Finite Element Analysis Study'. In: *Polymers* 14.4 (2022). ISSN: 2073-4360. DOI: 10.3390/polym14040723. URL: https://www.mdpi.com/2073-4360/14/4/723 (cit. on pp. 40 sq.).

[56] Rudy J. Lapeer, M.S. Chen and J. G. Villagrana. 'Simulating Obstetric Forceps Delivery in an Augmented Environment'. In: *Augmented environments for Medical Imaging including Augmented Reality in Computer-aided Surgery (AMI ARCS'04)* (2004) (cit. on pp. 41 sq.).

[57] Olivier Dupuis et al. 'A new obstetric forceps for the training of junior doctors: A comparison of the spatial dispersion of forceps blade trajectories between junior and senior obstetricians'. In: *American Journal of Obstetrics and Gynecology* 194 (6 June 2006), pp. 1524–1531. ISSN: 00029378. DOI: 10.1016/j.ajog.2006.01.013. URL: https://www.sciencedirect.com/science/article/pii/S000293780600055X (visited on 29th July 2024) (cit. on pp. 42 sq., 149).

[58] Gary Cunningham et al. 'Normal Labor'. In: 24th ed. McGraw-Hill, June 2014 (cit. on p. 44).

[59] Gary Cunningham et al. 'Diseases and Injuries of the Term Newborn'. In: 24th ed. McGraw-Hill, June 2014. ISBN: 978-0-07-179893-8 (cit. on p. 44).

[60] Gregg K. McPherson and Timothy J. Kriewall. 'The elastic modulus of fetal cranial bone: A first step towards an understanding of the biomechanics of fetal head molding'. In: *Journal of Biomechanics* 13 (1 January 1980), pp. 9–16. ISSN: 00219290. DOI: 10.1016/0021-9290(80)90003-2 (cit. on pp. 44, 65).

[61] Gregg K. McPherson and Timothy J. Kriewall. 'Fetal head molding: An investigation utilizing a finite element model of the fetal parietal bone'. In: *Journal of Biomechanics* 13 (1 January 1980), pp. 17–26. ISSN: 00219290. DOI: 10.1016/0021-9290(80)90004-4 (cit. on p. 44).

[62] Audinis Vilius. 'Computer-based simulation of the effects of instrumental delivery on the fetal head'. PhD thesis. University of East Anglia, 2017 (cit. on pp. 45 sq., 149 sq.).

[63] O. C. Zienkiewicz, R. L. Taylor and J. Z. Zhu. 'The Standard Discrete System and Origins of the Finite Element Method'. In: Elsevier, 2013. ISBN: 978-1-85617-633-0. URL: https://app.knovel.com/hotlink/khtml/id:kt012EC0R1/finite-element-method/standard-discrete-system (cit. on p. 47).

[64] Dimitrios G. Pavlou. 'An Overview of the Finite Element Method'. In: Elsevier, 2015. ISBN: 9780128023860. DOI: 10.1016/C2014-0-03143-7. URL: https://linkinghub.elsevier.com/retrieve/pii/C20140031437 (cit. on pp. 47 sqq.).

[65] Nam H. Kim, Bhavani V. Sankar and Ashok V. Kumar. 'Direct Method - Springs, Bars, and Truss Elements'. In: 2nd ed. John Wiley and Sons, 2018. ISBN: 9781119078746 (cit. on pp. 47 sqq., 51 sq.).

[66] I. M. Smith, D. V. Griffiths and L. Margetts. 'Spatial Discretisation by Finite Elements'. In: 5th ed. John Wiley and Sons, 2014. ISBN: 978-1-119-97334-8 (cit. on p. 47).

[67] Blender Foundation. *Blender*. Version 2.93.5. 2022. URL: https://www.blender.org/ (visited on 17th June 2022) (cit. on pp. 53, 160).

[68] Blender 3.4 Manual. *Blender Documentation*. 2022. URL: https://www.blender.org/get-involved/documentation/ (visited on 22nd March 2023) (cit. on pp. 53, 175).

[69] Dassault Systems - SIMULIA. *Abaqus*. 2021. URL: https://www.3ds.com/products-services/simulia/products/abaqus/ (visited on 22nd March 2023) (cit. on pp. 53 sq.).

[70] Rudy Lapeer et al. 'A Computer-Based Simulation of Obstetric Forceps Placement'. In: *Medical Image Computing and Computer-Assisted Intervention - MICCAI 2014*. 2014, pp. 57–64. DOI: 10.1007/978-3-319-10470-6_8. URL: http://link.springer.com/10.1007/978-3-319-10470-6_8 (cit. on pp. 55 sq., 159).

[71] Leda Lacaria et al. '2.2 Contact Mechanics'. In: *Biomedical Methods*. De Gruyter, February 2023, pp. 21–64. DOI: 10.1515/9783110640632-003. URL: https://hal.science/hal-04761046 (cit. on p. 74).

[72] Barbara Burden and Maria Simons. 'Anatomy of male and female reproduction'. In: *Mayes' Midwifery*. 14th. Elsevier Health Sciences UK, 2011. Chap. 24. ISBN: 978-0-7020-3105-2 (cit. on p. 155).

[73] Blender 3.4 Manual. *Retopology*. Version 3.4. 2023. URL: https://docs.blender.org/manual/en/latest/modeling/meshes/retopology.html (visited on 21st March 2023) (cit. on p. 161).

[74] Dassault Systems - SIMULIA User Assistance 2021. *Input Syntax Rules*. 2021. URL: https://help.3ds.com/2021/english/dssimulia_established/SIMACAEMODRefMap/simamod-c-inputsyntax.htm?contextscope=all&id=ecde9f4bf49343aab624b547266addc4 (visited on 21st October 2022) (cit. on p. 167).

[75] Dassault Systems - SIMULIA User Assistance 2021. *About element library*. 2021. URL: https://help.3ds.com/2021/english/dssimulia_established/SIMACAEELMRefMap/simaelm-c-general.htm?contextscope=all (visited on 9th February 2023) (cit. on p. 169).

[76] Wavefront Technologies. *Wavefront OBJ*. 1992. URL: https://www.iana.org/assignments/media-types/model/obj,%20https://www.loc.gov/preservation/digital/formats/fdd/fdd000507.shtml (visited on 5th February 2023) (cit. on pp. 171, 173, 175).

[77] Blender 3.4 Manual. *OBJ file format*. Version 3.4. February 2023. URL: https://docs.blender.org/manual/en/latest/files/import_export/obj.html (visited on 4th February 2023) (cit. on pp. 173, 175).

[78] Blender 3.4 Manual. *Collada file format*. Version 3.4. February 2023. URL: https://docs.blender.org/manual/en/latest/files/import_export/collada.html (visited on 4th February 2023) (cit. on p. 175).

[79] Khronos Group. *Collada*. February 2023. URL: https://www.khronos.org/collada/ (visited on 4th February 2023) (cit. on p. 175).

[80] Blender 3.4 Manual. *Alembic file format*. Version 3.4. February 2023. URL: https://docs.blender.org/manual/en/latest/files/import_export/alembic.html (visited on 4th February 2023) (cit. on p. 175).

[81] Sony Pictures Imageworks and Lucasfilm Ltd. *Alembic*. Version 1.8.4. August 2012. URL: http://www.alembic.io (visited on 4th February 2023) (cit. on p. 175).

[82] Blender 3.4 Manual. *Universal Scene Description file format*. Version 3.4. February 2023. URL: https://docs.blender.org/manual/en/latest/files/import_export/usd.html (visited on 4th February 2023) (cit. on p. 175).

[83] Pixar Animation Studios. *Universal Scene Description*. Version 23.02. July 2016. URL: https://graphics.pixar.com/usd/release/index.html (visited on 5th February 2023) (cit. on p. 175).

[84] Blender 3.4 Manual. *SVG file format*. Version 3.4. February 2023. URL: https://docs.blender.org/manual/en/latest/files/import_export/grease_pencil_svg.html (visited on 4th February 2023) (cit. on p. 175).

[85] World Wide Web Consortium. *SVG*. 2001. URL: https://www.w3.org/Graphics/SVG/%20https://www.w3.org/TR/SVG11/ (visited on 5th February 2023) (cit. on p. 175).

[86] Blender 3.4 Manual. *PDF file format*. Version 3.4. February 2023. URL: https://docs.blender.org/manual/en/latest/files/import_export/grease_pencil_pdf.html (visited on 5th February 2023) (cit. on p. 175).

[87] Adobe Inc. *PDF*. June 1993. URL: https://www.iso.org/obp/ui/#iso:std:iso:32000:-2:ed-2:v1:en (visited on 5th February 2023) (cit. on p. 175).

[88] Blender 3.4 Manual. *STL file format*. Version 3.4. February 2023. URL: https://docs.blender.org/manual/en/latest/files/import_export/stl.html (visited on 5th February 2023) (cit. on p. 175).

[89] 3D Systems. *STL*. 1987. URL: https://www.3dsystems.com/quickparts/learning-center/what-is-stl-file (visited on 5th February 2023) (cit. on p. 175).

[90] Dassault Systems - SIMULIA User Assistance 2021. *Abaqus Part Module*. 2021. URL: https://help.3ds.com/2021/english/dssimulia_established/SIMACAECAERefMap/simacae-m-Prt-sb.htm?contextscope=all&id=5924070f9de6406ba73bf114e57fcadf (visited on 13th March 2023).

[91] Dassault Systems - SIMULIA User Assistance 2021. *Abaqus Part Sets*. 2021. URL: https://help.3ds.com/2021/english/dssimulia_established/SIMACAECAERefMap/simacae-c-prtconcset.htm?contextscope=all&id=4bfd53d494b340038649d6408095126d (visited on 13th March 2023).

[92] Dassault Systems - SIMULIA User Assistance 2021. *Abaqus Property Module*. 2021. URL: https://help.3ds.com/2021/english/dssimulia_established/SIMACAECAERefMap/simacae-m-Prp-sb.htm?contextscope=all&id=2ef91c2ae8564f41b49de847180837cf (visited on 13th March 2023).

[93] Dassault Systems - SIMULIA User Assistance 2021. *Abaqus Materials*. 2021. URL: https://help.3ds.com/2021/english/dssimulia_established/SIMACAECAERefMap/simacae-c-prppropmaterial.htm?contextscope=all&id=1b822c2e6d5844a8ba3849395fb89223 (visited on 15th March 2023).

[94] Dassault Systems - SIMULIA User Assistance 2021. *Abaqus Sections*. 2021. URL: https://help.3ds.com/2021/english/dssimulia_established/SIMACAECAERefMap/simacae-c-prppropsection.htm?contextscope=all&id=744765b14c0d40b78864fb04c90e1b6c (visited on 15th March 2023).

[95] Dassault Systems - SIMULIA User Assistance 2021. *Abaqus property Assignment*. 2021. URL: https://help.3ds.com/2021/english/dssimulia_established/SIMACAECAERefMap/simacae-c-prppropassign.htm?contextscope=all&id=8d80edc1fef84329b964459ec305c2d4 (visited on 15th March 2023).

[96] Dassault Systems - SIMULIA User Assistance 2021. *Abaqus Assembly Module*. 2021. URL: https://help.3ds.com/2021/english/dssimulia_established/SIMACAECAERefMap/simacae-m-Asm-sb.htm?contextscope=all&id=7e89ec29a4474037a21e91c9f9f449db (visited on 15th March 2023).

[97] Dassault Systems - SIMULIA User Assistance 2021. *Abaqus Step Module*. 2021. URL: https://help.3ds.com/2021/english/dssimulia_established/SIMACAECAERefMap/simacae-m-Sim-sb.htm?contextscope=all&id=017b2a3238374fdf900ac7ced572127a (visited on 22nd March 2023).

[98] The International System of Units. *Base Units (SI)*. 2022. URL: https://www.bipm.org/en/measurement-units/si-base-units (visited on 10th August 2022).

[99] BIMP. *Bureau International des Poids et Measures*. 2022. URL: https://www.bipm.org/ (visited on 9th August 2022).

[100] Łukasz Skotny. *What are the applications of Finite Element Analysis*. May 2019. URL: https://enterfea.com/applications-of-finite-element-analysis/.

[101] Paul Govaert. *Cranial Haemorrhage In The Term New Born Infant*. 1st. Mac Keith Press, 1994. ISBN: 9780521451499.

[102] Rudy Jacques Lapeer. *Contact mechanics simulation for obstetric forceps delivery*. November 2004. URL: https://www.researchgate.net/publication/260963523.

[103] Dimitrios G. Pavlou. *Essentials of the Finite Element Method*. Elsevier, 2015. ISBN: 9780128023860. DOI: 10.1016/C2014-0-03143-7. URL: https://linkinghub.elsevier.com/retrieve/pii/C20140031437.

[104] Jarek R. Rossignac. 'Specification, representation, and construction of non-manifold geometric structures'. In: *ACM SIGGRAPH 1996, Course 29: Representation of Geometry for Computer Graphics* (May 1996). URL: https://faculty.cc.gatech.edu/~jarek/papers/SIG96sgc.pdf.

[105] The International System of Units. *SI Brochure*. 2019. URL: https://www.bipm.org/en/publications/si-brochure (visited on 13th August 2022).

[106] Antonio Malvasi et al. 'Asynclitism: a literature review of an often forgotten clinical condition'. In: *The Journal of Maternal-Fetal and Neonatal Medicine* 28 (16 November 2015), pp. 1890–1894. ISSN: 1476-7058. DOI: 10.3109/14767058.2014.972925.

[107] Richard T. Barret. 'Fastener Design Manual'. In: *NASA Reference Publication 1228* (March 1990). URL: https://ntrs.nasa.gov/api/citations/19900009424/downloads/19900009424.pdf (visited on 19th May 2023).

[108] A S Moolgaoker, S O Ahamed and P R Payne. 'A comparison of different methods of instrumental delivery based on electronic measurements of compression and traction.' In: *Obstetrics and gynecology* 54 (3 September 1979), pp. 299–309. ISSN: 0029-7844.

Alphabetical Index